

# Stellar weak interaction processes at finite temperature based on the relativistic energy density functional theory

---

Ravlić, Ante

Doctoral thesis / Disertacija

2023

Degree Grantor / Ustanova koja je dodijelila akademski / stručni stupanj: **University of Zagreb, Faculty of Science / Sveučilište u Zagrebu, Prirodoslovno-matematički fakultet**

Permanent link / Trajna poveznica: <https://um.nsk.hr/um:nbn:hr:217:972559>

Rights / Prava: [In copyright](#)/[Zaštićeno autorskim pravom.](#)

Download date / Datum preuzimanja: **2025-03-11**



Repository / Repozitorij:

[Repository of the Faculty of Science - University of Zagreb](#)





University of Zagreb

University of Zagreb  
Faculty of Science  
Department of Physics

Ante Ravlić

**Stellar weak interaction processes at finite  
temperature based on the relativistic  
energy density functional theory**

DOCTORAL DISSERTATION

Zagreb, 2023



University of Zagreb

University of Zagreb  
Faculty of Science  
Department of Physics

Ante Ravlić

**Stellar weak interaction processes at finite  
temperature based on the relativistic  
energy density functional theory**

DOCTORAL DISSERTATION

Supervisor:  
prof. dr. sc. Nils Paar

Zagreb, 2023



Sveučilište u Zagrebu

Sveučilište u Zagrebu  
Prirodoslovno-matematički fakultet  
Fizički odsjek

Ante Ravlić

**Procesi slabog međudjelovanja u  
zvijezdama u teoriji relativističkog  
nuklearnog energetskeg funkcionala  
gustoće**

DOKTORSKI RAD

Mentor:  
prof. dr. sc. Nils Paar

Zagreb, 2023

# Supervisor information

Nils Paar graduated physics study programme (Mag. phys.) at the Faculty of Science (PMF) of the University of Zagreb in 1998. From 2000 to 2003, he was a doctoral student at the Physik Department, Technische Universitaet Muenchen, Germany, where he defended his doctoral dissertation in theoretical nuclear physics in 2003, and obtained the academic title of Doctor rerum naturalium. From 2003 to 2006, he was postdoctoral researcher at the Institut fuer Kernphysik, Technische Universitaet Darmstadt, Germany. After returning to Croatia, he worked as an assistant professor (until 2008), associate professor (until 2013) and full professor (until today) at the Department of Physics, Faculty of Science of the University of Zagreb. In academic year 2014/2015 he was a Marie Curie research fellow at the Departement Physik, Universität Basel, Switzerland. Most of the scientific activity of Prof. Paar is in development and application of nuclear theory, especially for (1) non-linear phenomena in the vibrations of the atomic nucleus, (2) exotic excitations in unstable atomic nuclei, (3) weak interaction processes in supernova evolution, (4) neutrino-nucleus interaction, and (5) symmetry energy and neutron star properties. He is the author and co-author of 134 scientific publications, of which 88 original scientific papers were published in international peer-reviewed scientific journals, cited more than 3900 times according to the ISI Web of Science. He actively participated in international scientific conferences, workshops and schools, where he delivered 64 lectures, of which 33 were invited lectures. He was the leader of a number of competitive scientific research projects and mentor to numerous students on graduate and doctoral studies in physics, as well as postdoctoral researchers and visiting scientists from abroad. He received the state award for science for a significant scientific achievement in physics for 2017.

## Acknowledgements

I am deeply grateful to my supervisor, Prof. Nils Paar, for his support throughout my PhD work. He provided excellent guidance, numerous comments, and ideas that helped me to develop as a researcher.

I thank Prof. Tamara Nikšić, who has always found time for our discussions. Her guidance has helped me to accomplish much of the work.

Continuous support by Prof. Esra Yüksel is gratefully acknowledged. Her comments, corrections, and work on our models and publications have immensely helped. She was also an excellent host during my stay in Istanbul on two occasions. Thanks to Prof. Yifei Niu for inviting me to her research group in Lanzhou, China. Without her support throughout my PhD study, my understanding of the nuclear structure theory wouldn't be at the same level.

Furthermore, thanks to Prof. Remco Zegers and Prof. Witek Nazarewicz for their support during my stay at Michigan State University. I am also grateful for the discussions with Simon Giraud and Sylvester Agbemava. I thank Evan Ney for numerous discussions on the finite-temperature QRPA.

Part of the deformed FT-pnRQRPA was completed during my visit to GSI in Darmstadt, for whose support I am thankful to Prof. Gabriel Martínez-Pinedo. Thanks to Diana and Luis for all the discussions and fun we had.

I thank all my collaborators, Prof. Gianluca Colò, Prof. Elias Khan, Prof. Peter Ring, Prof. John Engel, Dr. Tomohiro Oishi, and others, for their contributions to our published (and soon-to-be) papers.

Special thanks to my office colleagues from F28, Ana, Lucija, Marija, Ivan, and Domagoj, on our "trač" parties. Also, to my friends from Ruđer, Nikola, Luka, Tea, Josipa, Neven, Igor, Deša, Isabela, and Margareta, thank you for all the coffee and cakes!

My mother Marijana and father Dobroslav deserve a special mention in this thesis. Thank you for everything! Just a few more postdocs and I can probably stand on my own feet.

And last, I am very grateful to have shared my PhD journey with Ivana. She celebrated with me when the code was working, comforted me when it wasn't, and helped to nurture my passion for science.

This work is supported by the QuantiXLie Centre of Excellence, a project co-financed by the Croatian Government and European Union through the European Regional Development Fund, the Competitiveness and Cohesion Operational Programme (KK.01.1.1.01.0004).

# Abstract

The processes mediated by the weak interaction have significant implications in nuclear physics, astrophysics, and particle physics. In particular, the electron capture (EC) plays a prominent role in driving the dynamics of core-collapse supernovae, while the  $\beta$ -decay determines the time scale of the nuclear r-process. Both processes are influenced by the underlying nuclear structure through the spin-isospin excitations and the associated resonances. The main aim of this work is to establish a theoretical framework for obtaining the spin-isospin transition strength at finite temperature and its extension to the description of stellar electron capture and  $\beta$ -decay. The nuclear ground state at finite temperature is determined by solving either the relativistic Hartree-Bogoliubov (FT-RHB) or Hartree Baarden-Cooper-Schrieffer (FT-HBCS) equations, while the relativistic quasiparticle random-phase approximation (FT-pnRQRPA) in the charge-exchange channel is developed to determine the excited states. The new theoretical approach combines the effects of nuclear pairing, finite temperature, and deformation. The limits of nuclear stability (drip lines) for hot nuclei are studied within the FT-RHB supplemented with the subtraction of continuum. Investigated spin-isospin excitations include the Fermi and Gamow-Teller (GT) transitions. While the Fermi transitions display one resonance peak independent of temperature and deformation, the GT transition strength has a much richer structure, more sensitive to the temperature and deformation effects. When considering the spherically symmetric nuclei, the GT strength separates into a low-lying, and a resonance region, as exemplified for even-even tin isotopes. However, the deformation effects lead to a substantial fragmentation of the GT transition strength, as demonstrated for selected  $pf$ -shell nuclei, exhibiting a crucial role of the nuclear shape. Results are presented for the EC rates of nuclei near the  $N = 50$  shell closure, with subsequent implications for the supernovae simulations. The large-scale  $\beta$ -decay rate calculations are shown for even-even nuclei in the range  $8 \leq Z \leq 82$ , displaying how the  $\beta$ -decay half-lives change with temperature and stellar density. Our study highlights the complex interplay between temperature, nuclear pairing, and deformation effects with subsequent implications for weak-interaction rates and their implementation in astrophysical models.

**Keywords:** relativistic energy density functionals, weak-interaction rates, electron capture, core-collapse supernovae,  $\beta$ -decay, nuclear pairing, hot nuclei, nuclear deformation, drip lines

# Prošireni sažetak

Procesi posredovani slabom nuklearnom silom su od velike važnosti za nuklearnu fiziku, kao i fiziku elementarnih čestica te astrofiziku. Takvi procesi primarno uključuju uhvat elektrona,  $\beta$ -raspade te reakcije između neutrina i jezgre. Uхват elektrona (EC) ima ključnu ulogu u evoluciji supernovi sa kolapsirajućom sredicom (CCSNe) odnosno kraja života masivnih zvijezda uzrokovanog propadanjem materijala iz vanjskih slojeva na kompaktnu sredicu zvijezde [1–3]. Evolucija CCSNe uglavnom ovisi o dva parametra: (i) omjeru broja elektrona i bariona ( $Y_e$ ) te (ii) entropiji sredice. Reakcije uhvata elektrona uklanjaju dostupne elektrone iz sustava te smanjuju  $Y_e$ , dok izlazni neutriini iznose entropiju iz sredice. Sredica masivne zvijezde se nalazi u delikatnoj ravnoteži između tlaka degeneriranog elektronskog plina i gravitacijskog privlačenja, sve dok joj masa ne dosegne Chandrasekharovu masu  $M_{ch}$ . U tom trenutku tlak degeneracije se više ne može oduprijeti gravitacijskom privlačenju i vanjski slojevi zvijezde propadaju na sredicu. Oni se zatim gotovo elastično odbijaju od sredice, koja ima gustoću sličnu gustoći nuklearne materije oko saturacije, i raspršuju u Svemir [1,2]. Ovisno o stopama uhvata elektrona mijenjat će se važni parametri koji određuju dinamiku kolapsa pa i same opservable kao što su masa nastale protoneutronske zvijezde te luminozitet izračenih neutrina [1,2]. S druge strane, tijekom razvoja zvijezde pred kolaps supernove,  $\beta$ -raspadi se mogu natjecati s uhvatom elektrona, budući da imaju podjednake vjerojatnosti odvijanja [3,4]. No kako se evolucija zvijezde nastavlja i gustoća postaje sve veća, fazni prostor  $\beta$ -raspada postaje značajno potisnutiji u odnosu na uhvat elektrona. S druge strane, na znatno nižim temperaturama,  $\beta$ -raspadi sudjeluju u stvaranju atomskih jezgara kroz brzi proces uhvata neutrona ( $r$ -proces) [5–7]. U nizu  $(n, \gamma)$  reakcija u uvjetima gdje su gustoće neutrona  $10^{20}$  g/cm<sup>3</sup> a temperature blizu milijardu kelvina nastaju neutronske bogate jezgre. Jednom kada vremenska skala uhvata neutrona bude usporediva s vremenom poluživota  $\beta$ -raspada, jezgra se raspada i  $r$ -proces nastavlja u novom izotopnom lancu. Zbog toga se obično kaže da  $\beta$ -raspadi određuju vremensku skalu  $r$ -procesu.

Teorijski opis atomske jezgre je zahtjevan pothvat, budući da se opis njezinih konstituenata



zasniva na teoriji kvantne kromodinamike (QCD). Na energetske skali nuklearnih procesa QCD je neperturbativna teorija što značajno otežava teorijske račune složenijih višečestičnih sustava. Stoga, danas postoje tri glavne teorijske metode. Prva su ab-initio modeli koji kreću od simetrija QCD-a da napišu najopćenitiji Hamiltonijan nukleon-nukleon interakcije, a zatim rješavaju kompliciranu višečestičnu Schrödingerovu jednadžbu [8–10]. Iako takvi modeli imaju značajan uspjeh u opisu nuklearne strukture lakih atomskih jezgara, jako komplicirane jednadžbe onemogućavaju primjenu ab-initio metoda na teže jezgre bez ozbiljnijeg smanjivanja konfiguracijskog prostora. S druge strane, imamo nuklearni model ljusaka koji se zasniva na teoriji srednjeg polja [11]. Naime, umjesto da gledamo ukupni potencijal kojeg generiraju svi nukleoni zasebno, možemo zamisliti da se jedan nukleon nalazi u efektivnom potencijalu (srednjem polju) kojeg generiraju svi ostali nukleoni. No, za detaljniji opis svojstava atomskih jezgara potrebno je Hamiltonijanu dodati i članove međudjelovanja koji značajno povećavaju dimenziju problema. Iako su se razvili numerički algoritmi koji omogućavaju dijagonalizaciju jako velikih matrica (reda  $10^9$ ), nuklearni model ljusaka je primjenjiv na jezgre do  $A \sim 80$ . Vjerojatno najekonomičniji model gledano s numeričke strane se zasniva na teoriji nuklearnog energetskog funkcionala gustoće (EDF) [12]. Teorija se zasniva na slici nukleona u srednjem polju a dodatne korelacije dolaze kroz samosuglasno rješavanje odgovarajućih jednadžbi gibanja. Teorija energetskih funkcionala gustoće (DFT) je prvi put korištena u fizici čvrstog stanja, zbog komplicirane strukture ne-lokalnog Fockovog člana, u do tada primarno zastupljenoj Hartree-Fock aproksimaciji. Temelji se na teoremima Hohenberga i Kohna [13] koji su dokazali da postoji funkcional gustoće  $E[\rho]$  koji je funkcija gustoće  $\rho$ , tako da njegova varijacija daje gustoću osnovnog stanja sustava. U fizici čvrstog stanja moguće je konstruirati egzaktni funkcional gustoće, budući da je interakcija kulonska. No u nuklearnoj fizici još nije moguće konstruirati funkcional gustoće krenuvši od nukleon-nukleon interakcije [14]. Stoga, funkcionali gustoće u nuklearnoj fizici su fenomenološki, što znači da se nepoznati parametri funkcionala određuju prilagodbom na eksperimentalne podatke. Postoje dva glavna tipa funkcionala gustoće u nuklearnoj fizici, to su relativistički i nerelativistički funkcionali. Nerelativistički funkcionali su zapisani pomoću jednočestičnih gustoća i struja, pri čemu zadovoljavaju općenite simetrije nukleon-nukleon interakcije [12]. S druge strane relativistički funkcionali poštuju načela Lorentz invarijantnosti [15, 16]. Formulirani su preko gustoće Lagrangiana i sastoje se od Diracovih spinora, koji omogućuju vezanje prostornih i spinskih komponenti valne funkcije. Bazirani su na teoriji kvantne hadrodinamike (QHD) koja pretpostavlja da su nukleoni točkaste Diracove čestice koje međudjeluju izmjenom mezona, poput izoskalarnog-skalarnog  $\sigma$ , izoskalarnog-vektorskog  $\omega$

i izovektorskog-vektorskog  $\rho$  mezona, zajedno s elektromagnetskim poljem [17, 18]. Teorija relativističkog srednjeg polja (RMF) se zasniva na razmatranju očekivanih vrijednosti mezonskih polja u osnovnom stanju jezgre, čime ona postaju klasična polja opisana odgovarajućim Klein-Gordonovim jednadžbama. Kako bi se postigao zadovoljavajući opis svojstava konačnih jezgara i nuklearne materije, potrebno je dodati nelinearne članove u gustoću Lagrangiana ili pretpostaviti vezanja ovisna o gustoći [15, 18]. Ovisnost o gustoći se može parametrizirati na fenomenološki način ili temeljeno na Dirac-Brueckner Hartree-Fock računima [15]. Primjerice, verzija relativističkog funkcionala gustoće sa izmjenom mezona i vezanjima ovisnima o gustoći, s DD-ME2 parametrizacijom, korištena je za račun svojstava osnovnog i pobuđenih stanja jezgara duž karte nuklida [19]. Drugu kategoriju funkcionala gustoće čine oni s točkastom interakcijom (PC), a dobiveni su razvijanjem mezonskih propagatora po odgovarajućim masama mezona [15]. Sastoje se od razvoja po bilinearnim kovarijantama Diracovog polja. Efekti nuklearnog medija se mogu uzeti u obzir ili kroz članove višeg reda ili vezanjima ovisnima o gustoći (DD-PC) [15, 16]. Najpoznatija parametrizacija DD-PC funkcionala je DD-PC1 [20]. Nedavno je razvijena i DD-PCX parametrizacija za čiju su prilagodbu osim svojstava osnovnog stanja jezgara korištena i pobuđena stanja [21]. Postoje i drugi tipovi relativističkih funkcionala kao što su oni s derivativnim vezanjima (DC), od kojih je najpoznatiji D3C funkcional [22]. Kako bi se razmatrale jezgre s otvorenim ljuskama potrebno je uključiti i nuklearnu interakciju sparivanja. Transformiranjem jednočestične baze u RMF teoriji u kvazičestičnu pomoću Bogoljubovljeve transformacije dobivamo relativističku Hartree-Bogoliubov (RHB) teoriju [23]. Zahvaljujući dobrom vezanju sa stanjima u kontinuumu, ona se može primijeniti na sve vezane jezgre, od doline stabilnosti pa sve do linija kapanja [23, 24]. U dijagonalnoj aproksimaciji, pri čemu Bogoljubovljeve matrice postaju realni brojevi, RHB teorija se svodi na Hartree Bardeen-Cooper-Schrieffer (HBCS) teoriju [24]. Njihova proširenja na konačnu temperaturu se nazivaju FT-RHB, odnosno FT-HBCS [25].

Pobuđena stanja jezgre možemo odrediti razmatranjem njenog odziva u vremenski ovisnom vanjskom polju. Jednadžbe koje opisuju vremensku evoluciju nuklearne gustoće se nazivaju vremenski-ovisne Hartree-Fock (TDHF) jednadžbe. Ako pretpostavimo harmoničnu vremensku ovisnost nuklearne gustoće i napravimo razvoj TDHF jednadžbe do linearnih članova u gustoći, izvodimo jednadžbe aproksimacije nasumičnih faza (RPA) [26]. Osim što razmatra doprinose nuklearnog srednjeg polja, RPA uzima u obzir i dvočestičnu rezidualnu interakciju. Krenuvši od potencijala srednjeg polja, pobuđena stanja se mogu konstruirati djelovanjem RPA fononskog operatora koji se sastoji od čestica-šupljina pobuđenja. U formalizmu funkcionala gustoće, rezidualna

interakcija se može izvesti konzistentno iz samog funkcionala, kao druga derivacija funkcionala po matrici gustoće [27]. Koristeći relativistički EDF izvodimo relativističku RPA (RRPA). Generalizacija RRPA na kvazičestična pobuđenja se naziva kvazičestična RRPA (RQRPA) [26]. Ona se može primijeniti na pobuđenja unutar iste jezgre ili u kanalu izmjene naboja (engl. charge-exchange), pri čemu govorimo o proton-neutron RQRPA (pnRQRPA) [27, 28].

Spinsko-izospinska pobuđenja su kolektivni vibracijski modovi koji povezuju prijelaze između različitih nabojnih stanja jezgara, pri čemu je ukupni spin ( $S$ ), izospin ( $T$ ), angularni moment ( $J$ ). Najpoznatija spinsko-izospinska gigantska rezonancija je Gamow-Teller (GT), koja predstavlja pobuđenje s  $J^\pi = 1^+$  između  $(Z, N)$  i  $(Z \pm 1, N \mp 1)$  jezgara, a eksperimentalno je prvi put otkrivena kao potpis u udarnom presjeku reakcija izmjene naboja poput  $(p, n)$  [29]. Osim što svojstva spinsko-izospinskih pobuđenja opisuju izovektorske članove  $NN$  interakcije, kao i nuklearnu energiju simetrije, njihova snaga određuje stope procesa posredovanih slabom silom, poput uhvata elektrona ili  $\beta$ -raspada [3].

Glavni cilj ovog doktorskog rada je razviti teorijski okvir za proučavanje procesa posredovanih slabom silom u ekstremnim astrofizičkim okruženjima. U tu svrhu teorijski model mora (i) sadržavati efekte konačne temperature, (ii) pravilno tretirati doprinose čestičnog kontinuuma, (iii) pravilno interpretirati različite tipove prijelaza na konačnoj temperaturi, poput de-ekscitacija te (iv) obuhvatiti važne efekte poput nuklearne interakcije sparivanja i deformacija.

Kao prvi korak prema ovom cilju, u poglavlju 3 razvili smo pnRQRPA u formalizmu linearnog odziva na konačnoj temperaturi (FT-pnRQRPA) pretpostavljajući sferične jezgre [30]. Formalizam linearnog odziva se zasniva na rješavanju Bethe-Salpeter jednadžbe koja određuje nuklearni odziv i rješava se inverzijom. Glavna prednost našeg modela je njegova numerička kompaktnost i brzina izvođenja računa. Naime, umjesto u konfiguracijskom prostoru kvazičestičnih pobuđenja, funkciju odziva smo definirali u koordinatnom prostoru pomoću separabilnih kanala interakcije. Takva definicija vrijedi ako se rezidualna interakcija može napisati kao suma produkata separabilnih članova, što je ispunjeno za relativističke točkaste interakcije. U reduciranom koordinatnom prostoru, dimenzija problema je znatno manja, što znači da je i odgovarajuća Bethe-Salpeter jednadžba manje zahtjevna za riješiti. Razvijeni model se temelji na funkcionalima s točkastim interakcijama poput DD-PC1 i DD-PCX. U kanalu sparivanja pretpostavljamo separabilnu interakciju sparivanja, koja ima isti oblik u izovektorskom ( $T = 1$ ) i izoskalaranom ( $T = 0$ ) kanalu. Snaga izoskalarne interakcije sparivanja nije određena na razini osnovnog stanja jezgre, stoga smo ju fiksirali na  $V^{is} = 1.5$ , što daje zadovoljavajući opis eksperimentalno određenih svojstava spinsko-izospinskih pobuđenja.

Izračune evolucije spinsko-izospinskih pobuđenja o temperaturi primijenili smo na parno-parne izotope kositra u intervalu temperature  $T = 0\text{--}1.5$  MeV. Pokazali smo da je Fermi funkcija snage gotovo neovisna o temperaturi i locirana u jednom vrhu rezonancije za sve razmatrane temperature. S druge strane, GT funkcija snage ima znatno kompliciraniju strukturu, pri čemu je snaga uglavnom raspodijeljena u dva vrha. Onaj na višim energijama predstavlja GT rezonanciju (GTR), dok je niskoenergetski vrh posljedica jake spin-orbit interakcije u jezgrama. Efekti temperature su jasno uočljivi u izotopima poput  $^{120}\text{Sn}$  i  $^{124}\text{Sn}$  gdje dolazi do fragmentacije GTR na niskim temperaturama. Povećanjem temperature na  $T = 0.9$  MeV fragmentacija nestaje. Glavni efekt temperature u razmatranim izotopima kositra je redukcija snage korelacija sparivanja koja iščezava na  $T_c^p \sim 1$  MeV. Usporedbom s eksperimentalno izmjerenom GT snagom u  $^{112}\text{Sn}$ ,  $^{116}\text{Sn}$  i  $^{132}\text{Sn}$  dobivamo slaganje centroida energije unutar 2 MeV.

Koristeći matrični FT-pnQRPA baziran na FT-HBCS u poglavlju 4, napravili smo izračune stopa uhvata elektrona na konačnoj temperaturi. Po prvi put, zajedno s efektima temperature, uključili smo efekte nuklearne interakcije sparivanja unutar relativističkog formalizma [31,32]. Prvo smo predstavili teorijski formalizam uhvata elektrona u tzv. dozvoljenoj aproksimaciji (engl. allowed approximation) gdje imamo doprinos samo GT prijelaza. Osim što model predviđa postojanje prijelaza između osnovnog stanja početne i konačne jezgre, na konačnoj temperaturi možemo imati i prijelaze između pobuđenih stanja. Posebna vrsta prijelaza su oni koji dolaze s negativnom energijom prijelaza, tzv. de-ekscitacije. Napravljeni su izračuni stopa uhvata u  $^{78}\text{Ni}$  u temperaturnom rasponu do 20 GK i relevantnom rasponu gustoća karakterističnih prije eksplozije supernove. Kod neutronske bogatih jezgara poput  $^{78}\text{Ni}$ , de-ekscitacije čine glavni doprinos stopama uhvata. Model smo nadogradili koristeći sofisticiraniju teoriju baziranu na struja-struja interakciji koja osim dozvoljenih uključuje i prve zabranjene prijelaze, zajedno s članovima ovisnima o prijenosu impulsa. Usporedbom s drugim teorijskim modelima dobili smo zadovoljavajuće rezultate. Model koji smo primijenili na globalne izračune zasniva se na D3C\* interakciji s Gogny interakcijom sparivanja u  $pp$  kanalu. Snaga sparivanja u osnovnom stanju  $V_{pair}$  određena je s obzirom na empirijske rascjepe sparivanja (engl. pairing gaps). U izoskalarnom kanalu rezidualne  $pp$  interakcije koristimo sličan oblik interakcije (suma dva Gaussijana) čija je snaga  $V^{is}$  određena iz globalne prilagodne na eksperimentalna vremena poluživota  $\beta$ -raspada. Model smo primijenili na račun stopa uhvata jezgara u okolini  $N = 50$  zatvorene ljske, koje su od velikog značaja za dinamiku CCSN [33]. Izračuni iz našeg relativističkog modela, zajedno s odgovarajućim nerelativističkim modelom su za  $^{86}\text{Kr}$  uspoređeni s  $GT^+$  snagom dobivenom iz modela ljsaka. Iako modeli bazirani na RPA

ne mogu reproducirati gustoću stanja iz modela ljusaka, opći trendovi funkcije snage pokazuju zadovoljavajuće slaganje između različitih modela. Stope uhvata smo iskoristili kao ulazne parametre za 1D simulaciju eksplozije CCSNe. Važne opservable, poput evolucije  $Y_e$  s gustoćom  $\rho$ , vršni luminozitet neutrina te masa sredice u trenutku eksplozije, pokazuju odlično slaganje između našeg relativističkog i nerelativističkog modela. Takav rezultat nas vodi na zaključak da su glavne korelacije u stopama uhvata elektrona dobro obuhvaćene unutar novo-razvijenih modela. To znači da su neodređenosti koje dolaze od modeliranja uhvata elektrona dobro ograničene. Naš relativistički pristup još uključuje i prve zabranjene prijelaze te smo pokazali da oni dovode do značajnijih promjena u opservablama supernova, primarno tako da povećavaju ukupne stope uhvata.

Nadalje, FT-HBCS+FT-pnRQRPA formalizam primijenili smo na račun  $\beta$ -raspada ovisan o temperaturi u zvijezdama u poglavlju 5. Na niskim temperaturama i gustoćama, usporedbom rezultata vremena poluživota s eksperimentalnim podacima, zaključili smo da naš model može dobro reproducirati eksperimentalne rezultate. Izračunali smo evoluciju vremena poluživota  $\beta$ -raspada o temperaturi do  $T = 1.5$  MeV, pri čemu smo pokazali da se vremena poluživota sustavno smanjuju s povećanjem temperature [34]. One jezgre koje imaju duga vremena poluživota na niskim temperaturama pokazuju najveće smanjenje. Takve jezgre se nalaze duž doline stabilnosti i oko zatvorenih ljusaka. S druge strane, jezgre koje imaju kratka vremena poluživota na niskim temperaturama, ne pokazuju značajne promjene s povećanjem temperature. Povećavanjem produkta zvjezdane gustoće i omjera broja elektrona i bariona  $\rho Y_e$  demonstrirali smo značajan porast vremena poluživota, koji primarno dolazi od reduciranja dostupnog faznog prostora za izlazne leptone. Konačno, napravili smo globalni račun vremena poluživota  $\beta$ -raspada za parno-parne jezgre  $8 \leq Z \leq 82$  za  $T = 5$  GK i 10 GK pri  $\rho Y_e = 10^7$  g/cm<sup>3</sup> i  $\rho Y_e = 10^9$  g/cm<sup>3</sup>, koji je od značaja za razne astrofizičke simulacije.

U poglavlju 6 proširujemo naša razmatranja na deformirane jezgre. Točnije ograničavamo se na aksijalnu deformaciju, kakvu pokazuje većina deformiranih jezgara. Prvo smo proširili RHB teoriju tako da obuhvaća i konačnu temperaturu (FT-RHB), a zatim smo implementirali Bonche-Levit-Vautherin (BLV) metodu suptrakcije kontinuuma [35–37]. Jednom kada se temperatura uključi u RHB račun, nukleoni se raspršuju iznad Fermijevog nivoa, a diktirano Fermi-Diracovom raspodjelom. Ako razmatramo slabo vezane jezgre (u blizini linija kapanja), čak i na niskim temperaturama može doći do slučaja gdje stanja u čestičnom kontinuumu ( $\varepsilon_i > 0$ ) imaju neiščezavajuće zauzeće stanja ( $v_i^2 > 0$ ). To dovodi do velikog problema, budući da je naša FT-RHB implementacija (kao i velika većina drugih) bazirana na razvoju Diracovih spinora u valne funkcije harmoničkog os-

cilatora. One nemaju dobro asimptotsko ponašanje valnih funkcija, što dovodi do krivog profila vektorske gustoće na većim udaljenostima od jezgre. Konkretno, javlja se doprinos nukleonskog plina, koji uzrokuje da naši rezultati ne konvergiraju s povećanjem baze (broja oscilatorskih ljusaka). Demonstrirali smo da BLV metoda dovodi do uklanjanja doprinosa nukleonskog plina i dobre konvergencije. Štoviše, opravdali smo korištenje oscilatorske baze unutar BLV metode usporedbom rezultata s odgovarajućom implementacijom u koordinatnoj bazi. Napravljeni su globalni računi svojstava jezgara u rasponu  $8 \leq Z \leq 104$  na temperaturama do 2 MeV, koristeći različite relativističke funkcionalne gustoće. Zaključili smo da povećanje temperature dovodi do (i) smanjivanja utjecaja korelacija sparivanja, (ii) faznog prijelaza pri čemu jezgre prelaze iz deformiranog u sferično stanje, (iii) iščezavanja magičnih brojeva i strukture ljusaka u jezgrama. Ovo posljednje dovodi do značajnih promjena u neutronske liniji kapanja s povećanjem temperature, pri čemu broj vezanih jezgara raste.

Kako bismo proučili utjecaj deformacije na pobuđena stanja jezgara razvili smo aksijalno-deformirani FT-pnRQRPA u formalizmu linearnog odziva. Iako sličan onome prezentiranom u poglavlju 7, razmatranje aksijalno-deformiranih jezgara zahtijeva važne promjene. Prvo, ukupni angularni moment  $J$  nije više dobar kvantni broj. No njegova projekcija na  $z$ -os,  $J_z \equiv K$ , je sačuvana. Ako pretpostavimo sačuvanje pariteta, i simetriju s obzirom na vremenski obrat, slijedi da je FT-pnRQRPA blok dijagonalna u  $K^\pi$  blokovima. Nadalje, broj separabilnih kanala koje treba uključiti u reduciranu odzivnu funkciju je znatno veći, budući da osim integracije u  $r$  smjeru, imamo i integraciju u  $z$  smjeru. Naš model smo primijenili na račun Fermi i GT funkcije snage, odnosno spinsko-izospinskih pobuđenja. Pokazali smo da je Fermi funkcija snage neovisna o deformaciji, dok GT funkcija snage pokazuje značajne promjene, prvenstveno fragmentaciju. Prvo, zanemarujući efekte temperature, napravili smo izračune  $GT^+$  snage u jezgrama  $pf$ -ljuske gdje su dostupni eksperimentalni podaci o distribuciji funkcije snage. Usporedbom sa sferičnim pnRQRPA računom, pokazali smo da razmatranje efekata deformacije dovodi do značajno boljeg slaganja između teorijskih izračuna i eksperimenta. Izračunali smo  $GT^-$  funkciju snage za  $^{58,60,62}\text{Fe}$  te za različite oblike jezgre dobivene RHB računom s kvadrupolnim ograničenjem (engl. constrained RHB). Oblik jezgre značajno utječe na izgled  $GT^-$  funkcije snage. Proširili smo naše istraživanje na konačnu temperaturu u rasponu do  $T = 2$  MeV te istražili utjecaj na  $GT^+$  pobuđenja za  $^{56}\text{Fe}$ . Račun za sfernu konfiguraciju ne pokazuje značajne promjene u funkciji snage s rastom temperature — ona je koncentrirana u jedan rezonantni vrh. Deformirani FT-pnRQRPA račun pokazuje značajne promjene već na  $T = 0.5$  MeV. Znatno bogatija struktura  $GT^+$  snage u deformiranom slučaju

je osjetljivija na manje promjene u temperaturi. Konačno, istražili smo kako deformacija utječe na vremena poluživota  $\beta$ -raspada. Oni su osjetljivi samo na uski raspon niskoležeće  $GT^-$  snage koja može doprinosti  $\beta$ -raspadu ( $Q_\beta$  prozor). Deformirana jezgra ima znatno veću gustoću stanja od sferične jezgre što dovodi do više prijelaza u  $Q_\beta$  prozoru. Naime, različite  $K$  projekcije u sferičnoj jezgri su međusobno degenerirane, dok u deformiranim jezgrama imamo razdvajanje  $K = 0$  i  $K = 1$  modova. Smjer tog razdvajanja (koji mod ide na višu energiju a koji na nižu) ovisi o geometriji jezgre. U svakom slučaju, deformacija dovodi do sustavnog smanjenja vremena poluživota  $\beta$ -raspada u odnosu na sferični pnRQRPA. Efekt smanjenja vremena poluživota zbog deformacije može biti veći od reda veličine. Takav zaključak vodi na potrebno smanjenje vrijednosti snage izoskalarne interakcije sparivanja  $V^{is}$  u odnosu na sferične račune.

Novorazvijeni teorijski formalizam u okviru ove doktorske disertacije uključuje efekte konačne temperature, nuklearne interakcije sparivanja te deformacije, čija međuigra može dovesti do novih i zanimljivih rezultata koji do sada nisu uočeni. Štoviše, sustavnim izračunima stopa uhvata elektrona duž karte nuklida i njihovom primjenom na simulacije supernovi s kolapsirajućom sredicom, napravili bismo prvo takvo istraživanje, gdje su sve jezgre izračunate koristeći jedan, samosuglasan model. Takvi rezultati bi bili od velikog značaja za nuklearnu astrofiziku. Utjecaj deformacije na  $\beta$ -raspade planiramo razmotriti u okviru simulacija nuklearnog  $r$ -procesa, što bi činilo direktnu poveznicu između našeg teorijskog modela i zastupljenosti kemijskih elementa u Svemiru.

**Ključne riječi:** relativistički energetske funkcionali gustoće, stope reakcija slabom silom, uhvat elektrona, supernove s kolapsirajućom sredicom,  $\beta$ -raspad, nuklearna interakcija sparivanja, vruće jezgre, nuklearna deformacija, linije kapanja

# Contents

<b>1</b>	<b>Introduction</b>	<b>1</b>
<b>2</b>	<b>Relativistic nuclear density functional theory</b>	<b>13</b>
2.1	The relativistic mean-field (RMF) theory . . . . .	15
2.2	Relativistic Hartree-Bogoliubov (RHB) theory . . . . .	25
2.2.1	The BCS approximation . . . . .	27
2.3	Extension to the finite-temperature RHB (FT-RHB) . . . . .	28
<b>3</b>	<b>Relativistic proton-neutron Quasiparticle Random-Phase Approximation (pnRQRPA) at finite temperature</b>	<b>34</b>
3.1	Linear response pnRQRPA . . . . .	38
3.1.1	Solving the linear response equations . . . . .	39
3.1.2	The DD-PC1(X) interaction with the separable pairing . . . . .	44
3.1.3	Angular momentum coupling . . . . .	48
3.2	Matrix FT-pnRQRPA . . . . .	51
3.3	Numerical tests . . . . .	53
3.4	Results . . . . .	56
<b>4</b>	<b>Stellar electron capture</b>	<b>62</b>
4.1	The allowed approximation . . . . .	63
4.2	Extension to the Walecka model . . . . .	70
4.3	Results . . . . .	73
4.3.1	Numerical techniques . . . . .	77
4.3.2	EC rates of the nuclei near $N = 50$ . . . . .	78
4.4	Implications for the core-collapse supernovae evolution . . . . .	83
<b>5</b>	<b><math>\beta</math>-decay rates in stellar environment</b>	<b>85</b>
5.1	Theoretical framework . . . . .	86
5.2	Results . . . . .	89



<b>6</b>	<b>Nuclear landscape at extreme temperatures</b>	<b>99</b>
6.1	The axially-deformed FT-RHB theory . . . . .	100
6.2	Continuum subtraction method . . . . .	104
6.2.1	Example calculations on a 1D model . . . . .	105
6.2.2	Comparison between the solvers based on the h.o. expansion and the coordinate-space solvers . . . . .	108
6.2.3	Continuum subtraction within the axially-deformed FT-RHB . . . . .	109
6.3	Results . . . . .	112
<b>7</b>	<b>The axially-deformed pnQRPA</b>	<b>124</b>
7.1	Theoretical formalism . . . . .	126
7.1.1	External field matrix elements . . . . .	127
7.1.2	Particle-hole matrix elements . . . . .	130
7.1.3	Particle-particle matrix elements . . . . .	133
7.1.4	Calculating the reduced response function $R_{cc'}$ . . . . .	136
7.2	Numerical tests . . . . .	139
7.3	Spin-isospin excitations in axially-deformed nuclei . . . . .	142
7.3.1	The Gamow-Teller resonance . . . . .	143
7.3.2	The Isobaric Analog Resonance . . . . .	151
7.4	Finite-temperature effects . . . . .	152
7.5	Influence of deformation on $\beta$ -decay half-lives . . . . .	156
<b>8</b>	<b>Conclusion</b>	<b>164</b>
<b>A</b>	<b>Linear response theory derivations</b>	<b>168</b>
A.1	Deriving the time-dependent Hartree-Fock-Bogoliubov equations . . . . .	168
A.2	Linear response equation in the proton-neutron basis . . . . .	169
A.3	Derivation of the interaction term $\mathbb{W}$ . . . . .	171
<b>B</b>	<b>Interpretation of the FT-pnQRPA strength function</b>	<b>176</b>
<b>C</b>	<b>Low-momentum transfer limit of the Walecka model</b>	<b>179</b>
<b>D</b>	<b>Shape factor for first-forbidden transitions</b>	<b>182</b>
	<b>Bibliography</b>	<b>192</b>
	<b>Curriculum Vitae</b>	<b>206</b>
	<b>List of Publications</b>	<b>209</b>

# List of Figures

2.1	The meson interaction vertices within the RMF theory. . . . .	16
3.1	The pnQRPA strength as calculated in the proton-neutron linear response formalism. Check Eq. (3.50). . . . .	43
3.2	The $GT^-$ strength function of $^{116}\text{Sn}$ at $T = 0.6$ MeV calculated with the FT-pnQRPA based on the linear response (red solid line) and the matrix formulation (blue peaks). Calculations are based on the FT-HBCS initial state with the delta-pairing interaction. Both implementations employ $N_{osc} = 10$ h.o. shells. . . . .	54
3.3	The $J^\pi = 0^+$ strength functions in $A = 112 - 122$ even-even tin isotopes with respect to the excitation energy of the parent nucleus for temperatures $T = 0, 0.5, 0.9$ and $1.5$ MeV, calculated by the linear response FT-pnQRPA using the DD-PC1 (upper panel) and DD-PCX (lower panel) interaction. Black arrows denote the experimental centroid energies from Ref. [95]. The figure is taken from Ref. [30]. . . . .	58
3.4	The $GT^-$ strength function for $^{112}\text{Sn}$ at zero temperature for changing values of the isoscalar pairing strength $V^{is}$ . Calculations are performed with the linear response pnQRPA using the DD-PCX interaction. . . . .	59
3.5	The $J^\pi = 1^+$ strength function for particular even-even tin isotopes with respect to the excitation energy of the parent nucleus for temperatures in the range $T = 0-1.5$ MeV, calculated by the linear response FT-pnQRPA using the DD-PCX interaction. The isoscalar pairing strength is set to $V^{is} = 1.5$ . Black arrows denote the experimental centroid energies from Refs. [95, 97]. The figure is taken from Ref. [30]. . . . .	61
4.1	The energy diagram for the EC between the initial ground state $E_i$ of the even-even $(Z, N)$ nucleus to the final excited state of the odd-odd $(Z - 1, N + 1)$ nucleus. See text for details. . . . .	65

- 
- 4.2 The temperature evolution of the GT strength in  $^{78}\text{Ni}$  as calculated by the FT-RMF+FT-RRPA with the D3C\* interaction. Red vertical line represents the  $Q$ -value threshold which separates the strength below the threshold (de-excitations) and strength above the threshold. Different panels (a)-(d) correspond to different temperatures in the range 0–2 MeV. The blue dashed line stands for the detailed balance temperature factor  $(1 - e^{-\beta\omega})$  [cf. Eq. (4.13)]. . . . . 67
- 4.3 The diagram demonstrates different kinds of transitions within the FT-pnRQRPA. The zero temperature pnRQRPA is characterized only by the transitions from the ground state of the parent nucleus to both the ground state and excited states in the daughter nucleus (blue transitions). The FT-pnRQRPA also introduces the transitions between excited states in the parent and daughter nuclei. They can be located above the  $Q$ -value threshold (red transitions) or below the threshold (violet transitions) in which case they are called the de-excitations. . . . . 68
- 4.4 The EC rates on  $^{78}\text{Ni}$  calculated within the allowed approximation assuming only the  $J^\pi = 1^+$  strength with respect to temperature  $T_9$  (denoting  $10^9$  K). Stellar densities are varied in the range  $10^8$ – $10^{11}$  g/cm $^3$ . Both  $\lambda_+^{ec}$  (red solid) and  $\lambda_-^{ec}$  (blue solid) are shown together with the total sum (black dashed). For comparison, data from Ref. [108] based on the TQRPA with SkM\* interaction is also shown. . . . . 70
- 4.5 The electron capture cross sections  $\sigma_e^+$  on  $^{78}\text{Ni}$  for the  $J^\pi = 1^+$  multipole calculated with the FT-RMF+FT-pnRRPA using the D3C\* interaction. Results between the allowed approximation (green dashed) are compared with the Walecka model results (red solid). . . . . 72
- 4.6 Same as in Fig. 4.4 but within the Walecka model including the  $J^\pi = 0^\pm, 1^\pm, 2^-$  multipoles. . . . . 73
- 4.7 The isotopic dependence of the pairing gaps  $\Delta_{uv}$  calculated using the HBCS and RHB with the Gogny D1S  $pp$  interaction and D3C\* EDF. The results for the HBCS are presented for the pairing strength  $V_{pair} = 1.15$  (blue) and  $V_{pair} = 1.25$  (orange), while the RHB results are calculated using the  $V_{pair} = 1.15$  (green) as in Ref. [23]. The experimental data (black triangles) are obtained by the 5-point formula with the binding energies from Ref [159]. . . . . 76
- 4.8 The neutrino spectrum distribution function  $n(E_\nu)$  for  $^{56}\text{Fe}$  at  $T_9 = 10$  with densities  $\rho Y_e = 10^8$  g/cm $^3$  (left panel) and  $\rho Y_e = 10^{11}$  g/cm $^3$  (right panel). Results are shown for different multipoles  $J^\pi$ . . . . . 79
- 4.9 The electron capture rates for  $^{56}\text{Fe}$  in the temperature range  $T_9 = 0$ – $10$  and the stellar densities  $\log \rho Y_e = 6$ – $12$ . The error bars denote the numerical integration error. The results are calculated using the FT-HBCS+FT-pnRQRPA with the D3C\* interaction. . . . . 80

4.10	(Left) The $GT^+$ strength in $^{86}\text{Kr}$ at $T = 0$ GK and $T = 10$ GK as a function of the transition energy $E_{if}$ calculated using the 3 theoretical models: (i) the relativistic FT-HBCS+FT-pnRQRPA (FT-PNRQRPA), (ii) the non-relativistic FT-HFB+FT-pnFAM (FT-QRPA) and the shell-model (SM). The red dashed line denotes the ground-state threshold energy. (Right) The temperature dependence of EC rates in $^{86}\text{Kr}$ at $\rho Y_e = 10^{11}$ g/cm <sup>3</sup> as calculated using the 3 theoretical models. In addition, the FT-PNRQRPA contains both the allowed (GT) and first-forbidden (GT+FF) transitions. The approx. and approx. mod refer to simple analytical expressions for the EC rates [33]. The figures are adapted from Ref. [33]. . . . .	81
4.11	(a) The part of the nuclide chart showing ratio between the EC rates calculated with the relativistic and non-relativistic QRPA calculations. (b) The ratio between the total EC rate including both the GT and first-forbidden transitions (GT+FF) and the EC rate which includes only the GT. The calculations are performed at $T_9 = 10$ and $\rho Y_e = 10^{11}$ g/cm <sup>3</sup> . The figure is adopted from Ref. [33]. . . . .	82
4.12	The results for the main observables of the CCSNe simulations using the GR1D code with NuLib [164, 170]. The different sets of EC rates for the diamond region nuclei are used (see text) for (a) the electron-to-baryon ratio $Y_e$ as a function of the central density $\rho$ , (b) the electron neutrino luminosity $L_{\nu_e^-}$ at radius of 500 km as a function of time after bounce, and (c) the central velocity as a function of the enclosed mass. The figure is adopted from Ref. [33]. . . . .	84
5.1	The energy diagram for the $\beta^-$ -decay between the initial state $E_i$ of the even-even parent nucleus to the final $m$ -th excited state of the odd-odd daughter nucleus. See text for details. . . . .	88
5.2	Comparison between the calculated (black) and experimental [159] (red) half-lives $T_{1/2}$ at zero temperature for titanium (a), iron (b), cadmium (c), and tin (d) isotopic chains. For Sn, we also show the results calculated by lowering the Landau-Migdal parameter $g'$ to 0.5 (green). We have adopted the figure from Ref. [34]. . . . .	90
5.3	(a)-(d) The temperature evolution of $\beta$ -decay half-lives in the temperature range $T = 0$ –1.5 MeV for selected even-even Ti, Fe, Cd and Sn isotopes. For $^{132}\text{Sn}$ , the red triangles label the FT-RTBA results from Ref. [135]. (e)-(h) Decomposition of the total rate $\lambda^\beta$ to contribution of allowed ( $1^+$ ) and first-forbidden ( $0^-$ , $1^-$ , $2^-$ ) multipoles for selected nuclei in respective isotopic chains. Calculations are performed at stellar density $\rho Y_e = 10^7$ g/cm <sup>3</sup> . Figure is adapted with permission from Ref. [34]. Copyrighted by the American Physical Society. . . . .	92
5.4	(a) The $GT^-$ strength function in $^{62}\text{Fe}$ at 5 GK (red bars) together with the corresponding phase-space factors at $\rho Y_e = 10^7$ g/cm <sup>3</sup> (dark red) and $10^9$ g/cm <sup>3</sup> (blue). (b) The $\beta$ -decay rate dependence of $^{62}\text{Fe}$ with respect to stellar density $\rho Y_e$ at $T = 0, 5$ and 10 GK. . . . .	93

5.5	Temperature dependence of the $\beta$ -decay rates for selected $pf$ -shell nuclei in the temperature range $T = 0\text{--}2$ MeV at $\rho Y_e = 10^7$ g/cm <sup>3</sup> (upper panels) and $\rho Y_e = 10^9$ g/cm <sup>3</sup> (lower panels). Results are calculated within the FT-HBCS+FT-pnRQRPA using the D3C* interaction (black dashed) and DD-ME2 (blue dash-dotted). Results are compared to LSSM [114] and shell model calculations based on the pf-GXPF1J interaction [126]. The figure is adopted from Ref. [34]. . . . .	94
5.6	The relative change (in %) of $\beta$ -decay half-lives at $T_9 = 5$ (a)-(c) and $T_9 = 10$ (b)-(d) with respect to zero temperature ( $T_9 = 0.01$ ) for $\rho Y_e = 10^7$ g/cm <sup>3</sup> (a)-(b) and $\rho Y_e = 10^9$ g/cm <sup>3</sup> (c)-(d). Only particle-bound even-even nuclei are shown in the range $8 \leq Z \leq 82$ . . . . .	96
6.1	Dependence of entropy $S$ (left panel) and the RMS neutron radius $\sqrt{\langle r_n^2 \rangle}$ on the box size $R_{box}$ with (blue circles) and without (red squares) the continuum subtraction procedure. Results are calculated for <sup>202</sup> Sm at $T = 1$ MeV using the DD-ME2 interaction and the FT-RMFBSPL solver. . . . .	106
6.2	The radial dependence of the total vector density $\rho_v$ (black) decomposed to the contribution of the Nucl+Vap system (red dashed) and Vap system (blue dotted), for $R_{box} = 30$ fm and 40 fm. Results are calculated for <sup>202</sup> Sm at $T = 1$ MeV using the DD-ME2 interaction and the FT-RMFBSPL solver. . . . .	107
6.3	Determining the optimal oscillator length $b_0$ that minimizes the subtracted free energy $\bar{F}$ for a changing number of h.o. shells $N_{osc} = 20\text{--}36$ . Also shown is the FT-RMFBSPL result (black straight line), which is independent of $b_0$ . The arrow indicates the optimal $b_0$ obtained from $\hbar\omega_0 = 41A^{-1/3}$ MeV. Results are calculated for <sup>202</sup> Sm at $T = 1$ MeV using the DD-ME2 interaction. . . . .	109
6.4	The isotopic dependence of the subtracted free energy $\bar{F}$ , entropy $\bar{S}$ , and neutron chemical potential $\lambda_n$ for samarium isotopes ( $Z = 62$ ) at $T = 2.0$ MeV. Calculations are performed using the FT-RMFHO with $N_{osc} = 20$ and FT-RMFBSPL with $R_{box} = 30$ fm employing the DD-ME2 interaction. . . . .	110
6.5	The potential energy surface of <sup>210</sup> Gd at $T = 0$ (a), 1 (b) and 2 MeV (c) calculated using the axially-deformed FT-RHB and $N_{osc} = 20, 24$ and 28 h.o. shells. No continuum subtraction is considered to demonstrate the convergence issues. The DD-ME2 interaction is employed. . . . .	111
6.6	Same as in Fig. 6.5 but with the subtracted free energy $\bar{F}$ calculated using the BLV continuum subtraction. . . . .	111
6.7	The temperature dependence of the isoscalar quadrupole deformation $\beta_2^{IS}$ across the nuclide chart at $T = 0, 0.5, 1.0$ and 2.0 MeV, calculated with DD-ME2, DD-PC1 and DD-PCX relativistic EDFs. . . . .	113

6.8	(a) The temperature evolution of the potential energy surface (PES) in $^{150}\text{Nd}$ in the temperature range $T = 0\text{--}2$ MeV, calculated with the DD-ME2 interaction. The $\Delta\bar{F}$ represents the relative subtracted free energy with respect to the minimum configuration. (b) The lowest occupied Nilsson states in $^{150}\text{Nd}$ for the optimal configuration $\beta_2^*$ for different temperatures, together with the spherical states at $T = 2$ MeV. . . . .	115
6.9	The total subtracted vector density $\bar{\rho}_v$ for $^{180}\text{Gd}$ and $^{210}\text{Gd}$ at $T = 0.5, 1$ and $2$ MeV for optimal $\beta_2^*$ . Insets show the potential energy surfaces constrained with respect to the isoscalar quadrupole deformation $\beta_2^{IS}$ for each density plot. . . . .	117
6.10	The isotopic dependence of entropy for $Z = 20, 60$ and $100$ for temperatures $T = 0.5, 1$ and $2$ MeV. The solid line denotes calculations with the axially-deformed FT-RHB, while the dotted line represents spherical FT-RHB (only shown for $T = 1$ and $2$ MeV). . . . .	118
6.11	The temperature evolution of entropy $S$ (red) and excitation energy $E^*$ (blue) for $^{150}\text{Nd}$ (a) and $^{126}\text{Sn}$ (b). The dotted lines show the fitting result of $T \geq 1.5$ MeV points on the Fermi gas model. Calculations are performed with the axially-deformed FT-RHB with the DD-ME2 interaction. . . . .	119
6.12	Temperature evolution of the two-neutron and two-proton drip lines for even-even $8 \leq Z \leq 104$ nuclei for temperatures $T = 0\text{--}2$ MeV. Results are calculated with the relativistic DD-ME2 EDF. Black squares denote the even-even stable nuclei [159]. Proton and neutron shell closure numbers are explicitly denoted. Inserted figure shows two-neutron separation energy $S_{2n}$ with increasing neutron number $N$ for cerium isotopic chain ( $Z = 58$ ) at temperatures $T = 0, 0.5, 1.0$ and $2.0$ MeV (using same color labels as in the main plot). Black dashed line denotes the drip-line condition $S_{2n} = 0$ . . . . .	120
6.13	(a)-(d) Two-neutron and two-proton drip lines calculated at $T = 0, 0.5, 1.0$ and $2.0$ MeV using three different parameterizations of the relativistic EDF: DD-ME2 (blue), DD-PC1 (red) and DD-PCX (orange). . . . .	122
7.1	Schematic pair selection for the Gamow-Teller transitions ( $J^\pi = 1^+$ ) for $K = 0$ (a) and $K = \pm 1$ (b). The angular momentum projections blocks $\Omega$ are separated for proton ( $\Omega_p$ ) and neutron ( $\Omega_n$ ) states. . . . .	129
7.2	Comparison between the spherical and axially-deformed pnRQRPA results for $^{28}\text{O}$ for the IAS $^-$ (a) and GT $^-$ (b) strength function, with $N_{osc} = 8$ oscillator shells. The strength function calculated with the spherical pnRQRPA is represented with red circles, while the solid line shows different components of the axially-deformed response: $K = 0$ mode is represented with solid blue and $K = 1$ mode with dashed green. The response function of the deformed FT-pnRQRPA is multiplied by 3 to account for degeneracy. . . . .	140

7.3	Comparison between the spherical and axially-deformed FT-pnRQRPA results at $T = 1$ MeV (a) and 3 MeV (b). Results are calculated for $^{28}\text{O}$ with $N_{osc} = 8$ and a modified pairing strength. . . . .	141
7.4	Convergence tests of the $\text{GT}^-$ strength for $^{70}\text{Fe}$ with $\beta_2 = +0.3$ for a varying number of oscillator shells $N_{osc}$ and no additional cut-off to the 2 q.p. basis. Results are shown for the $K = 0$ (a) and $K = 1$ (b) projections. . . . .	141
7.5	Convergence tests of the $K = 0$ $\text{GT}^-$ strength for $^{70}\text{Fe}$ with $\beta_2 = +0.3$ for $N_{osc} = 16$ and varying cut-off on 2 q.p. configuration energy $E_{cut}$ . . . . .	143
7.6	(a) The PES for $^{60}\text{Ni}$ as calculated with the axially-deformed RHB with the DD-PC1 interaction. Three stationary points (marked with an X) correspond to the oblate (blue), spherical (green), and prolate (red) configurations. (b) The $\text{GT}^+$ strength calculated from the corresponding stationary points in PES as a function of the excitation energy in the parent nucleus $\omega$ . . . . .	145
7.7	The $\text{GT}^+$ strength function for particular $pf$ -shell nuclei shown with respect to the excitation energy in parent nucleus $\omega$ . The calculations are performed with the axially-deformed pnRQRPA with DD-PC1 (blue) and DD-PCX (orange) interactions and the spherical pnRQRPA for the DD-PC1 interaction (green dashed). The results are compared with the available experimental data from Refs. [93,94,99,103] (black circles). The isoscalar pairing strength is set to $V^{is} = 0.8$ in all calculations. . . . .	146
7.8	The $\text{GT}^-$ strength function in selected even-even isotopes of iron, shown for the prolate (a)-(c), and oblate (d)-(f) configuration. The total strength function (solid black) is decomposed to the $K = 0$ (solid blue) and $K = 1$ (solid orange) projections of the total angular momentum $J = 1$ . Excitation energy $\omega$ is shown with respect to the ground state of the parent nucleus. . . . .	149
7.9	The total $\text{GT}^-$ strength function in $^{58}\text{Fe}$ , $^{60}\text{Fe}$ and $^{62}\text{Fe}$ , shown for the prolate (solid red), oblate (solid blue) and spherical (dashed green) configuration. Excitation energy $\omega$ is shown with respect to the ground state of the parent nucleus. . . . .	150
7.10	The $\text{IAS}^-$ strength function in selected even-even isotopes of iron, shown for the prolate, oblate, and spherical configuration. Excitation energy $\omega$ is shown with respect to the ground state of the parent nucleus. The experimental centroid energy from Ref. [206] is denoted with a black arrow. . . . .	151
7.11	(a)–(d) The potential energy surface in $^{56}\text{Fe}$ for temperatures $T = 0$ –2 MeV. The optimal deformation $\beta_2^*$ which minimizes the binding energy $E$ is denoted by a red circle. (e)–(h) Temperature evolution of the $\text{GT}^+$ strength distribution in $^{56}\text{Fe}$ calculated for optimal $\beta_2^*$ and temperatures $T = 0$ –2 MeV with the axially-deformed (solid blue) and spherical (dashed green) FT-pnRQRPA. Calculations are performed with the DD-PC1 interaction. The gray line in panels (e)–(h) is shown to guide the eye. . . . .	155

7.12	(a) The calculated values of the phase-space integral in Eq. (7.53) (red circles) together with a $N = 10$ polynomial fit (solid blue). (b) The circular contour for the complex integration of the rate integral in Eq. (7.52). (c) The $GT^-$ strength function in $^{44}\text{S}$ calculated with the axially-deformed pnRQRPA (solid black) decomposed to contributions of $K = 0$ (solid blue) and $K = 1$ (solid orange) projections. Also shown are the spherical pnRQRPA results (dashed green). (d) The real part of the integrand in Eq. (7.57) is calculated for $K = 0$ (blue circles) and $K = 1$ (orange circles). The solid lines denote the cubic spline interpolation of the calculated points.	158
7.13	(a) The isotopic dependence of the $\beta$ -decay half-lives $T_{1/2}$ for sulfur calculated with the axially-deformed (green) and spherical (blue) pnRQRPA, compared to the experimental data from Ref. [159]. Calculations are performed with the DD-PC1 interaction with isoscalar pairing strength $V^{is} = 1.0$ . (b) The axially-deformed pnRQRPA half-lives for different values of the isoscalar pairing strength $V^{is}$ in the range 0–1.2. The indicated area of the main plot is enlarged in the inserted axis for better visualization.	159
7.14	(a) Isotopic dependence of the quadrupole deformation $\beta_2^*$ for even-even nuclei in Ti, Cr, Fe, and Zn isotopic chains. The $\beta$ -decay half-lives calculated with the axially-deformed (green) and spherical pnRQRPA (blue), compared to the experimental data from Ref. [159] for Ti (b), Cr (c), Fe (d) and Zn (e) isotopic chains.	161
B.1	The schematic energy diagram concerning the transitions between the states in the parent nucleus $(i, f)$ and those in the daughter nucleus $(i', f')$ . Both the excitation transition $i \rightarrow f'$ dictated by the charge-exchange external field operator $\hat{F}$ and de-excitation transition $f \rightarrow i'$ dictated by $\hat{F}^\dagger$ are shown.	177



# List of Tables

2.1	The coupling parameters of the meson-exchange functionals used in this work, DD-ME2 [19], D3C [22] and D3C* [130]. . . . .	20
2.2	The coupling parameters of the point-coupling functionals used in this work, DD-PC1 [20] and DD-PCX [21]. . . . .	24
3.1	The comparison between the lrFT-QRPA and mFT-QRPA of the total $GT^-$ strength function $ \langle i \hat{F} 0\rangle ^2$ and contribution from the different 2 q.p. pairs $\langle i \hat{F} 0\rangle_{\pi\nu}$ for peak at $E = 17.16$ MeV in $^{116}\text{Sn}$ at $T = 0.6$ MeV. The integration is performed with 10 Simpson's integration mesh-points. The matching digits between the two calculations are boldfaced. . . . .	56
3.2	The neutron critical temperature $T_c^n$ and mean pairing gap $\Delta_n^0$ at zero temperature for even-even tin isotopes $A = 112-120$ . Results are calculated with the DD-PC1 and DD-PCX interactions. The table is adopted from Ref. [30]. . . . .	57
6.1	Comparison between the spherical and Nilsson basis numbers for a given principal number $N$ . Degeneracy of each shell in spherical basis is $2j + 1$ , while the degeneracy in Nilsson basis is 2. Number of nucleons contained in each shell is equal.	116
6.2	Number of even-even nuclei between the two-proton and two-neutron drip line in the range $8 \leq Z \leq 104$ , for DD-ME2, DD-PC1 and DD-PCX functionals at temperatures $T = 0, 0.5, 1.0$ and $2.0$ MeV. . . . .	122
7.1	The matrix elements of the external field Gamow-Teller operator in the basis of the axially-deformed harmonic oscillator for $K = 0$ and $K = 1$ . . . . .	129
7.2	Separable matrix elements of the isovector-vector (TV) interaction in the coordinate-space representation [cf. Eq. (7.18)]. We show the matrix elements for $pn$ and $\bar{p}\bar{n}$ types of transitions. . . . .	132
7.3	Same as in table 7.2 but for the TPV interaction. . . . .	132
7.4	Number of proton-neutron 2 q.p. pairs $N_{pair}$ for $K = 0$ and $K = 1$ projections of the Gamow-Teller response for an increasing number of oscillator shells $N_{osc}$ . . . . .	142
7.5	The optimal quadrupole deformation $\beta_2^*$ for particular $pf$ -shell nuclei using both the DD-PC1 and DD-PCX interactions. . . . .	148

# Chapter 1

## Introduction

The early attempts in understanding the nuclear structure date back to 1930s when C.F. Weizsäcker [38] and H. A. Bethe [39] postulated that nucleus can be described as a drop of incompressible liquid. They assumed that the total binding energy of the nucleus increases with its size (the volume term) and decreases proportional to its surface, and Coulomb repulsion between protons. In addition, one has to add the so called asymmetry term, which tells us that nucleus prefers states where the number of protons is close to the number of neutrons, as well as the pairing term which describes the odd-even staggering in nuclear masses [40, 41]. The latter two terms are purely quantal and stem from the fact that nucleons are fermions, and that nucleus is a superfluid system. By adjusting parameters of the liquid drop model to the available experimental data on nuclear masses, the first nuclear structure model was devised, able to extrapolate to the masses of yet unknown nuclei. However, it was noticed that such a model has large discrepancies between the predicted and measured masses of nuclei with specific number of protons and neutrons, corresponding to 8,20,28,50,82,...., which are called the magic numbers. To understand the occurrence of magic numbers, nuclear physicists had to establish a new theoretical model, taking into account correlations that go beyond the simple assumption that nucleus is a semi-classical liquid drop. One can imagine nucleus as a system of nucleons where each nucleon is thought of as being in an external field produced by the other nucleons around it. This means that a complex problem of solving a many-body Schrödinger equation for  $N$  nucleons was reformulated as solving  $N$  Schrödinger equations for only one nucleon in an external field. These kinds of models are called the *mean-field* models. Of course, one could go on and solve the many-body Schrödinger equation, but even if one could handle the complicated equations that resulted, the form of the underlying nucleon-nucleon interaction was unknown (and

still remains elusive). At the time, only the simplest systems with 2 and 3 nucleons, such as deuteron and  ${}^3\text{He}$  were solved [42, 43]. The first successful model of nuclear structure able to reproduce the magic numbers was the *shell-model* by Mayer and Jansen [44]. In order to reproduce the experimental data it required the addition of a strong spin-orbit potential. The spin-orbit effect was known previously from atomic physics, but its importance in nuclear physics was a novelty. The single-particle orbitals which nucleons occupy are split based on their total angular momentum  $j$ . This splitting caused a rearrangement of levels in such a way that gaps appeared between the certain numbers of nucleons. Those gaps exactly corresponded to the magic numbers. Therefore, a picture of nucleus in 1950s changed from a liquid drop to a quantum object where nucleons are occupying orbitals, corresponding to solutions of the mean-field equations, obeying the Pauli principle. Soon after the establishment of the theory of superconductivity in metals by Bardeen, Cooper and Schrieffer [45], Bohr, Mottelson and Pines realized that a similar theory could be applied to nuclear structure [46]. Theory of nuclear superconductivity could explain systematically increased energies of the first excited states in even-even open-shell nuclei, discrepancy between the moments of inertia calculated by the Inglis formula and experimental values [47, 48], measured spectroscopic factors in nucleon transfer reactions and others [49].

Today, no single microscopic theory exists to describe all experimentally discovered (and yet to be discovered nuclei) in great detail. In fact, the theoretical methods can be categorized in three main groups. First are the *ab-initio* models. Starting from the underlying symmetries of the QCD to write the most general Hamiltonian of the nucleon-nucleon interaction, they solve the resulting complicated many-body Schrödinger equation. The *ab-initio* theories include the no-core shell-model approaches [8], self-consistent Green function (SCGF) method and Green function Monte-Carlo (GFMC) methods [50, 51], the in-medium similarity renormalization group (IMSRG) theories [52] and coupled cluster theory [9]. Such models are characterized by a remarkable success in reproducing the experimental data on the structure of light nuclei [10]. However, due to great complexity of the underlying equations with increasing system size, application to heavier systems remains challenging. Another theoretical approach is the *nuclear shell-model* (SM), also known as the *configuration interaction* (CI) method. Today, shell-model calculations are based on a similar theory developed by Mayer and Jansen, however with significantly more complicated model interactions and configuration spaces. The dimension of the resulting Hamiltonian is intractably large (order of  $10^9$ ), requiring development of complicated numerical algorithms for its diagonalization. Therefore, the SM is applied to medium-mass nuclei ( $A \sim 80$ ) where it is able to reproduce the

experimentally measured transition strengths in great detail [11]. The third approach is based on the nuclear energy density functional (EDF) theory, starting from the picture of nucleons in a mean-field and providing additional correlations through the self-consistent solution of the underlying model equations [12]. Although today's EDFs are mostly phenomenological, and require adjusting their parameters to the available data, no other theoretical method compares even closely to the scalability of the EDF theory, therefore, it can be used for the study of nuclear properties throughout the nuclide chart.

The energy density functional theory (DFT) has its roots in solid-state physics. A well-established method in the field, the Hartree-Fock approximation was numerically very prohibitive, due to the non-local nature of the exchange term. To remedy this, Hohenberg and Kohn proved a series of theorems stating that there exists an energy functional  $E[\rho]$  which is a function of density  $\rho$ , such that its variation yields the ground-state density of the system  $\rho_{gs}$  [13]. However, the problem is that the theorem does not state how to construct such functional. In solid state physics where one deals with the Coulomb interaction, it is possible to find a form of this functional starting from the bare interaction (ab-initio). However, in nuclear physics, the interaction is a strong nuclear interaction and currently, its derivation from the first principles remains challenging [14]. The ground state density  $\rho_{gs}$  is only a function of three spatial coordinates, spin, and isospin, unlike  $5N$ , being the dimension of the  $N$ -body wave function. Therefore, the number of degrees of freedom within the DFT is independent of the system size, and the main advantage of the DFT is its excellent scalability. In fact, no other microscopic method is nearly computationally feasible as the DFT. It can be applied to the nuclei throughout the nuclear chart, either at the drip lines or in the valley of stability. It applies for medium mass as well as heavy nuclei [15, 16, 53]. However, one should be careful when applying the DFT to light nuclei since the fluctuations going beyond the mean-field become significant. Nevertheless, with proper projection methods, the DFT can be used to study the structure of very light nuclei [54–56]. The main object of the DFT is the energy density functional. There are two main categories of the EDFs in nuclear physics: (i) non-relativistic and (ii) relativistic. The most famous types of the non-relativistic EDFs are the Skyrme and Gogny, each consisting of numerous parameterizations [57]. They are written in the most general form in terms of one-body nuclear densities and currents, satisfying the general symmetries of the nucleus such as translational and Galilean invariance, angular momentum conservation in addition with time-reversal and space reflection invariance [58]. Both types are *phenomenological* functionals where the corresponding coupling constants are adjusted to a selected experimental data on finite nuclei and nuclear matter

properties. The Skyrme EDF is based on the underlying Skyrme interaction [59] consisting of a two-body and three-body interaction terms with zero-range. The Gogny interaction [60] is a finite-range interaction where the radial dependence of the interaction is represented in terms of a sum of two Gaussians. On the other hand, we have the relativistic EDFs. The main advantages of the relativistic treatment of a nucleus are: (i) a natural inclusion of nuclear spin and the strong spin-orbit coupling [61]. The relativistic wave functions are Dirac spinors consisting of both upper and lower components with coupled spatial and spin degrees of freedom. In the non-relativistic EDFs the spin-orbit term has to be added explicitly, together with the corresponding coupling strength. (ii) It provides a realistic account of the real part of the optical potential at intermediate energies [62], (iii) it offers a natural mechanism for the saturation of nuclear matter [19, 20, 22, 63], (iv) it offers to describe interaction of nucleus with other particles such as kaons, hyperons, antiprotons ... [64, 65], (v) it provides a natural explanation of the pseudospin symmetry in nuclei [66] and others [16]. The relativistic EDFs are based on the theory of *quantum hadrodynamics* (QHD) [67]. Starting from a field theory point of view, the Lagrangian density of the system is written in terms of nucleons, described as Dirac particles, that can exchange mesons in addition with the electromagnetic field. The mesons included correspond to energy scales that we are interested in nuclear physics, therefore, the theory is a form of an effective field theory, with interaction strength being reparameterized as to include the underlying degrees of freedom. For instance, a so-called *minimal set* of meson fields includes the isoscalar-scalar  $\sigma$ , isoscalar-vector  $\omega$  and isovector-vector  $\rho$  meson. This set constitutes a basis of the meson-exchange models, where exchange of each type of meson, together with its quantum numbers, corresponds to a region of the nucleon-nucleon ( $NN$ ) potential. The  $\sigma$  meson represents the two-pion exchange component of the  $NN$ -force corresponding to the intermediate-range attraction [68]. The  $\omega$  meson describes the repulsive part of the  $NN$ -interaction while the  $\rho$  meson determines its isovector properties. One could include more mesons in the consideration, however, there is no experimental data by which their interaction strength can be constrained. A minimal set of meson fields, together with the electromagnetic interaction and point-like Dirac nucleons constitutes the relativistic mean-field theory (RMF) first formulated by J. D. Walecka [17]. The meson fields are treated as classical by replacing their values with expectation values in the ground state. Although providing good qualitative description, such model was unable to predict nuclear properties with required precision [69]. Only after taking the in-medium effects into account by either adding non-linear terms to the Walecka model, within the so-called non-linear models, or by assuming the density dependence of coupling constants, the quantitative predictions of the

model became satisfactory [15, 18]. The density-dependence of the coupling constants can be either phenomenological or based on a Dirac-Brueckner Hartree-Fock calculations of nuclear matter properties [15]. For example, the density-dependent version of the meson-exchange (ME) RMF theory has been introduced and extensively used in studies of nuclear structure and dynamics [19, 70]. By reformulating it in terms of the ground-state density, and by calculating the energy-momentum tensor one obtains a covariant extension of the DFT. A very successful example is the DD-ME2 parameterization [19], that was applied to calculation of both ground-state and excited state properties throughout the nuclide chart. If we expand the ME functional in the power series of meson masses, replacing the meson propagators with the delta functions, we obtain the point-coupling (PC) functionals. The PC functionals consist of bilinear covariants in Dirac nucleon fields, where medium effects are either considered by adding higher powers of Dirac fields or by the density-dependence of coupling constants. Examples of the non-linear PC functionals are PC-PK1 [71] or PC-F1 [72], while the DD-PC1 is the density-dependent PC functional [20]. However, the RMF theory applies only to closed-shell nuclei. In order to consider open-shell nuclei, a Bogoliubov transformation from the single-particle to the quasi-particle basis has to be performed, yielding the relativistic Hartree-Bogoliubov (RHB) equations [23]. More fundamentally, using the Green function many-body methods, the RHB equations were derived by following the Gorkov factorization approach [73]. The RHB theory can be applied to bound nuclei throughout the nuclear chart [70, 74]. It combines the relativistic mean-field with the nuclear pairing interaction. Its main advantage is the proper coupling between the bound and continuum states of nuclei, thereby avoiding the unphysical results obtained by the simpler BCS approach [24].

The nuclear excited states can be determined by considering a nucleus in a time-dependent external field. Equations describing the time-dependence of the nucleon density are the time-dependent Hartree-Fock (TDHF) equations. By assuming a harmonic time-dependence of the external field and linearizing the TDHF equation keeping the terms linear in density, we obtain the random-phase approximation (RPA) [26, 58, 75]. Initially, the RPA was applied to study the giant resonances in nuclear excited states by employing the schematic model interactions [58, 76]. The main advantage of the RPA is that it allows treatment of the nuclear two-body residual interaction not included in the mean-field calculations. Starting from the appropriate mean-field vacuum, we can build the excited states by considering the one-particle one-hole excitations ( $1p1h$ ) satisfying the imposed selection rules by the external field operator, constituting the Tamm-Dancoff approximation (TDA). The RPA goes beyond the TDA by also taking into account not only the

direct residual interaction term  $v_{mjin}$  but also the exchange term  $v_{mjni}$ , representing the virtual  $2p2h$  excitations of the vacuum. The additional correlations within the RPA proved to be not only beneficial in reproducing the experimental data on nuclear excitations, but also by restoring the symmetries broken at the mean-field level, the so-called *spurious* modes [58]. The RPA can be built based on the ground-state EDF methods, determining the single-nucleon basis, and is also divided into non-relativistic [77–81] and relativistic RPA (RRPA) [27, 28]. Both approaches had significant success in describing both the like-particle and charge-exchange excitations for nuclear properties across the nuclide chart. In order to consider the open-shell nuclei one has to generalize the notion of  $1p1h$  excitations to quasi-particle excitations. The corresponding RPA equations in the quasiparticle basis are known as the QRPA equations. A great success of the RPA methods is reported in understanding the structure of the giant resonances, collective nuclear modes where multiple particle-hole excitations contribute coherently in determining the total strength [70]. Examples of the like-particle resonances are the giant electric monopole (IS)IVGMR, and giant dipole (IS)IVGDR resonances, either in the isoscalar (IS) or the isovector (IV) mode. The GMR is also known as the "breathing mode" and provides the information on the nuclear matter incompressibility  $K$  [82]. On the other hand, the isovector giant dipole resonance probes the symmetry energy of asymmetric nuclear matter in addition to the neutron skin thickness, *i.e.* the difference between the neutron and proton radii [83]. The spin-isospin excitations represent the collective mode where also the nuclear isospin is included in the vibrational mode, coupled through spin and orbital angular momentum degrees of freedom. The most famous spin-isospin resonance is the Gamow-Teller (GT) resonance [84]. Theoretically predicted earlier [85], it was experimentally confirmed through a  $^{90}\text{Zr}(p, n)^{90}\text{Nb}$  charge-exchange reaction in Ref. [29]. It is represented by the total angular momentum and parity number  $J^\pi = 1^+$ , and connects states in nuclei with different charges. In order to study such a mode, the RPA equations have to be extended to the so-called *proton-neutron* basis in the form of pnRPA equations [26]. The importance in theoretical description of spin-isospin excitations is in determining the isovector terms of the  $NN$  interaction as well as the nuclear symmetry energy [26]. Furthermore, their strength determines the rates of weak-interaction processes such as  $\beta$ -decay, electron capture, neutrino-nucleus reactions and scattering [1, 5]. Although microscopic, the weak-interaction rates can dictate dynamics of something as large as the explosions of massive stars and neutron star mergers.

The experimental study of spin-isospin excitations occurs through weak, strong, and electromagnetic probes [86]. Most effort is concentrated to Fermi and GT transitions. The weak-interaction

processes include the  $\beta^\pm$ -decay, limited to a small energy window determined by the transition  $Q$ -value ( $Q_\beta$  window). However, the connection between the measured half-lives and the GT strength function,  $B(\text{GT})$ , is well established and allows one to study the  $B(\text{GT})$  strength in nuclei far from stability [87]. The precise determination of  $B(\text{GT})$  value within the  $\beta$ -decay requires (i) precise knowledge of nuclear masses, (ii) measurement of half-life  $T_{1/2}$ , and (iii) determination of subsequent decay patterns [86]. With the development of Penning trap methods at Isotope Separator On-Line (ISOL) and fragmentation facilities in addition to storage rings, the nuclear masses are determined with high precision [88]. To measure the half-life, one studies the decay patterns of  $\gamma$ -decay or for more exotic nuclei, proton, or neutron emission. Most commonly, high-efficiency germanium detectors are employed to detect the emitted  $\gamma$ -rays [86]. With modern experimental facilities, one can pursue studies of the  $\beta$ -decays in exotic nuclei near the drip line, which have large  $B(\text{GT})$  values and  $Q_\beta$  window. One such example includes the  $^{100}\text{Sn}$ , whose  $B(\text{GT})$  was extracted from the  $\beta$ -decay at GSI Helmholtzzentrum für Schwerionenforschung, Germany, in Ref. [89], and at the RIKEN Nishina Center in Ref. [90].

Concerning the electromagnetic probes, it is possible to investigate the spin-isospin excitations through the spin part of M1 transitions. This can be realized either by the  $\gamma$ -decay, or the proton ( $p, p'$ ) or electron ( $e, e'$ ) inelastic scattering [86]. The spin part of the M1 transition operator has a structure like that of the GT [91]. However, the  $\gamma$ -decays and ( $e, e'$ ) inelastic scattering also excite the part corresponding to the orbital angular momentum, requiring special care.

The strong-interaction probes include the charge-exchange (CE) reactions of the type ( $p, n$ ) in the  $\beta^-$ , or ( $n, p$ ) in the  $\beta^+$  direction at intermediate beam energies ( $\sim 150$  MeV per nucleon) and  $0^\circ$  (low momentum transfer). Using the well-established relation of the differential cross-section at low-momentum transfer with the  $B(\text{GT})$  strength [92], they allow for the extraction of  $B(\text{GT})$  strength up to much higher excitation energies compared to  $\beta$ -decay. Some time ago, a significant number of experiments were conducted to investigate the GT strength in  $pf$ -shell nuclei using ( $n, p$ ) or ( $p, n$ ) and ( $^3\text{He}, t$ ) CE reactions [93–95], found near the valley of stability. However, with the advancement of the radioactive ion (RI) beams, the extraction of GT strength function in unstable isotopes has become possible [96, 97].

The experimental  $B(\text{GT})$  strength in the  $\beta^+$  direction provides important constraints for the electron capture (EC) rates. In the allowed approximation, the EC rate is theoretically well-described and determined by a product of the known phase-space factor and the  $B(\text{GT})$  strength [98]. The main focus of the experimental effort is on the nuclei whose EC rates significantly impact the



core-collapse supernovae (CCSNe) dynamics. Using the advanced  $\gamma$ -ray detectors the GT strength was precisely measured in  $^{64}\text{Zn}$  [99],  $^{93}\text{Nb}$  [100],  $^{45}\text{Sc}$  [101],  $^{86}\text{Kr}$  [102], and  $^{46}\text{Ti}$  [103] through the  $(t, ^3\text{He}+\gamma)$  reaction. Other reactions with measured GT strength of significance for CCSNe are listed in Refs. [104, 105]. Very recent experimental advances include the  $(d, ^2\text{He})$  reaction in inverse kinematics applied to  $^{14}\text{O}$  [106]. Thus, the combination of experimental efforts together with theoretical developments works together to provide better constraints for the CCSNe dynamics.

In order to consider processes mediated by the weak nuclear forces in extreme stellar environments, such as the interior of massive stars before the collapse (presupernova), the existing theoretical models have to be extended. Namely, the temperature in those environments can be high, of the order of MeV (10 billion kelvins), therefore, enough to influence the nuclear structure itself. On the other hand, nuclei can be found in excited states, and subsequent transitions from the excited states have to be explicitly considered. The stellar plasma consists of electrons and positrons which are in a thermal equilibrium determined by the interior properties. In order to consider the finite-temperature effects, the QRPA equations have to be extended by considering additional correlations which include transitions between the excited states both in initial and final nuclei [107]. The resulting set of equations has twice the dimension of the original problem, and is known as the finite-temperature QRPA (FT-QRPA). When extending the underlying RHB theory to finite temperature, which determines the initial nuclear state, we use the notion of thermal averages. The density matrix of the initial state is not simply a Slater determinant (product state), but is rather a mixture containing a sum over thermally excited states weighted by the Boltzmann factor. The corresponding equations of motion are known as the finite-temperature RHB (FT-RHB) [25]. Similarly, the FT-QRPA is derived by slightly perturbing the FT-RHB density and is also defined in terms of thermal averages. Therefore, one has to be careful when trying to obtain the physical strength from the FT-QRPA. In fact, there exist states with negative transition energy (*de-excitations*) which correspond to transitions from the highly excited states [31, 108]. Only after implementing all of the above considerations, we can employ our model to extreme stellar environments. In this work we focus on the electron capture and  $\beta$ -decay rates.

The electron capture plays a prominent role in the evolution of CCSNe, *i.e.* explosions of massive stars caused by the infall of material from outer layers on a compact core. H. A. Bethe [2] has demonstrated that evolution of the CCSNe depends mainly on two parameters: (i) electron-to-baryon ratio ( $Y_e$ ) and (ii) the core entropy. The EC reactions remove available electrons from the system thus lowering  $Y_e$ , while outgoing neutrinos carry out entropy from the core. The core of the

massive star is kept in a delicate equilibrium between the degeneracy pressure of the electrons and the gravitational attraction, until the core mass reaches the Chandrasekhar mass  $M_{ch} \sim Y_e^2$ . At that point the degeneracy pressure cannot hold the gravity any more and the core collapses. First steps in theoretical calculations of weak-interaction rates were made by Fuller, Fowler and Newmann (FFN) [109–112] in a set of 4 famous papers. By using the independent particle model, they have recognized the importance of EC in nuclei through Fermi and GT resonances. Prior to this work it was believed that the EC on free protons is of more significance than the capture on nuclei due to larger reaction rate. With the development in numerical techniques of the nuclear shell-model, significant amount of calculations were performed. First, Oda *et al.* [113] have tabulated weak-interaction rates for *sd*-shell nuclei. Later, this was extended to *pf*-shell nuclei by Langanke *et al.* [114] based on the large-scale shell-model (LSSM) calculations. Hindering the progress, one great disadvantage of the shell-model calculations is huge computational cost in order to describe neutron-rich nuclei due to enlargement of configuration space with increasing number of nucleons. In order to remedy this issue, the shell-model Monte Carlo (SMMC) approach was developed and EC rates have been calculated for allowed GT transitions in Ref. [115], however the model could not provide a detailed strength distribution. Juodagalvis *et al.* have calculated EC rates for roughly 2700 nuclei in presupernova environment [116] averaged over the Nuclear Statistical Equilibrium (NSE) distribution. Today, most simulations of the CCSNe dynamics employ the rate set of Juodagalvis. With the development of the RPA based on the EDF theory, the model calculations could be applied to heavier nuclei. Calculations were performed both with the non-relativistic [117, 118] and relativistic [32, 119] EDFs. However, those calculations did not consider pairing interaction, deformation, nor de-excitations, missing a considerable part of the strength function and were applied to only a handful of nuclei. Therefore, one of the main goals of this thesis is to develop a complete theoretical formalism for weak processes that will consider nuclear pairing, deformation, and finite temperature effects and also calculate rates for larger set of nuclei which can then be applied to astrophysical simulations of interest.

The nuclear  $\beta$ -decay stands out as one of the most important processes in understanding the nuclear weak-interaction. It was discovered at the end of the nineteenth century by the nuclear physics pioneers Henri Becquerel, Marie and Pierre Curie and Ernest Rutherford. Its profound implications for theoretical physics stem from the discovery of neutrino as well as the confirmation of the parity-violating character of the nuclear force [120]. Even nowadays, it still has a decisive role in nuclear astrophysics [5–7], particle physics [121, 122] and nuclear structure theory [123]. In

nuclear astrophysics it plays a main role in the rapid neutron capture ( $r$ -process) that is responsible for creating more than a half of chemical elements heavier than iron. The  $r$ -process occurs in explosive stellar environment where the temperature is measured in billions of degrees kelvin and neutron densities exceed  $10^{20}$  g/cm<sup>3</sup>. Such conditions allow for creation of extremely neutron rich nuclei in a series of  $(n, \gamma)$  reactions. The equilibrium is restored once the time-scale of the neutron capture becomes comparable with the  $\beta$ -decay lifetime. Therefore, it is often stated that  $\beta$ -decays determine the time-scale of the  $r$ -process. Nuclei that play an important role in the  $r$ -process are beyond the present experimental capabilities. In fact, the neutron drip line was experimentally reached only up to  $Z = 10$ , and possibly  $Z = 11$  [124]. This large discrepancy between the required and available experimental data necessitates robust theoretical calculations with excellent extrapolation ability across the nuclide chart. The  $\beta$ -decays have important role in the dynamics of the CCSNe, at times competing with the EC reactions [4]. As the collapse ensues the  $\beta$ -decay rates are severely Pauli blocked, while the EC rates increase. However, the equilibrium between the EC rates and  $\beta$ -decay rates sets the stage for the ongoing collapse of the star [125]. Both the CCSNe evolution and the  $r$ -process invite theoretical calculation of  $\beta$ -decay rates at high temperatures and densities. The developments of theoretical calculations for  $\beta$ -decay rates closely follow those of EC rates. Apart from different kinematics, the underlying interaction is the same. The independent-particle model of FFN [109–112] together with the LSSM calculations [114, 126] also included a tabulation of stellar  $\beta$ -decay rates. However, the shell-model calculations are limited to  $pf$ -shell nuclei. The large-scale calculations of  $\beta$ -decay half-lives were also performed with the QRPA on top of the finite-range droplet model (FRDM) [127]. In Refs. [77, 128, 129], the  $\beta$ -decay half-lives are calculated with the non-relativistic self-consistent QRPA. The pnQRPA based on the RHB with the D3C\* interaction was used to calculate the  $\beta$ -decay half-lives of neutron-rich nuclei near  $Z = 28$  and 50 shell closure [130]. The same model was later extended to the calculation of 5409 nuclei in the range  $8 \leq Z \leq 104$ , including GT and first-forbidden transitions [131]. The  $\beta$ -decay half-lives were also studied using the (quasi)particle-vibration coupling (QPVC) methods, which consider coupling to higher-order configurations going beyond the QRPA [132, 133]. Considerations of  $\beta$ -decay rates for hot nuclei are limited. In Ref. [134], the FT-pnQRPA was developed on top of the finite-temperature Skyrme-HF+BCS to determine the  $\beta$ -decay half-lives of  $N = 82$  isotones. However, they did not consider the contribution of first-forbidden transitions and the de-excitations, which become increasingly important at higher temperatures. The finite-temperature relativistic time-blocking approximation (FT-RTBA) was applied to study the  $\beta$ -decay half-lives of  $^{78}\text{Ni}$  and

$^{132}\text{Sn}$  up to  $T = 2$  MeV [135]. Although providing excellent agreement with experimental results at zero temperature, the FT-RTBA implementations are currently limited to spherical nuclei. In this thesis, we develop a theoretical formalism based on the FT-pnRQRPA to describe the  $\beta$ -decay half-lives in a stellar environment that includes nuclear pairing and deformation, as well as the finite temperature.

This thesis is organized as follows. In Chapter 2 we introduce the relativistic EDF theory, including both the finite temperature and pairing correlations. In Chapter 3, starting from the FT-RHB static limit, we perturb the nucleus in a charge-changing external field. The small-amplitude limit of the corresponding time-dependent equations yields the RQRPA equations in the proton-neutron basis at finite temperature (FT-pnRQRPA). Two methods of solving the FT-pnRQRPA equations are introduced, the linear response theory and the matrix FT-pnRQRPA. The linear response FT-pnRQRPA model is developed in the coordinate-space basis and spherical geometry, by assuming the relativistic point-coupling functionals and a separable pairing interaction. By transforming the resulting Bethe-Salpeter equation from the configuration to the space of the interaction channels, we obtain the equation for the reduced response, having a significantly smaller dimension compared to the original problem. The model calculations are benchmarked against the available matrix FT-pnRQRPA solvers and applied to the calculation of spin-isospin excitations in even-even tin isotopes. In Chapter 4 we give an overview of our work on the electron capture in stellar environment. Starting from the allowed approximation for the  $J^\pi = 1^+$  GT transitions, we demonstrate how to calculate the EC cross sections and rates within the FT-pnRQRPA. A proper treatment of finite-temperature effects in addition to de-excitations from highly excited states is crucial for description of EC rates. After exemplifying the model calculations in the allowed approximation we also include the first-forbidden transitions within the Walecka model [136], which introduces additional momentum-dependence in the transition matrix elements. We perform a calculation of both EC and neutrino energy loss rates for nuclei near the  $N = 50$  shell closure, and apply our results to the CCSNe simulations. As another weak-interaction process, we apply the FT-pnRQRPA to the calculation of the  $\beta$ -decay rates in stellar environment in Chapter 5. First, we present the theoretical framework, similar to the theoretical framework used in Chapter 4 for EC rates, but with different phase-space factors. Results are presented for systematic calculation of  $\beta$ -decay half-lives of even-even nuclei in the range  $8 \leq Z \leq 82$ , for temperatures and stellar densities relevant for extreme astrophysical processes. At very high temperatures  $T \sim 1$  MeV, the coupling of nuclear states to the particle continuum becomes very important, therefore in Chapter

6 we implement a continuum subtraction method in the FT-RHB, that removes the unphysical nucleon vapor. The model calculations are applied to the FT-RHB theory in axial-geometry. A systematic calculation of nuclear properties is performed in the temperature range  $T = 0-2$  MeV for even-even nuclei  $8 \leq Z \leq 104$ , to demonstrate that nucleus undergoes both pairing and shape phase-transitions as the temperature increases. Finally, in Chapter 7 we also generalize the FT-pnQRPA to axially-deformed nuclei. The model calculations are based on the linear response theory with point coupling functionals. It is shown that the approach demonstrated in Chapter 3 can be extended to axial-geometry, by increasing the dimension of the reduced response equations, and explicitly treating the time-reversed pairs. The resulting equations are significantly more complicated than the spherical pnQRPA equations, but still manageable on a moderate computer cluster. After benchmarking our model in the spherical limit, we apply it to calculate the spin-isospin excitations at both zero and finite temperature, as well as the  $\beta$ -decay half-lives. Additional formalism and derivations are presented in Appendices A–D.

# Chapter 2

## Relativistic nuclear density functional theory

The density functional theory (DFT) originates from the work of Hohenberg and Kohn [13], which proved that there exists an energy density functional  $E_s[\rho]$ , expressed in terms of density  $\rho(\mathbf{r})$  as [15, 16]

$$E_s[\rho] = F_{HK}[\rho] + \int d^3\mathbf{r} v_{ext}(\mathbf{r})\rho(\mathbf{r}), \quad (2.1)$$

where  $v_{ext}(\mathbf{r})$  is an external potential and  $F_{HK}$  functional independent of the system size. The boldfaced symbols denote the vectors in the coordinate space. The problem is that Hohenberg and Kohn have only shown the existence of  $F_{HK}$  and do not provide a method for obtaining it. By minimizing the energy density functional (EDF)  $E_s[\rho]$  with respect to the density  $\rho$ , and by solving the equations of motion self-consistently we obtain the ground-state density of the system  $\rho_{gs}(\mathbf{r})$ , which also includes the many-body correlations. In order to reproduce the shell effects, important in determining the nuclear magic numbers, Kohn and Sham have introduced the local single-particle potential  $v_{KS}[\rho](\mathbf{r})$ , such that the density of the system can be written as a sum over the single-particle auxiliary wave functions  $\phi_i[\rho](\mathbf{r})$  [137]

$$\rho(\mathbf{r}) = \sum_{i=1}^N |\phi_i[\rho](\mathbf{r})|^2, \quad (2.2)$$

where the summation goes over the single-particle occupied states  $i$ . Minimization of the  $E_s[\rho]$  leads to the Kohn-Sham (KS) equations [15, 16]

$$\left[ -\frac{\hbar^2}{2m} \nabla^2 + v_{KS}[\rho](\mathbf{r}) \right] \phi_i[\rho](\mathbf{r}) = \varepsilon_i \phi_i[\rho](\mathbf{r}), \quad (2.3)$$

where  $m$  is the nucleon mass and  $\varepsilon_i$  the single-particle energy. Therefore, a  $N$ -particle many-body equation has been reduced to  $N$  single-particle KS equations. Notice that the above equation has a form similar to the Schrödinger equation, although with interaction that depends on the density  $\rho(\mathbf{r})$ . In the case of relativistic EDFs, the KS equation corresponds to the single-particle Dirac equation. Since the KS potential  $v_{KS}[\rho]$  depends on the density, the equations are solved self-consistently. The exact functional  $F_{HK}[\rho]$  can be written as

$$F_{HK}[\rho] = T_s[\rho] + E_H[\rho] + E_{xc}[\rho], \quad (2.4)$$

where the first term corresponds to kinetic energy  $T_s$ , second term is the Hartree energy  $E_H$ , and all other correlations are included in the exchange-correlation term  $E_{xc}$ . The KS potential is obtained as

$$v_{KS}[\rho](\mathbf{r}) = \frac{\delta (E_H[\rho] + E_{xc}[\rho])}{\delta \rho}, \quad (2.5)$$

and the KS equations are solved until the convergence is reached. Although the DFT is similar to the Hartree-Fock (HF) theory, it avoids complicated calculations of non-local Fock terms. In principle, Fock terms are included in the exchange-correlation energy  $E_{xc}$ . The DFT is an exact theory for Coulombic systems, where the underlying interaction is known. However, in nuclear physics results depend on the chosen type of functional. The underlying theory describing the nucleon-nucleon ( $NN$ ) interactions is quantum chromodynamics (QCD). Unfortunately, at the energy scales relevant to nuclear physics, the QCD is highly non-perturbative. Therefore, calculations starting from the bare  $NN$  interactions are extremely computationally difficult and applicable only to the lightest nuclei. Even if one writes down the total  $NN$  interaction Hamiltonian consistent with the symmetries of the underlying QCD theory, the parameters of the Hamiltonian still have to be adjusted to the  $NN$  scattering data. Derivations of the EDFs starting from the  $NN$  interaction, the so-called *ab-initio* functionals, are still in development [14], and far from the required accuracy needed for practical calculations. Therefore, in this work, we resort to empirical functionals which contain contributions of nuclear densities and currents together with their expansion in gradient

terms, with parameter strengths adjusted to reproduce a handful of experimental data on finite nuclei and nuclear matter. In this work, we focus on relativistic functionals (also known as covariant) and refer the reader to Refs. [15, 18] for detailed review.

## 2.1 The relativistic mean-field (RMF) theory

The main ingredient for the calculation of ground-state properties within the relativistic EDF theory is the Lagrangian density which can be split into 3 parts [18]:

$$\mathcal{L} = \mathcal{L}_N + \mathcal{L}_m + \mathcal{L}_{int}, \quad (2.6)$$

where the first term represents nucleons as point-like Dirac particles

$$\mathcal{L}_N = \bar{\psi} (i\gamma^\mu \partial_\mu - m) \psi, \quad (2.7)$$

$\psi$  denotes the nucleon spinor and  $m$  its bare mass. In the following we work in the Minkowski metric where the metric tensor is defined as  $g_{\mu\nu} = \text{diag}(1, -1, -1, -1)$ . The second term is the meson term that describes fields of the free mesons (typically  $\sigma$ ,  $\omega$  and  $\rho$ ) as well as the electromagnetic field, and has the form

$$\begin{aligned} \mathcal{L}_m &= \mathcal{L}_\sigma + \mathcal{L}_\omega + \mathcal{L}_\rho + \mathcal{L}_A \\ &= \frac{1}{2} (\partial_\mu \sigma \partial^\mu \sigma - m_\sigma^2 \sigma^2) - \frac{1}{2} (\Omega_{\mu\nu} \Omega^{\mu\nu} - m_\omega^2 \omega_\mu \omega^\mu) \\ &\quad - \frac{1}{2} (\vec{R}_{\mu\nu} \vec{R}^{\mu\nu} - m_\rho^2 \vec{\rho}_\mu \vec{\rho}^\mu) - \frac{1}{4} F_{\mu\nu} F^{\mu\nu}, \end{aligned} \quad (2.8)$$

with the corresponding field tensors

$$\begin{aligned} \Omega^{\mu\nu} &= \partial^\mu \omega^\nu - \partial^\nu \omega^\mu \\ \vec{R}^{\mu\nu} &= \partial^\mu \vec{\rho}^\nu - \partial^\nu \vec{\rho}^\mu \\ F^{\mu\nu} &= \partial^\mu A^\nu - \partial^\nu A^\mu, \end{aligned} \quad (2.9)$$

$m_\sigma$ ,  $m_\omega$  and  $m_\rho$  being the  $\sigma$ ,  $\omega$  and  $\rho$ -meson masses, respectively. The arrows over symbols denote vectors in the isospin space, while the coordinate-space vectors are boldfaced. In principle, the pion field ( $\pi$ ) should be also included within the meson set, but due to keeping only the Hartree terms,



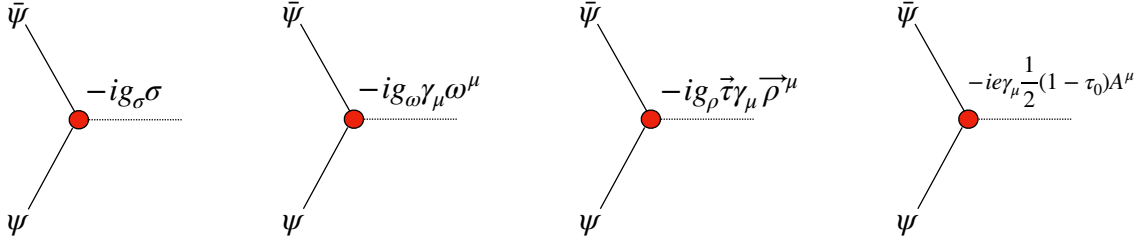


Figure 2.1: The meson interaction vertices within the RMF theory.

it drops out from the mean-field equations. The interaction term can be written in the general form

$$\mathcal{L}_{int} = -\bar{\psi}\Gamma_m\phi_m\psi, \quad (2.10)$$

where index  $m$  runs over different meson fields  $\phi_m \in \{\sigma, \omega_\mu, \vec{\rho}_\mu, A_\mu\}$ , and  $\Gamma_m$  is the interaction vertex. The meson vertex functions are shown in Fig. 2.1.

The equations of motion are obtained from the Euler-Lagrange equations

$$\partial_\mu \left( \frac{\partial \mathcal{L}}{\partial (\partial_\mu q_j)} \right) - \frac{\partial \mathcal{L}}{\partial q_j} = 0, \quad (2.11)$$

where  $q_j$  stands for either nucleon  $\psi_1 \dots \psi_A$  or meson  $\sigma, \omega, \vec{\rho}$ , and  $A$  fields. By varying  $\mathcal{L}$  with  $\bar{\psi}$  we obtain the single-particle Dirac equation [68]

$$[i\gamma_\mu \partial^\mu + V^\mu + m + S] \psi_i = 0, \quad (2.12)$$

where the scalar field is  $S(\mathbf{r}, t) = g_\sigma \sigma(\mathbf{r}, t)$  and the vector field is  $V^\mu(\mathbf{r}, t) = g_\omega \gamma_\mu \omega^\mu(\mathbf{r}, t) + g_\rho \vec{\tau} \gamma_\mu \vec{\rho}^\mu(\mathbf{r}, t) + e \gamma_\mu A^\mu(\mathbf{r}, t)$ . By varying with respect to meson fields we obtain a set of Klein-Gordon equations

$$\begin{aligned} [\square^2 + m_\sigma^2] \sigma(\mathbf{r}, t) &= -g_\sigma \rho_s(\mathbf{r}, t) \\ [\square^2 + m_\omega] \omega^\mu(\mathbf{r}, t) &= g_\omega j^\mu(\mathbf{r}, t) \\ [\square^2 + m_\rho] \vec{\rho}^\mu(\mathbf{r}, t) &= g_\rho \vec{j}^\mu(\mathbf{r}, t) \\ \square^2 A^\mu(\mathbf{r}, t) &= e j_c^\mu(\mathbf{r}, t), \end{aligned} \quad (2.13)$$

where  $\square^2 = \partial_t^2 - \nabla^2$ , and we have introduced the scalar density

$$\rho_s(\mathbf{r}, t) = \sum_{i=1}^A \bar{\psi}_i(\mathbf{r}, t) \psi_i(\mathbf{r}, t), \quad (2.14)$$

the vector current density

$$j^\mu(\mathbf{r}, t) = \sum_{i=1}^A \bar{\psi}_i(\mathbf{r}, t) \gamma^\mu \psi_i(\mathbf{r}, t), \quad (2.15)$$

with its time-like component being the vector density (known as baryon density)

$$\rho_v(\mathbf{r}, t) = \sum_{i=1}^A \bar{\psi}_i \gamma^0(\mathbf{r}, t) \psi_i(\mathbf{r}, t). \quad (2.16)$$

The isovector-vector current density is

$$\vec{j}^\mu(\mathbf{r}, t) = \sum_{i=1}^A \bar{\psi}_i(\mathbf{r}, t) \gamma^\mu \vec{\tau} \psi_i(\mathbf{r}, t), \quad (2.17)$$

and the electromagnetic current which has contribution only from proton states

$$j_c^\mu(\mathbf{r}, t) = \sum_{i=1}^A \bar{\psi}_i(\mathbf{r}, t) \frac{1}{2} (1 + \tau_0) \gamma^\mu \psi_i(\mathbf{r}, t), \quad (2.18)$$

where  $\tau_0$  is the third component of the isospin matrix  $\vec{\tau}$ . In the above expressions we perform summation only over occupied nucleon orbitals  $i = 1 \dots A$  in the Fermi sea, the so-called no-sea approximation [15, 18]. In the static approximation, the time-dependent meson fields can be written in the form

$$\psi_i(\mathbf{r}, t) = \psi_i(\mathbf{r}) e^{i\varepsilon_i t}. \quad (2.19)$$

Furthermore, assuming even-even nuclei with time-reversal invariance, the space-like components of vector currents  $\vec{j}, \vec{j}$ , and  $j_c$  vanish, while only the third component of isospin vectors,  $\tau_0$ , is non-vanishing. The single-particle Dirac equation in the static limit reduces to

$$[-i\boldsymbol{\alpha} \cdot \nabla + \beta(m + S) + V] \psi_i = \varepsilon_i \psi_i, \quad (2.20)$$

where  $\alpha, \beta$  are Dirac matrices. The Dirac equation can be written in a form of the eigenvalue problem  $\hat{h}\psi = \varepsilon\psi$ , where we have introduced the Dirac Hamiltonian  $\hat{h}$ . The time-independent Klein-Gordon equations for the time-like components of meson fields become

$$\begin{aligned} [-\nabla^2 + m_\sigma] \sigma(\mathbf{r}) &= -g_\sigma \rho_s(\mathbf{r}) \\ [-\nabla^2 + m_\omega] \omega^0(\mathbf{r}) &= -g_\omega \rho_v(\mathbf{r}) \\ [-\nabla^2 + m_\rho] \rho_0^0(\mathbf{r}) &= -g_\rho \rho_{tv}(\mathbf{r}) \\ -\nabla^2 A^0(\mathbf{r}) &= e\rho_c(\mathbf{r}), \end{aligned} \quad (2.21)$$

where the isovector and charge density are

$$\rho_{tv}(\mathbf{r}) = \sum_{i=1}^A \psi_i^\dagger(\mathbf{r}) \tau_0 \psi_i(\mathbf{r}), \quad \rho_c(\mathbf{r}) = \sum_{i=1}^A \psi_i^\dagger(\mathbf{r}) \frac{1}{2} (1 + \tau_0) \psi_i(\mathbf{r}), \quad (2.22)$$

respectively. The vector and scalar potentials in the static limit are

$$V(\mathbf{r}) = g_\omega \omega^0(\mathbf{r}) + g_\rho \tau_0 \rho_0^0(\mathbf{r}) + eA^0(\mathbf{r}), \quad S(\mathbf{r}) = g_\sigma \sigma(\mathbf{r}). \quad (2.23)$$

The set of equations (2.20) and (2.21) are known as the RMF equations. In order to reformulate the RMF equations to be more consistent with the nuclear DFT, we start by calculating the Hamiltonian density

$$\mathcal{H} = \sum_j \frac{\partial \mathcal{L}}{\partial \dot{q}_j} \dot{q}_j - \mathcal{L}, \quad (2.24)$$

where  $q_j \in \{\psi_1 \dots \psi_A, \sigma^0, \omega^0, \rho_0^0, A^0\}$  goes over the nucleon and meson fields. Finally, the relativistic EDF is constructed as

$$\begin{aligned} E_{RMF} [\psi_i, \bar{\psi}_i, \sigma, \omega^0, \rho_0^0, A^0] &= \int d^3r \mathcal{H}(\mathbf{r}) = \sum_{i=1}^A \int d^3r \psi_i^\dagger (-i\boldsymbol{\alpha} \cdot \nabla - \beta m) \psi_i \\ &+ \frac{1}{2} \int d^3r [(\nabla \sigma)^2 + m_\sigma \sigma^2] - \frac{1}{2} \int d^3r [(\nabla \omega^0)^2 + m_\omega^2 (\omega^0)^2] \\ &- \frac{1}{2} \int d^3r [(\nabla \rho_0^0)^2 + m_\rho^2 (\rho_0^0)^2] - \frac{1}{2} \int d^3r (\nabla A^0)^2 \\ &+ \int d^3r [g_\sigma \rho_s \sigma + g_\omega \rho_v \omega^0 + g_\rho \rho_{tv} \rho_0^0 + e\rho_c A^0]. \end{aligned} \quad (2.25)$$

In the following, assuming localized meson fields, we can express the gradients in above equations using Eq. (2.20) so that the EDF reduces to

$$\begin{aligned}
 E_{RMF} [\psi_i, \bar{\psi}_i, \sigma, \omega^0, \rho_0^0, A^0] &= \int d^3r \mathcal{H}(\mathbf{r}) \\
 &= \underbrace{\sum_{i=1}^A \int d^3r \psi_i^\dagger (-i\boldsymbol{\alpha} \cdot \nabla - \beta m) \psi_i}_{E_{kin}} \\
 &+ \underbrace{\frac{1}{2} \int d^3r g_\sigma \sigma \rho_s}_{E_\sigma} + \underbrace{\frac{1}{2} \int d^3r g_\omega \omega^0 \rho_v}_{E_\omega} + \underbrace{\frac{1}{2} \int d^3r g_\rho \rho_0^0 \rho_{tv}}_{E_\rho} + \underbrace{\frac{1}{2} \int d^3r e \rho_c A^0}_{E_{e.m.}},
 \end{aligned} \tag{2.26}$$

where the first term is the nucleon kinetic energy, and others correspond to interaction terms due to mesons and electromagnetic field. Following the prescription of the DFT the single-particle equations are now obtained by varying the EDF with respect to density. The first relativistic EDF we introduce is the density-dependent meson-exchange (DD-ME), which assumes that the couplings  $g_\sigma(\rho_v)$ ,  $g_\omega(\rho_v)$  and  $g_\rho(\rho_v)$  are functions of the vector density. When performing the variations, this leads to the Dirac equation of the form [18]

$$[-i\boldsymbol{\alpha} \cdot \nabla + V(\mathbf{r}) + \Sigma_R^0(\mathbf{r}) + \beta(m + S(\mathbf{r}))] \psi_i(\mathbf{r}) = \varepsilon_i \psi_i(\mathbf{r}), \tag{2.27}$$

where in addition to vector and scalar potential defined in Eq. (2.23) we also have the so-called *rearrangement* term [15]

$$\Sigma_R^0 = \frac{\partial g_\sigma}{\partial \rho_v} \rho_s \sigma + \frac{\partial g_\omega}{\partial \rho_v} \rho_v \omega^0 + \frac{\partial g_\rho}{\partial \rho_v} \rho_{tv} \rho_0^0, \tag{2.28}$$

which contains the derivatives of couplings with respect to vector density. The couplings for  $\sigma$  and  $\omega$  mesons are parameterized as [19, 138]

$$g_{\sigma,\omega}(\rho_v) = g_{\sigma,\omega}(\rho_{sat}) f_{\sigma,\omega}(x), \tag{2.29}$$

where

$$f_i(x) = a_i \frac{1 + b_i (x + d_i)^2}{1 + c_i (x + d_i)^2}, \quad i = \sigma, \omega, \tag{2.30}$$

with  $x = \rho_v / \rho_{sat}$ ,  $\rho_{sat}$  being the saturation density of the symmetric nuclear matter. The eight

Table 2.1: The coupling parameters of the meson-exchange functionals used in this work, DD-ME2 [19], D3C [22] and D3C\* [130].

	DD-ME2	D3C	D3C*
$m_\sigma$ [MeV]	550.1238	556.9862	574.8388
$g_\sigma(\rho_{sat})$	10.5396	11.0274	10.2991
$g_\omega(\rho_{sat})$	13.0189	13.7505	12.4820
$g_\rho(\rho_{sat})$	3.6836	3.9175	4.7884
$b_\sigma$	1.0943	3.5207	0.7006
$c_\sigma$	1.7057	7.0718	1.3923
$b_\omega$	0.9240	4.5637	0.9402
$c_\omega$	1.4620	9.8648	1.7942
$a_\rho$	0.5647	0.4220	0.0522
$\Gamma_S(\rho_{sat})$	0.0	-21.6321	-146.0897
$\Gamma_V(\rho_{sat})$	0.0	302.1887	180.8898
$\rho_{sat}$ [fm <sup>-3</sup> ]	0.152	0.129	0.152

parameters  $a_{\sigma,\omega}$ ,  $b_{\sigma,\omega}$ ,  $c_{\sigma,\omega}$ ,  $d_{\sigma,\omega}$  are further constrained by

$$f_i(1) = 1, \quad f''_\sigma = f''_\omega(1), \quad f''_i(0) = 0, \quad (2.31)$$

reducing the number of parameters to three, in addition to  $g_\sigma(\rho_{sat})$ ,  $g_\omega(\rho_{sat})$  and  $m_\sigma$ , being the mass of the  $\sigma$ -meson. The  $\rho$ -meson coupling is parameterized as [19, 138]

$$g_\rho(\rho_v) = g_\rho(\rho_{sat}) e^{-a_\rho(x-1)}, \quad (2.32)$$

having two parameters,  $g_\rho(\rho_{sat})$  and  $a_\rho$ . In table 2.1 we list the eight parameters of the DD-ME2 interaction, determined in Ref. [19] by a fit to nuclear matter properties, in addition to binding energies, nuclear radii and neutron radii of spherical nuclei.

Although it has enormous success in describing nuclear properties across the nuclide chart, including both the ground-state [19] and excited states [19, 28], a main drawback of the DD-ME2 functional is a low value of the effective Landau mass  $m_{eff}$  [22, 68]. The effective mass determines the density of states around the Fermi level, where a larger value leads to a more compressed single-particle spectrum, in a better agreement with the experiment. To allow for higher value of  $m_{eff}$ , a separate category of the meson-exchange functionals was devised, called the derivative-coupling (DC) interactions [22, 63]. They are developed by introducing additional couplings with

momentum-dependent self-energies into the Lagrangian density. We start by rewriting the Dirac single-particle equation (2.20) in a more general form

$$[i\Gamma_\mu \partial^\mu + V^\mu + m + S] \psi_i = 0, \quad (2.33)$$

where the vector potential is

$$V^\mu(\mathbf{r}, t) = g_\omega \Gamma_\mu \omega^\mu(\mathbf{r}, t) + g_\rho \vec{\tau} \Gamma_\mu \vec{\rho}^\mu(\mathbf{r}, t) + e \Gamma_\mu A^\mu(\mathbf{r}, t), \quad (2.34)$$

and the scalar potential is

$$S(\mathbf{r}, t) = g_\sigma \Gamma \sigma(\mathbf{r}, t). \quad (2.35)$$

The matrices  $\Gamma$  and  $\Gamma_\mu$  present the generalization of the unit matrix and the Dirac  $\gamma_\mu$  matrix, respectively, and are defined as [22]

$$\Gamma_\mu = \gamma^\nu g_{\mu\nu} + \gamma^\nu Y_{\mu\nu} - g_{\mu\nu} Z^\nu, \quad \Gamma = 1 + \gamma_\mu u_\nu Y^{\mu\nu} - u_\mu Z^\mu, \quad (2.36)$$

where

$$Y^{\mu\nu} = \frac{\Gamma_V}{m^4} m_\omega^2 \omega_\mu \omega^\nu, \quad Z^\mu = \frac{\Gamma_S}{m^2} \omega^\mu \sigma. \quad (2.37)$$

We note that  $\Gamma_S$  and  $\Gamma_V$  represent additional coupling terms of the DC models [cf. Tab. (2.1)]. Therefore, there are additional terms in the Lagrangian density which contain non-linear  $\sigma$  and  $\omega$  couplings. The four velocity  $u_\mu$  is defined in terms of the vector current density  $u_\mu = j_\mu / \rho_v$ , and introduces the momentum dependence in the vertex functions. Again, we take the static limit of the equations of motion, assuming time-reversal invariance and even-even nuclei. This means that only the time-like components of the meson fields contribute in addition to the third component of the isospin. It can be shown that the baryon current for DC models is [22]

$$\rho = \rho_v (1 + Y_{00}) - \rho_s Z_0, \quad (2.38)$$

which reduces to  $\rho_v$  if we neglect additional coupling terms  $Y_{00}$  and  $Z_0$ . The density dependence of the couplings is parameterized same as for the DD-ME2 interaction [19]. The additional coupling of the DC model are parameterized as [22]

$$\Gamma_V = \Gamma_V(\rho_{sat}) \frac{\rho_{sat}}{\rho_v}, \quad \Gamma_S = \Gamma_S(\rho_{sat}) \frac{\rho_{sat}}{\rho_v}. \quad (2.39)$$

Therefore, the DC models have 10 parameters, compared to 8 parameters of the DD-ME models. The corresponding parameters are determined in Ref. [22] by  $\chi^2$  minimization in a 8-dimensional space by using the saturation properties of symmetric nuclear matter as additional constraints. The fit was performed on properties of doubly-magic nuclei, such as binding energies, diffraction radii, surface thickness and others [22]. The fitted parameters are listed in table 2.1, and the corresponding EDF is called D3C. The main advantage of the DC models is that the effective Landau mass  $m_{eff}$  can be better adjusted due to additional couplings in the model, while keeping the effective Dirac mass  $m^*$  in the appropriate range — responsible for the magnitude of spin-orbit splitting. The Landau mass  $m_{eff}$  determines the density of states around the Fermi level, a known drawback of relativistic models, which have lower effective mass compared to non-relativistic models.

Therefore, in order to obtain better agreement with the experimental data for  $\beta$ -decay half-lives, the D3C EDF was refitted in Ref. [130], by increasing its effective mass to  $m_{eff} = 0.79$ , while still keeping a reasonable description of nuclear matter and finite-nuclei properties. The re-parametrization is called the D3C\*, and its parameters are displayed in table 2.1. The range of energies we are interested in is much lower compared to the corresponding meson masses. This means that we can expand the meson propagators in terms of meson masses, and instead of writing the meson fields in the Lagrangian density, rewrite it in terms of nucleon fields. Therefore, each meson vertex in Fig. 2.1 is replaced by a simple 4-point (or more) contact interaction vertex, consisting only of the delta function. There are no additional meson Klein-Gordon equations, and the self-consistent RMF equations are somewhat simplified. Functionals of that type are known as point-coupling (PC). Of course, the question is at which point do we truncate the expansion? In fact, some PC functionals contain higher 6-point  $(\bar{\psi}\psi)^3$  and 8-point  $(\bar{\psi}\psi)^4$  vertices, simulating the in-medium effects [16]. It was noted that for density-dependent interactions, only the 4-point vertices should be kept, in addition to the derivative term  $\partial_\nu(\bar{\psi}\psi)\partial^\nu(\bar{\psi}\psi)$ , taking into account the nuclear surface effects [15]. In order to construct the point-coupling functional we start by writing the possible bilinear covariants of the Dirac field  $\psi$  of the form  $\bar{\psi}\mathcal{O}\Gamma\psi$ , where

$$\Gamma \in \{1, \gamma_\mu, \gamma_5, \gamma_\mu\gamma_5\}, \quad \mathcal{O} \in \{1, \vec{\tau}\}. \quad (2.40)$$

The Lagrangian density consists of a series expansion of  $\bar{\psi}\mathcal{O}\Gamma\psi$  and their derivatives. For the

density-dependent PC interactions (DD-PC) the Lagrangian density has the form [20]

$$\begin{aligned} \mathcal{L} = & \bar{\psi} (i\gamma_\mu \partial^\mu - m) \psi - \frac{1}{2} \alpha_S (\rho_v) (\bar{\psi} \psi) (\bar{\psi} \psi) - \frac{1}{2} \alpha_V (\rho_v) (\bar{\psi} \gamma^\mu \psi) (\bar{\psi} \gamma_\mu \psi) \\ & - \frac{1}{2} \alpha_{TV} (\rho_v) (\bar{\psi} \vec{\tau} \gamma^\mu \psi) (\bar{\psi} \vec{\tau} \gamma_\mu \psi) - \frac{1}{2} \delta_S (\partial_\nu \bar{\psi} \psi) (\partial^\nu \bar{\psi} \psi) - e \bar{\psi} \gamma_\mu A^\mu \frac{1 - \tau_0}{2} \psi, \end{aligned} \quad (2.41)$$

where  $\alpha_S(\rho_v)$ ,  $\alpha_V(\rho_v)$  and  $\alpha_{TV}(\rho_v)$ , are the scalar, vector and isovector coupling constants, being a function of the vector density. The derivative coupling  $\delta_S$  is density-independent. We can immediately see correspondence between the PC and ME models; the scalar term corresponds to  $\sigma$  meson, vector to  $\omega$  meson, and isovector to  $\rho$  meson. Additionally, the PC models also require a derivative term. The EDF is constructed by assuming static limit of the time-reversal invariant ground-state of even-even nuclei, meaning that only the time-like components of nuclear currents contribute. Following the prescription from Eq. (2.24) we construct the EDF as

$$\begin{aligned} E_{RMF} [\psi, \bar{\psi}, A_0] = & \int d^3 \mathbf{r} \mathcal{H}(\mathbf{r}) \\ = & \sum_{i=1}^A \int d^3 \mathbf{r} \psi_i^\dagger (-i\boldsymbol{\alpha} \cdot \nabla - \beta m) \psi_i + e \int d^3 \mathbf{r} \rho_c(\mathbf{r}) A_0 \\ & + \frac{1}{2} \int d^3 \mathbf{r} [\alpha_S \rho_s^2 - \alpha_v \rho_v^2 - \alpha_{TV} \rho_{tv}^2 - \delta_S \rho_s \nabla^2 \rho_s], \end{aligned} \quad (2.42)$$

where we have used the Poisson equation  $\nabla^2 A^0 = -e\rho_c$  in addition to the assumption that the field  $A^0$  and nuclear currents are localized. Following the DFT prescription and varying with respect to density we derive the single-particle Dirac equation as in Eq. (2.20), but with modified vector and scalar fields. They have the form

$$V = \alpha_V \rho_v + \alpha_{TV} \tau_0 \rho_{tv} + eA_0 + \Sigma_R^0, \quad S = \alpha_S \rho_s + \delta_S \nabla^2 \rho_s, \quad (2.43)$$

where  $\Sigma_R^0$  is the rearrangement contribution

$$\Sigma_R^0 = \frac{\partial \alpha_S}{\partial \rho_v} \rho_s^2 + \frac{\partial \alpha_V}{\partial \rho_v} \rho_v^2 + \frac{\partial \alpha_{TV}}{\partial \rho_v} \rho_{tv}^2. \quad (2.44)$$

The couplings are parameterized as

$$\alpha_i (\rho_v) = a_i + (b_i + c_i x) e^{-d_i x}, \quad i = S, V, TV, \quad (2.45)$$



Table 2.2: The coupling parameters of the point-coupling functionals used in this work, DD-PC1 [20] and DD-PCX [21].

	DD-PC1	DD-PCX
$a_S$ [fm <sup>2</sup> ]	-10.0462	-10.9792
$b_S$ [fm <sup>2</sup> ]	-9.1504	-9.0383
$c_S$ [fm <sup>2</sup> ]	-6.4273	-5.3130
$d_S$	1.3724	1.3791
$a_V$ [fm <sup>2</sup> ]	5.9195	6.4301
$b_V$ [fm <sup>2</sup> ]	8.8637	8.8706
$d_V$	0.6584	0.6553
$b_{TV}$ [fm <sup>2</sup> ]	1.8360	2.9632
$d_{TV}$	0.6403	1.3098
$\delta_S$ [fm <sup>4</sup> ]	-0.8149	-0.8789
$G_n$ [MeV fm <sup>3</sup> ]	-728.0	-800.6631
$G_p$ [MeV fm <sup>3</sup> ]	-728.0	-773.7768

where  $x = \rho_v/\rho_{sat}$ . The parameters  $c_V$ ,  $a_{TV}$  and  $c_{TV}$  are set to zero, while the ten remaining parameters  $a_S$ ,  $b_S$ ,  $c_S$ ,  $d_S$ ,  $a_V$ ,  $b_V$ ,  $d_V$ ,  $b_{TV}$ ,  $d_{TV}$  and  $\delta_S$  are adjusted to nuclear matter properties together with binding energies of axially-deformed nuclei in Ref. [20]. The resulting parameter set is called DD-PC1 and its parameters are shown in table 2.2.

Recently, in Ref. [21], using the same form of the DD-PC functional, the parameters were constrained in addition to the ground-state properties by also considering the nuclear excitations in the fitting procedure. Apart from binding energies, the  $\chi^2$  minimization procedure also included charge radii and pairing gaps in the ground state, together with the isoscalar giant monopole resonance energy and dipole polarizability, obtained by considering small oscillations around the ground state density (within the RQRPA to be explained in Chapter 3). The corresponding parameter set DD-PCX is shown in table 2.2. We note that in addition to the RMF, the pairing interaction was also considered in the optimization procedure, characterized by the pairing strength constants for proton(neutron) states  $G_{p(n)}$ . We will describe the generalization of the RMF equations to the superfluid nuclei in the next section.

## 2.2 Relativistic Hartree-Bogoliubov (RHB) theory

To introduce the pairing correlations in the mean-field calculation we perform the Bogoliubov transformation from the single-particle  $\{c_i^\dagger, c_i\}$  to quasi-particle (q.p.)  $\{\alpha_i^\dagger, \alpha_i\}$  basis [23]

$$\alpha_k^\dagger = \sum_k U_{mk} c_m^\dagger + V_{mk} c_m \implies \alpha_k |\Phi\rangle = 0, \quad (2.46)$$

where  $|\Phi\rangle$  is the Bogoliubov vacuum. The relativistic Hartree Bogoliubov (RHB) equations are usually derived by introducing the generalized density matrix [23]

$$\mathcal{R} = \begin{pmatrix} \rho & \kappa \\ -\kappa^* & 1 - \rho^* \end{pmatrix}, \quad (2.47)$$

where  $\rho_{ij} = \langle \Phi | c_i^\dagger c_j | \Phi \rangle$  is the single-particle density matrix and  $\kappa_{ij} = \langle \Phi | c_i c_j | \Phi \rangle$  is the pair density, with the following form in the single-particle basis [58]

$$\rho = V^* V^T, \quad \kappa = V^* U^T. \quad (2.48)$$

The total EDF now not only depends on the mean-field but also on the *pairing* term, which is a functional of  $\kappa$

$$E[\rho, \kappa] = E_{RMF}[\rho] + E_{pair}[\kappa], \quad (2.49)$$

where the pairing energy is given by  $E_{pair}[\kappa] = 1/4 \text{Tr}[\kappa^* V^{pp} \kappa]$ , and  $V^{pp}$  is the effective particle-particle force in the pairing channel. Performing the variation of the functional with respect to the density  $\delta E / \delta \mathcal{R}$  we obtain the following form

$$\frac{\delta E[\rho, \kappa]}{\delta \mathcal{R}} = \begin{pmatrix} h - \lambda & \Delta \\ -\Delta^* & -h^* + \lambda \end{pmatrix}, \quad (2.50)$$

where  $h$  is the Dirac Hamiltonian defined in Eq. (2.20), and  $\Delta$  is the pairing field of the following form in the configuration space

$$\Delta_{ab} = \frac{1}{2} \sum_{cd} V_{abcd}^{pp} \kappa_{cd}. \quad (2.51)$$

The condition  $\delta E/\delta \mathcal{R} = 0$ , yields the RHB equation of the form [23]

$$\begin{pmatrix} h - \lambda & \Delta \\ -\Delta^* & -h^* + \lambda \end{pmatrix} \begin{pmatrix} U_k \\ V_k \end{pmatrix} = E_k \begin{pmatrix} U_k \\ V_k \end{pmatrix}, \quad (2.52)$$

where the chemical potential  $\lambda$  is determined from the particle number subsidiary condition  $N = \text{Tr}\rho$ . The RHB spinor is defined as  $\Psi_k = \begin{pmatrix} U_k & V_k \end{pmatrix}^T$ , where both  $U$  and  $V$  components consist of large and small Dirac component. For each solution with eigenvalue  $E_k$  and eigenvector  $(U_k, V_k)$ , there exists a solution  $-E_k$  with eigenvector  $(V_k^*, U_k^*)$ . In practical calculation, one often chooses positive eigenvalues  $E_k > 0$ .

What is the form of the relativistic  $V^{pp}$ ? In general, different types of pairing interactions are used with different types of relativistic functionals. Initially, the same form of the relativistic Lagrangian was used for the pairing interaction, as was for the mean-field. This produced too large pairing gaps compared to empirical data [23, 139]. On the other hand, use of the non-relativistic forces has led to more reasonable results, a successful example being the Gogny force [60]. Furthermore, in the Dirac basis, the pairing potential can be written in the form

$$\Delta = \begin{pmatrix} \Delta_{++} & \Delta_{+-} \\ \Delta_{-+} & \Delta_{--} \end{pmatrix}, \quad (2.53)$$

where "+" refers to the large components of Dirac spinor and "-" to small components. The RHB calculations with the phenomenological Gogny force neglect the  $\Delta_{+-}$ ,  $\Delta_{-+}$  and  $\Delta_{--}$  components, which contain small components of Dirac spinor. Such method has led to success in describing the properties of open-shell nuclei across the nuclide chart [23]. Therefore, in the following we adopt only the  $\Delta_{++}$  part of the pairing potential. In this work we employ two forms of the pairing interaction within the RHB

- pairing part of the Gogny interaction with the D1S parameter set from Ref. [140] (defined in Sec. 4.3)
- the separable pairing interaction from Ref. [141] (defined in Sec. 6.1)

### 2.2.1 The BCS approximation

Instead of constructing and diagonalizing the full RHB matrix, we can use the following strategy. We solve the RMF equations, obtaining a set of single-particle energies  $\{\varepsilon_k\}$ . Next, we calculate the pairing field  $\Delta_{\alpha\beta}$  from Eq. (2.51) in a basis of choice (such as the harmonic oscillator basis) and then calculate the state-dependent pairing gaps

$$\Delta_k = \sum_{\alpha\beta} f_k^{(\alpha)} \Delta_{\alpha\beta} f_k^{(\beta)}, \quad (2.54)$$

where  $f_k^{(\alpha)}$  is the expansion coefficient of the upper component of Dirac spinor in a specified basis. Using the Baarden-Cooper-Schrieffer (BCS) approximation of the nuclear pairing, the corresponding occupation factors  $v_k$  and  $u_k$  can be calculated from [40, 58]

$$v_k^2 = \frac{1}{2} \left( 1 - \frac{\varepsilon_k - \lambda}{\sqrt{(\varepsilon_k - \lambda)^2 + \Delta_k^2}} \right), \quad u_k^2 = 1 - v_k^2, \quad (2.55)$$

where  $\lambda$  is the chemical potential (either of proton or neutron states), determined from the condition  $\sum_k g_k v_k^2 = N$ , where  $g_k$  is the degeneracy of state  $k$ . Instead of only having fully occupied ( $v_k^2 = 1$ ) and empty ( $v_k^2 = 0$ ) single-particle levels, the occupation of states can be scattered around the Fermi level (determined by  $\lambda$ ). Therefore, various single-particle densities defined in Eq. (2.14), (2.16) and (2.22) entering the RMF equations have the following form

$$\begin{aligned} \rho_v(\mathbf{r}) &= \sum_k v_k^2 \psi_k^\dagger(\mathbf{r}) \psi_k(\mathbf{r}), & \rho_s(\mathbf{r}) &= \sum_k v_k^2 \psi_k^\dagger(\mathbf{r}) \gamma^0 \psi_k(\mathbf{r}) \\ \rho_{tv}(\mathbf{r}) &= \sum_k v_k^2 \psi_k^\dagger(\mathbf{r}) \tau_0 \psi_k(\mathbf{r}), & \rho_c(\mathbf{r}) &= \sum_k v_k^2 \psi_k^\dagger(\mathbf{r}) \frac{1}{2} (1 + \tau_0) \psi_k(\mathbf{r}), \end{aligned} \quad (2.56)$$

weighted by the corresponding occupation factor of the level. The set of RMF equations is again solved self-consistently according to the above prescription. The total energy is now given by a sum of the RMF energy  $E_{RMF}$  and a pairing energy  $E_{pair}$ ,  $E = E_{RMF} + E_{pair}$ , where the latter is calculated as

$$E_{pair} = - \sum_k g_k u_k v_k \Delta_k. \quad (2.57)$$

Instead, if we assume a fixed pairing strength, so that  $V_{k\bar{k}k'\bar{k}'}^{pp} = -G\delta_{kk'}$ ,  $\bar{k}$  being the time-reversed state of  $k$ , then the pairing gap  $\Delta$  is obtained by solving the gap equation [58]

$$\Delta = \frac{G}{2} \sum_k \frac{\Delta}{\sqrt{(\varepsilon_k - \lambda)^2 + \Delta^2}}. \quad (2.58)$$

For instance, the pairing strength  $G$  can be determined by adjusting the calculated pairing gaps  $\Delta$  to empirical pairing gaps [40].

### 2.3 Extension to the finite-temperature RHB (FT-RHB)

The nuclei at finite temperatures are found in excited states. Extension of the RHB used to describe the ground state to the description of hot nuclei requires special care. The expectation values of observables cannot be evaluated by simply taking the ground-state expectation values. For instance, for the observable  $\mathcal{O}$ , the expectation value is defined as  $\langle \Psi_0 | \mathcal{O} | \Psi_0 \rangle$ , where  $|\Psi_0\rangle$  is the correlated ground-state wavefunction of the nucleus. In the gist of the EDF theory, it can also be rewritten as  $\text{Tr}[\mathcal{O}\hat{\rho}]$ , where  $\hat{\rho}$  is the ground-state density operator. At finite temperature the expectation value is defined as the sum of expectation values for each excited state, weighted by the corresponding Boltzmann factors. Furthermore, it requires the definition of external heat and particle reservoir for the construction of a grand-canonical ensemble. One can follow two approaches in evaluating the ensemble averages. First approach is to define the non-interacting density at finite-temperature and proceed with the derivations as for the zero-temperature RHB. This method was used to derive the FT-RHB equations by A.L. Goodman in Refs. [25]. Second approach is to try and keep the notion of a vacuum even at finite temperature, known as the *thermal vacuum*. It requires doubling the degrees of freedom of the many-body Hilbert space and is known as the *thermofield dynamics* (TFD) [142, 143].

Here we present the derivation of the FT-RHB equation following the approach of Goodman [25]. The original derivation was applied to non-relativistic Hartree-Fock-Bogoliubov (HFB) theory, however, the extension to the RHB is straightforward. The nucleus is treated as an open system, that can exchange both heat and particles with its environment. For such a system the equilibrium condition is obtained by minimizing the grand-canonical potential  $\delta\Omega = 0$ , which is defined as

$$\Omega = E - TS - \lambda N, \quad (2.59)$$

where  $E$ ,  $S$  and  $N$  stand for the expected energy, entropy and particle number. We define the density operator  $\hat{D}$ , with the property  $\text{Tr}\hat{D} = 1$  so that the expectation value of observable  $\mathcal{O}$  is defined as  $\langle \mathcal{O} \rangle = \text{Tr}(\hat{D}\mathcal{O})$  and the expected values of energy, entropy and particle number are

$$E = \langle \hat{H} \rangle = \text{Tr}(\hat{D}\hat{H}), \quad S = -k_B \text{Tr}(\hat{D}\ln\hat{D}), \quad N = \text{Tr}(\hat{D}\hat{N}). \quad (2.60)$$

In the above,  $\hat{H}$  is the Hamiltonian operator,  $k_B$  the Boltzmann constant and  $\hat{N} = \sum_i c_i^\dagger c_i$  is the particle number operator. Variation condition  $\delta\Omega \rightarrow 0$  is realized with respect to the density operator  $\delta\hat{D}$ , and gives the following equation

$$\begin{aligned} \delta\Omega &= \text{Tr}(\delta\hat{D}\hat{H}) - kT\text{Tr}(\delta\hat{D}\ln\hat{D} + \delta\hat{D}) - \mu\text{Tr}(\delta\hat{D}\hat{N}) - \lambda\text{Tr}(\delta\hat{D}) \\ &= \text{Tr} \left[ \delta\hat{D}(\hat{H} + kT\ln\hat{D} + kT - \lambda\hat{N} - \lambda) \right] = 0. \end{aligned} \quad (2.61)$$

In order to satisfy the condition  $\text{Tr}\hat{D} = 1$  we can set  $\lambda = kT - \frac{1}{\beta}\ln Z$ , which gives the following expression for the density operator

$$\hat{D} = Z^{-1} e^{-\beta(\hat{H} - \lambda\hat{N})}, \quad Z = \text{Tr} \left[ e^{-\beta(\hat{H} - \lambda\hat{N})} \right], \quad (2.62)$$

where  $Z$  is the partition function and  $\beta = 1/(k_B T)$ . Within the RHB theory the Hamiltonian  $\hat{H}$  is approximated by an independent q.p. Hamiltonian with  $E_i$  the q.p. energy

$$\hat{H} - \lambda\hat{N} \approx \hat{H}_{RHB} = E_0 + \sum_i E_i \alpha_i^\dagger \alpha_i, \quad (2.63)$$

where the Bogoliubov transformation is defined as in Eq. (2.46), or in the matrix form

$$\begin{pmatrix} \alpha^\dagger \\ \alpha \end{pmatrix} = \begin{pmatrix} U^T & V^T \\ V^\dagger & U^\dagger \end{pmatrix} \begin{pmatrix} c^\dagger \\ c \end{pmatrix}. \quad (2.64)$$

Within the RHB approximation the partition function is given by

$$Z_{RHB} = e^{-\beta E_0} \prod_i (1 + e^{-\beta E_i}), \quad (2.65)$$

while the RHB density operator has the form

$$\hat{D}_{RHB} = \prod_i [f_i \hat{n}_i + (1 - f_i)(1 - \hat{n}_i)], \quad (2.66)$$

where  $f_i = (1 + \exp(\beta E_i))^{-1}$  is the Fermi-Dirac factor and  $\hat{n}_i = c_i^\dagger c_i$ .

Next, we have to evaluate the particle density  $\tilde{\rho} = \langle \alpha_j^\dagger \alpha_i \rangle$  and the pairing density  $\tilde{\kappa} = \langle \alpha_j \alpha_i \rangle$  in the q.p. basis, from which we obtain [25]

$$\tilde{\rho}_{ij} = \langle \hat{D}_{RHB} \alpha_j^\dagger \alpha_i \rangle = f_i \delta_{ij}, \quad \tilde{\kappa}_{ij} = \langle \hat{D}_{RHB} \alpha_j \alpha_i \rangle = 0, \quad (2.67)$$

which constitute the expressions of the generalized Wick theorem. Now we can transform  $\tilde{\rho}$  and  $\tilde{\kappa}$  back to the single-particle basis to get

$$\rho = U f U^\dagger + V^*(1 - f)V^T, \quad \kappa = U f V^\dagger + V^*(1 - f)U^T. \quad (2.68)$$

Notice that at zero temperature, above expressions reduce to the well-known form in Eq. (2.2).

Looking back at the grand-canonical potential in Eq. (2.59), we can now calculate the ensemble averages in the RHB approximation to get

$$\Omega = \text{Tr} \left[ \left( t + \frac{1}{2} \Gamma - \lambda \right) \rho + \frac{1}{2} \Delta \kappa^\dagger \right] + kT \sum_\mu [(1 - f_\mu) \ln(1 - f_\mu) + f_\mu \ln f_\mu], \quad (2.69)$$

where the *mean-field* interaction is  $\Gamma_{ij} = \sum_{kl} \bar{v}_{ijkl} \rho_{lk}$ , with  $t$  being the kinetic energy, and *pairing* field is  $\Delta_{ij} = \frac{1}{2} \sum_{kl} \bar{v}_{ijkl} \kappa_{kl}$ .

In the following, the variations in expression for  $\Omega$  have to be performed with respect to  $U$ ,  $V$  and  $f$ . As a first step we want to obtain expressions for the variation of densities  $\rho' = \rho + \delta\rho$  and  $\kappa' = \kappa + \delta\kappa$ . An infinitesimal transformation of the Bogoliubov transformation can be represented as

$$\begin{pmatrix} \alpha'^\dagger \\ \alpha' \end{pmatrix} = \left[ 1 + \begin{pmatrix} \varepsilon_1^T & \varepsilon_2^T \\ \varepsilon_2^\dagger & \varepsilon_1^\dagger \end{pmatrix} \right] \begin{pmatrix} \alpha^\dagger \\ \alpha \end{pmatrix} = \begin{pmatrix} U'^T & V'^T \\ V'^\dagger & U'^\dagger \end{pmatrix} \begin{pmatrix} c^\dagger \\ c \end{pmatrix}. \quad (2.70)$$

Since the infinitesimal transformation has to be unitary it follows that  $\varepsilon_1 = -\varepsilon_1^\dagger$  and  $\varepsilon_2 = -\varepsilon_2^\dagger$ .

New Bogoliubov wave functions ( $U', V'$ ) can be now found from

$$\left[ 1 + \begin{pmatrix} \varepsilon_1^T & \varepsilon_2^T \\ \varepsilon_2^\dagger & \varepsilon_1^\dagger \end{pmatrix} \right] \begin{pmatrix} U^T & V^T \\ V^\dagger & U^\dagger \end{pmatrix} = \begin{pmatrix} U'^T & V'^T \\ V'^\dagger & U'^\dagger \end{pmatrix}. \quad (2.71)$$

Since  $U' = U + \delta U$ ,  $V' = V + \delta V$  we get for the variations

$$\delta U = U\varepsilon_1 + V^*\varepsilon_2, \quad \delta V = V\varepsilon_1 + U^*\varepsilon_2. \quad (2.72)$$

By inserting these variations into expressions for single-particle densities  $\rho$  and  $\kappa$  in Eq. (2.68) we get

$$\begin{aligned} \delta\rho &= U\delta\bar{\rho}U^\dagger - U\delta\bar{\kappa}V^T + V^*\delta\bar{\kappa}^*U^\dagger - V^*\delta\bar{\rho}^*V^T, \\ \delta\kappa &= U\delta\bar{\rho}V^\dagger - U\delta\bar{\kappa}U^T + V^*\delta\bar{\kappa}^*V^\dagger - V^*\delta\bar{\rho}^*U^T, \end{aligned} \quad (2.73)$$

where we have defined  $\delta\bar{\rho} = \delta f + [\varepsilon_1, f]$  and  $\delta\bar{\kappa} = \varepsilon_2^* + \{f, \varepsilon_2^*\}$  as in Ref. [25]. We can perform variation of  $\Omega$  which gives

$$\delta\Omega = \text{Tr}[(t - \lambda)\delta\rho + \Gamma\delta\rho] + \frac{1}{2}\text{Tr}[\Delta\delta\kappa^\dagger + \text{c.c.}] + kT \sum_i \ln\left(\frac{f_i}{1 - f_i}\right) \delta f_i. \quad (2.74)$$

The variations can be expressed in terms of  $\delta\bar{\rho}$  and  $\delta\bar{\kappa}$  as

$$\delta\Omega = \text{Tr} \left[ (H_{11} - E)\delta\bar{\rho} + \frac{1}{2} \left( H_{20}^\dagger \delta\bar{\kappa} + \text{h.c.} \right) \right], \quad (2.75)$$

with the definitions

$$\begin{aligned} H_{11} &= U^\dagger \mathcal{H} U - V^\dagger \mathcal{H}^* V + U^\dagger \Delta V - V^\dagger \Delta^* U, \\ H_{20} &= V^\dagger \mathcal{H}^* U^* - U^\dagger \mathcal{H} V^* + V^\dagger \Delta^* V^* - U^\dagger \Delta U^*, \\ E_i &= -kT \ln\left(\frac{f_i}{1 - f_i}\right), \end{aligned} \quad (2.76)$$

where  $\mathcal{H} = h - \lambda$  and  $h = t + \Gamma$  being the single-particle Dirac Hamiltonian. The variations  $\delta\bar{\rho}$



and  $\delta\bar{\kappa}$  are independent as can be seen from their definitions

$$\begin{aligned}
 (\delta\bar{\rho})_{ii} &= \delta f_i, \\
 (\delta\bar{\rho})_{ij} &= (f_i - f_j)(\varepsilon_1^*)_{ij}, \quad i \neq j, \\
 (\delta\bar{\kappa})_{ii} &= 0, \\
 (\delta\bar{\kappa})_{ij} &= (f_i + f_j - 1)(\varepsilon_2^*)_{ij}, \quad i \neq j,
 \end{aligned} \tag{2.77}$$

where  $\varepsilon_1, \varepsilon_2$  and  $\delta f$  are varied independently. Except for the accidental case where  $f_i - f_j = 0$  or  $f_i + f_j - 1 = 0$  it follows that  $\delta\bar{\rho}$  and  $\delta\bar{\kappa}$  are independent [25]. The variational principle  $\delta\Omega = 0$  requires that the coefficients of  $\delta\bar{\rho}$  and  $\delta\bar{\kappa}$  vanish

$$H_{11} = E, \quad H_{20} = 0. \tag{2.78}$$

We define the following matrices [25]

$$\alpha = (\mathcal{H}U + \Delta V)E^{-1}, \beta = (-\Delta^*U - \mathcal{H}^*V)E^{-1}, \tag{2.79}$$

so that Eqs. (2.78) can be written as

$$\begin{aligned}
 U^\dagger \alpha E + V^\dagger \beta E &= E \\
 V^\dagger \alpha^* E + U^\dagger \beta^* E &= 0.
 \end{aligned} \tag{2.80}$$

By comparing above relations with unitarity condition of Bogoliubov transformation

$$\begin{aligned}
 U^\dagger U + V^\dagger V &= 1 \\
 U^T V + V^T U &= 0,
 \end{aligned} \tag{2.81}$$

we get  $\alpha = U, \beta = V$  and inserting in Eq. (2.79)

$$\begin{aligned}
 \mathcal{H}U + \Delta V &= UE, \\
 -\mathcal{H}^*V - \Delta^*U &= VE.
 \end{aligned} \tag{2.82}$$

In the matrix form

$$\begin{pmatrix} h - \lambda & \Delta \\ -\Delta^* & -h^* + \lambda \end{pmatrix} \begin{pmatrix} U \\ V \end{pmatrix} = E \begin{pmatrix} U \\ V \end{pmatrix}. \tag{2.83}$$

Thus, the FT-RHB equations have the same form as the  $T = 0$  RHB equations [cf. Eq. (2.52)]. Also the Dirac Hamiltonian  $h$ , the mean-field potential  $\Gamma$  and the pairing potential  $\Delta$  have the same definitions as for zero temperature. However, the densities  $\rho$  and  $\kappa$  have different definitions given by Eq. (2.68). The chemical potential  $\lambda$  is adjusted to reproduce the correct particle number  $N = \text{Tr}\rho$ . As we will demonstrate in Chapter 6, the FT-RHB equation in the above form is applicable only to well-bound nuclei in the vicinity of the stability valley, and for temperatures up to  $T = 1$  MeV. Namely, as the temperature increases, nucleons can scatter above the Fermi level and into the particle continuum, becoming unbound. The FT-RHB equation has to be supplemented with the continuum subtraction technique if we want to obtain reliable results, independent of the basis size used to discretize the problem.

## Chapter 3

# Relativistic proton-neutron Quasiparticle Random-Phase Approximation (pnRQRPA) at finite temperature

The relativistic Hartree-Bogoliubov theory describes ground state of the nucleus. In order to study the excited states as well as the collective excitations of nuclei one has to extend the mean-field theory and include the residual interaction. We can study the behavior of nucleus in a perturbing time-dependent external field  $\mathcal{F}(t)$ . If the field has a harmonic time-dependence and only linear terms in the generalized density expansion are considered, one obtains the linear response approximation. To have a complete picture we will work in a generalized basis assuming that the system is in an equilibrium with a heat bath at temperature  $T$ . Our system can be described as a statistical ensemble

$$|n\rangle = |m_1 \dots m_n\rangle = \alpha_{m_1}^\dagger \dots \alpha_{m_n}^\dagger |\phi\rangle, \quad (3.1)$$

here  $m_1 \dots m_n$  are quantum numbers denoting the basis states and  $|\phi\rangle$  is the vacuum for q.p. operators  $\alpha_m |\phi\rangle = 0$ ,  $\forall m = 1 \dots M$ . The thermal average of a single-particle operator  $\hat{O}$  is then given by

$$\langle \hat{O} \rangle_T = \sum_n \langle n | \hat{O} | n \rangle p_n = \frac{\text{Tr} \hat{O} \rho}{\text{Tr} \rho}, \quad (3.2)$$

where  $p_n = 1/Z e^{-\beta E_n}$  are the Boltzmann factors,  $Z$  being the partition function defined in Eq. (2.65),  $\rho = 1/Z \sum_n p_n |n\rangle \langle n|$  is the density matrix, and  $E_n$  the q.p. energy. By introducing a set of

complete basis states  $\sum_i |i\rangle \langle i|$  we get

$$\langle \hat{O} \rangle_T = \frac{\sum_{ni} \langle n | \hat{O} | i \rangle \langle i | \rho | n \rangle}{\sum_n \langle n | \rho | n \rangle}. \quad (3.3)$$

Assuming a non-interacting Hamiltonian of the form  $\hat{H} - \lambda \hat{N} = \sum_m E_m \alpha_m^\dagger \alpha_m$  the matrix element of the density matrix is

$$\langle i | \rho | n \rangle = \langle i | e^{-\beta(\hat{H} - \lambda \hat{N})} | n \rangle = \langle i | e^{-\beta E_n} | n \rangle = e^{-\beta E_n} \delta_{in}. \quad (3.4)$$

Now the thermal average can be written in the following form

$$\langle \hat{O} \rangle_T = \frac{\sum_n \langle n | \hat{O} | n \rangle e^{-\beta E_n}}{\sum_n e^{-\beta E_n}}, \quad (3.5)$$

which when normalized to unity yields

$$\langle \hat{O} \rangle_T = \sum_n \langle n | \hat{O} | n \rangle e^{-\beta E_n}, \quad (3.6)$$

where the quasiparticle energies are defined by  $E_m = \langle \phi | \{[\alpha_m, \hat{H} - \lambda \hat{N}], \alpha_m^\dagger\} | \phi \rangle$ . Thermal averages of any operator can be expressed by the single-particle density matrix

$$\mathcal{R} = \begin{pmatrix} \langle c_{k'}^\dagger c_k \rangle_T & \langle c_{k'} c_k \rangle_T \\ \langle c_{k'}^\dagger c_k^\dagger \rangle_T & \langle c_{k'} c_k^\dagger \rangle_T \end{pmatrix}, \quad (3.7)$$

where operators  $c_k, c_k^\dagger$  represent an arbitrary single-particle basis. It is convenient to introduce the set of operators  $a_\mu$  which combine creation and annihilation operators [75]

$$\left. \begin{array}{l} a_\mu = \alpha_m \\ a_{\bar{\mu}} = \alpha_m^\dagger \end{array} \right\} m = 1 \dots M; \mu = 1 \dots M, -1, -2, \dots, -M, \quad (3.8)$$

and obey the commutation relations

$$\{a_\mu, a_{\bar{\mu}'}\} = \delta_{\mu\bar{\mu}'}. \quad (3.9)$$

In the finite-temperature q.p. representation the density matrix  $\mathcal{R}$  is diagonal

$$\mathcal{R} = \begin{pmatrix} \langle \alpha_{m'}^\dagger \alpha_m \rangle_T & \langle \alpha_{m'} \alpha_m \rangle_T \\ \langle \alpha_{m'}^\dagger \alpha_m^\dagger \rangle_T & \langle \alpha_{m'} \alpha_m^\dagger \rangle_T \end{pmatrix} = \begin{pmatrix} f_m & 0 \\ 0 & 1 - f_m \end{pmatrix}, \quad (3.10)$$

where the Fermi-Dirac occupation factor is  $f_m = (1 + e^{\beta E_m})^{-1}$ . Assuming that operators  $a_\mu$  are time-dependent (Heisenberg picture)

$$a_\mu(t) = e^{iHt} a_\mu(0) e^{-iHt}, \quad (3.11)$$

follows the equation of motion for the density  $\mathcal{R}$

$$i\dot{\mathcal{R}} = [\mathcal{H}(\mathcal{R}), \mathcal{R}], \quad (3.12)$$

with  $\mathcal{H}_{\mu\mu'} = \langle \{ [a_\mu, H], a_{\mu'}^\dagger \} \rangle_T$ , known as the time-dependent HFB equation. Derivation of above equation can be found in Appendix A. If there is no external field, equation above reduces to the static HFB equation

$$[\mathcal{H}(\mathcal{R}^0), \mathcal{R}^0] = 0, \quad (3.13)$$

at finite temperature. Extension to the RHB equation is straightforward [23]. In this basis  $\mathcal{R}^0$  and  $\mathcal{H}(\mathcal{R}^0)$  are diagonal, with the eigenvalues

$$\left. \begin{array}{l} f_\mu = f_m, \quad f_{\bar{\mu}} = 1 - f_m \\ E_\mu = E_m, \quad E_{\bar{\mu}} = -E_m \end{array} \right\} \mu > 0. \quad (3.14)$$

To describe the charge-exchange transitions we have to introduce the charge-exchange external field operator  $\mathbb{F}(t)$  in the super-matrix space, which has the following form

$$\mathbb{F}(t) = \begin{pmatrix} 0 & \mathbb{F}^{(pn)}(t) \\ \mathbb{F}^{(np)}(t) & 0 \end{pmatrix}, \quad (3.15)$$

where only the  $pn$  and  $np$  blocks are relevant. The matrix elements of  $\mathbb{F}^{(pn)}$  are denoted as  $F_{\pi\nu}$ . The density  $\mathcal{R}_{\pi\nu}$  is the matrix element of the  $\mathbb{R}^{(pn)}$  matrix, while the generalized density super-matrix is

$$\mathbb{R} = \begin{pmatrix} \mathbb{R}^{(pp)} & \mathbb{R}^{(pn)} \\ \mathbb{R}^{(np)} & \mathbb{R}^{(nn)} \end{pmatrix}. \quad (3.16)$$

Starting from Eq. (3.12) for the generalized density  $\mathbb{R}$  we write

$$i\delta\dot{\mathbb{R}}(t) = [\mathbb{H}_0, \delta\mathbb{R}(t)] + [\delta\mathbb{H}(t) + \mathbb{F}(t), \mathbb{R}_0], \quad (3.17)$$

where we introduce the following notation [77]

$$\mathbb{H}_0 = \begin{pmatrix} \mathbb{H}_0^{(p)} & 0 \\ 0 & \mathbb{H}_0^{(n)} \end{pmatrix}, \quad \mathbb{R}_0 = \begin{pmatrix} \mathbb{R}_0^{(p)} & 0 \\ 0 & \mathbb{R}_0^{(n)} \end{pmatrix}, \quad (3.18)$$

denoting super-matrices in the enlarged proton-neutron space. The proton-neutron induced density takes the form

$$\delta\mathbb{R} = \begin{pmatrix} 0 & \delta\mathbb{R}^{(pn)} \\ \delta\mathbb{R}^{(np)} & 0 \end{pmatrix}. \quad (3.19)$$

By taking the  $(pn)$  block from the above equation one can derive the linear response equation at finite temperature in the q.p. basis as

$$-\omega\delta\mathcal{R}_{\pi\nu} = E_\pi\delta\mathcal{R}_{\pi\nu} - E_\nu\delta\mathcal{R}_{\pi\nu} - (f_\pi - f_\nu)(\delta H_{\pi\nu} + F_{\pi\nu}), \quad (3.20)$$

where the time-dependent fields have been expanded as

$$\delta\mathcal{R}_{\pi\nu}(t) = \delta\mathcal{R}_{\pi\nu}(\omega)e^{-i\omega t} + \text{h. c.} \quad (3.21)$$

Details can be found in Appendix A. The label  $\pi(\nu)$  denotes the proton(neutron) q.p. indices and is used in the following. The induced Hamiltonian can be written as [30, 75]

$$\delta H_{\pi\nu} = \sum_{\pi'\nu'} \frac{\delta H_{\pi\nu}}{\delta\mathcal{R}_{\pi'\nu'}} \delta\mathcal{R}_{\pi'\nu'} \equiv \sum_{\pi'\nu'} \mathbb{W}_{\pi\nu\pi'\nu'} \delta\mathcal{R}_{\pi'\nu'}. \quad (3.22)$$

There are two approaches to solve Eq. (3.20): (i) to search for its eigenvalues obtained by setting the external field to zero *i.e.*  $F_{\pi\nu} = 0$ , which is called the **matrix pnRQRPA** and (ii) approach based on introduction of the response function known as the **linear response pnRQRPA**. Of course, all calculated observables should be independent of the method we choose to solve Eq. (3.20), however, based on peculiarities of the interaction selected, one approach could be more numerically advantageous compared to the other. In Sec. 3.1 we introduce the linear response formalism at finite temperature, while in Sec. 3.2 we define the matrix pnRQRPA.

### 3.1 Linear response pnQRPA

We define the response function  $\mathbb{R}$ , starting from the induced density as

$$\delta\mathcal{R}_{\pi\nu} = \sum_{\pi'\nu'} \mathbb{R}_{\pi\nu\pi'\nu'} F_{\pi'\nu'}, \quad (3.23)$$

and by inserting the above definition in Eq. (3.20) we get

$$\mathbb{R}_{\pi\nu\pi'\nu'} = \mathbb{R}_{\pi\nu\pi'\nu'}^0 + \sum_{\mu\mu'} \mathbb{R}_{\pi\nu\mu\mu'}^0 \sum_{\pi''\nu''} \mathbb{W}_{\pi\nu\pi''\nu''} \mathbb{R}_{\pi''\nu''\pi'\nu'}, \quad (3.24)$$

which is known as the *Bethe-Salpeter equation* [75]. We used the definition of the unperturbed response as [75]

$$\mathbb{R}_{\pi\nu\pi'\nu'}^0 = \frac{(f_\pi - f_\nu)}{\omega - E_\pi - E_\nu + i\eta} \delta_{\pi\pi'} \delta_{\nu\nu'}, \quad (3.25)$$

where a small smearing parameter  $\eta$  is added due to the singular behaviour of the denominator. The linear response equation is significantly simplified if the following separable interaction form of the Hamiltonian is used

$$\hat{H} = \hat{H}_0 + \chi \sum_{\rho} D_{\rho}^{\dagger} D_{\rho}, \quad (3.26)$$

where  $\hat{H}_0$  is the single particle Hamiltonian (at the RHB level) and  $\rho$  runs over a set of single-particle operators  $D_{\rho}$ , which in the charge-exchange case are not necessarily Hermitian or anti-Hermitian. However, the full Hamiltonian has to remain Hermitian. Now, by solving for  $\mathbb{W}_{\pi\nu\pi'\nu'}(f_{\pi'} - f_{\nu'}) = \langle [a_{\pi}^{\dagger}, a_{\nu'}^{\dagger}, \{[a_{\pi}, H], a_{\nu'}^{\dagger}\}] \rangle_T$  and keeping only *direct* terms we get

$$\mathbb{W}_{\pi\nu\pi'\nu'} = \chi \mathcal{D}_{\pi\nu}^* \mathcal{D}_{\pi'\nu'} + \chi \mathcal{D}_{\bar{\pi}'\bar{\nu}'}^* \mathcal{D}_{\bar{\pi}\bar{\nu}}. \quad (3.27)$$

Note that the second term arises due to using the charge-exchange residual interaction instead of the like particle one. Derivations of the interaction matrix can be found in Appendix A.3. Instead of solving the Bethe-Salpeter equation in the q.p. configuration space, we introduce the reduced response function as in Ref. [75]

$$R_{\rho\rho'}(\omega) = \sum_{\pi\nu\pi'\nu'} \mathcal{D}_{\rho\pi\nu}^* \mathbb{R}_{\pi\nu\pi'\nu'}(\omega) \mathcal{D}_{\rho'\pi'\nu'}. \quad (3.28)$$

The unperturbed reduced response function is given by a simple substitution of  $\mathbb{R}^0$  in the above definition

$$R_{\rho\rho'}^0 = \sum_{\pi\nu} \frac{D_{\rho\pi\nu}^* D_{\rho'\pi\nu}}{\omega - E_\pi + E_{\nu'} + i\eta} (f_\nu - f_\pi), \quad (3.29)$$

which now yields the *reduced Bethe-Salpeter equation* in the coordinate space

$$R_{\rho\rho'} = R_{\rho\rho'}^0 + \sum_{\rho''} R_{\rho\rho''}^0 \chi R_{\rho''\rho'}. \quad (3.30)$$

Compared to the linear response equation in the configuration space [cf. Eq. (3.24)], above equation has a substantially lower dimension, and thus is more suitable for the large-scale calculations of nuclear properties across the nuclide chart.

The *physical* strength function is calculated as [75, 107]

$$S_F(\omega) = \sum_{\text{if}} p_i |\langle \text{f} | \hat{F} | \text{i} \rangle|^2 \delta(\omega - E_f + E_i), \quad (3.31)$$

where  $p_i = e^{-\beta E_i} / \sum_j e^{-\beta E_j}$ ,  $E_{i(f)}$  is the initial(final) state energy and  $\langle \text{f} | \hat{F} | \text{i} \rangle$  is the external field matrix element. By defining the response function

$$R_{FF} = \sum_{\mu\mu'\nu\nu'} F_{\mu\mu'}^* \mathbb{R}_{\mu\mu'\nu\nu'} F_{\nu\nu'}, \quad (3.32)$$

we can write the strength function within the linear response approximation as

$$S_F(\omega) \approx -\frac{1}{\pi} \frac{1}{1 - e^{-\beta\omega}} \text{Im} R_{FF}(\omega), \quad (3.33)$$

where  $(1 - e^{-\beta\omega})^{-1}$  is often termed as a detailed balance factor and will be clarified in Appendix B.

### 3.1.1 Solving the linear response equations

To simplify the following discussion, in this section we assume spherical symmetry. Extension to axial-symmetry is straightforward and demonstrated in Chapter 7. Suppose that the total interaction



Hamiltonian of the proton-neutron interaction can be written as [144]

$$\hat{H} = \hat{H}_0 + \frac{1}{2} \sum_{c=1}^{N_c} \int_0^\infty dr r^2 \sum_{pn p' n'} Q_{cp,n}^{(1)}(r) v_c(r) Q_{cp'n'}^{*(2)}(r) dr c_p^\dagger c_n c_n^\dagger c_{p'}, \quad (3.34)$$

here we assume that the residual interaction can be written as a sum of  $N_c$  separable terms denoted as  $Q_{cp,n}^{(1,2)}$  with interaction strength  $v_c(r)$ . Separable terms appearing in the interaction Hamiltonian can be written as

$$\hat{Q}_{pn} = \sum_{pn} \langle p|Q|n \rangle c_p^\dagger c_n, \quad (3.35)$$

in an arbitrary single-particle proton-neutron basis  $\{c_p^\dagger, c_n\}$  (later we will assume either spherical or axial symmetry and further determine the basis). We want to represent the above operator in the q.p. basis by employing the Bogoliubov transformation [58]

$$c_p = \sum_{\pi} U_{p\pi} \alpha_{\pi} + V_{p\pi}^* \alpha_{\pi}^{\dagger}, \quad c_n = \sum_{\nu} U_{n\nu} \alpha_{\nu} + V_{n\nu}^* \alpha_{\nu}^{\dagger}, \quad (3.36)$$

where  $U, V$  are Bogoliubov matrices and  $\{\alpha, \alpha^\dagger\}$  set of q.p. operators. Inserting transformation in Eq. (3.35) we get

$$\begin{aligned} \hat{Q}_{pn} &= \sum_{pn} \sum_{\pi\nu} \{ (U^\dagger Q U)_{\pi\nu} \alpha_{\pi}^{\dagger} \alpha_{\nu} + (U^\dagger Q V^*)_{\pi\nu} \alpha_{\pi}^{\dagger} \alpha_{\nu}^{\dagger} + (V^T Q U)_{\pi\nu} \alpha_{\pi} \alpha_{\nu} + (V^T Q V^*)_{\pi\nu} \alpha_{\pi} \alpha_{\nu}^{\dagger} \} \\ &= \sum_{pn} \sum_{\pi\nu} \begin{pmatrix} U^\dagger Q U & U^\dagger Q V^* \\ V^T Q U & V^T Q V^* \end{pmatrix} = \sum_{pn\pi\nu kk'} Q_{kk'}^{(pn)} a_{k\pi} a_{k'\nu}, \end{aligned} \quad (3.37)$$

where we have written the q.p. operator in matrix form according to the basis defined in Eq. (3.8). Notice that the operators  $\alpha_{\pi,\nu}$  are replaced with  $a_{\pi,\nu}$ .

Rather than solving the Bethe-Salpeter equation in the q.p. space, it is significantly easier to solve the above equation in the coordinate-space by introducing the reduced response [75]

$$R_{cc'}(\omega; r, r') = \sum_{\mu\mu'\nu\nu'} Q_{c\mu\mu'}^*(r) \mathbb{R}_{\mu\mu'\nu\nu'} Q_{c'\nu\nu'}(r'), \quad (3.38)$$

where  $Q_{c\mu\mu'}(r) = \langle \mu | Q_c(r) | \mu' \rangle$  is the separable channel of the interaction. In the case when the

interaction matrix  $\mathbb{W}$  can be written as a sum of separable channels and using result of Eq. (3.27)

$$\mathbb{W}_{\mu\mu'\nu\nu'} = \sum_c \int r^2 dr Q_{c\mu\mu'}(r) v_c(r) Q_{c\nu\nu'}^*(r) + \underbrace{\sum_c \int r^2 dr Q_{c\bar{\nu}\bar{\nu}'}(r) v_c(r) Q_{c\bar{\mu}\bar{\mu}'}^*(r)}_{\text{this can be treated as another channel}}. \quad (3.39)$$

The second term can be treated as another channel, doubling the dimension of the reduced response function. If there are  $N_c$  separable interaction channels then in the proton-neutron picture there will be total of  $2N_c$  channels in the response equation. Keeping this in mind we get the reduced Bethe-Salpeter equation in the coordinate space

$$R_{cc'}(\omega; r, r') = R_{cc'}^0(\omega; r, r') + \sum_{c''} \int r''^2 dr'' R_{cc''}^0(\omega; r, r'') v_{c''}(r'') R_{c'',c'}(\omega; r'', r'), \quad (3.40)$$

where the reduced unperturbed response is defined as

$$R_{cc'}^0(\omega; r, r') = \sum_{\mu\mu'} \frac{(f_{\mu'} - f_{\mu})}{\omega - E_{\mu} + E_{\mu'} + i\eta} Q_{c\mu\mu'}^*(r) Q_{c'\mu\mu'}(r'). \quad (3.41)$$

In order to solve for the response function  $R_{FF}$  perturbed by the external field  $F$  we use the definition

$$R_{FF} = \sum_{\mu\mu'\nu\nu'} F_{\mu\mu'}^* \mathbb{R}_{\mu\mu'\nu\nu'} F_{\nu\nu'}, \quad (3.42)$$

and insert the Bethe-Salpeter equation (3.24) to get the equation

$$R_{FF} = R_{FF}^0 + \sum_c \int r^2 dr R_{Fc}^0(r) v_c(r) R_{cF}(r), \quad (3.43)$$

where we have defined the following response functions

$$\begin{aligned} R_{FF}^0 &= \sum_{\mu\mu'\nu\nu'} F_{\mu\mu'}^* \mathbb{R}_{\mu\mu'\nu\nu'}^0 F_{\nu\nu'}, \\ R_{Fc}^0(r) &= \sum_{\mu\mu'\nu\nu'} F_{\mu\mu'}^* \mathbb{R}_{\mu\mu'\nu\nu'}^0 Q_{\nu\nu'}(r), \\ R_{cF}(r) &= \sum_{\mu\mu'\nu\nu'} Q_{c\mu\mu'}^*(r) \mathbb{R}_{\mu\mu'\nu\nu'} F_{\nu\nu'}. \end{aligned}$$

The next step is to solve for  $R_{cF}(r)$  from

$$R_{cF}(r) = R_{cF}^0(r) + \sum_{c'} \int r^2 dr R_{cc'}^0(r) v'_c(r) R_{c'F}(r), \quad (3.44)$$

where  $R_{cc'}^0$  is defined in Eq. (3.41). To solve the above system of equations we simply use the matrix inversion.

To illustrate the calculation procedure, suppose there are  $N_c$  interaction channels and that the radial integration mesh is discretized in  $N_r$  mesh-points. Let's denote  $N = N_c \times N_r$ . We can then write the above coupled system of equations in the matrix form as

$$\begin{aligned} R_{QF} &= R_{QF}^0 + R_{QQ}^0 \times V_{N \times N} \times R_{QF}, \\ R_{FF} &= R_{FF}^0 + R_{FQ}^0 \times V_{N \times N} \times R_{QF}, \end{aligned} \quad (3.45)$$

where  $V_{N \times N}$  is a matrix of dimension  $N \times N$  with elements consisting of  $v_c(r)$ , the response functions  $R_{QF}$  and  $R_{QF}^0$  are of the dimension  $N \times N_r$ , while  $R_{FF}$  and  $R_{FF}^0$  are  $N_r \times N_r$ . The reduced response matrix  $R_{QQ}^0$  is  $N \times N$  matrix. Since the interaction matrix elements are real,  $R_{QF} = R_{FQ}^T$ , reducing the number of required equations. We can calculate the  $R_{QF}$  response by matrix inversion

$$R_{QF} = R_{QF}^0 (1_{N \times N_r} - R_{QQ}^0 V_{N \times N})^{-1}, \quad (3.46)$$

which is substituted to obtain the response  $R_{FF}$  in Eq. (3.43).

The unperturbed response is calculated from the external field matrix elements as

$$R_{FF}^0(\omega; r) = \sum_{\pi\nu} \frac{(f_\nu - f_\pi)}{\omega - E_\pi + E_\nu + i\eta} F_{\pi\nu}^*(r) F_{\pi\nu}(r), \quad (3.47)$$

and the external field operator in the q.p. basis is

$$F_{\pi\nu}(r) = f(r) \begin{pmatrix} (U^\dagger F U)_{\pi\nu} & (U^\dagger F V^*)_{\pi\bar{\nu}} \\ (V^T F U)_{\bar{\pi}\nu} & -(V^T F V^*)_{\bar{\pi}\bar{\nu}} \end{pmatrix}, \quad (3.48)$$

with  $f(r)$  denoting its radial dependence. Thus, the unperturbed response at zero-temperature has

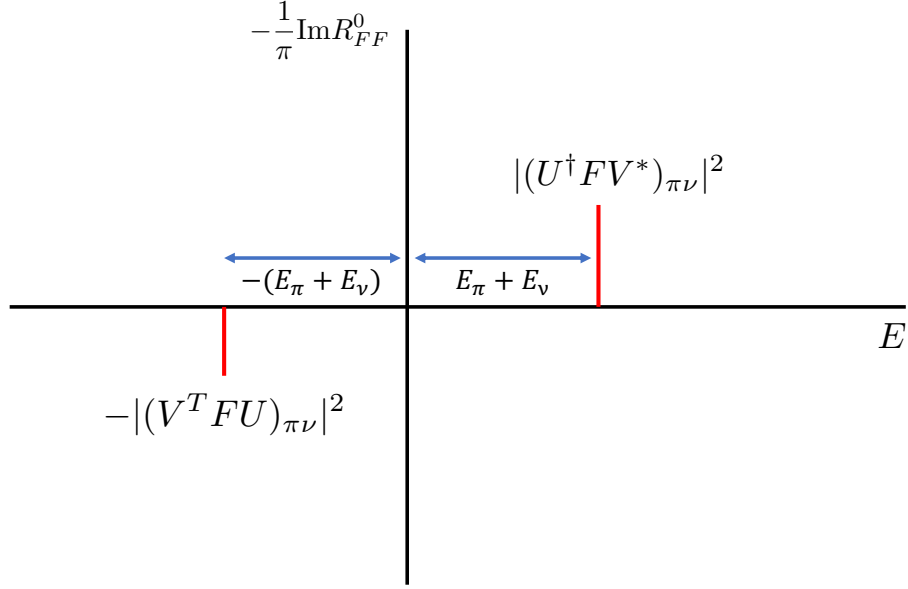


Figure 3.1: The pnQRPA strength as calculated in the proton-neutron linear response formalism. Check Eq. (3.50).

the form

$$R_{FF}^0(\omega; r) = \sum_{\pi\nu} \frac{(U^\dagger F V^*)_{\pi\nu}^*(r)(U^\dagger F V^*)_{\pi\nu}(r)}{\omega - E_\pi - E_\nu + i\eta} - \frac{(V^T F U)_{\pi\nu}^*(r)(V^T F U)_{\pi\nu}(r)}{\omega + E_\pi + E_\nu + i\eta}. \quad (3.49)$$

If we assume that  $\eta \rightarrow 0^+$  and use  $1/(\omega + i\eta) = P(1/\omega) - i\pi\delta(\omega)$ , then the imaginary part of the unperturbed response is

$$\begin{aligned} \text{Im} R_{FF}^0(\omega; r) = & \sum_{\pi\nu} -\pi (U^\dagger F V^*)_{\pi\nu}^*(r)(U^\dagger F V^*)_{\pi\nu}(r)\delta(\omega - (E_\pi + E_\nu)) \\ & + \pi (V^T F U)_{\pi\nu}^*(r)(V^T F U)_{\pi\nu}(r)\delta(\omega + (E_\pi + E_\nu)). \end{aligned} \quad (3.50)$$

The total strength is then obtained by integrating with  $\int r^2 dr f(r)$ . From the form of the above expression, we observe that at  $\omega = E_\pi + E_\nu$  we obtain the  $\beta^-$  unperturbed strength (for  $pn$  pairs) while for  $\omega = -(E_\pi + E_\nu)$  we get the  $\beta^+$  unperturbed strength. This is shown in Fig. 3.1 in the case of only one 2 q.p. pair. It means that we can calculate the response function on a symmetric energy interval and get both  $\beta^-$  and  $\beta^+$  strength.

### 3.1.2 The DD-PC1(X) interaction with the separable pairing

To take the full advantage of writing the response function in the reduced form we make use of the point-coupling interactions such as DD-PC1 [20] and DD-PCX [21], already introduced in Chapter 2. The use of the point-coupling interactions allows for the residual interaction to be written as

$$V_{\alpha\beta\alpha'\beta'}^{ph} = \sum_c Q_{\alpha\beta}^{\dagger c} v_c^{ph} Q_{\alpha'\beta'}^c, \quad (3.51)$$

where  $c$  is the number of the separable channels<sup>1</sup>,  $Q_{\alpha\beta}^c$  is the matrix element of the separable channel and  $v_c^{ph}$  is the diagonal interaction matrix — now we assume particle-hole ( $ph$ ), but extend to particle-particle ( $pp$ ) later. Since we are considering the charge-exchange case only two terms in the residual interaction Lagrangian contribute [cf. Sec. 2.1]

- isovector-vector (TV) interaction

$$\mathcal{L}_{TV} = -\frac{1}{2}\alpha_{TV}(\rho_v)(\bar{\psi}\vec{\tau}\gamma_\mu\psi) \cdot (\bar{\psi}\vec{\tau}\gamma^\mu\psi)\delta(\mathbf{r}_1 - \mathbf{r}_2), \quad (3.52)$$

- isovector-pseudovector (TPV) interaction

$$\mathcal{L}_{TPV} = g_0(\gamma_0\gamma_5\gamma_\mu\vec{\tau}) \cdot (\gamma_0\gamma_5\gamma^\mu\vec{\tau})\delta(\mathbf{r}_1 - \mathbf{r}_2), \quad (3.53)$$

where  $\cdot$  implies integration over the radial coordinates as well as a summation over  $\mu$ . The parameter  $g_0$  is the TPV interaction coupling constant. Its strength is  $g_0 = 0.734$  for the DD-PC1 interaction and  $g_0 = 0.621$  for the DD-PCX, as determined by reproducing the experimental  $GT^-$  centroid energy in  $^{208}\text{Pb}$  [145]. We note that at the FT-RHB level, only the TV term is present in the Lagrangian density [30, 145]. The Dirac spinors in the central field with spherical symmetry have the form [138, 146]

$$|\psi\rangle = \begin{pmatrix} f_i(r) [\chi_{1/2} \otimes Y_l]_{jm} \\ ig_i(r) [\chi_{1/2} \otimes Y_{\tilde{l}}]_{jm} \end{pmatrix}, \quad (3.54)$$

where  $f_i(r)$  ( $g_i(r)$ ) are upper (lower) components of the Dirac spinor,  $j$  labels the total angular momentum with projection  $m$  and orbital angular momentum  $l$  ( $\tilde{l}$ ) for upper (lower) components, while  $\chi_{1/2m_s}$  are spin-1/2 wave functions with projection  $m_s$ . The Dirac spinors are expanded in

<sup>1</sup>Here we assume that  $v_c$  is a diagonal matrix. To treat the derivative terms in the residual interaction it has to be expanded as  $v_{cc'}$ , having off-diagonal elements.

$N_{osc}$  ( $\tilde{N}_{osc}$ ) harmonic oscillator shells for upper(lower) components [146]

$$f_i(r) = \sum_{n=0}^{N_{osc}} f_n^{(i)} R_{nl_i}(r, b_0), \quad g_i(r) = \sum_{n=0}^{\tilde{N}_{osc}} g_n^{(i)} R_{n\tilde{l}_i}(r, b_0), \quad (3.55)$$

where  $R_{nl_i}(r, b_0)$  are radial harmonic oscillator wavefunctions, and  $b_0$  the oscillator length [146]. If the number of upper components is  $n_f$  and lower  $n_g$  we define the spinor dimension  $n_h = n_f + n_g$ . The RHB wave function has the dimension  $n_{RHB} = n_h + n_h$  and is of the form

$$\begin{aligned} & \underbrace{\left( \underbrace{U_f(r)}_{n_f} \quad \underbrace{U_g(r)}_{n_g} \quad \underbrace{V_f(r)}_{n_f} \quad \underbrace{V_g(r)}_{n_g} \right)_i}_{n_{RHB}} \\ &= \begin{pmatrix} 1_{n_h} \\ 0_{n_h} \end{pmatrix} \otimes \left( \sum_{n=0}^{N_{osc}} u_f^{n,l(i)} R_{nl}(r) [\chi_{1/2} \otimes Y_l]_{jm} \quad \sum_{n=0}^{\tilde{N}_{osc}} u_g^{n,\tilde{l}(i)} R_{n\tilde{l}}(r) [\chi_{1/2} \otimes Y_{\tilde{l}}]_{jm} \right) \\ &+ \begin{pmatrix} 0_{n_h} \\ 1_{n_h} \end{pmatrix} \otimes \left( \sum_{n=0}^{N_{osc}} v_f^{n,l(i)} R_{nl}(r) [\chi_{1/2} \otimes Y_l]_{jm} \quad \sum_{n=0}^{\tilde{N}_{osc}} v_g^{n,\tilde{l}(i)} R_{n\tilde{l}}(r) [\chi_{1/2} \otimes Y_{\tilde{l}}]_{jm} \right), \end{aligned}$$

where  $\begin{pmatrix} 1_{n_h} & 0_{n_h} \end{pmatrix} = \left( \underbrace{1 \dots 1}_{n_h} \quad \underbrace{0 \dots 0}_{n_h} \right)$ .

Separable interaction terms can be distinguished between natural parity and unnatural parity transitions. By abbreviating  $f_{nl_i} \equiv f_n^{(i)} R_{nl_i}(r, b)$  we have the following channels corresponding to  $ph$  residual interaction in Eq. (3.51):

- **natural parity transitions** ( $J^\pi = 0^+, 1^-, 2^+$ ):

$$\begin{aligned} Q_{1k_1 k_3}(r) &= f_{n_{k_1} l_{k_1}}(r) f_{n_{k_3} l_{k_3}}(r) \langle l_{k_1} j_{k_1} || Y_J(\Omega) \vec{\tau} || l_{k_3} j_{k_3} \rangle \\ &+ g_{n_{k_1} \tilde{l}_{k_1}}(r) g_{n_{k_3} \tilde{l}_{k_3}}(r) \langle \tilde{l}_{k_1} j_{k_1} || Y_J(\Omega) \vec{\tau} || \tilde{l}_{k_3} j_{k_3} \rangle, \end{aligned} \quad (3.56)$$

$$\begin{aligned} Q_{2k_1 k_3}(r) &= f_{n_{k_1} l_{k_1}}(r) g_{n_{k_3} \tilde{l}_{k_3}}(r) \langle l_{k_1} j_{k_1} || [\sigma_S Y_{J-1}(\Omega)]_J \vec{\tau} || \tilde{l}_{k_3} j_{k_3} \rangle \\ &- g_{n_{k_1} \tilde{l}_{k_1}}(r) f_{n_{k_3} l_{k_3}}(r) \langle \tilde{l}_{k_1} j_{k_1} || [\sigma_S Y_{J-1}(\Omega)]_J \vec{\tau} || l_{k_3} j_{k_3} \rangle, \end{aligned} \quad (3.57)$$

$$\begin{aligned}
 Q_{3k_1k_3}(r) &= f_{n_{k_1}l_{k_1}}(r)g_{n_{k_3}\tilde{l}_{k_3}}(r)\langle l_{k_1}j_{k_1}||[\sigma_S Y_{J+1}(\Omega)]_J \vec{\tau}||\tilde{l}_{k_3}j_{k_3}\rangle \\
 &\quad - g_{n_{k_1}\tilde{l}_{k_1}}(r)f_{n_{k_3}l_{k_3}}(r)\langle \tilde{l}_{k_1}j_{k_1}||[\sigma_S Y_{J+1}(\Omega)]_J \vec{\tau}||l_{k_3}j_{k_3}\rangle,
 \end{aligned} \tag{3.58}$$

$$\begin{aligned}
 Q_{4k_1k_3}(r) &= f_{n_{k_1}l_{k_1}}(r)f_{n_{k_3}l_{k_3}}(r)\langle l_{k_1}j_{k_1}||[\sigma_S Y_J(\Omega)]_J \vec{\tau}||l_{k_3}j_{k_3}\rangle \\
 &\quad + g_{n_{k_1}\tilde{l}_{k_1}}(r)g_{n_{k_3}\tilde{l}_{k_3}}(r)\langle \tilde{l}_{k_1}j_{k_1}||Y_J(\Omega) \vec{\tau}||\tilde{l}_{k_3}j_{k_3}\rangle,
 \end{aligned} \tag{3.59}$$

with  $v_1(r, r') = \frac{\alpha_{TV}(r)}{r^2}\delta(r - r')$ ,  $v_2(r, r') = -\frac{\alpha_{TV}(r)}{r^2}\delta(r - r')$ ,  $v_3(r, r') = -\frac{\alpha_{TV}(r)}{r^2}\delta(r - r')$ ,  $v_4(r, r') = -\frac{g_0}{r^2}\delta(r - r')$ .

- **unnatural parity transitions** ( $J^\pi = 0^-, 1^+, 2^-$ )

$$\begin{aligned}
 Q_{1k_1k_3}(r) &= g_{n_{k_1}\tilde{l}_{k_1}}(r)f_{n_{k_3}l_{k_3}}(r)\langle \tilde{l}_{k_1}j_{k_1}||[\sigma_S Y_J(\Omega)]_J \vec{\tau}||l_{k_3}j_{k_3}\rangle \\
 &\quad - f_{n_{k_1}l_{k_1}}(r)g_{n_{k_3}\tilde{l}_{k_3}}(r)\langle l_{k_1}j_{k_1}||[\sigma_S Y_J(\Omega)]_J \vec{\tau}||\tilde{l}_{k_3}j_{k_3}\rangle,
 \end{aligned} \tag{3.60}$$

$$\begin{aligned}
 Q_{2k_1k_3}(r) &= f_{n_{k_1}l_{k_1}}(r)g_{n_{k_3}\tilde{l}_{k_3}}(r)\langle l_{k_1}j_{k_1}||Y_J(\Omega) \vec{\tau}||\tilde{l}_{k_3}j_{k_3}\rangle \\
 &\quad - g_{n_{k_1}\tilde{l}_{k_1}}(r)f_{n_{k_3}l_{k_3}}(r)\langle \tilde{l}_{k_1}j_{k_1}||Y_J(\Omega) \vec{\tau}||l_{k_3}j_{k_3}\rangle,
 \end{aligned} \tag{3.61}$$

$$\begin{aligned}
 Q_{3k_1k_3}(r) &= f_{n_{k_1}l_{k_1}}(r)f_{n_{k_3}l_{k_3}}(r)\langle l_{k_1}j_{k_1}||[\sigma_S Y_{J-1}(\Omega)]_J \vec{\tau}||l_{k_3}j_{k_3}\rangle \\
 &\quad + g_{n_{k_1}\tilde{l}_{k_1}}(r)g_{n_{k_3}\tilde{l}_{k_3}}(r)\langle \tilde{l}_{k_1}j_{k_1}||Y_{J-1}(\Omega) \vec{\tau}||\tilde{l}_{k_3}j_{k_3}\rangle,
 \end{aligned} \tag{3.62}$$

$$\begin{aligned}
 Q_{4k_1k_3}(r) &= f_{n_{k_1}l_{k_1}}(r)f_{n_{k_3}l_{k_3}}(r)\langle l_{k_1}j_{k_1}||[\sigma_S Y_{J-1}(\Omega)]_J \vec{\tau}||l_{k_3}j_{k_3}\rangle \\
 &\quad + g_{n_{k_1}\tilde{l}_{k_1}}(r)g_{n_{k_3}\tilde{l}_{k_3}}(r)\langle \tilde{l}_{k_1}j_{k_1}||Y_{J-1}(\Omega) \vec{\tau}||\tilde{l}_{k_3}j_{k_3}\rangle,
 \end{aligned} \tag{3.63}$$

with  $v_1(r, r') = -\frac{g_0}{r^2}\delta(r - r')$ ,  $v_2(r, r') = \frac{g_0}{r^2}\delta(r - r')$ ,  $v_3(r, r') = -\frac{\alpha_{TV}(r)}{r^2}\delta(r - r')$ ,  $v_4(r, r') = -\frac{g_0}{r^2}\delta(r - r')$ .

The spin rank is either  $S = 0, 1$ , therefore the rank of spherical harmonics is  $J, J \pm 1$  so that the total matrix element can be coupled to  $J$ . The isospin Pauli matrix is denoted by  $\vec{\tau}$ , while the spin matrix is  $\sigma_S$ . There are only 4 channels for both cases of natural parity.

Two-body matrix elements of the residual pairing interaction in the basis of spherical harmonic oscillator are calculated as

$$\langle n_{l_1} l_{l_1} j_{l_1}, n_{l_2} l_{l_2} j_{l_2} | \hat{V}_{pp}(\mathbf{r}_1, \mathbf{r}_2, \mathbf{r}'_1, \mathbf{r}'_2) | n_{l_3} l_{l_3} j_{l_3}, n_{l_4} l_{l_4} j_{l_4} \rangle, \quad (3.64)$$

where we assume the separable pairing interaction of the form [141]

$$\hat{V}_{pp}(\mathbf{r}_1, \mathbf{r}_2, \mathbf{r}'_1, \mathbf{r}'_2) = -G \delta(\mathbf{R} - \mathbf{R}') P(r) P(r') \frac{1}{2} (1 - P^r P^\sigma P^\tau), \quad (3.65)$$

with  $P^r, P^\sigma, P^\tau$  being coordinate, spin and isospin exchange operators respectively,  $\mathbf{R} = \frac{1}{2}(\mathbf{r}_1 + \mathbf{r}_2)$  and  $\mathbf{r} = \mathbf{r}_1 - \mathbf{r}_2$  are the center-of-mass and relative coordinates while

$$P(r) = \frac{1}{(4\pi a)^{3/2}} e^{-\frac{r^2}{4a^2}}, \quad (3.66)$$

where  $a$  and  $G$  are free parameters depending on the underlying EDF. By calculating the matrix element in Eq. (3.64) and coupling to good angular momentum  $J$ , residual pairing matrix elements assume the separable form in the harmonic oscillator basis

$$V_{l_1 l_2, l_3 l_4}^J = -G f \sum_{NLS} V_{l_1 l_2}^{NLSJ} V_{l_3 l_4}^{NLSJ}, \quad (3.67)$$

where we define the separable terms as [145]

$$\begin{aligned} V_{l_1 l_2}^{NLSJ} &= \frac{\hat{L} \hat{S}}{2^{3/2} \pi^{3/4} b^{3/2}} \frac{(1 - \alpha^2)^n}{(1 + \alpha^2)^{n+3/2}} \times \\ &\times \frac{(2n+1)!}{2^n n!} \hat{j}_{l_1} \hat{j}_{l_2} \begin{Bmatrix} l_2 & 1/2 & j_{l_2} \\ l_1 & 1/2 & j_{l_1} \\ L & S & J \end{Bmatrix} M_{n_1 l_1 n_2 l_2}^{NLSn0}, \end{aligned} \quad (3.68)$$

with  $\alpha = a/b_0$ ,  $b_0$  being the harmonic oscillator constant and  $M_{n_1 l_1 n_2 l_2}^{NLSn0}$  the Talmi-Moschinsky bracket [141]. We use the usual abbreviation  $\hat{j} = \sqrt{2j+1}$ . Due to constraints imposed by coupling



charge-exchange channel and exchange operators of Eq. (3.64)

$$f = \begin{cases} 1, & \text{if } T = 1, S = 0 \\ V^{is}, & \text{if } T = 0, S = 1. \\ 0 & \text{otherwise} \end{cases} \quad (3.69)$$

For the charge-exchange channel total isospin operator can assume values  $T = 0, 1$ .

### 3.1.3 Angular momentum coupling

Assuming spherical and time-reversal symmetry, the total angular momentum  $J$  is a good quantum number, in addition to the parity  $\pi$ . Therefore, the dimensions of the problem can be significantly reduced by solving the linear response equations within well defined  $J^\pi$  blocks. To achieve that, we have to couple the separable interaction channels  $Q_c$  to  $Q_c^J$  which have a well defined angular momentum. In order to couple the fermion operators we use [30, 58, 147]:

$$[\alpha_{pj}^\dagger \alpha_{nj'}^\dagger]_{JM} = \sum_{mm'} C_{jmj'm'}^{JM} \alpha_{pjm}^\dagger \alpha_{nj'm'}^\dagger, \quad [\tilde{\alpha}_{pj} \tilde{\alpha}_{nj'}]_{JM} = -(-)^{J+M} \sum_{mm'} C_{jmj'm'}^{J-M} \alpha_{pjm} \alpha_{nj'm'}, \quad (3.70)$$

with the definitions

$$[\alpha_{pj}^\dagger \otimes \tilde{\alpha}_{nj'}]_{JM} = \sum_{mm'} (-)^{j'-m'} C_{jmj'-m'}^{JM} \alpha_{pjm}^\dagger \alpha_{nj'm'}, \quad (3.71)$$

$$[\tilde{\alpha}_{pj} \otimes \alpha_{nj'}^\dagger]_{JM} = -(-)^{J+M} \sum_{mm'} (-)^{j'-m'} C_{jmj'-m'}^{J-M} \alpha_{pjm} \alpha_{nj'm'}^\dagger. \quad (3.72)$$

Also,  $\tilde{\alpha}_{jm} = (-)^{j+m} \alpha_{j-m}$ . Here, we have explicitly denoted the angular momentum and projection of the q.p. operator as  $j$  and  $m$ , respectively. The Bogoliubov transformation between spherical fermion operators is [147]:

$$c_{kj-m} = \sum_l U_{kl}^j \alpha_{lj-m} + (-)^{j+m} V_{kl}^{j*} \alpha_{ljm}^\dagger, \quad (3.73)$$

$$c_{kjm}^\dagger = \sum_l (-)^{j-m} V_{kl}^j \alpha_{lj-m} + U_{kl}^{j*} \alpha_{ljm}^\dagger, \quad (3.74)$$

where  $U, V$  are independent of the projection  $m$ . The coupling has to be performed separately for the  $ph$  and  $pp$  residual interaction. In addition to the  $ph$  and  $pp$  channels, we also demonstrate coupling of the external field matrix element.

### The $ph$ residual interaction

The single-particle  $ph$  operator can be transformed to the spherical q.p. basis as

$$\begin{aligned}
 \hat{Q}_{pn} &= \sum_{pn;jj';mm'} Q_{pjm;nj'm'} c_{pjm}^\dagger c_{nj'm'} \\
 &= \sum_{pn;jj';mm'} Q_{pjm;nj'm'} \left( (-)^{j-m} V_{p\pi} U_{n\nu} \alpha_{\pi j-m} \alpha_{\nu j'm'} + (-)^{j+j'-m-m'} V_{p\pi} V_{n\nu}^* \alpha_{\pi j-m} \alpha_{\nu j'-m'}^\dagger \right. \\
 &\quad \left. + U_{p\pi}^* U_{n\nu} \alpha_{\pi j m}^\dagger \alpha_{\nu j'm'} + (-)^{j'-m'} U_{p\pi}^* V_{n\nu}^* \alpha_{\pi j m}^\dagger \alpha_{\nu j'-m'}^\dagger \right),
 \end{aligned} \tag{3.75}$$

by performing the coupling of the  $ph$  matrix element to angular momentum  $J$  we have

$$Q_{pjm;nj'm'} = \sum_{JM} Q_{pj;nj'}^J (-)^{j'-m'} C_{jmj'-m'}^{JM}, \tag{3.76}$$

and inserting in the above derivation with the use of Eqs. (3.70,3.71) we get

$$\begin{aligned}
 \hat{Q}_{pn} &= \sum_{p\pi n\nu jj' JM} Q_{pj;nj'}^J \left( V_{p\pi} U_{n\nu} [\tilde{\alpha}_{\pi j} \tilde{\alpha}_{\nu j'}]_{JM} - V_{p\pi} V_{n\nu}^* [\tilde{\alpha}_{\pi j} \otimes \alpha_{\nu j'}^\dagger]_{JM} \right. \\
 &\quad \left. + U_{p\pi}^* U_{n\nu} [\alpha_{\pi j}^\dagger \otimes \tilde{\alpha}_{\nu j'}]_{JM} + U_{p\pi}^* V_{n\nu}^* [\alpha_{\pi j}^\dagger \alpha_{\nu j'}^\dagger]_{JM} \right).
 \end{aligned} \tag{3.77}$$

In the matrix notation introduced previously in Eq. (3.37)

$$\hat{Q}_{pn} = \sum_{pj;nj'} \sum_{JM} \sum_{\pi\nu} \begin{pmatrix} (U^\dagger Q^J U)_{\pi\nu} & (U^\dagger Q^J V^*)_{\pi\nu} \\ (V^T Q^J U)_{\pi\nu} & -(V^T Q^J V^*)_{\pi\nu} \end{pmatrix} = \sum_{\pi\nu kk'} Q_{kk'}^{(pn)} a_{k\pi} a_{k'\nu}. \tag{3.78}$$

### External field operator

As an example of the charge-changing external field operator we take the Gamow-Teller  $\hat{F} = \sigma \tau_\pm$ , for  $\beta^\pm$  direction corresponding to the  $GT^\pm$  transitions. The external field operator for the  $GT^-$

strength can be written as

$$\hat{F}^{pn} = \sum_{pnjj'mm'} F_{pjm;nj'm'} c_{pjm}^\dagger c_{nj'm'} = \sum_{pnjj'mm'} \langle pjm | [\boldsymbol{\sigma}\tau_-]_{JM} | nj'm' \rangle c_{pjm}^\dagger c_{nj'm'}, \quad (3.79)$$

where  $\tau_- |n\rangle = |p\rangle$ . For the  $GT^+$  strength we have

$$(\hat{F}^{pn})^\dagger = \sum_{pnjj'mm'} F_{njm;pj'm'} c_{njm}^\dagger c_{pj'm'} = \sum_{pnjj'mm'} \langle njm | [\boldsymbol{\sigma}\tau_+]_{JM} | pj'm' \rangle c_{njm}^\dagger c_{pj'm'}, \quad (3.80)$$

where  $\tau_+ |p\rangle = |n\rangle$ . Hence, these two operators are related through the Hermitian conjugation. Written in the q.p. basis with coupled angular momentum, their form corresponds exactly to Eq. (3.78) for the  $ph$  interaction.

### The $pp$ residual interaction

Based on the similar analysis of the  $ph$  channel, the residual pairing separable term has the form

$$\hat{V}_{pn}^\dagger = \sum_{pn} V_{pn}^{NJ} c_p^\dagger c_n^\dagger, \quad (3.81)$$

where  $V_{pn}^{NJ}$  is the separable residual pairing channel corresponding to expression in Eq. (3.68).

The  $pp$ -part of the residual interaction has the form

$$\hat{V}_{pn}^\dagger \hat{V}_{pn} = \sum_{pnp'n'} V_{pn}^{NJ} V_{p'n'}^{NJ*} c_p^\dagger c_n^\dagger c_{n'} c_{p'}, \quad (3.82)$$

and above is Hermitian as it should be, since it is a term in the Hamiltonian. We can now write for a separable term in the spherical h.o. basis

$$\hat{V}_{pn} = \sum_{pjm;nj'm'} V_{pjm;nj'm'} c_{pjm}^\dagger c_{nj'm'}^\dagger, \quad (3.83)$$

which we will transform in the q.p. representation in the following. Using Eqs. (3.70) and (3.71) we get

$$\begin{aligned}
 \hat{V}_{pn} &= \sum_{pj:nj'} \sum_{JM} \sum_{\pi\nu} V_{pj:nj'}^J \left\{ -(V^T V^J V)_{\pi\nu} [\tilde{\alpha}_{\pi j} \tilde{\alpha}_{\nu j'}]_{JM} - (V^T V^J U^*)_{\pi\nu} [\tilde{\alpha}_{\pi j} \otimes \alpha_{\nu j'}^\dagger]_{JM} \right. \\
 &\quad \left. - (U^\dagger V^J V)_{\pi\nu} [\alpha_{\pi j}^\dagger \otimes \tilde{\alpha}_{\nu j'}]_{JM} + (U^\dagger V^J U^*)_{\pi\nu} [\alpha_{\pi j}^\dagger \alpha_{\nu j'}^\dagger]_{JM} \right\} \\
 &= \sum_{pj:nj'} \sum_{JM} \sum_{\pi\nu} \begin{pmatrix} -(U^\dagger V^J V)_{\pi\nu} & (U^\dagger V^J U^*)_{\pi\nu} \\ -(V^T V^J V)_{\pi\nu} & -(V^T V^J U^*)_{\pi\nu} \end{pmatrix} = \sum_{\pi\nu k k'} V_{kk'}^{(pn)} a_{k\pi} a_{k'\nu},
 \end{aligned} \tag{3.84}$$

where in the above we have used the matrix notation as introduced in Eq. (3.37).

## 3.2 Matrix FT-pnRQRPA

The FT-QRPA equations in the matrix form were derived in Refs. [107, 148, 149] for both the like-particle and charge-exchange channels. Here we follow the work presented in Refs. [31, 34] which connects the matrix QRPA to the linear response QRPA formalism. Starting from the linearized TD-HFB equation in Eq. (3.20) we can write it in the matrix form [31, 34]

$$[T\mathbb{W} + \mathcal{E} - \omega\mathcal{M}]T\delta\mathcal{R} = -T\mathcal{F}, \tag{3.85}$$

where we have expanded the interaction matrix  $\delta\mathcal{H}_{\pi\nu}$  as in Eq. (3.22). The matrix of Fermi-Dirac factors is defined as

$$T_{\mu\mu'} = \text{diag}(f_{\mu'} - f_{\mu}, 1 - f_{\mu'} - f_{\mu}, 1 - f_{\mu'} - f_{\mu}, f_{\mu'} - f_{\mu}), \tag{3.86}$$

the norm matrix is

$$\mathcal{M} = \text{diag}(1, 1, -1, -1), \tag{3.87}$$

and the q.p. energy matrix

$$\mathcal{E}_{\mu\mu'} = \text{diag}(E_{\mu} + E_{\mu'}, E_{\mu} - E_{\mu'}, -E_{\mu} - E_{\mu'}, -E_{\mu} + E_{\mu'}). \tag{3.88}$$

These are diagonal matrices of the dimension  $4N_{ph} \times 4N_{ph}$  where  $N_{ph}$  is the number of q.p. pairs. The interaction matrix  $\mathbb{W}$  has the structure

$$\mathbb{W}_{\mu\mu'\nu\nu'} = \frac{\delta\mathcal{H}_{\mu\mu'}}{\delta\mathcal{R}_{\nu\nu'}} = \begin{pmatrix} C' & a & b & D \\ a^\dagger & A' & B & b^T \\ b^\dagger & B^* & A'^* & a^T \\ D^* & b^* & a^* & C'^* \end{pmatrix}, \quad (3.89)$$

where the definition of submatrices  $a, a^T, a^\dagger, b, b^T, b^\dagger, A', B, D$  and  $C'$  can be found in Ref. [107]. The external field operator  $\mathcal{F}$  and the induced density  $\delta\mathcal{R}$  have the following structure in the q.p. basis, respectively

$$\mathcal{F}_{\mu\mu'} = \begin{pmatrix} F^{11} & F^{20} & F^{02} & F^{\bar{1}\bar{1}} \end{pmatrix}_{\mu\mu'}^T, \quad \delta\mathcal{R}_{\mu\mu'}(\omega) = \begin{pmatrix} P(\omega) & X(\omega) & Y(\omega) & Q(\omega) \end{pmatrix}_{\mu\mu'}^T, \quad (3.90)$$

with  $F^{11}, F^{20}, F^{02}, F^{\bar{1}\bar{1}}$  defined in Ref. [58]. By setting the external field to zero in Eq. (3.85) we obtain the FT-pnRQRPA eigenvalue problem

$$[\mathcal{E} + T\mathbb{W}]T\mathcal{X} = \mathcal{M}T\mathcal{X}\Omega, \quad (3.91)$$

where  $\mathcal{X}$  is the matrix whose columns consist of the FT-pnRQRPA eigenvectors

$$\mathcal{X} = \begin{pmatrix} P_1 \dots P_{2N_{ph}} & Q_1^* \dots Q_{2N_{ph}}^* \\ X_1 \dots X_{2N_{ph}} & Y_1^* \dots Y_{2N_{ph}}^* \\ Y_1 \dots Y_{2N_{ph}} & X_1^* \dots X_{2N_{ph}}^* \\ Q_1 \dots Q_{2N_{ph}} & P_1^* \dots P_{2N_{ph}}^* \end{pmatrix}, \quad (3.92)$$

with the matrix of eigenvalues defined as  $\Omega = \text{diag}(E_1 \dots E_{2N_{ph}}, -E_1 \dots -E_{2N_{ph}})$ . We introduce the 2 q.p. excitation operator as [107]

$$\Gamma_n = \sum_{\nu\nu'} P_{\nu\nu'}^{n*} \alpha_\nu \alpha_{\nu'}^\dagger - X^{n*} \alpha_\nu \alpha_{\nu'} + Y_{\nu\nu'}^{n*} \alpha_\nu^\dagger \alpha_{\nu'}^\dagger - Q_{\nu\nu'}^{n*} \alpha_\nu^\dagger \alpha_{\nu'}. \quad (3.93)$$

The transition matrix element of the external field has to be generalized from the zero temperature form  $|\langle 0|\hat{F}|n\rangle|^2$  to

$$\begin{aligned} \langle [\Gamma_n, \hat{F}] \rangle &= \sum_{\nu\nu'} F_{\nu\nu'}^{n*} F_{\nu\nu'}^{11} (f_{\nu'} - f_{\nu}) + X_{\nu\nu'}^{n*} F_{\nu\nu'}^{20} (1 - f_{\nu'} - f_{\nu}) \\ &+ Y_{\nu\nu'}^{n*} F_{\nu\nu'}^{02} (1 - f_{\nu'} - f_{\nu}) + Q_{\nu\nu'}^{n*} F_{\nu\nu'}^{\bar{1}1} (f_{\nu'} - f_{\nu}), \end{aligned} \quad (3.94)$$

where  $\langle \cdot \rangle$  denotes the thermal average with respect to the non interacting density matrix  $\mathcal{R}^0$  [107]. The equation (3.91) is solved by matrix diagonalization, which yields set of eigenvalues  $\Omega$  and the corresponding eigenvectors  $\mathcal{X}$  which are used to calculate the transition matrix element in Eq. (3.94). The dimension of the matrix which has to be diagonalized is  $4N_{ph} \times 4N_{ph}$ . For spherical nuclei where the number of q.p. pairs is  $N_{ph} \sim 1000$  the problem is easily solved with moderate amount of computer resources. However, as we will demonstrate later, once the spherical symmetry is broken, the number of q.p. pairs raises to  $N_{ph} \sim 50000$  which is computationally quite demanding.

### 3.3 Numerical tests

In this section we perform the numerical comparisons between the linear response FT-pnRQRPA and matrix FT-pnRQRPA. Detailed investigation was carried in Ref. [30] and here we use this section to illustrate numerical differences between the two implementations. The tests are performed for the  $GT^-$  strength function in  $^{116}\text{Sn}$  at finite temperature. The initial state of the nucleus is calculated with the FT-HBCS solver using the delta-pairing interaction as described in Ref. [30] and section 2.2.1. The FT-HBCS presents an approximation to the FT-RHB but requires less calculation time compared to the full FT-RHB. Nevertheless, for our purposes in this work it is sufficient. The matrix FT-pnRQRPA is developed in Refs. [145, 149] and offers an independent test of the implementation. The wave functions of the FT-HBCS are expanded in  $N_{osc} = 10$  h.o. shells at  $T = 0.6$  MeV using the DD-PC1 interaction. The strength of the isoscalar pairing is set to  $V^{is} = 1.0$ . In Figure 3.2 we compare the  $GT^-$  strength function between the two implementations, the linear response FT-pnRQRPA (lrFT-QRPA) and the matrix FT-pnRQRPA (mFT-QRPA).

The lrFT-QRPA result represents a continuous line for which we have used a smearing parameter  $\eta = 0.25$  MeV, while the mFT-QRPA results are discrete peaks at corresponding pnFT-RQRPA eigenvalues. The height of the peaks and the continuous line should not be compared, however,

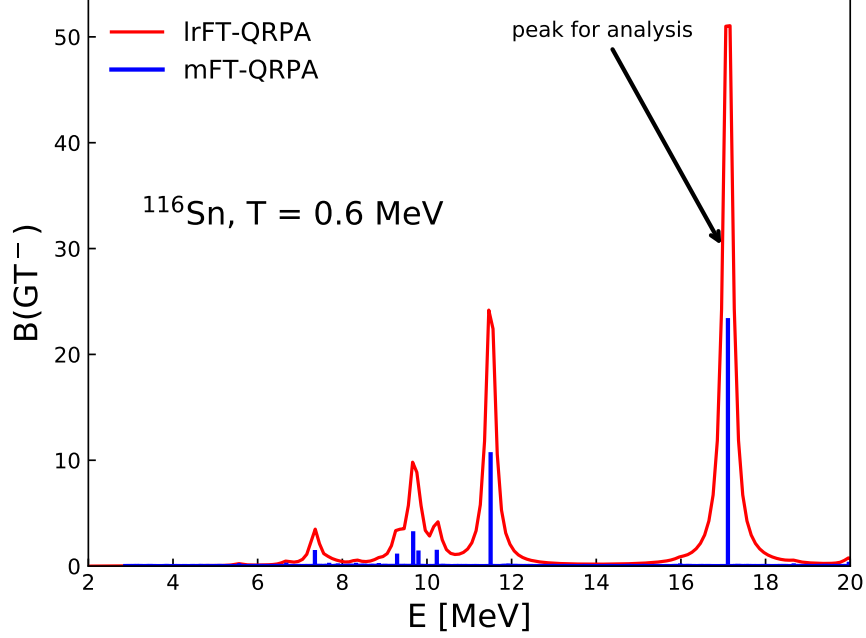


Figure 3.2: The  $GT^-$  strength function of  $^{116}\text{Sn}$  at  $T = 0.6$  MeV calculated with the FT-pnQRPA based on the linear response (red solid line) and the matrix formulation (blue peaks). Calculations are based on the FT-HBCS initial state with the delta-pairing interaction. Both implementations employ  $N_{osc} = 10$  h.o. shells.

their energies agree. The strength function in Eq. (3.33) is given as the imaginary part of the response function, whose poles correspond to the mFT-QRPA eigenvalues. To directly compare the matrix elements between the two approaches we have to compare the IrFT-QRPA induced densities to the mFT-QRPA eigenvectors. In Ref. [30] we have defined the linear response amplitudes as  $\delta\mathcal{R}_{\pi\bar{\nu}} = X_{\pi\nu}(\omega)$ ,  $\delta\mathcal{R}_{\bar{\pi}\nu} = Y_{\pi\nu}(\omega)$ ,  $\delta\mathcal{R}_{\pi\nu} = P_{\pi\nu}(\omega)$  and  $\delta\mathcal{R}_{\bar{\pi}\bar{\nu}} = Q_{\pi\nu}(\omega)$ . Starting from the linear response amplitudes the mFT-QRPA eigenvectors of the  $i$ -th mode can be calculated as

$$\begin{aligned} X_{\pi\nu}^i &= e^{-i\theta} |\langle i|\hat{F}|0\rangle|^{-1} \frac{1}{2\pi i} \oint_{C_i} X_{\pi\nu}(\omega) d\omega, & P_{\pi\nu}^i &= e^{-i\theta} |\langle i|\hat{F}|0\rangle|^{-1} \frac{1}{2\pi i} \oint_{C_i} P_{\pi\nu}(\omega) d\omega, \\ Y_{\pi\nu}^i &= e^{-i\theta} |\langle i|\hat{F}|0\rangle|^{-1} \frac{1}{2\pi i} \oint_{C_i} Y_{\pi\nu}(\omega) d\omega, & Q_{\pi\nu}^i &= e^{-i\theta} |\langle i|\hat{F}|0\rangle|^{-1} \frac{1}{2\pi i} \oint_{C_i} Q_{\pi\nu}(\omega) d\omega, \end{aligned} \quad (3.95)$$

where the FT-QRPA external field matrix element is  $|\langle i|\hat{F}|0\rangle|$ , and  $e^{-i\theta}$  is the overall phase which

remains undetermined. The above system of equations can be solved on a circular contour of small radius  $\eta$  using the Simpson's rule. To calculate the mFT-QRPA matrix element numerically we parameterize the integration around the circular contour of radius  $\eta$  as:

$$\begin{aligned}
 |\langle i|\hat{F}|0\rangle|^2 &= \frac{1}{2\pi i} \oint R_{FF}(\omega) d\omega = \frac{1}{2\pi i} \int_0^{2\pi} R_{FF}(\omega_0 + \eta e^{i\phi}) i\eta e^{i\phi} d\phi = \frac{\eta}{2\pi} \int_0^{2\pi} R_{FF}(\omega_0 + \eta e^{i\phi}) e^{i\phi} d\phi \\
 &= \left| \begin{array}{l} t = \frac{\phi}{2\pi} \\ dt = \frac{d\phi}{2\pi} \end{array} \right| = \eta \int_0^1 R_{FF}(\omega_0 + \eta e^{i2\pi t}) e^{2\pi i t} dt \\
 &= \eta \int_0^1 (\text{Re}R_{FF} + i\text{Im}R_{FF})(\cos 2\pi t + i \sin 2\pi t) dt \\
 &= \eta \left( \int_0^1 \text{Re}R_{FF} \cos 2\pi t dt - \int_0^1 \text{Im}R_{FF} \sin 2\pi t dt \right) \\
 &\quad + i\eta \underbrace{\left( \int_0^1 \text{Im}R_{FF} \cos 2\pi t dt + \int_0^1 \text{Re}R_{FF} \sin 2\pi t dt \right)}_0.
 \end{aligned}$$

In order for the strength to be real, second term should be 0, which is a nice test of the implementation. We find that around 10 mesh-points for Simpson's rule are sufficient for a good convergence. To test the approach, in Fig. 3.2 we select the peak located at  $E = 17.16$  MeV and integrate around it using a contour with  $\eta = 0.05$  MeV. Results for the total  $\text{GT}^-$  matrix element  $|\langle i|\hat{F}|0\rangle|^2$  as well as contribution from different 2 q.p. pairs are shown in Table 3.1. We observe that the agreement between the two different implementations of the FT-pnRQRPA yields the same results up to seven decimal places (boldfaced digits are the same in both columns in Tab. 3.1). Sign of the matrix elements is different, but this is of no concern since the overall phase in Eqs. (3.95) is undetermined. The above test includes both pairing and finite-temperature effects and constitutes the most general test of the linear response FT-pnRQRPA implementation.



Table 3.1: The comparison between the lrFT-QRPA and mFT-QRPA of the total  $GT^-$  strength function  $|\langle i|\hat{F}|0\rangle|^2$  and contribution from the different 2 q.p. pairs  $\langle i|\hat{F}|0\rangle_{\pi\nu}$  for peak at  $E = 17.16$  MeV in  $^{116}\text{Sn}$  at  $T = 0.6$  MeV. The integration is performed with 10 Simpson's integration mesh-points. The matching digits between the two calculations are boldfaced.

$E = 17.16$ MeV, $T = 0.6$ MeV	lrFT-QRPA	mFT-QRPA
$ \langle i \hat{F} 0\rangle ^2$	<b>23.23101</b>	<b>23.23101</b>
pair	$\langle i \hat{F} 0\rangle_{\pi\nu}$	$\langle i \hat{F} 0\rangle_{\pi\nu}$
$(\nu 2d_{5/2}, \pi 2d_{3/2})$	<b>0.3245577984955</b>	<b>-0.3245577473408</b>
$(\nu 2d_{5/2}, \pi 2d_{5/2})$	<b>0.1863725292102</b>	<b>-0.1863725334486</b>
$(\nu 1g_{7/2}, \pi 1g_{7/2})$	<b>0.1700622943878</b>	<b>-0.1700622569598</b>
$(\nu 1g_{9/2}, \pi 1g_{7/2})$	<b>3.9183937066269</b>	<b>-3.918393471595</b>

### 3.4 Results

In this section we provide illustrative calculations of the spin-isospin excitations in even-even tin isotopes ( $Z = 50$ ) in the range  $A = 112 - 134$  and for temperatures  $T = 0-1.5$  MeV. Results shown in this section are adapted from our work published in Ref. [30]. These are open-shell nuclei for neutron states (except  $^{132}\text{Sn}$ ), while they have a closed number of shells ( $Z = 50$ ) for proton states. The calculations are based on the FT-RHB initial state with the DD-PC1 [20] or DD-PCX [21] relativistic EDFs, and the separable pairing interaction [141]. The calculations are performed for  $N_{osc} = 20$  with no other cut-offs on the 2 q.p. basis. The proton pairing gaps  $\Delta_p$  vanish irrespective of the temperature, due to shell closure. However, because of the grand-canonical description of nuclei, the neutron pairing gaps  $\Delta_n$  vanish at a critical temperature  $T_c^n$ . Above the critical temperature, pairing properties collapse and only effects of the finite-temperature influence the nuclear excitations. In table 3.2 we show the critical temperature for neutron states of selected even-even tin isotopes using the DD-PC1 and DD-PCX interactions. We notice that the zero-temperature neutron pairing gaps  $\Delta_n^0$  for the DD-PCX interaction are larger than those for the DD-PC1 interaction, meaning that the corresponding critical temperatures will also be higher. This is a consequence of the larger neutron pairing strength of the separable interaction within the DD-PCX parameter set [21].

First, we focus on the Fermi strength function governed by the external field operator  $\hat{F} = \tau_-$  with quantum numbers  $J^\pi = 0^+$ . It is characterized by a total coupling to spin zero ( $S = 0$ ) and no orbital angular momentum ( $L = 0$ ). The Fermi transitions give rise to the Isobaric Analog Resonance (IAR) connecting the isobaric analog states between the parent even-even and daughter

Table 3.2: The neutron critical temperature  $T_c^n$  and mean pairing gap  $\Delta_n^0$  at zero temperature for even-even tin isotopes  $A = 112$ – $120$ . Results are calculated with the DD-PC1 and DD-PCX interactions. The table is adopted from Ref. [30].

nucleus	DD-PC1		DD-PCX	
	$T_c^n$ [MeV]	$\Delta_n^0$ [MeV]	$T_c^n$ [MeV]	$\Delta_n^0$ [MeV]
$^{112}\text{Sn}$	0.81	1.31	1.06	1.73
$^{114}\text{Sn}$	0.81	1.23	1.05	1.67
$^{116}\text{Sn}$	0.79	1.25	1.04	1.65
$^{118}\text{Sn}$	0.80	1.30	1.00	1.65
$^{120}\text{Sn}$	0.80	1.34	1.00	1.64

odd-odd nucleus. In Fig. 3.3 we display the Fermi strength function for even-even  $A = 112$ – $122$  tin nuclei for different temperatures with respect to the energy of the parent nucleus  $E$ . Upper panel shows the results with the DD-PC1 interaction and lower panel with the DD-PCX. The experimental centroid energies are taken from Ref. [95] and represented as black arrows. We observe that the temperature does not impact the IAR much, so we can focus our discussion to zero temperature only. The IAR excitation energy slightly reduces with increasing number of neutrons, starting from 13.60 MeV for  $^{112}\text{Sn}$  to 13.27 MeV for  $^{122}\text{Sn}$  for the DD-PC1 interaction. Since the excitation energy of the IAR when measured with respect to the parent nucleus is directly proportional to the difference between the Coulomb energy in parent and daughter nuclei, this shift is related to softening of the Coulomb repulsion with increasing neutron number. Indeed, if the Coulomb interaction is neglected in the FT-RHB mean-field, the IAR excitation energy is exactly zero (providing a good test of the numerical implementation). The calculation of the Fermi transitions within the FT-pnRQRPA is fully self-consistent, requiring no additional terms in the residual interaction apart from those derived from the underlying EDF at the Hartree level. The agreement with experimental centroids from Ref. [95] is excellent for both DD-PC1 and DD-PCX functionals. Therefore, in the following discussion we employ only the DD-PCX, results with DD-PC1 being consistent.

The Gamow-Teller (GT) transition strength is characterized by the total spin  $S = 1$  and the total orbital angular momentum  $L = 0$  coupled to total angular momentum  $J^\pi = 1^+$ . The  $\text{GT}^-$  external field operator has the form  $\hat{F} = \sigma\tau_-$  and connects the single particle states with the same orbital angular momentum number  $l$  and the total angular momentum  $j = l \pm 1/2$ . Based on the structure of the operator, the  $\text{GT}^-$  strength will be split into the two main peaks: (i) the low-lying peak composed of the core-polarization ( $\nu j = l \pm 1/2, \pi j = l \pm 1/2$ ) and back spin-flip

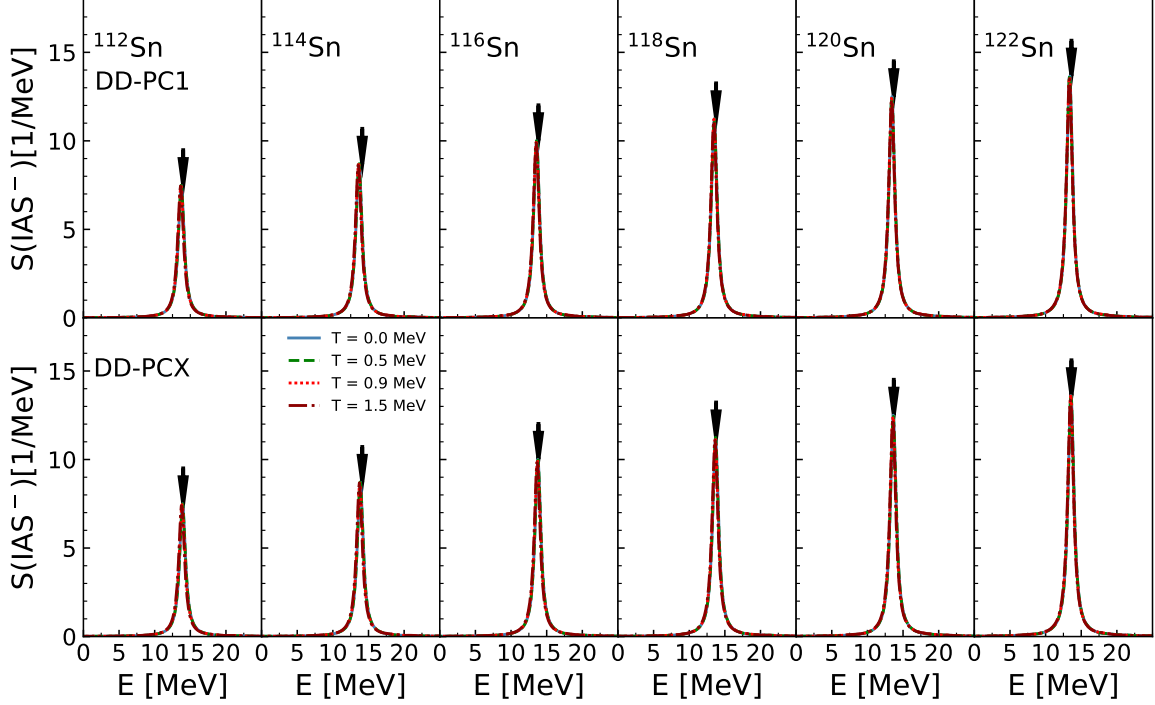


Figure 3.3: The  $J^\pi = 0^+$  strength functions in  $A = 112 - 122$  even-even tin isotopes with respect to the excitation energy of the parent nucleus for temperatures  $T = 0, 0.5, 0.9$  and  $1.5$  MeV, calculated by the linear response FT-*pnRQRPA* using the DD-PC1 (upper panel) and DD-PCX (lower panel) interaction. Black arrows denote the experimental centroid energies from Ref. [95]. The figure is taken from Ref. [30].

( $\nu j = l - 1/2, \pi j = l + 1/2$ ) transitions and (ii) the GT resonance (GTR), mainly composed of spin-flip ( $\nu j = l + 1/2, \pi j = l - 1/2$ ) transitions. Unlike the Fermi excitations which are determined self-consistently from the underlying EDF, for the description of the GT transitions we have to include the isovector-pseudovector (TPV) interaction as in Eq. (3.53). It corresponds to the exchange of the  $\pi$  meson and is vanishing at the Hartree level, because the  $\pi$  meson interaction would be manifested only in the exchange (Fock) term [146]. This means that its strength  $g_0$  is not constrained by the EDF fitting procedure. Therefore, we determine its value in order to reproduce the experimental GTR energy in  $^{208}\text{Pb}$  as in Ref. [145]. Furthermore, the residual  $pp$  interaction is fully determined by the isoscalar pairing ( $T = 0, S = 1$ ). Since we neglect the proton-neutron

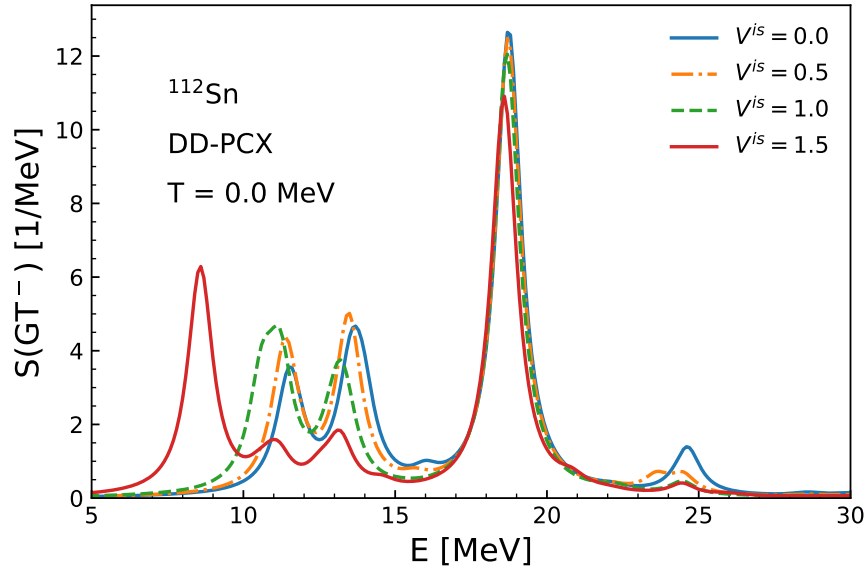


Figure 3.4: The  $GT^-$  strength function for  $^{112}\text{Sn}$  at zero temperature for changing values of the isoscalar pairing strength  $V^{is}$ . Calculations are performed with the linear response  $pnRQRPA$  using the  $DD\text{-}PCX$  interaction.

mixing at the FT-RHB level, this means that only the isovector component ( $T = 1, S = 0$ ) of the pairing interaction contributes. Therefore, the isoscalar pairing strength  $V^{is}$  [cf. Eq. (3.69)] is also not determined from the EDF. There is no a priori reason for the isoscalar pairing strength to be the same as in the isovector case (corresponding to  $V^{is} = 1.0$ ). To demonstrate the influence of changing  $V^{is}$ , in Fig. 3.4 we show the  $GT^-$  strength function of  $^{112}\text{Sn}$  at zero-temperature for  $V^{is} = 0, 0.5, 1.0$  and  $1.5$ . We observe that with increasing  $V^{is}$  the strength function changes quite substantially. As the  $V^{is}$  is increased, the GTR strength is slightly reduced and shifted to lower excitation energies. On the other hand, the low-lying strength demonstrates drastic changes. This is because the low-lying part of the strength function is mainly composed of transitions with nearly empty shells (quasi-*particles*, unlike the quasi-*holes*) which are strongly influenced by the  $pp$  interaction. Incidentally, it turns out that the low-lying strength is the one contributing to  $\beta$ -decay half-lives. Therefore, it is imperative to get a reliable estimate of the isoscalar pairing strength, that, once fixed can be used for calculations throughout the nuclide chart. We return to this question in Chapter 4. In the following, based on the study on the centroid energy difference between IAR and GTR in Ref. [145] we employ  $V^{is} = 1.5$ .

In Fig. 3.5 we display the temperature evolution of the  $GT^-$  strength function for selected

even-even tin isotopes. Starting our discussion at zero temperature, we observe that with increasing neutron number the total  $GT^-$  strength increases and shifts to lower excitation energies. The strength function is clearly separated between the GTR peak and the low-lying strength. Our results for GTR energies in  $^{112,116,120}\text{Sn}$  agree within 2 MeV with the experimental results from Ref. [95]. Especially satisfying is the agreement for the doubly-magic  $^{132}\text{Sn}$  with the centroid energy from Ref. [97]. Comparing the pnRQRPA strength distribution with the experimental distribution is impractical, since the pnRQRPA cannot reproduce the resonance width. For such comparison we would have to include correlations stemming from coupling to higher order phonons within the particle-vibration coupling (PVC) [133, 150] or the second RPA (SRPA) [151]. In this work we simulate this width by a smearing parameter  $\eta = 1$  MeV. In  $^{120,124}\text{Sn}$ , for  $T = 0$  MeV we observe an interesting splitting of the GTR strength into two peaks, that is later restored for increasing neutron number. The fragmentation disappears as the temperature is increased. The mechanisms of this splitting were described in Ref. [28]. Namely, the splitting occurs already at the level of the unperturbed strength (without the residual interaction), and the attractive residual interaction cannot bring the peaks together, leaving the main GTR split in two. As the temperature increases, the pairing correlations vanish, restoring the degeneracy in the unperturbed strength and subsequently at the residual interaction level. For temperatures below  $T = 0.5$  MeV, the strength function is almost unchanged with increasing temperature, however, for  $T > 0.5$  MeV rapid changes occur in the strength function. This is because of the reduction of the neutron pairing gap as the temperature increases. These changes are especially visible in the low-lying strength of  $^{116,120}\text{Sn}$ , being most influenced by the  $pp$  interaction. Looking at Tab. 3.2 for the DD-PCX interaction we observe that for temperatures above 1 MeV pairing collapses. This signals a transition from the superfluid to the normal state of the nucleus, in which the single-particle levels are described only by the Fermi-Dirac distribution. At  $T = 1.5$  MeV, the strength function is slightly shifted to lower excitation energies due to softening of the repulsive  $ph$  residual interaction as discussed in Refs. [30, 32, 149].

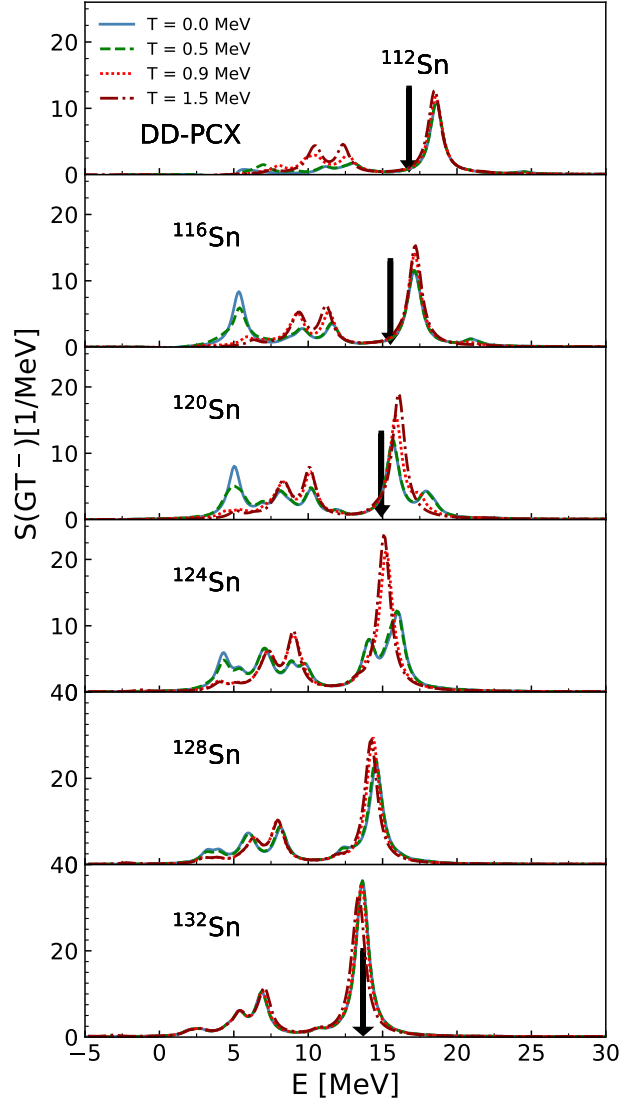


Figure 3.5: The  $J^\pi = 1^+$  strength function for particular even-even tin isotopes with respect to the excitation energy of the parent nucleus for temperatures in the range  $T = 0\text{--}1.5$  MeV, calculated by the linear response FT- $pnRQRPA$  using the DD-PCX interaction. The isoscalar pairing strength is set to  $V^{is} = 1.5$ . Black arrows denote the experimental centroid energies from Refs. [95, 97]. The figure is taken from Ref. [30].

# Chapter 4

## Stellar electron capture

The electron capture (EC) is a reaction mediated by the weak nuclear force where an electron is captured by a nucleus upon which one proton is converted to a neutron with an outgoing electron neutrino  $\nu_e$  [105]. The reaction can be written as

$$(Z, N) + e^- \rightarrow (Z - 1, N + 1) + \nu_e. \quad (4.1)$$

The term *stellar* signifies that the reaction occurs inside of massive stars, characterized by high temperature and density. More specifically, we are interested in the final moments before a star collapses within a core-collapse supernova (CCSN) [1]. The electrons are degenerate, their distribution being described by the Fermi-Dirac function. Since the EC is process mediated by the weak nuclear interaction, we can study it based on the Fermi theory, similar to that of the  $\beta$ -decay. If the momentum transfer in the EC is much lower than the  $W$ -boson mass, the complex weak-interaction vertices reduce to a simple contact interaction.

In the following discussion we will first focus on the so-called allowed approximation, which neglects the higher multipoles in the lepton-nucleus expansion. We show how to calculate the EC rates and demonstrate their dependence on the previously mentioned GT strength function (this time in the  $\beta^+$  direction). To include the dependence of matrix elements on the momentum transfer we employ the Walecka model of weak-interaction developed in Refs. [136, 152, 153]. Expressions within the Walecka model are much more complex and hide some important details in the EC rate calculations. Lastly, we perform large-scale calculations of EC rates in the *diamond* region in the vicinity of the  $N = 50$  shell closure and study their implications on the main observables of the

CCSNe.

## 4.1 The allowed approximation

Within the allowed approximation, the EC rates are determined by the Fermi ( $S = 0, L = 0$ ) and Gamow-Teller ( $S = 1, L = 0$ ) transitions. Usually, Fermi transitions can be neglected and the GT transitions determine the rates. Considering only the contribution of the GT transitions, the EC rate is calculated as [33, 98]

$$\lambda^{ec} = \frac{\ln 2}{K} \frac{1}{Z} \sum_{i,f} e^{-\beta E_i} g_A^2 |\langle f | \sigma \tau_+ | i \rangle|^2 f(W_0^{(i,f)}), \quad (4.2)$$

where the sum goes over the set of initial(final) states  $|i(f)\rangle$ ,  $Z = \sum_i (2J_i + 1) e^{-\beta E_i}$  is the partition function with  $J_i$  the initial angular momentum,  $K = 6147$  s and  $B(\text{GT}^+)_{if} = g_A^2 |\langle f | \sigma \tau_+ | i \rangle|^2$  is the  $\text{GT}^+$  operator. The axial coupling  $g_A = -1.26$  is quenched from its free value to  $g_A = -1.0$  [32]. The phase-space factor is dimensionless and defined in terms of the maximum lepton energy  $W_0^{(i,f)}$

$$f(W_0^{(i,f)}) = \int_{W_{th}^{(i,f)}}^{\infty} p W (W_0^{(i,f)} + W)^2 F_0(Z, W) f_e(W, \mu_e) dW, \quad (4.3)$$

where the total electron energy is  $E_e$  and  $W = E_e / (m_e c^2)$  is the electron energy in terms of the electron mass  $m_e$ . The electron momentum is  $p = \sqrt{W^2 - 1}$  and  $f_e(W, \mu_e)$  is the electron Fermi-Dirac factor

$$f_e(W, \mu_e) = \left[ 1 + e^{\frac{W - \mu_e / (m_e c^2)}{k_B T}} \right]^{-1}, \quad (4.4)$$

with  $\mu_e$  the electron chemical potential and  $k_B$  the Boltzmann constant. The difference between the initial and final nuclear states in terms of electron mass is defined as

$$W_0^{(i,f)} = (M_{N_i} - M_{N_f} + E_i^* - E_f^*) / (m_e c^2), \quad (4.5)$$

where  $M_{N_i}(M_{N_f})$  is the initial(final) nuclear mass and  $E_i^*(E_f^*)$  excitation energy of the parent(daughter) nucleus. The condition that neutrino energy should be positive  $E_\nu > 0$  defines



the threshold energy

$$W_{th}^{(i,f)} = \begin{cases} 1, & W_0^{(i,f)} \geq -1, \\ |W_0^{(i,f)}|, & W_0^{(i,f)} < -1. \end{cases} \quad (4.6)$$

The Fermi function  $F_0(Z, W)$  takes into account the distortion of the electron wavefunction due to the nuclear charge [154]. The electron chemical potential is determined from the charge neutrality condition in stellar environment

$$\rho Y_e = \frac{m_u}{\pi^2} \left( \frac{m_e c}{\hbar} \right) \int_0^\infty [f_e(W, \mu_e) - f_e(W, -\mu_e)] p^2 dp, \quad (4.7)$$

where  $m_u$  is the atomic mass unit,  $\rho$  is the stellar density and  $Y_e$  is the electron-to-baryon ratio. The factor  $f_e(W, -\mu_e)$  stands for the Fermi-Dirac distribution of positrons with negative chemical potential.

In the following we have to connect above definitions with the FT-pnRQRPA. We seek for transitions between the initial states in the even-even  $(Z, N)$  nucleus to the final states in the odd-odd  $(Z - 1, N + 1)$  nucleus. The energy diagram for the EC is shown in Fig. 4.1.

Within the FT-pnRQRPA, the initial-final energy difference can be expressed as

$$W_0^{(i,f)}(m_e c^2) \approx -W_0^m(m_e c^2) = \Delta_{np} + \Delta B + E_{1_m^+}^* = \Delta_{np} + E_{QRPA}^m + (\lambda_n - \lambda_p), \quad (4.8)$$

where  $\Delta B$  is the binding energy difference between the parent and the daughter nucleus,  $\Delta_{np} = 1.293$  MeV is the neutron-proton mass difference,  $E_{1_m^+}^*$  is the energy of the  $m$ -th  $1^+$  excited state with respect to the ground state of the daughter nucleus, and  $\lambda_n - \lambda_p$  is the neutron-proton chemical potential difference. The excitation energy of the  $m$ -th  $1^+$  excited state with respect to the parent nucleus is  $E_{1_m^+} = E_{1_m^+}^* + \Delta B$ , where the excitation energy is approximated within the FT-pnRQRPA as

$$E_{1_m^+} = E_{QRPA}^m + (\lambda_n - \lambda_p). \quad (4.9)$$

In this way, we can express the sum over initial-final states  $\sum_{i,f}$  as the sum over discrete FT-pnRQRPA eigenvalues  $\sum_m$ . Finally, the ensemble averaged matrix element is obtained as the residue of the strength function  $S_F(\omega)$  in Eq. (3.33)

$$\text{Res} \left[ \frac{S_F(\omega)}{1 - e^{-\beta\omega}}, E_{QRPA}^m \right] \approx \frac{1}{Z} \sum_{i,f} e^{-\beta E_i} |\langle f | \sigma \tau_+ | i \rangle|^2, \quad (4.10)$$

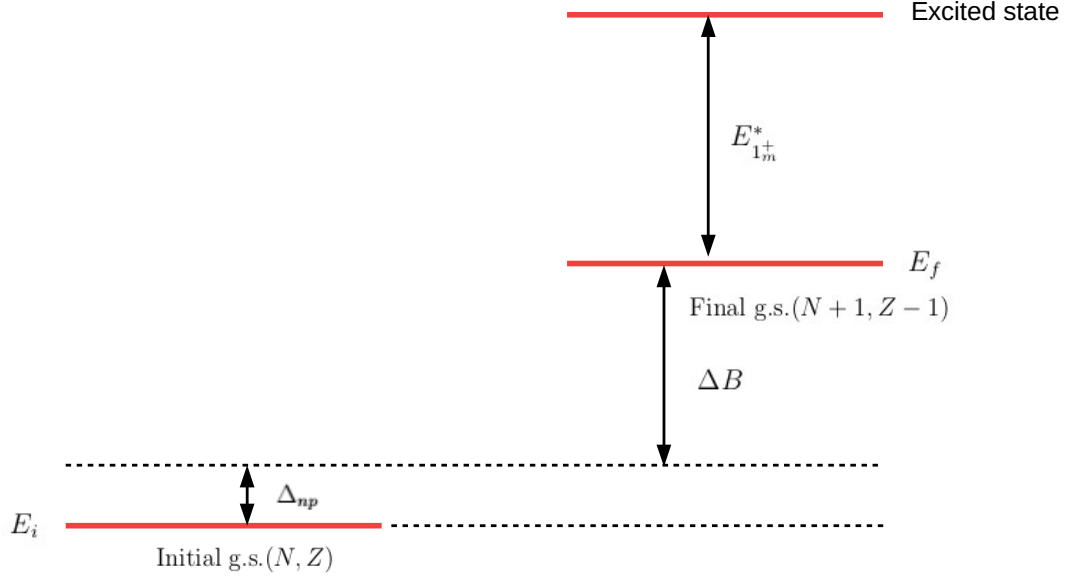


Figure 4.1: The energy diagram for the EC between the initial ground state  $E_i$  of the even-even  $(Z, N)$  nucleus to the final excited state of the odd-odd  $(Z - 1, N + 1)$  nucleus. See text for details.

where  $(1 - e^{-\beta\omega})^{-1}$  is the detailed balance factor [31, 33]. Depending on the computational method of choice, there are two main ways of calculating the residue in Eq. (4.10):

- **linear response** FT-pnRQRPA where the residue is obtained by a contour integration over the suitably defined contour  $\mathcal{C}_i$ , so that the total EC rate is

$$\lambda^{ec} = \frac{\ln 2}{K} \frac{1}{2\pi i} \oint_{\mathcal{C}_i} \frac{S_F(\omega)}{1 - e^{-\beta\omega}} f(W_0) d\omega, \quad (4.11)$$

which was explained in detail in Refs. [31, 33]. The strategy consists of setting the circular contours around the poles both at  $\text{Re}(\omega) > 0$  and  $\text{Re}(\omega) < 0$ , taking the special care of the  $\omega = 0$  point. Furthermore, one has to be careful in the analytic continuation of the phase-space factor  $f(W_0)$  [77].

- **matrix FT-pnRQRPA** where the EC rate is calculated as a summation

$$\lambda^{ec} = \frac{\ln 2}{K} \sum_m B_m \int_{W_0^{th,m}}^{\infty} W p[-(E_{QRPA}^m + \Delta_{np} + \lambda_{np})/(m_e c^2) + W]^2 F_0(Z, W) f_e(W, \mu_e) dW, \quad (4.12)$$

where  $W_0^{th,m}$  is the threshold energy of the  $m$ -th eigenenergy [cf. Eq. (4.6)],  $\lambda_{np} = \lambda_n - \lambda_p$ , and  $B_m$  is the transition matrix element defined as

$$\begin{aligned} B_m &\equiv B_m^+ = \frac{|\langle [\Gamma_m, \hat{F}] \rangle|^2}{1 - e^{-\beta\omega}}, & E_m > 0, \\ B_m &\equiv B_m^- = -\frac{|\langle [\Gamma_m, \hat{F}^\dagger] \rangle|^2}{1 - e^{-\beta\omega}}, & E_m < 0, \end{aligned} \quad (4.13)$$

where the ensemble averaged matrix element  $\langle [\Gamma_m, \hat{F}] \rangle$  is defined in Eq. (3.94). This approach was applied in Refs. [31–33].

In the following we apply the matrix FT-pnRQRPA approach assuming spherical symmetry and explain the meaning of *positive* and *negative* energy transitions. As an example we will select the doubly magic  $^{78}\text{Ni}$ , and study its  $\text{GT}^+$  strength for temperatures  $T_9 = 0, 5, 10$  and  $20$  ( $T_9$  labeling the temperature in  $10^9$  kelvin), that correspond to  $T = 0, 0.43, 0.86$  and  $1.72$  MeV. Since there is no pairing in  $^{78}\text{Ni}$ , it suffices to employ the FT-pnRRPA based on the FT-RMF approach [119, 155]. The relativistic EDF of choice is the D3C\* [130, 131].

In Fig. 4.2(a)-(d) we show the  $\text{GT}^+$  strength function in  $^{78}\text{Ni}$  at selected temperatures. The red vertical line denotes the reaction threshold ( $Q$ -value) which can be approximated as the chemical potential difference  $\lambda_n - \lambda_p$  for even-even nuclei. The strength below the threshold is called the *de-excitation* strength, having the *negative* transition energy (*negative* here means that the strength function is located below the threshold). According to Eq. (4.13) if the external field operator is  $\hat{F} = \sigma\tau_+$ , then the strength above the threshold corresponds to the  $\text{GT}^+$  strength, while the strength below threshold is determined by the operator  $\hat{F}^\dagger = \sigma\tau_-$  corresponding to the  $\text{GT}^-$  strength. To obtain the total strength, both contributions have to be included, multiplied by the detailed balance factor  $(1 - e^{-\beta\omega})^{-1}$ , shown as the blue dashed line in the figure. Notice that below the threshold, the detailed balance factor falls off rapidly and effectively determines the minimum energy which contributes to the strength function. As the temperature is increased further, the  $\text{GT}^-$  strength contributes more, and increases the influence of the de-excitation strength. This implies that as the

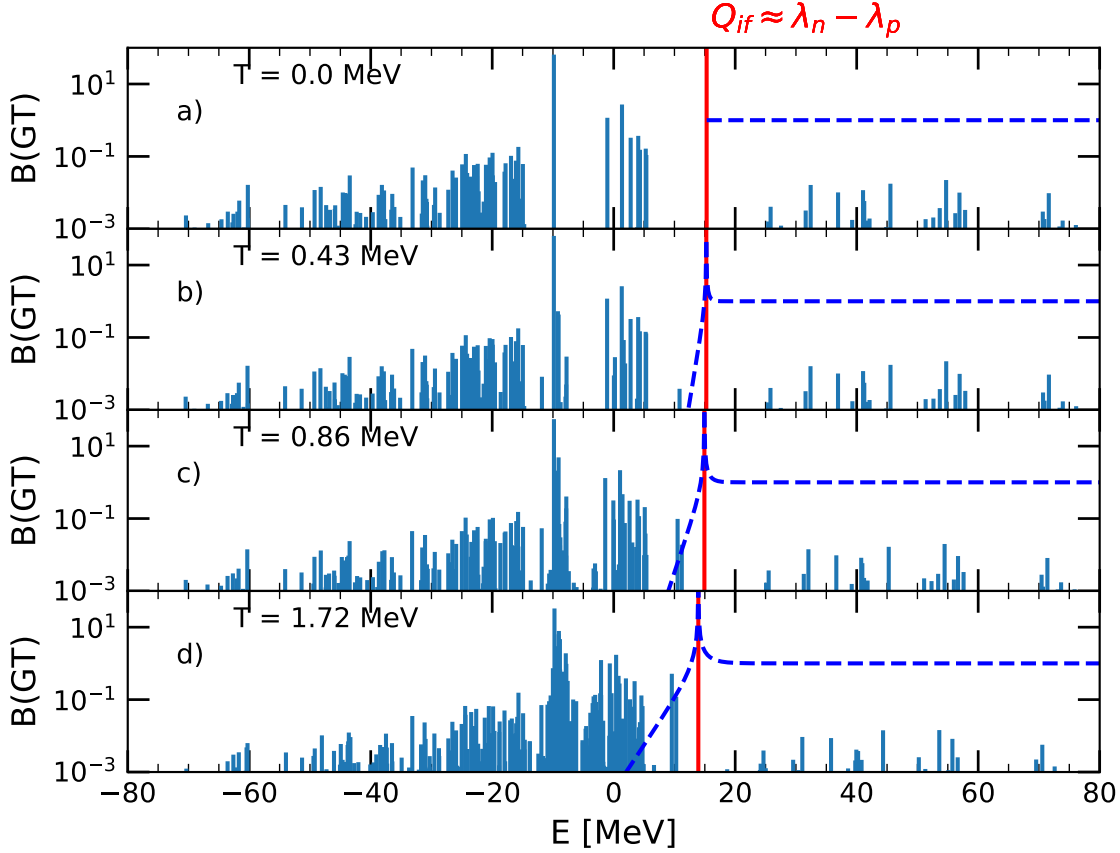


Figure 4.2: The temperature evolution of the GT strength in  $^{78}\text{Ni}$  as calculated by the FT-RMF+FT-RRPA with the D3C\* interaction. Red vertical line represents the  $Q$ -value threshold which separates the strength below the threshold (de-excitations) and strength above the threshold. Different panels (a)-(d) correspond to different temperatures in the range 0–2 MeV. The blue dashed line stands for the detailed balance temperature factor  $(1 - e^{-\beta\omega})$  [cf. Eq. (4.13)].

temperature increases, the de-excitation strength becomes increasingly important in determining the EC rate. This is especially because of the large phase-space factor that accompanies the de-excitation strength in the EC rate integral, as in Eq. (4.12).

To better demonstrate different kinds of transitions that we have within the FT-pnRQRPA we refer to the diagram in Fig. 4.3. Unlike the zero-temperature pnRQRPA which describes transitions from the ground state of the parent nucleus to both the ground and excited states of the daughter (blue arrows), the FT-pnRQRPA also introduces the transitions from the excited states in the parent.

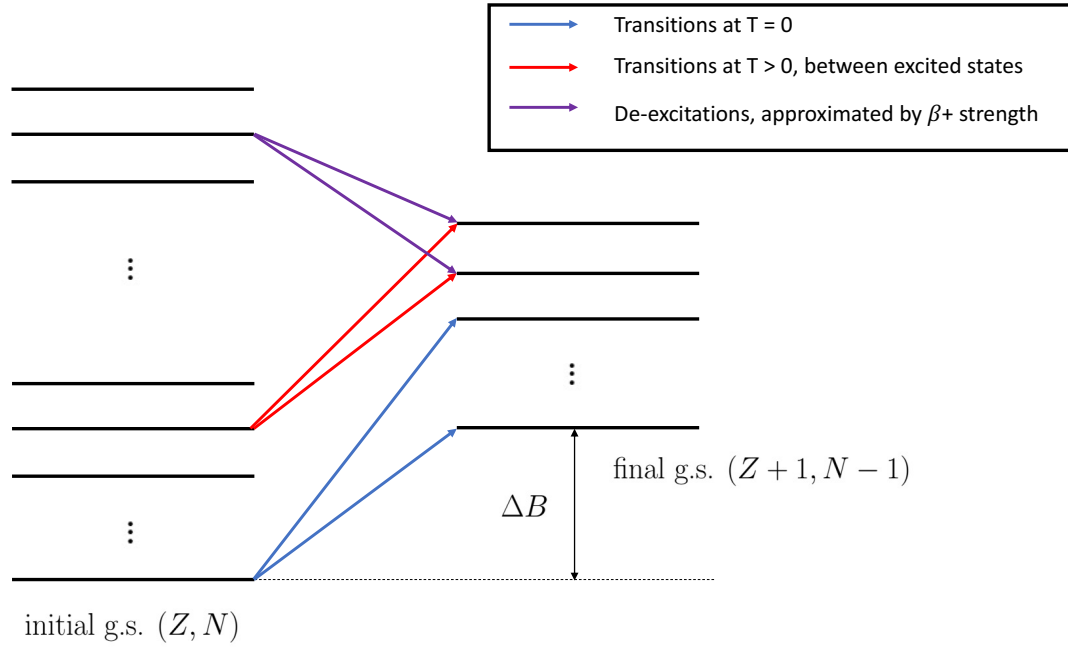


Figure 4.3: The diagram demonstrates different kinds of transitions within the FT-pnRQRPA. The zero temperature pnRQRPA is characterized only by the transitions from the ground state of the parent nucleus to both the ground state and excited states in the daughter nucleus (blue transitions). The FT-pnRQRPA also introduces the transitions between excited states in the parent and daughter nuclei. They can be located above the  $Q$ -value threshold (red transitions) or below the threshold (violet transitions) in which case they are called the de-excitations.

If the transition energy is located above the  $Q$ -value threshold it is shown with red arrows, while the transitions that contribute below the threshold are shown as violet (de-excitations). Therefore, the de-excitations can be understood as transitions from the highly-excited states in the parent nucleus. We present a more detailed account of de-excitations in Appendix B.

Finally, having the strength function, we are able to calculate the EC rates for  $^{78}\text{Ni}$  using Eq. (4.12). Again, we note that this calculation includes only the GT transition strength ( $J^\pi = 1^+$ ) and neglects the momentum dependence of the matrix element. In order to calculate the electron chemical potential  $\mu_e$  we have to supply the  $\rho Y_e$  product as in Eq. (4.7). To mimic the conditions in the late stages of the CCSNe, we vary the density in the range  $\rho Y_e = 10^8\text{--}10^{11} \text{ g/cm}^3$ , while the

temperature is in the interval  $T_9 = 0\text{--}20$  (corresponding to  $0\text{--}1.72$  MeV). We divide the total rate as

$$\lambda^{ec} = \lambda_+^{ec} + \lambda_-^{ec}, \quad (4.14)$$

where  $\lambda_+^{ec}$  denotes the contribution from the strength above the threshold (*excitation* strength), while  $\lambda_-^{ec}$  is the rate from the *de-excitation* strength. In Fig. 4.4 we show the EC rate contributions from both the  $\lambda_+^{ec}$  (red solid line) and  $\lambda_-^{ec}$  (blue solid line) along with the total strength  $\lambda^{ec}$  (black dashed line) as a function of temperature  $T_9$ . Our rates are also compared with those from Ref. [108] (green triangles) based on the thermal QRPA (TQRPA) with the non-relativistic SkM\* interaction. For all densities, the total rate  $\lambda^{ec}$  is mostly dominated by the de-excitation contribution  $\lambda_-^{ec}$ , starting from  $T_9 \sim 4$ . Once the temperature is large enough for the de-excitation strength to be relevant, its contribution to the total rate starts increasing abruptly. The  $^{78}\text{Ni}$  is a neutron-rich nucleus consisting of  $N = 50$  neutrons, which means that the  $\text{GT}^+$  transitions are mostly blocked due to the shell closure. However, once the temperature is increased, the nucleons scatter from closed shells according to the Fermi-Dirac distribution and unblock previously forbidden transitions due to the Pauli blocking. This mechanism was described in details in Refs. [105, 156]. It explains why we observe an increasing  $\lambda_+^{ec}$  rate with temperature. Also, as the density  $\rho Y_e$  increases, so does the electron chemical potential, allowing for larger contribution of the lepton phase-space factor. It means that the EC rate will increase significantly with stellar density, as observed in Fig. 4.4. A large contribution of de-excitation strength can be inferred by inspecting Fig. 4.2. For  $^{78}\text{Ni}$ , the  $\text{GT}^-$  strength below the threshold is much larger compared to the strength above the threshold. As the temperature increases, and the detailed balance factor allows for more  $\text{GT}^-$  strength to contribute, it quickly starts dominating the EC rate. In the lower two panels of Fig. 4.4, for densities  $\rho Y_e = 10^{10}$  and  $10^{11}$  g/cm<sup>3</sup>, we have compared our results with those from Ref. [108]. Notice that if we only considered the excitation contribution ( $\lambda_+^{ec}$ ) we would underestimate their results by almost 5 orders of magnitude. Addition of the de-excitations ( $\lambda_-^{ec}$ ) improves the agreement between the two models. However, it should be mentioned that the EC rates in Ref. [108], also include contributions from first-forbidden transitions ( $J^\pi = 0^-, 1^-, 2^-$ ), together with dependence on the lepton momentum transfer. Therefore, in the following section we extend our model.

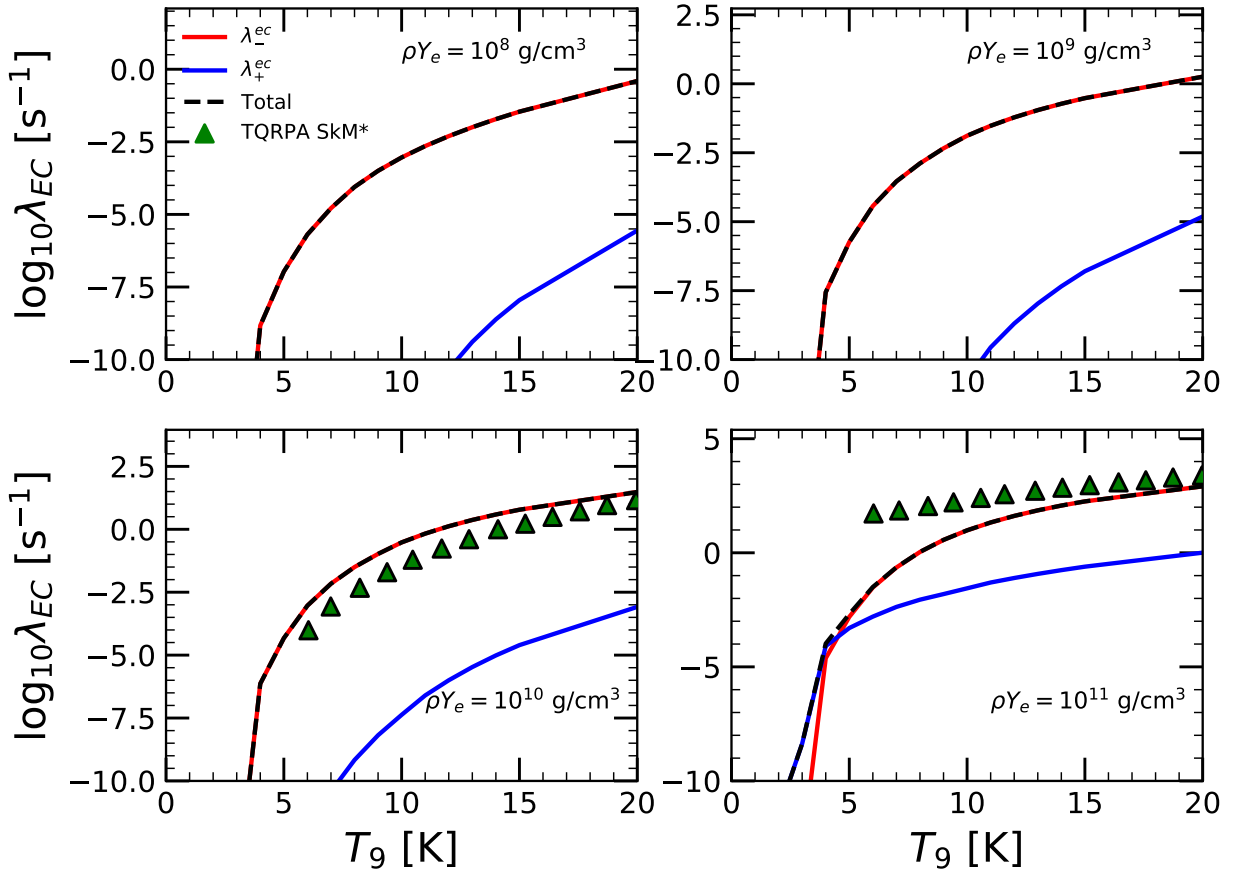


Figure 4.4: The EC rates on  $^{78}\text{Ni}$  calculated within the allowed approximation assuming only the  $J^\pi = 1^+$  strength with respect to temperature  $T_9$  (denoting  $10^9$  K). Stellar densities are varied in the range  $10^8$ – $10^{11}$   $\text{g/cm}^3$ . Both  $\lambda_+^{ec}$  (red solid) and  $\lambda_-^{ec}$  (blue solid) are shown together with the total sum (black dashed). For comparison, data from Ref. [108] based on the TQRPA with SkM\* interaction is also shown.

## 4.2 Extension to the Walecka model

We extend the allowed approximation using the model of the weak-interaction rates developed by J. D. Walecka *et al.* in Refs. [136, 152, 153], which we denote in the following as the Walecka model. It starts from the Fermi's golden rule

$$\frac{d\sigma_{ec}}{d\Omega} = \frac{1}{(2\pi)^2} \Omega^2 E_\nu^2 \frac{1}{2} \sum_{lept.spin.} \frac{1}{2J_i + 1} \sum_{M_i M_f} |\langle f | \hat{H}_W | i \rangle|^2, \quad (4.15)$$

where  $\hat{H}_W$  is the weak-interaction Hamiltonian in the form of the current-current interaction

$$\hat{H}_W = -\frac{G}{\sqrt{2}} \int d^3r j_\mu^{lept}(\mathbf{r}) \mathcal{J}^\mu(\mathbf{r}), \quad (4.16)$$

where  $G$  is the Fermi constant,  $j_\mu^{lept}(\mathbf{r})$  is the lepton current and  $\mathcal{J}^\mu(\mathbf{r})$  is the hadron current. The EC cross section is then derived by the multipole expansion of the current-current Hamiltonian, and calculation of the lepton traces  $\frac{\Omega^2}{2} \sum_{lept.spin.}$ , where  $\Omega$  is the normalization volume. Details of the derivations can be found in Refs. [136, 152, 153], with the resulting EC cross section presented in Appendix C. Here we note that the final expression contains four different reduced matrix elements that can be calculated within the FT-pnRQRPA: transverse magnetic  $\langle J_f | | \hat{\mathcal{T}}_J^{mag} | | J_i \rangle$  and electric  $\langle J_f | | \hat{\mathcal{T}}_J^{el} | | J_i \rangle$ , longitudinal  $\langle J_f | | \hat{\mathcal{L}}_J | | J_i \rangle$  and charge  $\langle J_f | | \hat{\mathcal{M}}_J | | J_i \rangle$  operators, containing both the squares of their absolute values and products. They are calculated between the initial  $|J_i\rangle$  and final  $|J_f\rangle$  nuclear and lepton states. Final expression is complicated in a sense that momentum-transfer is also included in the calculation of EC cross-section, which is not the case in Eq. (4.2). Finally, once the EC cross section is calculated, EC rates are given by folding the cross section with respect to the Fermi-Dirac distribution of electrons

$$\lambda^{ec} = \frac{(m_e c^2)^3}{\pi^2 \hbar^3} \frac{1}{Z} \sum_{if} e^{-\beta E_i} \int_{W_0^{th(i,f)}}^{\infty} p W \sigma_{ec}^{(i,f)}(W) f_e(W, \mu_e) dW, \quad (4.17)$$

where the average is taken with respect to the initial state and sum over the final states. The above expression should be directly compared with Eq. (4.2), that assumes the allowed approximation. Analogously to the EC rate in Eq. (4.14) we can divide the total cross section as the sum of the excitation ( $\sigma_{ec}^+$ ) and de-excitation ( $\sigma_{ec}^-$ ) contribution so that the total cross section is  $\sigma_{ec} = \sigma_{ec}^+ + \sigma_{ec}^-$ . To investigate the effects of including the momentum transfer terms within the EC calculation, we compare the cross sections obtained with: (i) the allowed approximation and (ii) within the Walecka model. The EC cross sections within the allowed approximation are calculated as

$$\begin{aligned} \sigma_{ec}^+ &= \frac{G^2 (m_e c^2)^2}{2\pi (\hbar c)^2} F(Z, W) \sum_m \frac{B_m^+(W_0^m - W)^2}{1 - e^{-\beta\omega}} \delta(\omega - E_m), \\ \sigma_{ec}^- &= \frac{G^2 (m_e c^2)^2}{2\pi (\hbar c)^2} F(Z, W) \sum_m -\frac{B_m^-(W_0^m - W)^2}{1 - e^{\beta\omega}} \delta(\omega + E_m), \end{aligned} \quad (4.18)$$



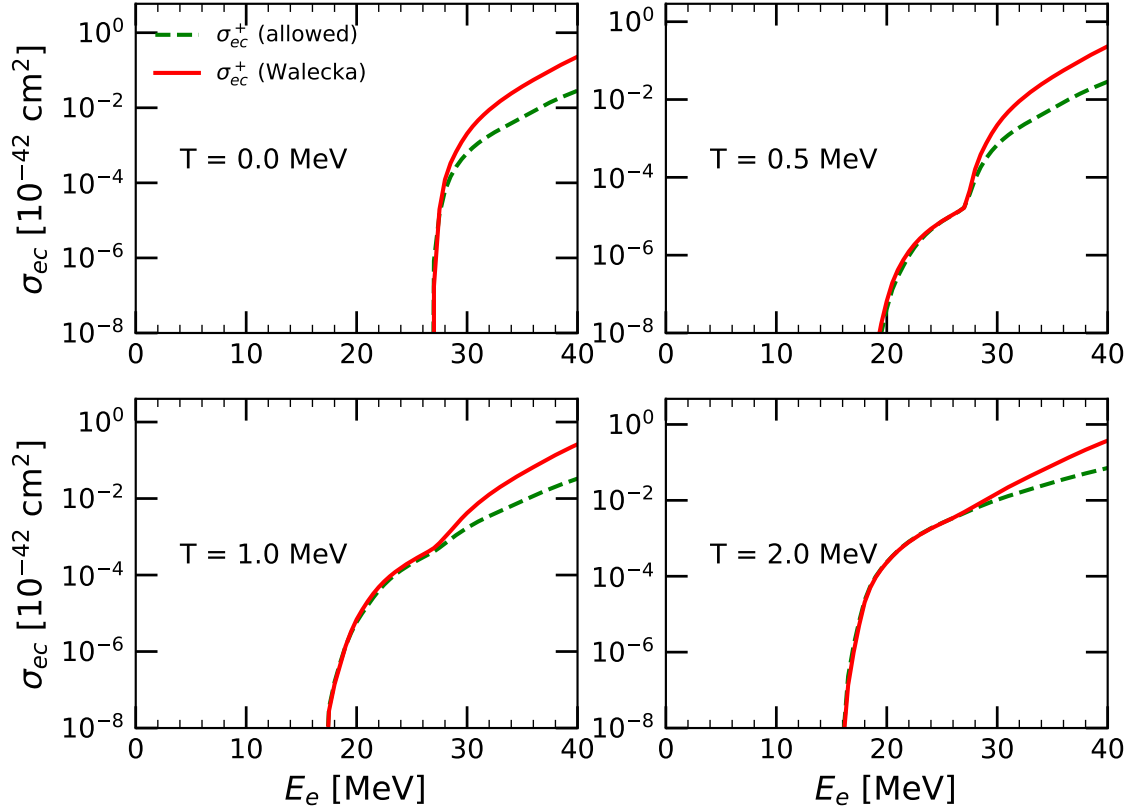


Figure 4.5: The electron capture cross sections  $\sigma_e^+$  on  $^{78}\text{Ni}$  for the  $J^\pi = 1^+$  multipole calculated with the FT-RMF+FT-pnRRPA using the D3C\* interaction. Results between the allowed approximation (green dashed) are compared with the Walecka model results (red solid).

containing no momentum dependent terms in the matrix elements. First, in Fig. 4.5 we compare the  $\sigma_{ec}^+$  cross sections between the allowed approximation and the full Walecka model for the  $J^\pi = 1^+$  transitions and temperatures  $T = 0, 0.5, 1$  and  $2$  MeV. We observe that for the electron energies up to  $30$  MeV, results between the two calculation methods agree. This is expected from the fact that the Walecka model reduces to the allowed approximation when  $q \rightarrow 0$  (check Appendix C). Once the electron energies are high enough we observe differences between the two approaches, results of the allowed approximation underestimating the Walecka model results. Such conclusions were also reproduced in Ref. [108].

In the following we employ only the Walecka model by also including the first-forbidden

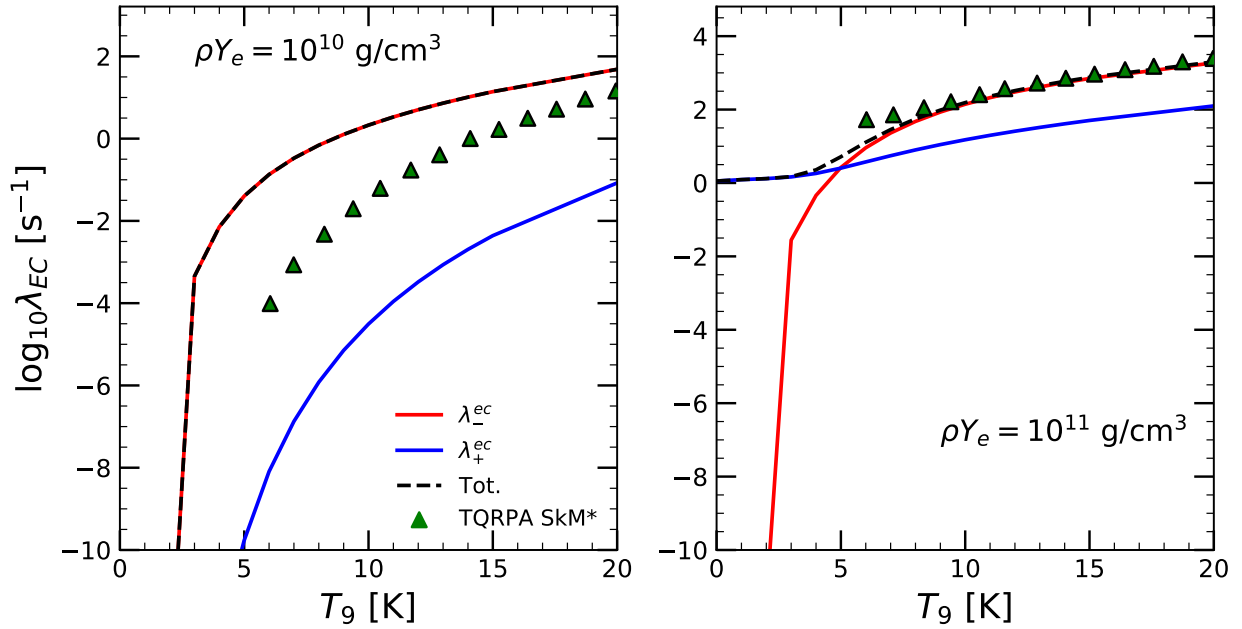


Figure 4.6: Same as in Fig. 4.4 but within the Walecka model including the  $J^\pi = 0^\pm, 1^\pm, 2^-$  multipoles.

multipoles  $J^\pi = 0^-, 1^-, 2^-$  in addition to the allowed  $J^\pi = 0^+, 1^+$ . Again, we compare our results with those from Ref. [108], noting that they also contain the first-forbidden transitions. Results are shown in Fig. 4.6 for densities  $\rho Y_e = 10^{10}$  and  $10^{11}$  g/cm<sup>3</sup>. At  $\rho Y_e = 10^{10}$  g/cm<sup>3</sup> we overestimate the results of Ref. [108], however, at  $\rho Y_e = 10^{11}$  g/cm<sup>3</sup> the agreement between the models is excellent. We note that in Ref. [108] the non-relativistic SkM\* interaction is implemented, unlike our relativistic D3C\*, which causes systematic differences between the two model calculations. These differences are more pronounced at lower densities, where the EC rates are more dependent on the peculiarities of the strength function. At this point our model can be applied to nuclei across the nuclide chart and benchmarked against other theoretical results.

### 4.3 Results

Results presented in this section were published in Refs. [31–33]. The model we employ for the large-scale calculations of EC rates is the FT-HBCS+FT-pnRQRPA in the matrix form [cf. Sec. 3.2]. The FT-HBCS is an approximation to the FT-RHB, however, it is more suitable for the large

scale calculations due to its smaller dimension of the pairing space, while maintaining reasonable accuracy when compared to the FT-RHB. In the  $ph$  channel we use the derivative coupling D3C\* interaction [130]. For the  $pp$  channel in the FT-HBCS initial state we employ the pairing part of the Gogny D1S interaction of the form

$$V_{pp}(\mathbf{r}_1, \mathbf{r}_2) = V_{pair} \sum_{i=1,2} e^{(|\mathbf{r}_1 - \mathbf{r}_2|/\mu_i)^2} (W_i + B_i P^\sigma - H_i P^\tau - M_i P^\sigma P^\tau), \quad (4.19)$$

where  $P^\sigma, P^\tau$  are the spin and isospin exchange operators. Parameters  $\mu_i, W_i, B_i, H_i$  and  $M_i$  are adopted from Ref. [157]. Within the RHB the overall interaction is multiplied by a factor  $V_{pair} = 1.15$  [23]. However, the HBCS theory usually underestimates the pairing gaps obtained in the RHB, therefore a different value of  $V_{pair}$  could be optimal. To this aim we calculate the  $\Delta_{uv}$  pairing gaps [158] for the isotopic chains with magic proton numbers  $Z = 20, 28, 50$  and  $82$ , and compare the results with those obtained from the 5-point (5p) formula [40]. Results are shown in Fig. 4.7, for both the zero temperature HBCS and RHB calculations. In the case of the RHB we use the original prescription where  $V_{pair} = 1.15$ , while for the HBCS we use both  $V_{pair} = 1.15$  and  $V_{pair} = 1.25$ . The experimental data is calculated by using the 5-point formula and experimental binding energies from Ref. [159]. First, we observe that the HBCS pairing gaps underestimate the RHB pairing gaps, as expected. Furthermore, there is not a single value of  $V_{pair}$  that works for all isotopic chains. Although  $V_{pair} = 1.25$  reproduces the pairing gaps reasonably in Ca, Ni and Sn chains, it overestimates the experimental data in Pb. This points to an isotopic dependent formula which will vary across the nuclide chart. Here, we have analyzed both the isotopic  $Z = 20, 28, 50$  and  $82$  chains along with the isotonic  $N = 20, 28, 50, 82$  and  $126$ , and formulated the following prescription

$$V_{pair} = \begin{cases} 1.25, & 8 \leq Z \leq 50, \\ 1.15, & 50 \leq Z \leq 120, \end{cases} \quad (4.20)$$

with the same values for both proton and neutron pairing. Note that such behavior is in agreement with the trends of scaling the pairing strength used in the work of Agbemava *et al.* in Ref. [158].

At the level of the residual interaction the  $ph$  channel is derived self-consistently from the D3C\* EDF. However, similar to the TPV term [cf. Sec. 3.1], to account for the contact part of the nucleon-nucleon interaction, additional zero-range Landau-Migdal term is added [28]

$$V_{\delta\pi} = g' \left( \frac{f_\pi}{m_\pi} \right)^2 \vec{\tau}_q \vec{\tau}_2 \Sigma_1 \cdot \Sigma_2 \delta(\mathbf{r}_1 - \mathbf{r}_2), \quad (4.21)$$

where  $f_\pi^2/(4\pi) = 0.08$ ,  $m_\pi = 138$  MeV and  $\Sigma = \begin{pmatrix} \sigma & 0 \\ 0 & \sigma \end{pmatrix}$ . The coupling  $g' = 0.76$  is adjusted to reproduce the GTR centroid energy in  $^{208}\text{Pb}$  [130]. We have verified that  $g' = 0.76$  reproduces the experimental GTR excitation energy in  $^{132}\text{Sn}$  measured in Ref. [97] within the uncertainty limits, while  $g' = 0.79$  reproduces the mean value of the experimental GTR energy. A change from  $g' = 0.76$  to 0.79 makes no significant alterations in the EC rates. Furthermore, our calculations are also able to reproduce the measured GTR centroid energy in  $^{48}\text{Ca}$  [160], for  $g' = 0.76$  within the experimental error.

In the  $pp$  channel of the residual interaction we have both the isovector ( $T = 1, S = 0$ ) and isoscalar ( $T = 0, S = 1$ ) type, depending on the quantum numbers of the transitions. The isovector pairing is derived from the FT-HBCS self-consistently. On the other hand, the isoscalar pairing is not present in the FT-HBCS and here we assume the following form [28, 32]

$$V_{pp}^{is} = V^{is} \sum_{j=1}^2 g_j e^{-r_{i2}^2/\mu_j} \prod_{S=1, T=0}, \quad (4.22)$$

which represents a sum of a repulsive and an attractive Gaussian. The projector  $\prod_{S=1, T=0}$  ensures  $T = 0, S = 1$  states, while for the parameters we use  $\mu_1 = 1.2$  fm,  $\mu_2 = 0.7$  fm,  $g_1 = 1$  and  $g_2 = -2$  [28].

As already stressed in Sec. 3.1 the isoscalar pairing strength is not constrained at the FT-HBCS (or FT-RHB) level. Therefore, we use the following functional form [131, 161]

$$V^{is} = V_L + \frac{V_D}{1 + e^{a+b(N-Z)}}, \quad (4.23)$$

with parameters  $V_L = 153.2$  MeV,  $V_D = 8.4$  MeV,  $a = 6.0$  and  $b = -0.6$ , adjusted to reproduce the available experimental data on the  $\beta$ -decay half-lives in the range  $8 \leq Z \leq 82$  [34]. With this procedure there are no unconstrained parameters in the model and we can continue with the large-scale calculation. The FT-HBCS calculation is performed with 20 h.o. shells for both fermion and boson states. At the FT-pnRQRPA level, two cut-offs are used to limit the total number of 2 q.p. excitations: (i) a maximal 2 q.p. energy cutoff  $E_{cut} = 100$  MeV, set for the sum of q.p. energies  $E_\pi + E_\nu$  and (ii) threshold on the product of FT-HBCS occupation factors for proton(neutron) states  $u_{\pi(\nu)}, v_{\pi(\nu)}$  as  $|u_\pi v_\nu| < 0.01$  and  $|v_\pi u_\nu| < 0.01$  which excludes pairs with small contributions to the FT-pnRQRPA matrix. With these constraints, the FT-pnRQRPA matrix is limited to a size

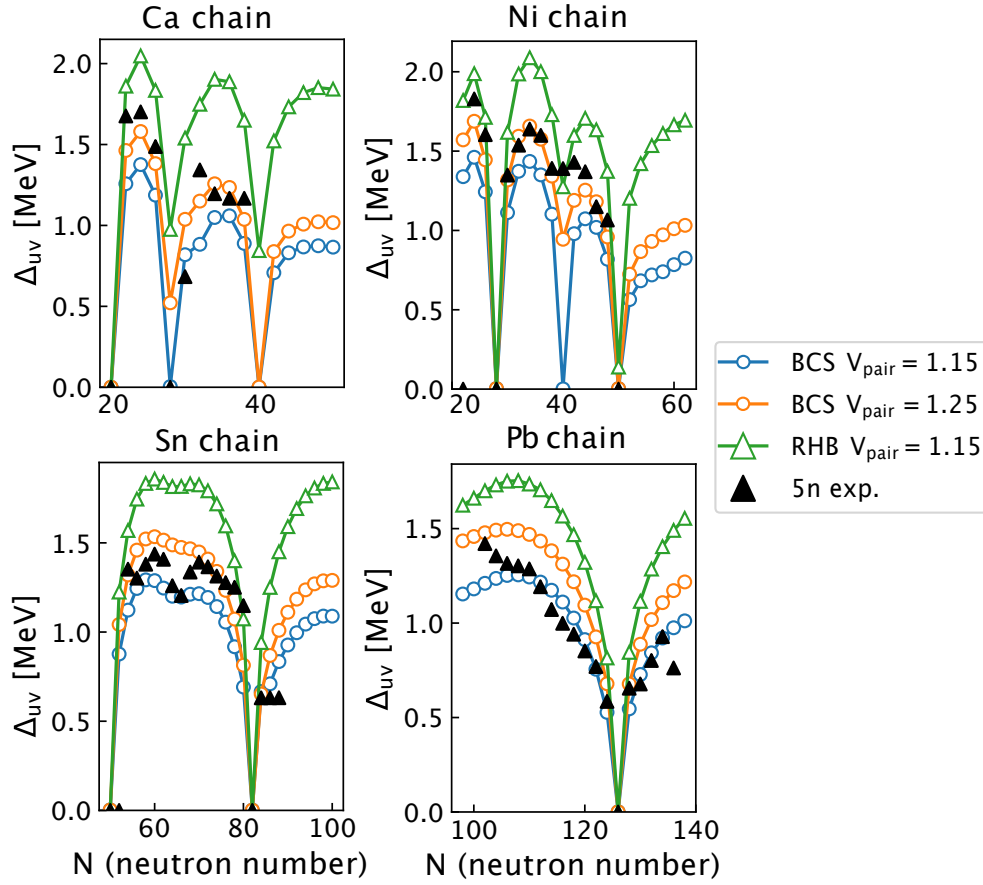


Figure 4.7: The isotopic dependence of the pairing gaps  $\Delta_{uv}$  calculated using the HBCS and RHB with the Gogny D1S  $pp$  interaction and D3C\* EDF. The results for the HBCS are presented for the pairing strength  $V_{pair} = 1.15$  (blue) and  $V_{pair} = 1.25$  (orange), while the RHB results are calculated using the  $V_{pair} = 1.15$  (green) as in Ref. [23]. The experimental data (black triangles) are obtained by the 5-point formula with the binding energies from Ref [159].

$10000 \times 10000$ . Furthermore, the contribution of antiparticle states is neglected, which is a good approximation for the charge-exchange transitions [162, 163].

### 4.3.1 Numerical techniques

The main object of the calculation is the EC rate in Eq. (4.17), which we can reformulate by defining the neutrino distribution function  $n(E_\nu)$  so that the rate is defined as

$$\lambda^{ec} = \int_0^\infty n(E_\nu) dE_\nu, \quad (4.24)$$

where the  $n(E_\nu)$  within the FT-pnRQRPA is calculated as

$$n(E_\nu) = \frac{(m_e c^2)^2}{\pi^2 \hbar^3} \sum_m p W \sigma_{ec}^m(W) f(W, \mu_e), \quad (4.25)$$

the neutrino energy is  $E_\nu = (W - W_0^m) m_e c^2$  [cf. Eq. (4.8)],  $m$  is the FT-pnRQRPA eigenvalue and  $\sigma_{ec}^m$  is the EC cross-section for the  $m$ -th eigenvalue. The integration is changed from integrating over the electron energy  $E_e$  to the neutrino energy  $E_\nu$ . The main reason for such substitution is more convenient calculation of the neutrino energy loss (NEL) rate, which is defined as

$$\lambda^{nl} = \int_0^\infty E_\nu n(E_\nu) dE_\nu. \quad (4.26)$$

Therefore, once we obtain the neutrino distribution function from Eq. (4.25), we can easily calculate both the EC and NEL rate. This is because both the EC and NEL rates are required as an input for the CCSNe simulations [164]. A similar strategy was used for large-scale calculation of EC rates in Refs. [165, 166].

To demonstrate the calculation of the neutrino distribution function we use  $^{56}\text{Fe}$  as an example nucleus. We focus on  $T_9 = 10$  and  $\rho Y_e = 10^8 \text{ g/cm}^3$  and  $\rho Y_e = 10^{11} \text{ g/cm}^3$ , latter being the most sensitive point for the influence of the EC rates on CCSNe dynamics. Results for  $n(E_\nu)$  are shown in Fig. 4.8, where we have displayed contributions from both allowed and first-forbidden multipoles  $J^\pi = 0^\pm, 1^\pm, 2^-$ . Starting from  $\rho Y_e = 10^8 \text{ g/cm}^3$  in the left panel, we observe that  $n(E_\nu)$  is dominated only by the  $J^\pi = 1^+$  multipole (Gamow-Teller) other contributions being negligible. This is a common result for most  $pf$ -shell nuclei where the EC rates are mostly dominated by the GT transition strength [165, 166]. The EC rate is given as the integral of the  $n(E_\nu)$  as in Eq. (4.24). The distribution function has a simple singly-peaked form and is smooth. This implies that a simple

Simpson's integration should be sufficient. As the stellar density is increased to  $\rho Y_e = 10^{11} \text{ g/cm}^3$ , the first-forbidden transitions gain increasing importance. In fact, the distribution function (and hence the EC rate) is dominated by the  $J^\pi = 1^-$ , closely followed by  $J^\pi = 1^+$  and  $2^-$ . Unlike the singly-peaked distribution function at  $\rho Y_e = 10^8 \text{ g/cm}^3$ , we have a complicated energy dependence spanning a large interval in the neutrino energy. The upper limit of the neutrino energy is close to the electron chemical potential  $\mu_e \approx 111 \text{ MeV}$ , smeared by the finite-temperature Fermi-Dirac distribution. In this case, a simple Simpson's integration would produce a large error and a better numerical integration technique is needed. We employ the adaptive integration algorithm, which is a part of the GSL numerical library [167]. It divides the integration domain in a maximum of  $N_{int}^{max}$  intervals, and performs a Gauss-Laguerre integration with  $N_{GL}$  points on a given subinterval. Initially starting from two intervals, it estimates the integration error of each subinterval. If the error is larger than some threshold  $\epsilon$ , it subdivides the interval, until a maximum number of subintervals  $N_{int}^{max}$  is reached. In this way, the algorithm is able to detect local jumps in the neutrino distribution function quite efficiently. However, the calculation of  $n(E_\nu)$  can be very costly, so a trade-off should be devised to determine the optimal  $N_{int}^{max}$  and  $N_{GL}$ . In our calculations we have found that using the following prescription guarantees reasonable results:  $N_{GL} = 15$ , and if the temperature is  $T_9 < 5$  then  $N_{int}^{max} = 4$ , while for temperatures above 5 GK we use  $N_{int}^{max} = 3$ .

Finally, in Fig. 4.9, we present the results for calculation of EC rates in  $^{56}\text{Fe}$  using the above prescription. The result is shown for the stellar density range  $\log \rho Y_e = 6\text{--}12$  and temperatures on the FFN mesh [168]. The set of stellar densities and temperatures was chosen to be convenient for the CCSNe simulations. Apart from the rate itself we also plot the errors stemming from numerical integration. We can observe that they are barely visible, which means that the prescription introduced above offers reliable integration of the neutrino distribution function. The neutrino distribution function we calculate is stored and used to also compute the neutrino energy loss function  $\lambda^{nl}$ . A set of  $\lambda^{ec}$  and  $\lambda^{nl}$  on a FFN grid of temperatures and densities is suitable as an input for CCSNe simulations.

### 4.3.2 EC rates of the nuclei near $N = 50$

In Ref. [164] a comprehensive study of the influence of the EC rates on the CCSNe was performed. The rates were systematically varied using the Monte-Carlo sampling to determine which nuclei, when their EC rate is changed, alter the CCSNe observables the most. A region of the nuclide chart near the  $N = 50$  shell closure, consisting of around 70 nuclei, displayed the most influence

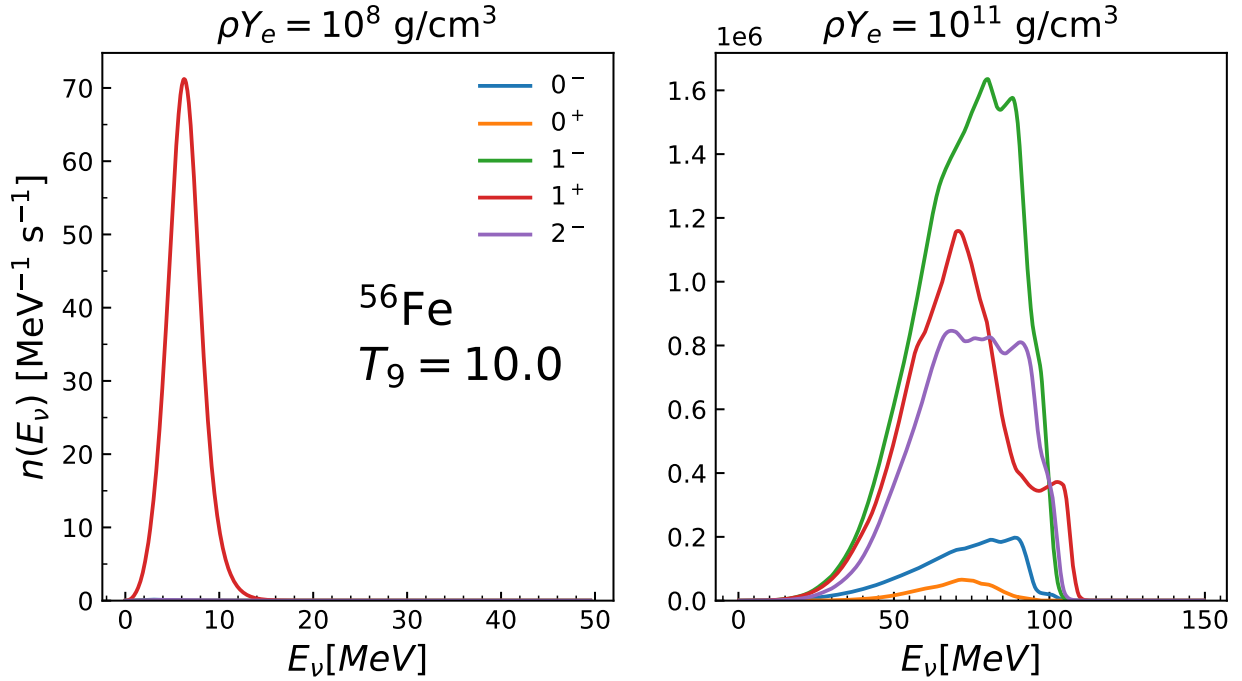


Figure 4.8: The neutrino spectrum distribution function  $n(E_\nu)$  for  $^{56}\text{Fe}$  at  $T_9 = 10$  with densities  $\rho Y_e = 10^8 \text{ g/cm}^3$  (left panel) and  $\rho Y_e = 10^{11} \text{ g/cm}^3$  (right panel). Results are shown for different multipoles  $J^\pi$ .

on the CCSNe. Hereafter we refer to this area of the nuclide chart as the *diamond region*. It was our motivation in Ref. [33] to provide a self-consistent microscopic calculation of the EC rates for diamond region nuclei. To account for the systematic variations between the EDFs, we employed two model calculations: (i) the relativistic FT-HBCS+FT-pnRQRPA based on the D3C\* interaction (introduced in this Chapter) and (ii) the non-relativistic FT-HFB+FT-pnFAM using the SkM\* interaction [79]. The two approaches based on the EDF theory were benchmarked against the shell-model calculation on  $^{86}\text{Kr}$  where the experimental data exists [102].

To compare the three calculations in Fig. 4.10(left panel) we show the  $\text{GT}^+$  strength in  $^{86}\text{Kr}$  as a function of the transition energy  $E_{if}$  at  $T_9 = 0$  and  $T_9 = 10$ . The relativistic FT-HBCS+FT-pnRQRPA is labeled as the FT-PNRQRPA, while the FT-QRPA stands for the non-relativistic FT-HFB+FT-pnFAM. The shell-model strength is labelled as SM. The transition energy is  $E_{if} = -(m_e c^2) W_0^{(i,f)}$ , while the red dashed line indicates the threshold energy. Starting at zero temperature we note that the relativistic calculation predicts the first peak at slightly higher



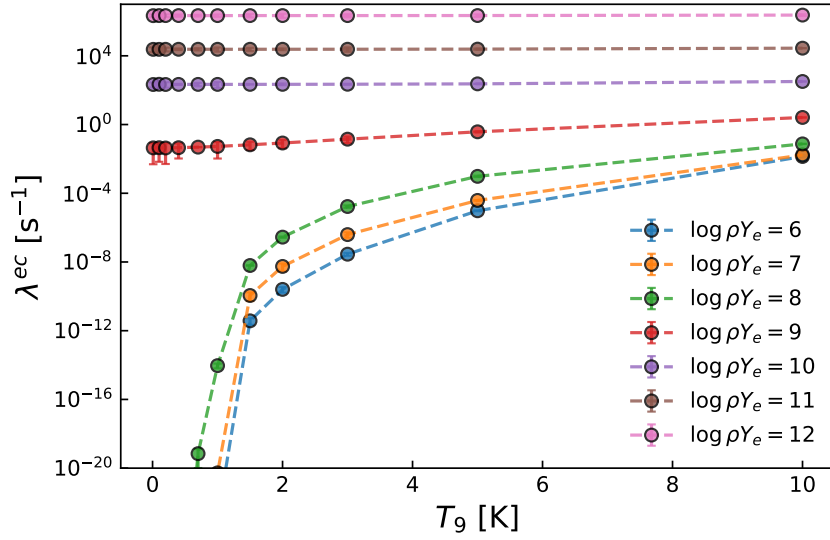


Figure 4.9: The electron capture rates for  $^{56}\text{Fe}$  in the temperature range  $T_9 = 0-10$  and the stellar densities  $\log \rho Y_e = 6-12$ . The error bars denote the numerical integration error. The results are calculated using the FT-HBCS+FT-pnRQRPA with the D3C\* interaction.

energies, compared to both the non-relativistic and SM calculations. Overall, the structure of the  $\text{GT}^+$  strength between the calculations is similar, with both QRPA calculations unable to reproduce the density of states in the SM. However, the SM calculations had to be cut for  $E_{if} \leq 20$  MeV due to computational limits. At  $T_9 = 10$ , a significant part of the total  $\text{GT}^+$  strength appears below the threshold energy ( $\sim 8.1$  MeV), stemming from de-excitations. The effect of the temperature on the  $\text{GT}^+$  strength function is twofold, it allows for additional  $\text{GT}^+$  transitions which were previously blocked at zero temperature, and leads to the appearance of strength below the ground-state threshold (de-excitations). Combined, we should expect these two effects to significantly increase the EC rate as the temperature raises.

In Figure 4.10(right panel) we show the temperature evolution of EC rates in  $^{86}\text{Kr}$  up to  $T_9 = 100$  at  $\rho Y_e = 10^{11}$  g/cm $^3$ . First, we consider the allowed approximation which contains only the GT transitions and compare the shell-model (SM) results together with two calculations based on the QRPA (FT-PNRQRPA GT and FT-QRPA GT). For low temperatures, the SM EC rate is larger than both QRPA rates by almost an order of magnitude. This comes as no surprise since the QRPA calculations are unable to reproduce the density of states obtained within the SM calculations. On the other hand, both QRPA calculations predict more consistent rates. The EC rates for all calculations are almost constant up to 5 GK, above which we have a steep increase in the rate.

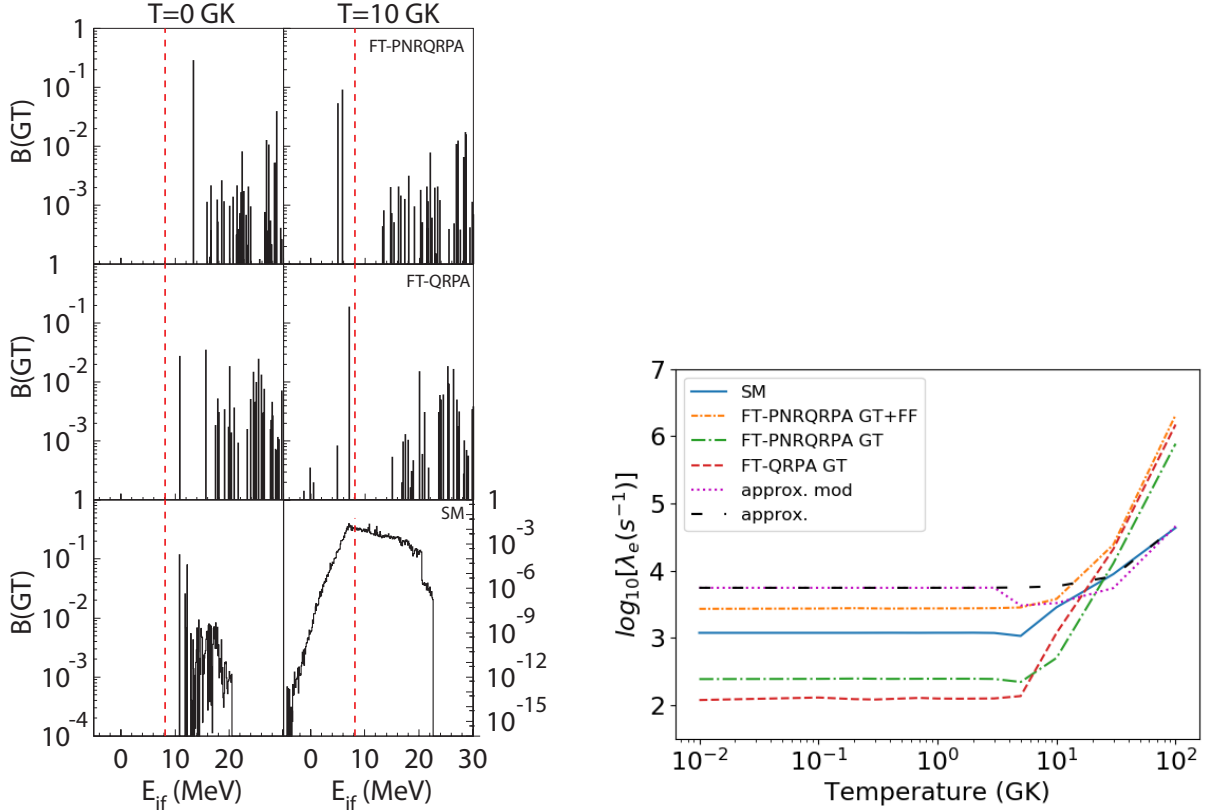


Figure 4.10: (Left) The  $\text{GT}^+$  strength in  $^{86}\text{Kr}$  at  $T = 0$  GK and  $T = 10$  GK as a function of the transition energy  $E_{if}$  calculated using the 3 theoretical models: (i) the relativistic FT-HBCS+FT-pnQRPA (FT-PNRQRPA), (ii) the non-relativistic FT-HFB+FT-pnFAM (FT-QRPA) and the shell-model (SM). The red dashed line denotes the ground-state threshold energy. (Right) The temperature dependence of EC rates in  $^{86}\text{Kr}$  at  $\rho Y_e = 10^{11} \text{ g/cm}^3$  as calculated using the 3 theoretical models. In addition, the FT-PNRQRPA contains both the allowed (GT) and first-forbidden (GT+FF) transitions. The approx. and approx. mod refer to simple analytical expressions for the EC rates [33]. The figures are adapted from Ref. [33].

At  $T = 5$  GK the temperature is finally high enough to allow for thermal unblocking as well as the appearance of de-excitations leading to an exponential increase in the EC rate. Again, both the relativistic and non-relativistic QRPA calculations are consistent, especially as the temperature increases. With higher temperature the EC rate becomes mostly independent of the details in the  $\text{GT}^+$  strength function and agreement between the different models is expected. However, in the case of  $^{86}\text{Kr}$ , the rate is comparable for all temperatures, indicating consistency for models based on different EDFs. The SM rates have a lower slope of the EC rate temperature evolution signifying

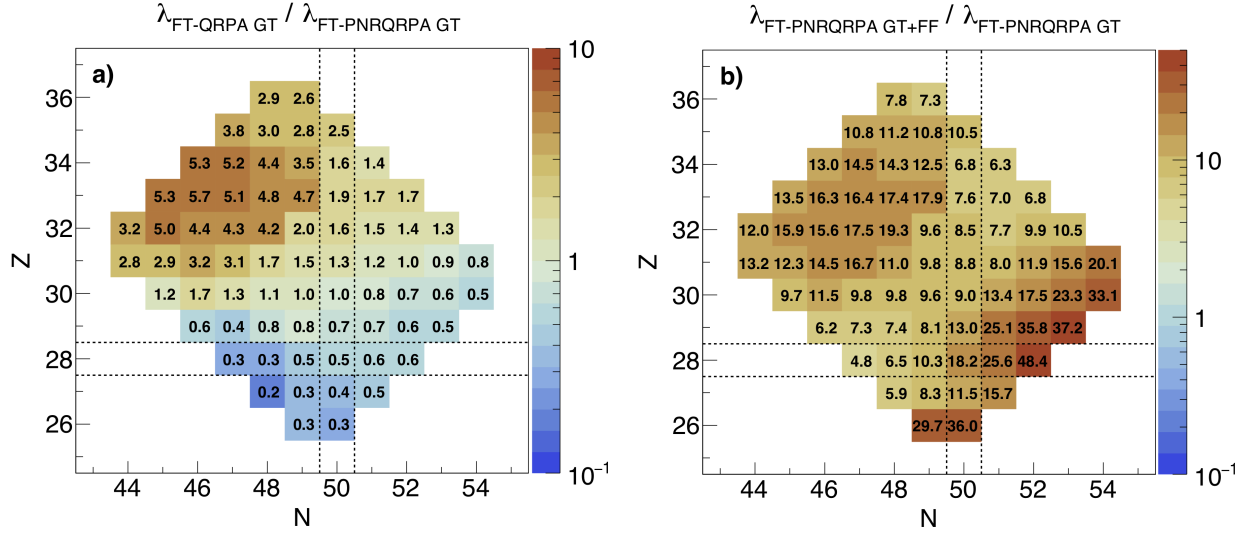


Figure 4.11: (a) The part of the nuclide chart showing ratio between the EC rates calculated with the relativistic and non-relativistic QRPA calculations. (b) The ratio between the total EC rate including both the GT and first-forbidden transitions (GT+FF) and the EC rate which includes only the GT. The calculations are performed at  $T_9 = 10$  and  $\rho Y_e = 10^{11}$  g/cm<sup>3</sup>. The figure is adopted from Ref. [33].

that  $E_{if} \leq 20$  MeV was probably too low for a cut-off in the calculation.

For a neutron rich nucleus such as <sup>86</sup>Kr, the first-forbidden (FF) transitions play an important role in the total EC rate, even for low temperatures. Therefore, in Fig. 4.10(right panel) we also show the relativistic FT-PNRQRPA rate which includes both the GT and FF transitions  $J^\pi = 0^\pm, 1^\pm, 2^-$ . Clearly, for low temperatures, addition of FF transitions enhances the EC rate by more than an order of magnitude. For temperatures  $T \geq 10$  GK, the GT transitions become increasingly unblocked and "catch up" with the FF transitions. Above  $T \geq 20$  GK, both calculations are matching in their predictions. In addition to microscopic calculations, we also show the results obtained using simple analytical expressions for the EC rates (approx. and approx. mod) [3, 169]. They predict overall correct trend for the EC temperature evolution, however they are underestimating the slope of the EC rate increase for high temperatures.

Finally, we compare the EC rates for the diamond region nuclei at  $T_9 = 10$  and  $\rho Y_e = 10^{11}$  g/cm<sup>3</sup>. For the allowed approximation (including only the GT transition) in Fig. 4.11(a) we compare the EC rates for relativistic and non-relativistic calculations. Overall, we observe that the agreement is well within one order of magnitude for all nuclei in the diamond region. The non-relativistic FT-HFB+FT-pnFAM calculations assume axially-deformed shape of the nuclei, while the relativistic

FT-HBCS+FT-pnQRPA is based on the spherical symmetry. One would assume that a different choice of the EDF formulation together with deformation effects would lead to large differences between the model calculations. However, as the temperature is increased, nuclei tend to undergo a shape transition from deformed to a spherical configuration (see Chapter 6), thereby decreasing the differences between the models. In Fig. 4.11(b), for the relativistic QRPA we compare the rate which includes both the GT and FF transitions and the rate with GT transitions only. It is observed that differences can be up to 5 orders of magnitude. For most nuclei the ratio is around one order of the magnitude (as we have seen for  $^{86}\text{Kr}$ ), while for those which are more neutron-rich (lower right part of the diamond region) the ratio is more substantial.

## 4.4 Implications for the core-collapse supernovae evolution

We have performed the CCSNe simulation using the spherically-symmetric 1D code GR1D [170]. It simulates the early stages of the post-bounce phase assuming general-relativistic hydrodynamics and neutrino transport based on the NuLib library [33, 164]. The simulations are performed with the s15WW95 progenitor [171] and the SFHo equation of state [172]. We have performed 5 simulations with different sets for the EC rates of the diamond region nuclei, as discussed previously. The results are shown in Fig. 4.12(a)-(c).

The evolution of the electron-to-baryon ratio  $Y_e$  with the central density  $\rho$  is shown in Fig. 4.12(a). The results for the calculations based on the QRPA match almost exactly, meaning that the differences observed in the EC rates [cf. Fig. 4.11(a)] play almost no role in the evolution of  $Y_e$ . Addition of FF transitions changes the  $Y_e$  trends mostly in the region between  $10^{11}$  and  $10^{12}$  g/cm<sup>3</sup>. Indeed, the increased EC rates of diamond region nuclei (most abundant in these conditions) leads to lower  $Y_e$  as predicted by the GT only calculation. The approximations (approx. and approx. mod) have overall reduced  $Y_e$  due to higher overall EC rates compared to other microscopic calculations. In addition, due to higher EC rates, inclusion of FF transitions produces slightly reduced peak for electron-neutrino luminosity ( $\sim 3\%$ ) in Fig. 4.12(b) and the lower mass of the inner homologous core ( $\sim 4\%$ ) in Fig. 4.12(c). The latter leads to a slightly less massive proto-neutron star once the FF transitions are included in the calculations, while the former is a consequence of the slower neutrino diffusion leading to the quenching of the peak neutrino luminosity, as noted in Ref. [164]. On the other hand, in the case of the allowed GT transitions there is almost no difference between the relativistic and non-relativistic calculations based on the QRPA. Since the EC rates of the diamond

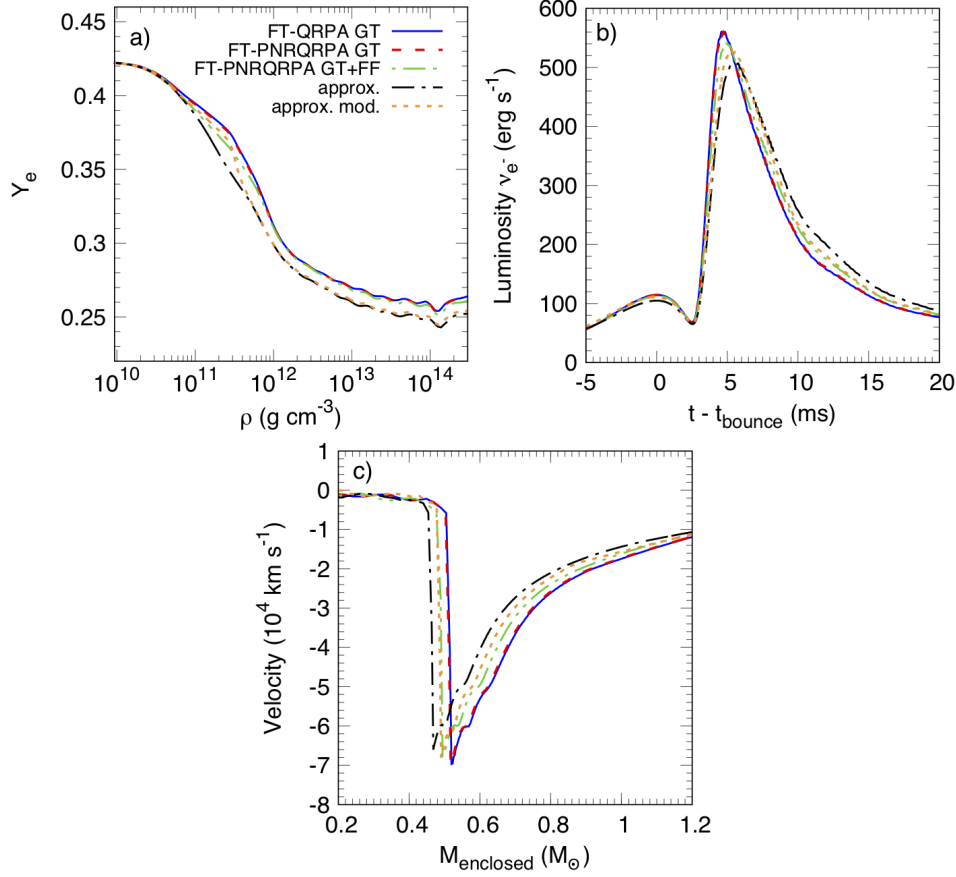


Figure 4.12: The results for the main observables of the CCSNe simulations using the GR1D code with NuLib [164, 170]. The different sets of EC rates for the diamond region nuclei are used (see text) for (a) the electron-to-baryon ratio  $Y_e$  as a function of the central density  $\rho$ , (b) the electron neutrino luminosity  $L_{\nu_e}$  at radius of 500 km as a function of time after bounce, and (c) the central velocity as a function of the enclosed mass. The figure is adopted from Ref. [33].

region nuclei are shown to impact the CCSNe dynamics the most, this observation leads us to the conclusion that the theoretical models for EC rates are well constrained. Therefore, the uncertainties in the CCSNe evolution due to EC rates are significantly reduced. However, even though the EC rate uncertainties between different models have almost no influence on the CCSNe, they could have significant impact to other astrophysical scenarios such as the thermal properties of the neutron star crust [173] where the temperatures are much lower, and a state-by-state evaluation of the EC rates becomes important.

# Chapter 5

## $\beta$ -decay rates in stellar environment

The nuclear  $\beta$ -decay is the process mediated by the weak-nuclear force upon which the nucleus decays either in the direction of increasing proton number

$$(Z, N) \rightarrow (Z + 1, N - 1) + e^- + \bar{\nu}_e, \quad (5.1)$$

where an electron is emitted together with the electron anti-neutrino ( $\bar{\nu}_e$ ), which we call the  $\beta^-$ -decay, or by increasing the neutron number

$$(Z, N) \rightarrow (Z - 1, N + 1) + e^+ + \nu_e, \quad (5.2)$$

where a positron is emitted, together with the electron neutrino, which is called the  $\beta^+$ -decay. In this work, we focus on the  $\beta^-$ -decay, which is an important theoretical input for the nuclear  $r$ -process as well as the  $s$ -process. Of course, since the  $s$ -process occurs near the stability valley, the half-lives are much more constrained by the experimental data, unlike the  $r$ -process which extends to the neutron drip line. We are again interested in *stellar* conditions characterized by high temperature  $T$  and stellar density  $\rho Y_e$ . The underlying theory describing the transition rate is the Fermi theory, in a similar form as for the electron capture, differing only in the kinematics.

First, we present the theoretical formalism used for calculating the  $\beta$ -decay rates, based on the theory of Behrens and Bühring in Ref. [154]. The lepton wavefunction is obtained by expanding the radial Dirac equations, which introduces the so-called *shape factors*. It turns out that the  $\beta$ -decays are rather sensitive to the charge distribution in the decaying nucleus. The problem is complicated also by an outgoing neutrino which carries momentum, making the kinematics of the problem more

involving compared to the EC. This means that the electron spectrum is a distribution rather than a delta function. This Chapter is based on the results published in Ref. [34]. We present our results for  $\beta$ -decay rates of even-even nuclei in the temperature range  $T = 0\text{--}2$  MeV and densities  $\rho Y_e = 10^7$  and  $10^{10}$  g/cm<sup>3</sup>. All calculations performed in this section assume spherical symmetry. Our model calculations are benchmarked against the experimental data at zero temperature and compared with other theoretical models where the data exists.

## 5.1 Theoretical framework

The thermally averaged expression for the  $\beta$ -decay rate is [34, 98]

$$\lambda^\beta = \frac{\ln 2}{K} \frac{1}{Z} \sum_{i,f} e^{-\beta E_i} \int_1^{W_{th}^{(i,f)}} C(W)_{i,f} W p(W_0^{(i,f)} - W)^2 F_0(Z + 1, W) [1 - f_e(W, \mu_e)] dW, \quad (5.3)$$

where we have introduced the definition of the *shape factor*  $C(W)_{i,f}$ , other expressions being defined in Sec. (4.1). In the case of the allowed transitions, the shape factor has the form

$$C(W)_{if} = g_A^2 |\langle i | \sigma \tau^- | f \rangle|^2, \quad (5.4)$$

where  $g_A = -1.0$  is the quenched axial coupling constant (similar in Chapter 4) and the matrix element corresponds to the  $GT^-$  transitions. Note that the shape factor in the allowed approximation is independent of lepton energy. The shape factor for the first-forbidden transitions ( $J^\pi = 0^-, 1^-, 2^-$ ) has the following form

$$C(W)_{i,f} = k_{i,f} + (ka)_{i,f} W + (kb)_{i,f} / W + (kc)_{i,f} W^2, \quad (5.5)$$

where the expressions for  $k_{i,f}$ ,  $(ka)_{i,f}$ ,  $(kb)_{i,f}$  and  $(kc)_{i,f}$  are listed in Appendix D and correspond to those in Ref. [131].

As in the case for EC in Chapter 4, we have to evaluate the above matrix elements within the FT-pnRQRPA, taking into account also the de-excitation strength (lying below the  $Q$ -value threshold). We assume the allowed approximation since the expressions are easier to handle. The  $\beta$ -decay rate

is obtained from Eq. (5.3)

$$\lambda^\beta = \frac{\ln 2}{K} \frac{1}{Z} \sum_{i,f} e^{-\beta E_i} |\langle f | \sigma \tau_- | i \rangle|^2 f(W_0^{(i,f)}), \quad (5.6)$$

where the phase-space factor is defined as

$$f(W_0^{(i,f)}) = \int_1^{W_{th}^{(i,f)}} p W (W_0^{(i,f)} - W)^2 F_0(Z, W) [1 - f_e(W, \mu_e)] dW. \quad (5.7)$$

We are considering the  $\beta^-$ -decay of the initial state of even-even ( $Z, N$ ) nucleus, to a final state of the odd-odd ( $Z + 1, N - 1$ ) nucleus. The diagram explaining the decay is shown in Fig. 5.1. The initial-final energy difference is written as

$$W_0^{(i,f)}(m_e c^2) = E_0^{(i,f)} = E_i - E_f, \quad (5.8)$$

where  $E_i = E_i^* + M_{N_i}$  and  $E_f = E_f^* + M_{N_f}$ . Looking at diagram in Fig. 5.1, this energy difference can be written as  $E_0^{(i,f)} = E_i - E_{1_m^+}$ , where  $E_{1_m^+}$  is the energy of the  $m$ -th excited state in the daughter nucleus ( $E_f$ ). We can then rewrite it as

$$E_0^{(i,f)} = E_i - E_{1_m^+} = \Delta B + \Delta_{np} - E_{1_m^+}^*, \quad (5.9)$$

where  $E_{1_m^+}^*$  is the excitation energy of the  $m$ -th state, now measured with respect to the daughter. Within the FT-pnRQRPA  $E_{1_m^+}^*$  can be approximated as

$$E_{1_m^+}^* \approx E_{QRPA}^m + (\lambda_n - \lambda_p) - \Delta B, \quad (5.10)$$

so that the initial-final energy difference reduces to

$$W_0^{(i,f)}(m_e c^2) \approx W_0^m(m_e c^2) = \Delta B + \Delta_{np} - [E_{QRPA}^m + (\lambda_n - \lambda_p) - \Delta B] = \Delta_{np} - E_{QRPA}^m - (\lambda_n - \lambda_p). \quad (5.11)$$

Using the notation of the matrix FT-pnRQRPA [cf. Sec. 3.2] this means that the total rate in the



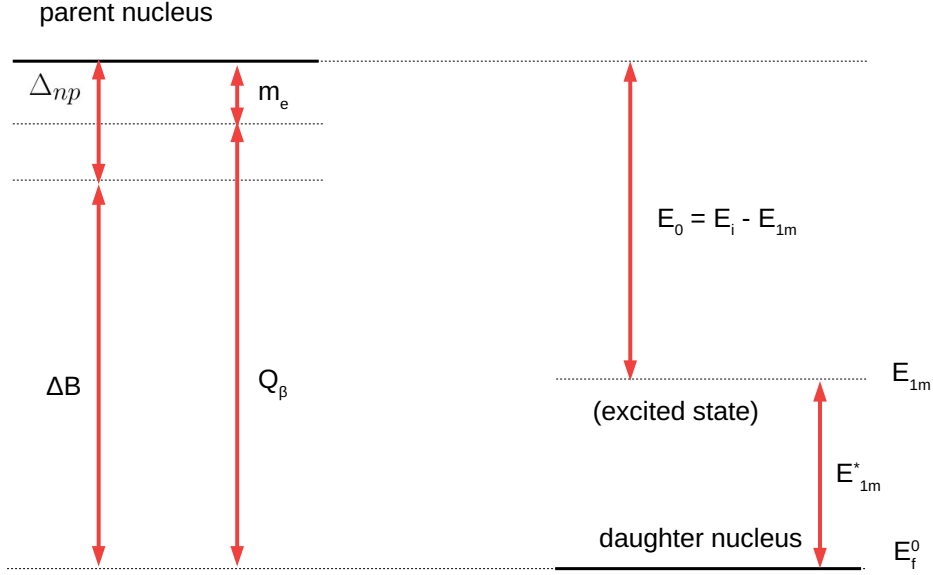


Figure 5.1: The energy diagram for the  $\beta^-$ -decay between the initial state  $E_i$  of the even-even parent nucleus to the final  $m$ -th excited state of the odd-odd daughter nucleus. See text for details.

allowed approximation is

$$\lambda^\beta = \frac{\ln 2}{K} \sum_m B_m \int_1^{W_0^{th,m}} W P [(\Delta_{np} - E_{QRPA}^m - \lambda_{np}) / (m_e c^2) - W]^2 F_0(Z, W) [1 - f_e(W, \mu_e)] dW, \quad (5.12)$$

where the thermally averaged matrix element is defined as

$$B_m \equiv B_m^- = \frac{|\langle [\Gamma_m, \sigma \tau_-] \rangle|^2}{1 - e^{-\beta \omega}}, \quad E_m > 0, \quad (5.13)$$

$$B_m \equiv B_m^+ = -\frac{|\langle [\Gamma_m, \sigma \tau_+] \rangle|^2}{1 - e^{-\beta \omega}}, \quad E_m < 0,$$

in analogy with Eq. (4.13) but with the opposite direction of the isospin.

The phase space of the  $\beta$ -decay is much more constrained compared to the EC phase space. The lowest value the initial-final state difference energy can assume is equal to the electron mass, so that

$$W_0^{(i,f)}(m_e c^2) = m_e c^2 = \Delta_{np} - E_{QRPA}^{th,m} - \lambda_{np}, \quad (5.14)$$

where we have defined the threshold QRPA eigenvalue  $E_{QRPA}^{th,m}$  for which the above condition is fulfilled. This means that the following inequality should hold for the FT-pnRQRPA eigenvalues to contribute to  $\beta$ -decay phase-space integral

$$E_{QRPA}^m \leq \Delta_{nH} - \lambda_{np}, \quad (5.15)$$

where  $\Delta_{nH} = \Delta_{np} - m_e c^2 = 0.782$  MeV. Since for the *excitation* strength  $E_{QRPA}^m > 0$ , the strength interval which contributes to the *excitation*  $\beta$ -decay strength is  $\Delta_{nH} + \lambda_{np}$ . This is an intuitive result since it confirms that more strength for  $\beta^-$ -decay contributes to neutron-rich nuclei having larger chemical potential difference  $\lambda_{np}$ . On the other hand, for *de-excitation* strength,  $E_{QRPA}^m < 0$ , which always satisfies the threshold condition in Eq. (5.15). In the case of de-excitations, the limit on  $E_{QRPA}^m$  is determined by an exponential decrease of the detailed balance factor  $(1 - e^{-\beta\omega})^{-1}$ .

## 5.2 Results

The model we employ in the calculation of  $\beta$ -decay rates is the FT-HBCS+FT-pnRQRPA in spherical symmetry described in Sec. 4.3. It is based on the D3C\* relativistic EDF, known for its success in reproducing the experimental data of the  $\beta$ -decay rates at zero temperature [130, 131]. Here, compared to the model in Sec. 4.3 the  $pp$  interaction in the FT-HBCS solver is different. We adopted a monopole pairing characterized by strengths  $G_{p(n)}$  for proton(neutron) states. The pairing strength is determined for each nucleus separately by reproducing the experimental pairing gaps calculated using the 5-point formula [40]. First, we have to benchmark our model at zero temperature by calculating the half-lives  $T_{1/2} = \ln 2 / \lambda^\beta$  and comparing them to the available experimental data. This is shown in Fig. 5.2(a)-(d) for the isotopic chains of titanium, iron, cadmium, and tin. Overall, the experimental data are well reproduced for Ti and Cd chains. Our calculations underestimate the results for the Fe chain. We note that the present calculation is spherical, while most of the shown iron isotopes have axially deformed ground states. Later, in Chapter 7, we recalculate the iron isotopic chain half-lives by also considering the deformation effects. For the tin isotopic chain, calculations overestimate results for  $A < 134$  and underestimate those for  $A \geq 134$ . Such discrepancy cannot be attributed to deformation effects since most of these nuclei are spherical. To describe the half-life of these nuclei, one has to go beyond the QRPA, which considers only the 2 q.p. excitations and include coupling to more complex configurations. Examples are the particle-vibration coupling (PVC) models based on either relativistic [135, 150] or non-relativistic [132, 133]

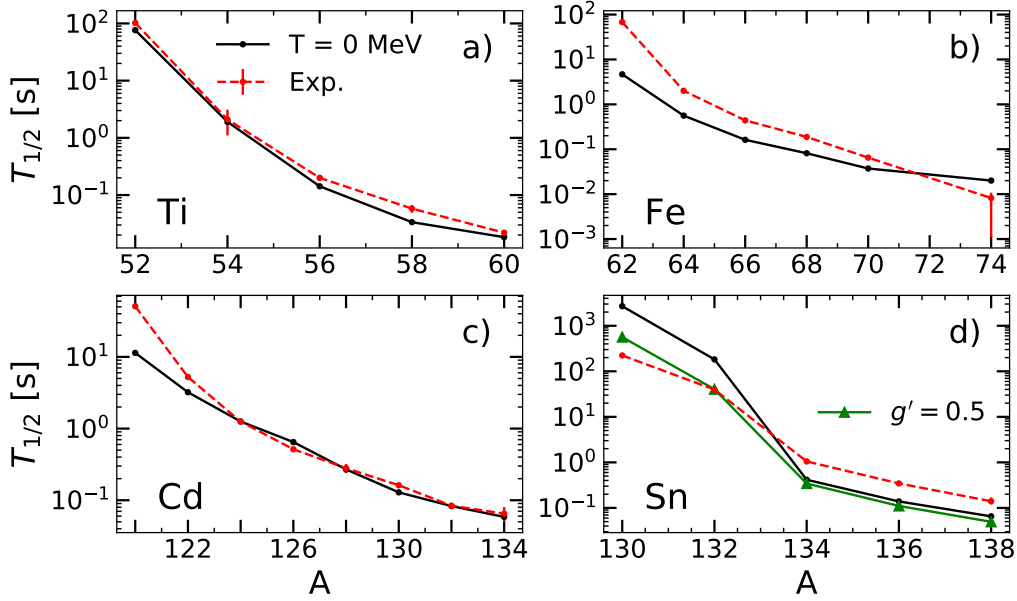


Figure 5.2: Comparison between the calculated (black) and experimental [159] (red) half-lives  $T_{1/2}$  at zero temperature for titanium (a), iron (b), cadmium (c), and tin (d) isotopic chains. For Sn, we also show the results calculated by lowering the Landau-Migdal parameter  $g'$  to 0.5 (green). We have adopted the figure from Ref. [34].

EDFs. Such models tend to better reproduce the half-lives of the doubly-magic and semi-magic nuclei by inducing more transition strength in the  $\beta$ -decay kinematic window (also known as the  $Q_\beta$  window). To partially remedy this issue within our model, we have artificially induced more transitions in the  $Q_\beta$  window for Sn isotopes by lowering the strength of the Landau-Migdal interaction to  $g' = 0.5$  [cf. Eq. (4.21)]. This is shown in Fig. 5.2(d) where we see that  $g'$  is adjusted to reproduce the half-life of  $^{132}\text{Sn}$ .

Now, we extend our calculations to finite temperatures and stellar densities. In Figure 5.3(a)-(d) we present the temperature evolution of selected even-even isotopes of titanium, iron, cadmium, and tin in the temperature range  $T = 0\text{--}1.5$  MeV and at stellar density  $\rho Y_e = 10^7$  g/cm $^3$ . We observe the following general trends: (i) half-lives tend to decrease with temperature, and (ii) this decrease is more substantial for nuclei with initially higher half-lives at zero temperature. For instance, compared to zero temperature, the half-life of  $^{52}\text{Ti}$  is reduced by almost two orders of magnitude at  $T = 1.5$  MeV. On the other hand, for more neutron-rich  $^{60}\text{Ti}$ , the half-life is almost temperature independent. Similar trends are observed in other isotopic chains. For temperatures below  $T = 0.3$  MeV half-lives are temperature independent, after which they start to decrease.

The reasons for decreasing half-lives are threefold. (i) As the temperature increases, previously blocked transitions become possible. If those transitions are found within the  $Q_\beta$  window, they will modify the half-life. (ii) With increasing temperature, the pairing correlations weaken until the critical temperature where they vanish completely. For  $^{52}\text{Ti}$ , the FT-HBCS predicts critical temperature for neutrons at around 0.6 MeV and around 0.9 MeV for protons. Therefore, above 0.9 MeV, the half-life is purely determined by the finite-temperature effects. With the temperature approaching the critical temperature, significant changes occur to the low-lying strengths, which is incidentally the most important for the half-lives. (iii) Since we are considering highly-excited nuclei, transitions with negative  $Q$ -value (de-excitations) also become possible. They are especially important for  $pf$ -shell nuclei where the  $\beta^-$ -strength is considerably lower than the corresponding  $\beta^+$ -strength. As the temperature increases, the detailed balance factor allows more de-excitation strength to contribute to the total rate. Which of these three effects is more important depends on the nucleus under consideration. For instance, de-excitations are the dominant contribution to half-lives of  $^{52,54}\text{Ti}$  and  $^{62}\text{Fe}$  starting already at  $T \geq 0.3$  MeV. For more neutron-rich nuclei, their contribution to the total rate is more moderate, up to 10% [34]. However, more neutron-rich nuclei already display very short lifetimes, meaning that the temperature effects are moderate at most (showing changes within an order of magnitude). In Fig. 5.3(d), we have compared the half-life of  $^{132}\text{Sn}$  with calculations from Ref. [135], which employs the finite-temperature relativistic time-blocking approximation (FT-RTBA). It is encouraging that the temperature dependence predicted by the two models is similar. Our calculations show an initial decreasing trend in half-life  $\approx 0.1$  MeV below the temperature for which it occurs for the FT-RTBA. As the temperature increases both models agree at  $T = 1$  MeV. Considering substantial differences between the model calculations, such as consideration of complex configurations within the FT-RTBA and different underlying EDFs the results are more than reasonable.

For a complete understanding of  $\beta$ -decay rates, we also have to consider first-forbidden (FF) transitions. The temperature dependence of the total rate decomposed to individual multipoles is shown in Fig. 5.3(e)-(h). For  $pf$ -shell nuclei such as  $^{54}\text{Ti}$  and  $^{62}\text{Fe}$ , Gamow-Teller is the most dominant multipole. Although the contribution of FF transitions increases with increasing temperature, their overall impact remains negligible. On the other hand, the FF transitions play a more important role in heavier nuclei such as  $^{120}\text{Cd}$  and  $^{132}\text{Sn}$ . In  $^{120}\text{Cd}$  up to  $T = 0.6$  MeV, the most dominant multipole is GT, above which  $1^-$  FF multipole gains more importance. At  $T \sim 1.5$  MeV, the  $1^-$  FF multipole becomes comparable to the GT, eventually surpassing it in the contribution

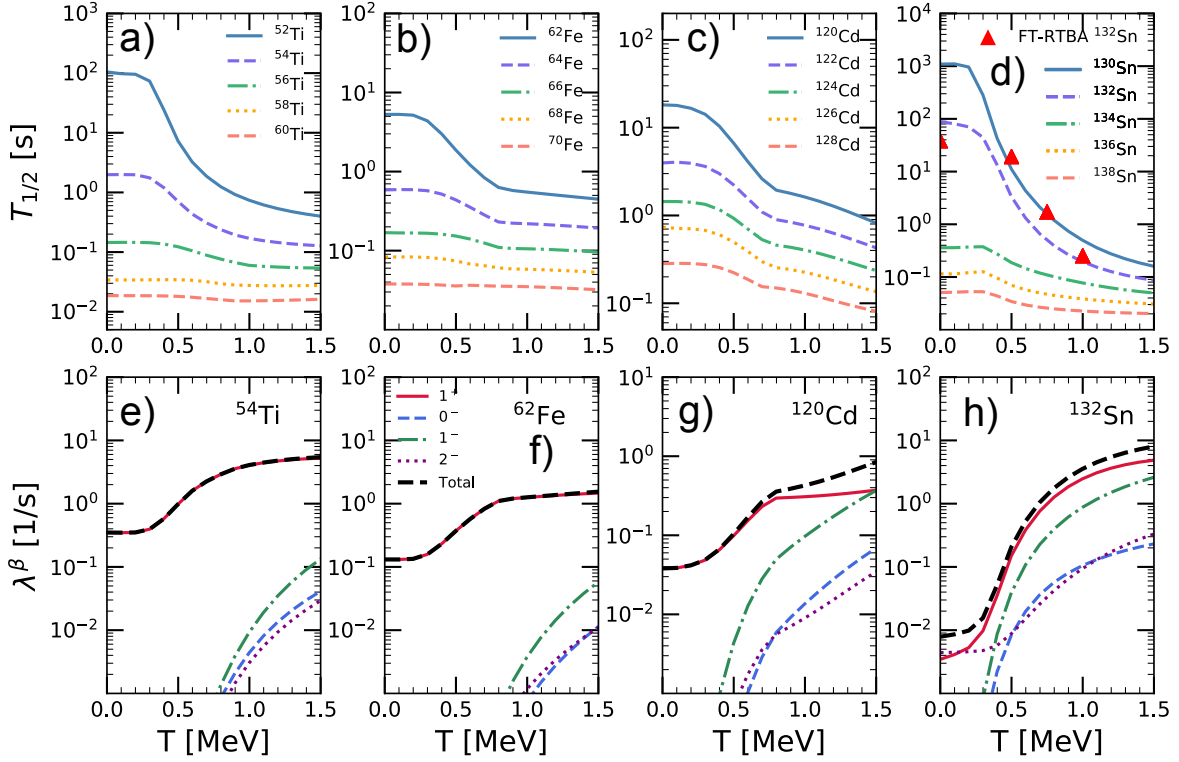


Figure 5.3: (a)-(d) The temperature evolution of  $\beta$ -decay half-lives in the temperature range  $T = 0$ – $1.5$  MeV for selected even-even Ti, Fe, Cd and Sn isotopes. For  $^{132}\text{Sn}$ , the red triangles label the FT-RTBA results from Ref. [135]. (e)-(h) Decomposition of the total rate  $\lambda^\beta$  to contribution of allowed ( $1^+$ ) and first-forbidden ( $0^-$ ,  $1^-$ ,  $2^-$ ) multipoles for selected nuclei in respective isotopic chains. Calculations are performed at stellar density  $\rho Y_e = 10^7$  g/cm $^3$ . Figure is adapted with permission from Ref. [34]. Copyrighted by the American Physical Society.

to the total rate. For  $^{132}\text{Sn}$  at low temperatures, GT competes with the  $2^-$  multipole. At higher temperatures, the GT multipole starts increasing almost exponentially up to  $T \sim 1$  MeV, being larger more than an order of magnitude compared to  $2^-$  at  $T = 1.5$  MeV. The  $1^-$  FF transitions also grow significantly with increasing temperature being within the same order of magnitude as GT at  $T = 1.5$  MeV.

In previous considerations, we have kept the density constant. What happens to  $\beta$ -decay rates as the density increases? As the electron chemical potential increases with higher density, the lepton phase space becomes significantly Pauli blocked, decreasing the  $\beta$ -decay rate and prolonging the

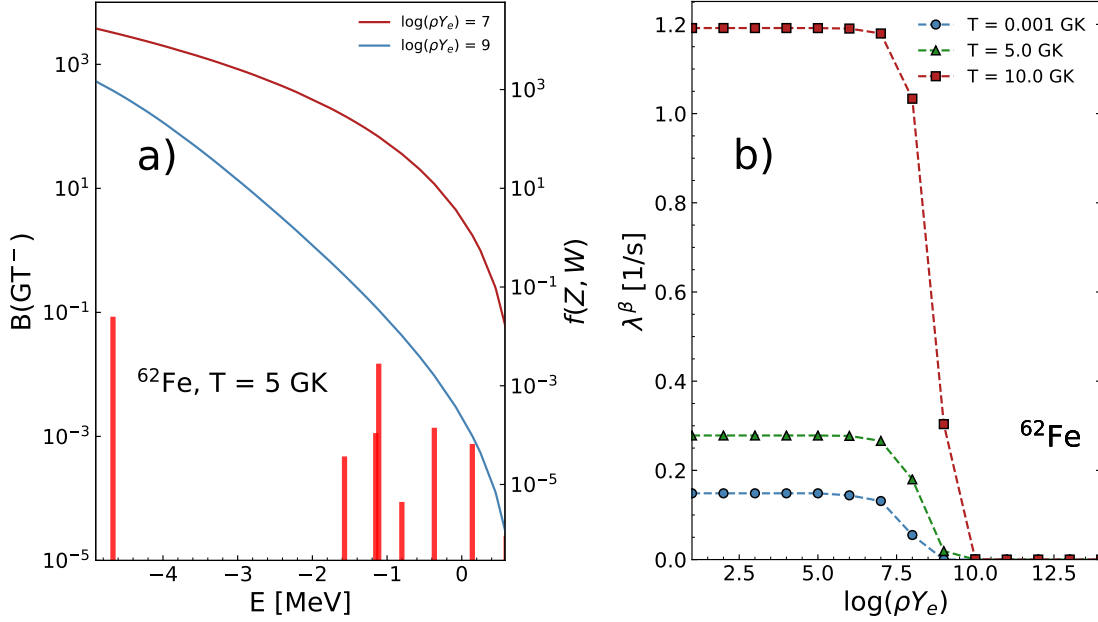


Figure 5.4: (a) The GT<sup>-</sup> strength function in  $^{62}\text{Fe}$  at 5 GK (red bars) together with the corresponding phase-space factors at  $\rho Y_e = 10^7$  g/cm<sup>3</sup> (dark red) and  $10^9$  g/cm<sup>3</sup> (blue). (b) The  $\beta$ -decay rate dependence of  $^{62}\text{Fe}$  with respect to stellar density  $\rho Y_e$  at  $T = 0, 5$  and  $10$  GK.

half-lives. The conclusion is exactly the opposite of that from EC, where the total rate is proportional to electron Fermi-Dirac factor  $f_e$  [cf. Eq. (4.3)], while the  $\beta$ -decay rate is proportional to  $1 - f_e$  as in Eq. (5.3). To illustrate how the stellar density  $\rho Y_e$  influences the  $\beta$ -decay rate, in Fig. 5.4(a), we plot the GT<sup>-</sup> strength in  $^{62}\text{Fe}$  at  $T = 5$  GK (0.43 MeV) together with the corresponding phase-space factors [cf. Eq. (5.7)] at  $\rho Y_e = 10^7$  g/cm<sup>3</sup> and  $10^9$  g/cm<sup>3</sup>. The rate in the allowed approximation is defined as the product of strength and phase-space factor at a given excitation energy. The strength is independent of the  $\rho Y_e$ , while the phase-space factor shows significant changes. As the density increases due to the lepton phase-space blocking, the phase-space factor decreases significantly, lowering the effective strength in the  $Q_\beta$  window. In Figure 5.4(b) we show the total  $\beta$ -decay rate for  $^{62}\text{Fe}$  as a function of the density  $\rho Y_e$  for temperatures  $T = 0.001$  (effectively zero), 5 and 10 GK. Notice that the rate is independent of  $\rho Y_e$  up to  $\rho Y_e = 10^7$  g/cm<sup>3</sup>, after which it decreases abruptly. Of course, since the temperature correlations induce additional transitions in the  $Q_\beta$  window, they increase the rate for a given density. For instance, at  $\rho Y_e = 10^9$  g/cm<sup>3</sup> the rate almost vanishes for both  $T = 0$  and 5 GK, while it is still significant for higher  $T = 10$  GK. This illustration leads us to the interesting conclusion that the interplay between the finite temperature and Pauli blocking

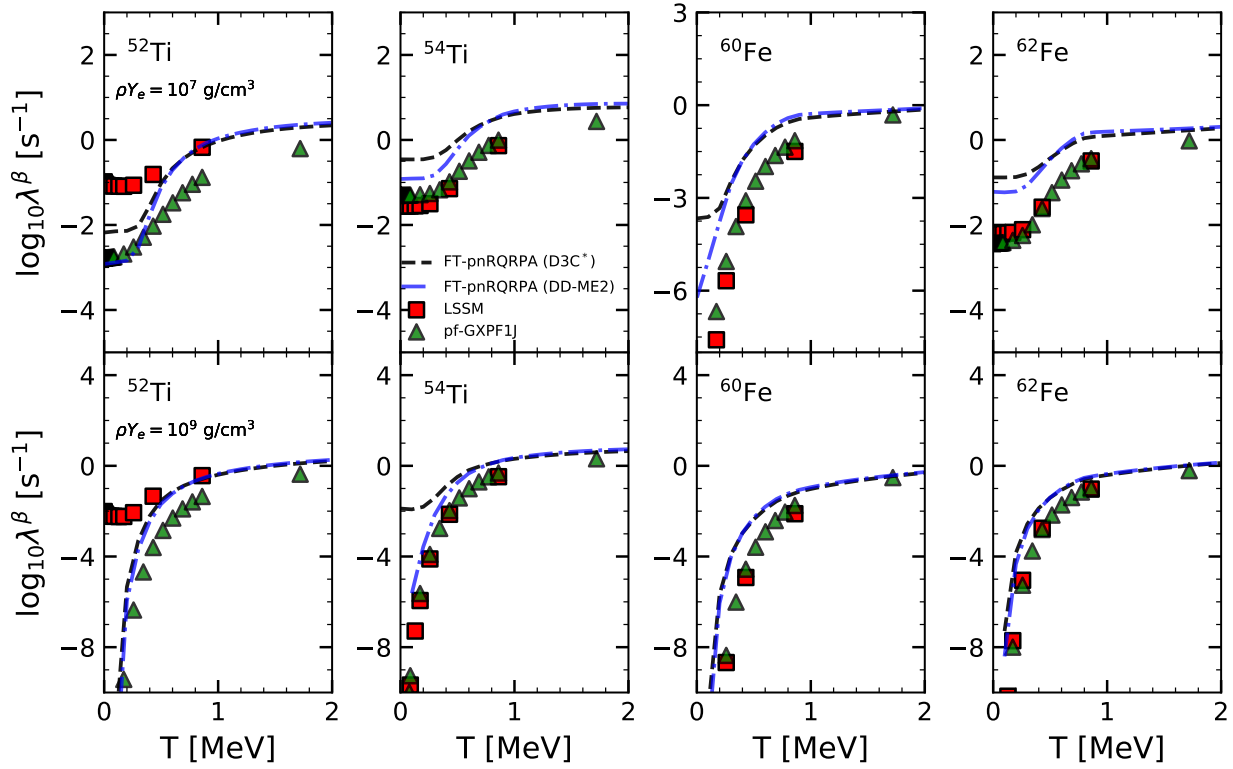


Figure 5.5: Temperature dependence of the  $\beta$ -decay rates for selected  $pf$ -shell nuclei in the temperature range  $T = 0\text{--}2$  MeV at  $\rho Y_e = 10^7$  g/cm<sup>3</sup> (upper panels) and  $\rho Y_e = 10^9$  g/cm<sup>3</sup> (lower panels). Results are calculated within the FT-HBCS+FT-pnRQRPA using the D3C\* interaction (black dashed) and DD-ME2 (blue dash-dotted). Results are compared to LSSM [114] and shell model calculations based on the pf-GXPF1J interaction [126]. The figure is adopted from Ref. [34].

effects is crucial for understanding the  $\beta$ -decay rates in stellar environments.

We have calculated the  $\beta$ -decay rates of selected  $pf$ -shell nuclei using two relativistic EDFs: D3C\* and DD-ME2, and compared our results with the large-scale shell model (LSSM) calculations from Ref. [114] and shell model calculations based on pf-GXPF1J interaction [126]. The results are shown in Fig. 5.5 for  $\rho Y_e = 10^7$  g/cm<sup>3</sup> (upper panels) and  $\rho Y_e = 10^9$  g/cm<sup>3</sup> (lower panels), in the temperature range  $T = 0\text{--}2$  MeV. Since the shell model calculations omit FF transitions, in our calculations we only consider the GT transitions. First, as the  $\rho Y_e$  increases, the rates decrease, as discussed previously. For  $T \geq 0.3$  MeV, the temperature effects are large enough for the decay rate to increase abruptly. As we discussed, this is mostly due to an interplay between lowering the pairing correlations and the introduction of de-excitations (especially for  $pf$ -shell nuclei). We

note that results calculated with the D3C\* and DD-ME2 interactions are comparable. In cases where differences occur (such as  $^{54}\text{Ti}$ ), the D3C\* results predict a higher rate at lower temperatures. This is expected since the main motivation behind developing the D3C\* EDF was to induce more strength in the  $Q_\beta$  window by increasing the effective Landau mass [130]. Our calculations tend to agree with shell model calculations by predicting similar temperature and density dependence. For lower temperatures, the discrepancy between the shell model calculations and our FT-pnQRPA calculations is larger than at higher temperatures. However, the respective shell model calculations also show differences under these conditions in  $^{52}\text{Ti}$ . As the temperature increases, the rates tend to agree within an order of magnitude. Unlike the EC, the  $Q_\beta$  window does not increase with increasing temperature, but only the low-lying strength remains important. For these  $pf$ -shell nuclei at temperatures above  $T \geq 1$  MeV, the de-excitations dominate the total rate. Thus, the inclusion of de-excitations within our model is the key to reasonably reproduce the shell-model results. To treat the transitions from highly-excited states, shell model calculations assume the Brink hypothesis, which presupposes that the strength function for excited states has the same form as for the ground state, only shifted by the excitation energy [174]. This assumption is a consequence of prohibitively large configuration spaces that are required to perform shell model calculations at finite temperature. It doesn't help that the Brink hypothesis was shown to be invalid under certain conditions [108, 174]. On the other hand, the de-excitations within the FT-QRPA stem from equating the physical strength function to the FT-QRPA strength function [31, 34]. Of course, at low temperatures where the rates depend only on a few transitions, relatively simple FT-QRPA cannot reproduce the details of the strength function, and shell model calculations are advantageous. However, considering the scalability of the FT-HBCS+FT-pnQRPA calculations, both with the temperature and system size, they are well suited to perform global  $\beta$ -decay calculations, not only for a given temperature–density grid but also using different EDFs. Such insight can be useful for an estimate of the systematic uncertainty in the rates.

Finally, we present the results for the large-scale calculation of  $\beta$ -decay half-lives in the range  $8 \leq Z \leq 82$  for which the half-lives are below  $10^4$  s. As previously mentioned, the pairing strength of the monopole pairing in the FT-HBCS is adjusted for each nucleus using the 5-point formula [40]. To compensate for overestimating the half-lives of doubly-magic nuclei, the Landau-Migdal coupling  $g'$  is adjusted to reproduce the experimental half-life for  $^{78}\text{Ni}$  and  $^{132}\text{Sn}$ , and the optimal  $g'$  value is used for the whole Ni and Sn chains. The particle-bound nuclei are determined by the condition that the chemical potential of neutron states should be negative ( $\lambda_n < 0$ ).



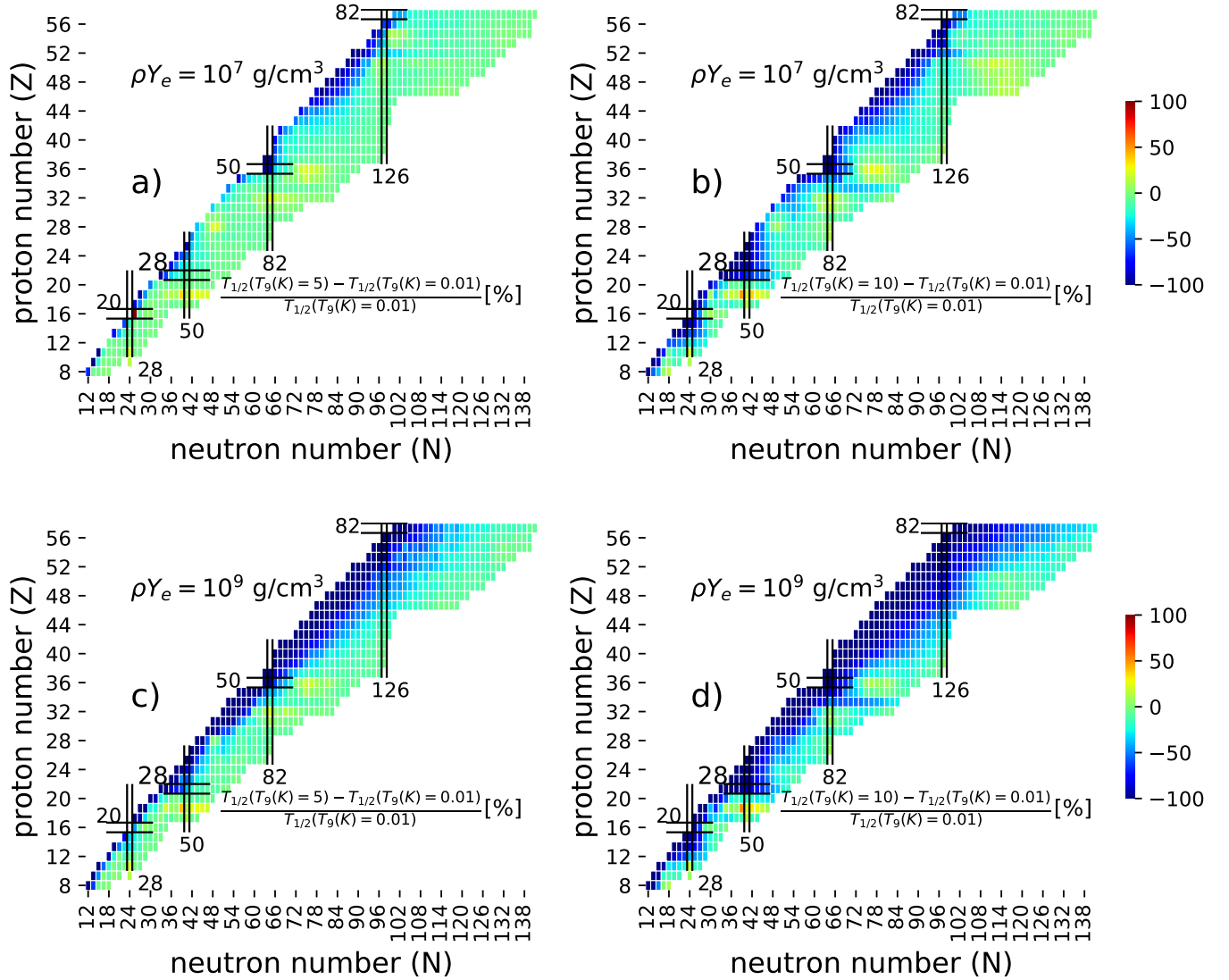


Figure 5.6: The relative change (in %) of  $\beta$ -decay half-lives at  $T_9 = 5$  (a)-(c) and  $T_9 = 10$  (b)-(d) with respect to zero temperature ( $T_9 = 0.01$ ) for  $\rho Y_e = 10^7 \text{ g/cm}^3$  (a)-(b) and  $\rho Y_e = 10^9 \text{ g/cm}^3$  (c)-(d). Only particle-bound even-even nuclei are shown in the range  $8 \leq Z \leq 82$ .

Results for  $\beta$ -decay half-lives are shown in Fig. 5.6 for temperatures  $T = 5$  and 10 GK and stellar densities  $\rho Y_e = 10^7$  g/cm<sup>3</sup> and  $\rho Y_e = 10^9$  g/cm<sup>3</sup>. We display the results as a percentage change in half-life with respect to zero temperature ( $T = 0.01$  GK)<sup>1</sup>. Already at 5 GK, we observe that temperature enhances the half-lives. The nuclei that are most influenced are those near the valley of stability and shell-closure numbers. Nuclei that have longer half-lives at zero temperature are more impacted by temperature effects. The change in half-lives is more pronounced for higher density [Fig. 5.6(c)] compared to lower density [Fig. 5.6(a)]. This is related to the fact that the half-life at higher density is more sensitive to changes in the phase-space integral since the lepton phase-space is Pauli blocked. For a fixed density, as the temperature increases, the electron chemical potential  $\mu_e$  is slightly reduced, allowing more strength to contribute to the decay rate. Therefore, if there is a temperature influence on the strength in the  $Q_\beta$  window, it will be more pronounced at higher  $\rho Y_e$ , even though the overall rate is reduced. At  $T = 10$  GK, the half-lives decrease more significantly, and the effects permeate deeper into the neutron-rich side of the nuclide chart. Again, the changes are especially pronounced near magic and semi-magic shell closures together with those close to the valley of stability. On the other hand, nuclei closer to the neutron drip line show mostly a moderate decrease of half-lives, with some even slightly increasing with temperature. Therefore, the effect of temperature on nuclei is to generally shorten the half-lives, especially those around the shell closure and near the stability valley. However, precise details of this half-life decrease mechanism depend on individual nuclear properties.

The  $r$ -process occurs at fairly low temperatures from the nuclear structure standpoint, being around 1 GK at most [6, 7]. We have shown that  $\beta$ -decays start to be influenced by the temperature only above 3 GK. Therefore, it is unlikely that finite-temperature effects on  $\beta$ -decay half-lives play a role in the nucleosynthesis of nuclei in the  $r$ -process. However, in collapsing cores of massive stars temperatures and densities are high enough to influence the  $\beta$ -decay lifetimes. Indeed, it was confirmed that in certain stages of collapse, the conditions are such that  $\beta$ -decays compete with the EC [4]. The main aim of our work is to provide the astrophysics community with a reliable model that describes the  $\beta$ -decay rates under such conditions. It remains to investigate how the dynamics of CCSNe will change once our calculations are applied to astrophysics simulations. Since the temperature in presupernova conditions is quite high (10 GK and above), deformation effects tend to be less relevant — the spherical approximation of nuclear geometry assumed in this chapter becomes applicable for all nuclei. Nevertheless, we steer the discussion of deformation effects in

<sup>1</sup>Note that a small non-vanishing temperature should be used to avoid divergences in the phase-space factor in Eq. (5.7)

excited states to Chapter 7 since they are crucial for zero temperature where the experimental data is available.

# Chapter 6

## Nuclear landscape at extreme temperatures

Nuclei in the universe appear at finite temperatures. Those temperatures can be either high or low from the nuclear structure viewpoint. For instance, the temperatures inside most stars measure keVs (millions of kelvins), much lower than the shell gaps in nuclei (measured in MeV). On the other hand, in the late stages of CCSNe and neutron star mergers, temperatures are of the order of MeVs (billions of kelvin) and thus able to alter the nuclear structure [1, 175]. Incidentally, those events are responsible for the creation of exotic neutron-rich nuclei via the mechanism of rapid neutron capture (*r*-process). Therefore, establishing a robust theoretical model that can describe nuclei in such extreme conditions is a necessity, not only for nuclear physics but also for astrophysics.

It is a known fact that most nuclei in existence are deformed. Only those that appear near shell closure numbers are spherical. Out of deformed nuclei, most show axial symmetry, while some are triaxial [176]. Therefore, to successfully describe nuclei within our model, we have to consider deformation effects. In this chapter, we consider axial deformation where the symmetry axis is the  $z$ -axis. In these cases, the total angular momentum  $J$  is not a conserved quantum number in the laboratory system, but its projection  $\Omega$  is, with the condition  $|\Omega| \leq J$ . In addition to axial symmetry, we also assume reflection-symmetric shapes such that parity  $\pi$  is also a conserved quantum number. Therefore, instead of coupling our equations to specific  $J^\pi$  blocks, we can only perform coupling to  $\Omega^\pi$  blocks. However, the size of the  $\Omega^\pi$  blocks is much larger than the corresponding  $J^\pi$  blocks meaning that the system of equations does not scale well with size. Indeed, solutions of both RHB and QRPA equations in axial symmetry require advanced numerical methods and larger numerical resources compared to spherical calculations. We start by describing the axially-deformed FT-RHB equations and their solutions. It turns out that naively extending the RHB to finite temperatures

leads to convergence problems. Namely, as nucleons start to increasingly populate the continuum states, solutions start to depend on the box size in which the RHB equations are discretized. We solve this convergence issue by adopting the method developed by Bonche, Levit, and Vautherin (BLV) in Refs. [36, 37], where the continuum solutions are successfully isolated from the nuclear bulk properties. The FT-RHB theory supplemented by the BLV subtraction procedure is then employed to calculate nuclear properties at finite-temperature across the nuclide chart and applied to determine the dependence of nuclear drip lines with temperature. We show that for a proper description of nuclei in the vicinity of drip lines, the subtraction procedure becomes necessary already at  $T = 1$  MeV. Such a conclusion is in contrast to previous theoretical works where it was stated that continuum becomes relevant only for temperatures above 4 MeV [36, 37, 177]. We find that up to  $T = 0.5$  MeV, the nuclear landscape is only moderately influenced by temperature properties, related to the reduction of pairing interaction. As the temperature increases to  $T \geq 1$  MeV, the temperature has a significant effect on the nuclear structure, reducing both the deformation and shell effects. Calculations are performed with three state-of-the-art relativistic EDFs: meson-exchange DD-ME2, point-coupling DD-PC1, and DD-PCX. Multiple functionals are employed to assess the systematic uncertainties stemming from different underlying interactions and fitting protocols used to optimize the functionals.

## 6.1 The axially-deformed FT-RHB theory

For the axially-deformed nuclei,  $J_z$  component of total angular momentum  $J$  is a conserved quantity that we usually denote as  $\Omega_i$ , and that together with parity  $\pi_i$  determines the nuclear spinor [138, 146]

$$\psi_i(\mathbf{r}, s, t) = \begin{pmatrix} f_i^+(r, z)e^{i\Lambda-\phi} \\ f_i^-(r, z)e^{i\Lambda+\phi} \\ ig_i^+(r, z)e^{i\Lambda-\phi} \\ ig_i^-(r, z)e^{i\Lambda+\phi} \end{pmatrix} \chi_{1/2t_i}, \quad (6.1)$$

where  $\Lambda_{\pm} = \Omega_i \pm 1/2$ ,  $\{r, z, \phi\}$  are the usual cylindrical coordinates and  $\chi_{1/2t_i}$  are the isospin wave functions. Nuclear wave functions are expanded in terms of the axially deformed harmonic oscillator wave functions in the potential defined as

$$V_{osc}(z, r) = \frac{1}{2}m\omega_z^2 z^2 + \frac{1}{2}m\omega_{\perp}^2 r^2, \quad (6.2)$$

with two parameters  $\hbar\omega_{\perp}$  and  $\hbar\omega_z$  that can be expressed in terms of deformation parameter  $\beta_0$ :

$$\hbar\omega_z = \hbar\omega_0 e^{-\sqrt{\frac{5}{4\pi}}\beta_0}, \quad \hbar\omega_{\perp} = \hbar\omega_0 e^{\frac{1}{2}\sqrt{\frac{5}{4\pi}}\beta_0}. \quad (6.3)$$

Corresponding oscillator length parameters for two directions are defined as

$$b_z = \sqrt{\frac{\hbar}{m\omega_z}}, \quad b_{\perp} = \sqrt{\frac{\hbar}{m\omega_{\perp}}}, \quad (6.4)$$

with  $b_{\perp}^2 b_z = b_0^3$  because of the volume conservation. The basis is fully determined by the  $\hbar\omega_0$ , which is calculated from the mass number  $A$  as  $\hbar\omega_0 = 41A^{-1/3}$  MeV [138], in addition with the basis deformation  $\beta_0$ . Later, we verify the prescription to determine  $\hbar\omega_0$ . The eigenfunctions of the axially deformed oscillator can be labeled as

$$|\alpha\rangle = |n_z n_r \Lambda m_s\rangle, \quad (6.5)$$

where  $n_z$  and  $n_r$  are the number of nodes in  $z$  and  $r$  directions.  $\Lambda$  and  $m_s$  are the projections of the orbital angular momentum and spin on the intrinsic  $z$ -axis. Using the dimensionless variables

$$\xi = z/b_z, \quad \eta = r^2/b_{\perp}^2, \quad (6.6)$$

the harmonic oscillator eigenfunctions read [138]

$$\Phi_{\alpha}(\mathbf{r}, s) = \phi_{n_z}(z, b_z) \phi_{n_r}^{\Lambda}(r, b_{\perp}) \frac{e^{i\Lambda\phi}}{\sqrt{2\pi}} \chi_{1/2m_s}, \quad (6.7)$$

where

$$\begin{aligned} \phi_{n_z}(z, b_z) &= b_z^{-1/2} \phi_{n_z}(\xi) = b_z^{-1/2} \mathcal{N}_{n_z} H_{n_z}(\xi) e^{-\xi^2/2}, \\ \phi_{n_r}^{\Lambda}(r, b_{\perp}) &= b_{\perp}^{-1} \phi_{n_r}^{\Lambda}(\eta) = b_{\perp}^{-1} \mathcal{N}_{n_r}^{\Lambda} \sqrt{2} \eta^{|\Lambda|/2} L_{n_r}^{|\Lambda|}(\eta) e^{-\eta/2}. \end{aligned} \quad (6.8)$$

In the above,  $H_{n_z}(\xi)$  and  $L_{n_r}^{|\Lambda|}(\eta)$  denote Hermite and associated Laguerre polynomials respectively [178], and  $\chi_{1/2m_s}$  are the spin wavefunctions. The normalization factors are

$$\mathcal{N}_{n_z} = (\sqrt{\pi} 2^{n_z} n_z!)^{-1/2}, \quad \mathcal{N}_{n_r}^{\Lambda} = (n_r! / (n_r + |\Lambda|)!)^{1/2}. \quad (6.9)$$

Large and small components are expanded independently in terms of the oscillator eigenfunctions

$$f_i(\mathbf{r}, s, t) = \frac{1}{\sqrt{2\pi}} \begin{pmatrix} f_i^+(r, z)e^{i\Lambda-\phi} \\ f_i^-(r, z)e^{i\Lambda+\phi} \end{pmatrix} = \sum_{\alpha}^{\alpha_{max}} f_{\alpha}^{(i)} \Phi_{\alpha}(\mathbf{r}, s) \chi_{1/2t_i}, \quad (6.10)$$

$$g_i(\mathbf{r}, s, t) = \frac{1}{\sqrt{2\pi}} \begin{pmatrix} g_i^+(r, z)e^{i\Lambda-\phi} \\ g_i^-(r, z)e^{i\Lambda+\phi} \end{pmatrix} = \sum_{\alpha}^{\tilde{\alpha}_{max}} g_{\alpha}^{(i)} \Phi_{\alpha}(\mathbf{r}, s) \chi_{1/2t_i}, \quad (6.11)$$

To avoid the appearance of spurious states, quantum numbers  $\alpha_{max}$  and  $\tilde{\alpha}_{max}$  are chosen in a way that the corresponding major quantum number  $N = 2n_r + |\Lambda| + n_z$  is not larger than  $N_{max}$  and  $N_{max} + 1$  for the large and small components respectively.

The single-particle Dirac equation derived from the mean-field Lagrangian can be represented as in Sec. 2.1

$$\{\boldsymbol{\alpha}(-i\nabla - \mathbf{V}(\mathbf{r})) + \beta M^*(\mathbf{r}) + V(\mathbf{r})\} \psi_i(\mathbf{r}) = \varepsilon_i \psi_i(\mathbf{r}), \quad (6.12)$$

where the details of scalar and vector fields depend on specific EDFs under consideration (See Chapter 2). In the following we assume even-even nuclei so that the space-like components vanish  $\mathbf{V} = 0$ . By inserting the definition of the spinor in the axially-deformed oscillator basis, we obtain an eigenvalue problem as in Ref. [138]. Assuming the time-reversal symmetry, for each solution with  $\Omega > 0$

$$\psi_i = \{f_i^+, f_i^-, g_i^+, g_i^-, \Omega_i\}, \quad (6.13)$$

we have the time-reversed solution with the same energy and opposite  $\Omega$

$$\psi_i = \hat{T} \psi_i = \{-f_i^-, f_i^+, g_i^-, g_i^+, -\Omega_i\}, \quad (6.14)$$

with the time-reversal operator defined as  $\hat{T} = i\sigma_y \hat{K}$  ( $\hat{K}$  is the complex conjugation). For nuclei with time-reversal symmetry, the contributions to the densities of the two time-reversed states  $i$  and  $\bar{i}$  are identical. Therefore, the densities are defined as

$$\rho_{s,v} = 2 \sum_{i>0} n_i ( (|f_i^+|^2 + |f_i^-|^2) \mp (|g_i^+|^2 + |g_i^-|^2) ), \quad (6.15)$$

where "+" corresponds to the scalar density  $\rho_s$  and "-" to the vector density  $\rho_v$ . Factor  $n_i$  is the occupation number of the state, and sum  $i > 0$  runs only over the states with  $\Omega_i > 0$ . Similar expressions are also obtained for other densities being bilinear covariants in Dirac fields.

By addition of the nuclear pairing field into the consideration, we obtain the RHB equation as defined in Sec. 2.2

$$\sum_{l'} \begin{pmatrix} h_{ll'} - \lambda - M & \Delta_{ll'} \\ -\Delta_{ll'}^* & -h_{ll'}^* + \lambda + M \end{pmatrix} \begin{pmatrix} U_{lk} \\ V_{lk} \end{pmatrix} = E_k \begin{pmatrix} U_{lk} \\ V_{lk} \end{pmatrix}, \quad (6.16)$$

where the single-particle Hamiltonian can be rewritten as

$$\begin{aligned} h &= \boldsymbol{\alpha} \cdot \mathbf{p} + V + \beta(M + S) = \begin{pmatrix} 0 & \boldsymbol{\sigma} \cdot \mathbf{p} \\ \boldsymbol{\sigma} \cdot \mathbf{p} & 0 \end{pmatrix} + V + \begin{pmatrix} 1_{2 \times 2} & 0 \\ 0 & -1_{2 \times 2} \end{pmatrix} (M + S) \\ &= \begin{pmatrix} V + M + S & \boldsymbol{\sigma} \cdot \mathbf{p} \\ \boldsymbol{\sigma} \cdot \mathbf{p} & V - M - S \end{pmatrix}. \end{aligned}$$

Since we assume the axial symmetry, the product of the Pauli matrix  $\boldsymbol{\sigma}$  and momentum operator  $\mathbf{p}$  is

$$\boldsymbol{\sigma} \cdot \mathbf{p} = \sigma_\rho p_\rho + \sigma_z p_z = -i\sigma_\rho \frac{d}{d\rho} - i\sigma_z \frac{d}{dz}, \quad (6.17)$$

where  $\sigma_\rho = \sigma_x \cos \phi + \sigma_y \sin \phi$  and  $\sigma_\rho^2 = 1$ . The pairing field has the form as in Eq. 2.53. We can simplify the calculations by imposing the time-reversal symmetry and setting the matrix elements  $\Delta_{+-}, \Delta_{-+}, \Delta_{--}$  to zero [23]. The RHB equation has to be written in a basis represented by states  $\{|\alpha\rangle, |\bar{\alpha}\rangle\}$ , however, by using the time-reversal symmetry, it can be shown [23, 179] that the equations decouple to a smaller dimension. Now the RHB equation assumes the following form in the oscillator basis

$$\begin{pmatrix} A_{\alpha\alpha'} & B_{\alpha\bar{\alpha}'} & (\Delta_{++})_{\alpha\bar{\alpha}'} & 0 \\ D_{\bar{\alpha}\alpha'} & C_{\bar{\alpha}\bar{\alpha}'} & 0 & 0 \\ (\Delta_{++})_{\alpha\bar{\alpha}'} & 0 & -A_{\alpha\alpha'} & -B_{\alpha\bar{\alpha}'} \\ 0 & 0 & -D_{\bar{\alpha}\alpha'} & -C_{\bar{\alpha}\bar{\alpha}'} \end{pmatrix} \begin{pmatrix} f_\alpha^U \\ g_{\bar{\alpha}'}^U \\ f_{\bar{\alpha}'}^V \\ g_{\bar{\alpha}'}^V \end{pmatrix} = E_\alpha^{(1)} \begin{pmatrix} f_\alpha^U \\ g_{\bar{\alpha}'}^U \\ f_{\bar{\alpha}'}^V \\ g_{\bar{\alpha}'}^V \end{pmatrix}, \quad (6.18)$$

with matrix elements  $A_{\alpha\alpha'}$ ,  $B_{\alpha\bar{\alpha}'}$ ,  $C_{\bar{\alpha}\bar{\alpha}'}$ , and  $D_{\bar{\alpha}\alpha'}$  defined in Ref. [138]. Therefore, the RHB equations in the h.o. space reduce to a diagonalization problem with eigenvalues  $E_\alpha^{(1)}$  and eigenvectors  $\begin{pmatrix} f_\alpha^U & g_{\bar{\alpha}'}^U & f_{\bar{\alpha}'}^V & g_{\bar{\alpha}'}^V \end{pmatrix}$  [138, 146]. The RHB equations are simply extended to the FT-RHB equations as presented in Sec. 2.3.



For the pairing interaction, we employ the separable pairing force of Ref. [141] in the form

$$V^{pp}(1, 2) = -G\delta(\mathbf{R} - \mathbf{R}')P(\mathbf{r})P(\mathbf{r}'), \quad (6.19)$$

where  $\mathbf{R} = \frac{1}{2}(\mathbf{r}_1 + \mathbf{r}_2)$  and  $\mathbf{r} = \mathbf{r}_1 - \mathbf{r}_2$  denote the center-of-mass and relative coordinate, respectively, while  $P(\mathbf{r})$  has the form

$$P(\mathbf{r}) = \frac{1}{(4\pi a^2)^{3/2}} e^{-r^2/4a^2}, \quad (6.20)$$

where parameters  $G$  and  $a$  can be found in Ref. [141].

## 6.2 Continuum subtraction method

Before presenting calculations obtained with the FT-RHB model, we have to handle the particle continuum explicitly. As the temperature increases, nucleons scatter above the Fermi level. At large enough temperatures, we would have a non-vanishing probability  $v_i^2 > 0$  of finding particles with positive single-particle energies  $\varepsilon_i > 0$ . To explicitly take into account the continuum states, we define the subtracted grand-canonical potential as in Refs. [36, 37]

$$\bar{\Omega} = \Omega[\mathcal{R}] - \Omega[\tilde{\mathcal{R}}] + E_C[\rho_c, \tilde{\rho}_c], \quad (6.21)$$

where  $\mathcal{R}$  stands for the generalized density of the Nucleus+Vapor system (Nucl+Vap) and  $\tilde{\mathcal{R}}$  corresponds to the vapor system (Vap). To account for the vapor-nucleus Coulomb interaction, the BLV prescription proposes a form of the Coulomb term  $E_C[\rho_c, \tilde{\rho}_c]$  which subtracts the long-range vapor Coulomb repulsion [36, 37]. Here,  $\rho_c, \tilde{\rho}_c$  are the proton particle densities of the Nucl+Vap and Vap systems, respectively. Variation of  $\bar{\Omega}$  with  $\mathcal{R}$  leads to the FT-RHB equation for the Nucl+Vap system

$$\begin{pmatrix} h - \lambda & \Delta \\ -\Delta^* & -h - \lambda \end{pmatrix} \begin{pmatrix} U \\ V \end{pmatrix} = E \begin{pmatrix} U \\ V \end{pmatrix}, \quad (6.22)$$

where  $(U, V)$  is a set of q.p. wave functions with energy  $E$ . By performing variations of  $\bar{\Omega}$  with  $\tilde{\mathcal{R}}$  we get the FT-RHB equations for the Vap system

$$\begin{pmatrix} \tilde{h} - \lambda & \tilde{\Delta} \\ -\tilde{\Delta}^* & -\tilde{h} - \lambda \end{pmatrix} \begin{pmatrix} \tilde{U} \\ \tilde{V} \end{pmatrix} = \tilde{E} \begin{pmatrix} \tilde{U} \\ \tilde{V} \end{pmatrix}, \quad (6.23)$$

with the corresponding set of wave functions  $(\tilde{U}, \tilde{V})$  and energies  $\tilde{E}$ . The subsidiary condition for the chemical potential  $\lambda$  is

$$\int d\mathbf{r} [\rho(\mathbf{r}) - \tilde{\rho}(\mathbf{r})] = N, \quad (6.24)$$

where  $N$  stands for either neutron or proton particle number. The  $\tilde{h}$  is the single particle Hamiltonian of the Vap system, defined by the vapor vector and scalar fields  $\tilde{V}$  and  $\tilde{S}$ , respectively. The difference between the Nucl+Vap Dirac field  $h$  and Vap fields  $\tilde{h}$  is in the initialization of the scalar and vector fields. For the Nucl+Vap system, we assume an initial Woods-Saxon form of the scalar and vector potentials, while the Vap fields are only initialized with the Coulomb field. The Poisson equation for the time-like component of the Coulomb field  $A^0$  of both Nucl+Vap and Vap systems has the form

$$-\nabla^2 A^0 = e[\rho_c(\mathbf{r}) - \tilde{\rho}_c(\mathbf{r})]. \quad (6.25)$$

It results in a coupling between the Nucl+Vap and Vap FT-RHB equations. The pairing field is calculated as

$$\Delta_{ll'} = \frac{1}{2} \sum_{kk'} V_{ll'k\bar{k}'}^{pp} \kappa_{k\bar{k}'}, \quad \tilde{\Delta}_{ll'} = \frac{1}{2} \sum_{kk'} V_{ll'k\bar{k}'}^{pp} \tilde{\kappa}_{k\bar{k}'}, \quad (6.26)$$

for Nucl+Vap and Vap systems, respectively. We initialize the Nucl+Vap pairing field with a constant value, while the initial value of  $\tilde{\Delta}$  is zero. We have confirmed that irrespective of its initial value, the pairing field of the Vap system always vanished as the convergence of the self-consistent iteration scheme is reached.

### 6.2.1 Example calculations on a 1D model

To exemplify the BLV method demonstrated above for the FT-RHB we construct a simplified model which displays the main results more clearly. To this aim, we neglect the pairing correlations and assume spherical symmetry, and therefore solve the spherically-symmetric FT-RMF equations. The wave functions of the spherical harmonic oscillator are unable to reproduce the asymptotic tail of

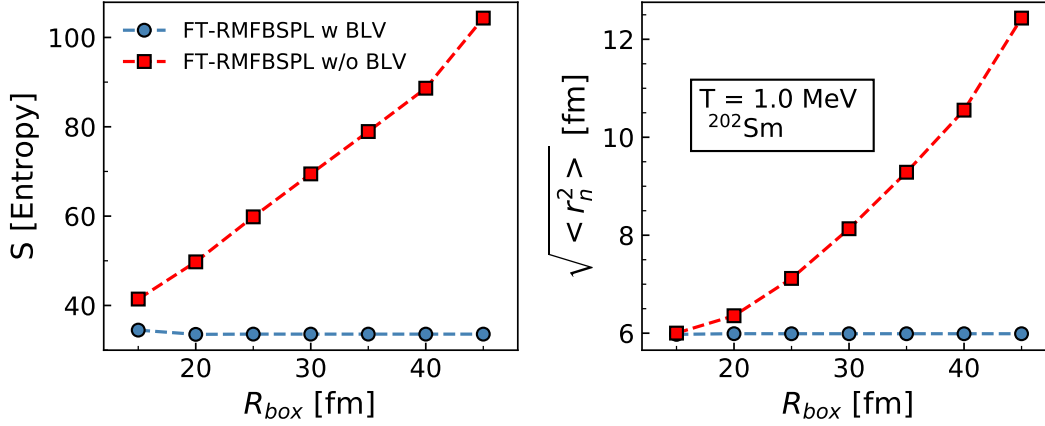


Figure 6.1: Dependence of entropy  $S$  (left panel) and the RMS neutron radius  $\sqrt{\langle r_n^2 \rangle}$  on the box size  $R_{box}$  with (blue circles) and without (red squares) the continuum subtraction procedure. Results are calculated for  $^{202}\text{Sm}$  at  $T = 1$  MeV using the DD-ME2 interaction and the FT-RMFBSPL solver.

the nuclear density [180, 181]. Namely, instead of an exponential decrease of the density  $e^{-r}$ , they have a Gaussian tail of the form  $e^{-r^2}$ . In principle, this issue could be remedied by increasing the number of h.o. shells  $N_{osc}$  to very large numbers, at significant expense of computational time. Therefore, to omit the incorrect asymptotic behavior of the h.o. wavefunctions we constructed an FT-RMF solver in the coordinate space (FT-RMFBSPL) based on the code in Ref. [182]. It employs the finite-element method (FEM) by discretizing the wave functions on a B-spline mesh in a coordinate space. Its basis is defined by: the number of finite elements  $N_{fe}$ , the order of the B-splines  $N_{ord}$ , and the box size  $R_{box}$ . For weakly-bound nuclei, main observables do not converge with increasing the box size  $R_{box}$ . To test the BLV subtraction procedure we have chosen a nucleus in the vicinity of the drip line,  $^{202}\text{Sm}$  at  $T = 1.0$  MeV. Calculations are performed with the FT-RMFBSPL code using the DD-ME2 interaction. We show the results in Fig. 6.1 for the temperature dependence of entropy  $S$  (left panel) and RMS neutron radius  $\sqrt{\langle r_n^2 \rangle}$  (right panel) on the box size  $R_{box}$ . Calculations without the continuum subtraction procedure show an almost exponential-like increase of both entropy and RMS neutron radius as  $R_{box}$  is increased. On the other hand, with the BLV prescription of the continuum subtraction, the observables are independent of the box size starting already from  $R_{box} = 20$  fm. This drastic example shows that a proper treatment of continuum states is a necessity for nuclei in the vicinity of the drip line for calculations to be meaningful.

The reason behind such behavior can be understood by inspecting Fig. 6.2 where we show

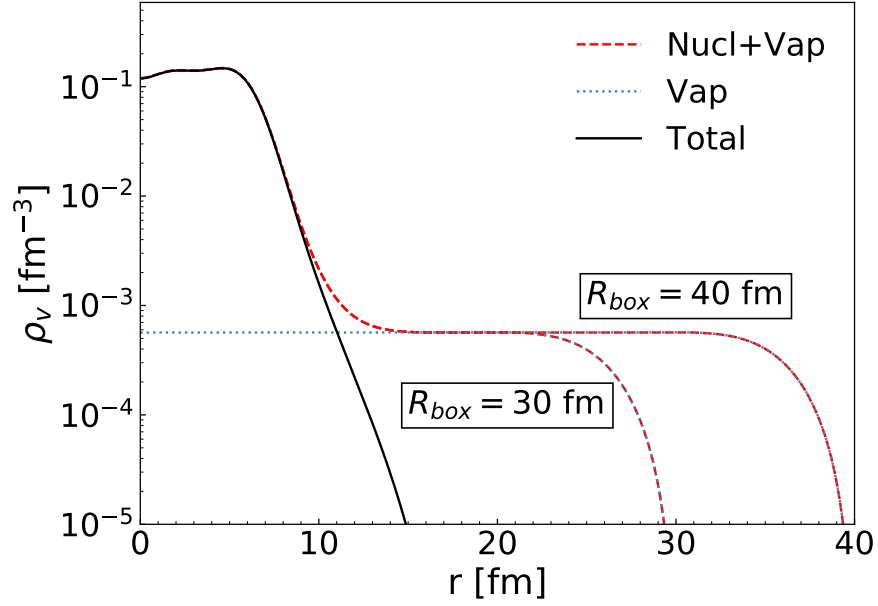


Figure 6.2: The radial dependence of the total vector density  $\rho_v$  (black) decomposed to the contribution of the Nucl+Vap system (red dashed) and Vap system (blue dotted), for  $R_{box} = 30$  fm and 40 fm. Results are calculated for  $^{202}\text{Sm}$  at  $T = 1$  MeV using the DD-ME2 interaction and the FT-RMFBSPL solver.

the radial dependence of the vector density  $\rho_v$ . Results are shown for the total vector density of the Nucl+Vap system with  $R_{box} = 30$  fm and 40 fm. Imposed box boundary conditions mean that density vanishes at  $R_{box}$ . From the figure, we observe that the total system consisting both of nucleus and vapor (Nucl+Vap) displays a long tail in the density. As the box size is increased from 30 fm to 40 fm, so does the tail. Precisely this tail originates from the contribution of continuum states and behaves as a vapor surrounding the nucleus. It is the culprit for box-size dependence of observables such as entropy and the RMS radius. By employing the BLV subtraction procedure, we can isolate the contribution of this vapor from a combined solution. By subtracting the vapor density ( $\tilde{\rho}_v$ ) from the Nucl+Vap density ( $\rho_v$ ) we obtain the subtracted density  $\bar{\rho}_v = \rho_v - \tilde{\rho}_v$  that is independent of the box-size.

## 6.2.2 Comparison between the solvers based on the h.o. expansion and the coordinate-space solvers

As already mentioned, our axially-deformed FT-RHB solver is based on the h.o. expansion, and is limited by the improper boundary conditions of the density. Is the BLV subtraction procedure still valid in such cases? To find an answer to this question we have to compare the results obtained with the solver based on the h.o. expansion to the solver based on the discretization in the coordinate space. To keep the discussion simple, we neglect the pairing and deformation effects, and therefore solve the spherically-symmetric RMF equations. We label the h.o. solver as FT-RMFHO, and compare its results to the coordinate-space FT-RMFBSPL.

First, we have to select an optimal number of h.o. shells  $N_{osc}$  and the oscillator length  $b_0$  in the FT-RMFHO. The box size within the h.o. based solvers is approximately determined as  $R_{box} \approx \sqrt{2N_{osc}}b_0$  [24]. In principle, results should be independent of the oscillator length  $b_0$ . To determine the optimal  $b_0$  we fix the number of shells  $N_{osc}$  and minimize the free energy  $F$ . In this case, we replace the free energy  $F$  by the subtracted free energy  $\bar{F}$  defined as

$$\bar{F} = F_{Nucl+Vap} - F_{Vap}, \quad (6.27)$$

where  $F_{Nucl+Vap(Vap)}$  is the free energy of the Nucl+Vap(Vap) system. In Fig. 6.3 we show the  $(\bar{F}, b_0)$  plot for  $N_{osc} = 20-36$ . Again we choose  $^{202}\text{Sm}$  at  $T = 1.0$  MeV and DD-ME2 interaction. Results are compared with the FT-RMFBSPL (black full line) with  $R_{box} = 30$  fm. We observe that there exists an optimal interval in  $b_0$ , within which the results of the FT-RMFHO are independent of  $b_0$ , and agree with the FT-RMFBSPL results. This interval seems to be larger as the number of h.o. shells is increased, finally abruptly increasing if  $b_0$  is too large. Notice that above  $b_0 > 3$  fm the free energy tends to show oscillations. These are purely artificial and stem from the anti-particle contribution within the RMF theory. To obtain the optimal  $b_0 = \sqrt{\hbar/(m\omega_0)}$  (where  $m$  is the nucleon mass), we use the mass-dependent formula  $\hbar\omega_0 = 41A^{-1/3}$  fm as in Ref. [138]. Results obtained using the formula are indicated by an arrow. We have verified that such a formula works well across the Sm isotopic chain, even at higher temperatures. From this discussion, it seems reasonable to expect good agreement between the FT-RMFHO and FT-RMFBSPL, once the  $b_0$  is optimized.

Now, we select the samarium ( $Z = 62$ ) isotopic chain and consider even-even nuclei for neutron numbers  $N = 100-150$  at a higher temperature of  $T = 2$  MeV. Comparison is performed for

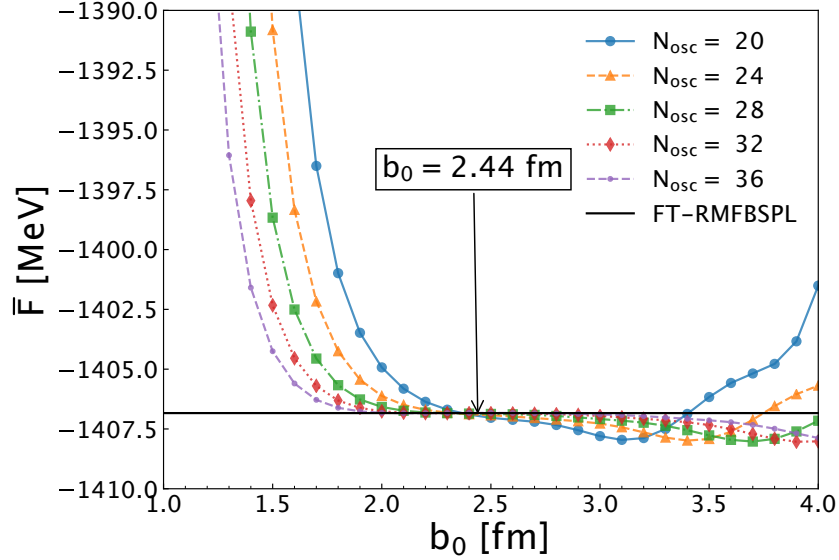


Figure 6.3: Determining the optimal oscillator length  $b_0$  that minimizes the subtracted free energy  $\bar{F}$  for a changing number of h.o. shells  $N_{osc} = 20\text{--}36$ . Also shown is the FT-RMFBSPL result (black straight line), which is independent of  $b_0$ . The arrow indicates the optimal  $b_0$  obtained from  $\hbar\omega_0 = 41A^{-1/3}$  MeV. Results are calculated for  $^{202}\text{Sm}$  at  $T = 1$  MeV using the DD-ME2 interaction.

the FT-RMFHO with  $N_{osc} = 20$  and the FT-RMFBSPL with  $R_{box} = 30$  fm, for the subtracted free energy  $\bar{F}$ , entropy  $\bar{S}$  and neutron chemical potential  $\lambda_n$  in Fig. 6.4(a)-(c), respectively. The agreement between the two solvers is excellent, even considering the fact that only 20 h.o. shells are employed in the FT-RMFHO. Small differences are only visible in the entropy, however, when used to calculate the free energy, they vanish. The neutron chemical potential shows very good agreement across the whole isotopic chain. The latter two are very important in determining the drip lines at finite temperatures. As we will clarify in the next section, at such a high temperature of  $T = 2$  MeV, most of these samarium isotopes are spherical and in a normal state (pairing correlations vanish). Therefore, illustrative calculations performed here are not only for comparison purposes but should also apply to the axially-deformed FT-RHB based on the h.o. expansion. This gives us confidence that the global calculations presented in the next section are credible.

### 6.2.3 Continuum subtraction within the axially-deformed FT-RHB

We want to verify that the continuum subtraction procedure indeed works once applied to the axially-deformed FT-RHB. The optimal quadrupole deformation  $\beta_2$  is obtained by finding a minimum in

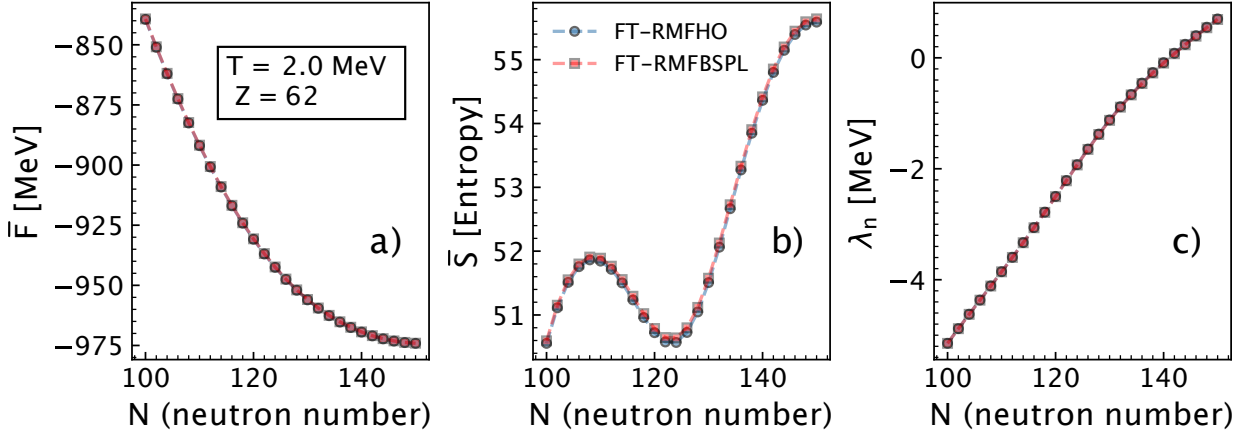


Figure 6.4: The isotopic dependence of the subtracted free energy  $\bar{F}$ , entropy  $\bar{S}$ , and neutron chemical potential  $\lambda_n$  for samarium isotopes ( $Z = 62$ ) at  $T = 2.0$  MeV. Calculations are performed using the FT-RMFHO with  $N_{osc} = 20$  and FT-RMFB SPL with  $R_{box} = 30$  fm employing the DD-ME2 interaction.

the potential energy surface (PES), defined as the  $(F, \beta_2)$  dependence. We choose  $^{210}\text{Gd}$ , which is predicted as a drip-line nucleus (DD-ME2 interaction), and calculate its PES at  $T = 0, 1$  and  $2$  MeV. First, we show the results without the continuum subtraction. Results are shown in Fig. 6.5(a)-(c) for a different number of h.o. shells,  $N_{osc} = 20, 24$  and  $28$ . In Fig. 6.5(a) the minimum configuration converges well already for 20 h.o. shells. The difference between the binding energy of predicted minimum ( $\beta_2 \sim 0.35$ ) between 28 and 20 shells is only around 50 keV. However, as the temperature is increased to 1 MeV in Fig. 6.5(b) the PES does not converge. The minimum is lowered around 1 MeV for additional 4 shells. At  $T = 2$  MeV, in Fig. 6.5(c), the convergence problem is even more obvious, where 4 additional shells shift the minimum by more than 6 MeV.

We obtain the converged results by the BLV prescription which isolates the continuum states contributing to the nuclear vapor and subtracts them from the observable under consideration. Results are shown in Fig. 6.6(a)-(b) and converge well with increasing basis size. As the number of shells is increased from 10 to 28, the free energy is changed at most by 100 keV. Such a result is enough precise to determine the drip lines with precision below that originating from the systematic uncertainty.

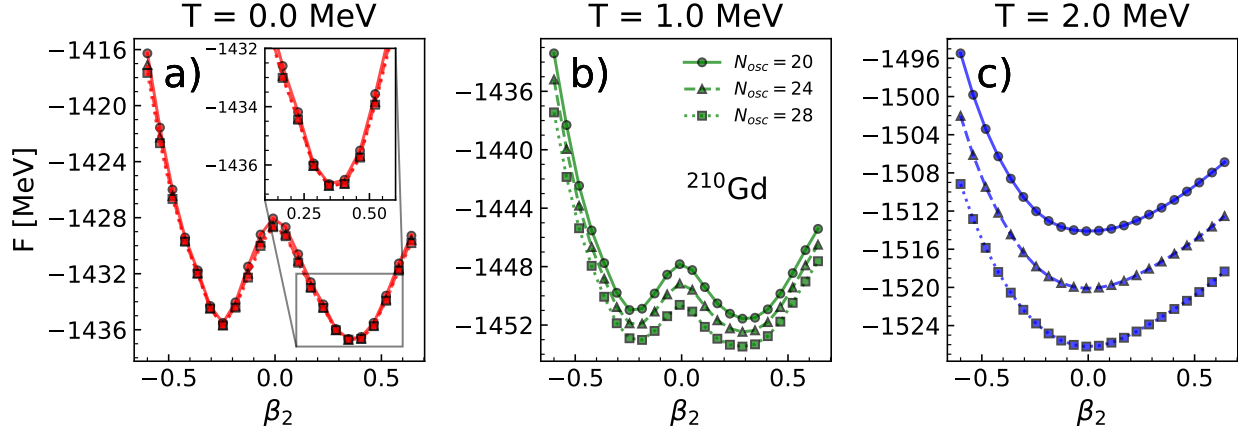


Figure 6.5: The potential energy surface of  $^{210}\text{Gd}$  at  $T = 0$  (a), 1 (b) and 2 MeV (c) calculated using the axially-deformed FT-RHB and  $N_{osc} = 20, 24$  and 28 h.o. shells. No continuum subtraction is considered to demonstrate the convergence issues. The DD-ME2 interaction is employed.

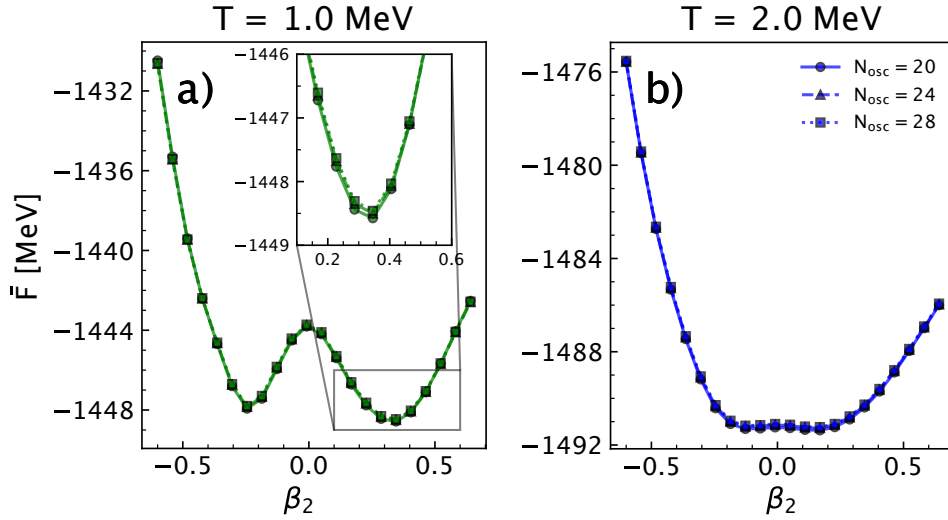


Figure 6.6: Same as in Fig. 6.5 but with the subtracted free energy  $\bar{F}$  calculated using the BLV continuum subtraction.



### 6.3 Results

After properly implementing the continuum subtraction within our model, we perform global calculations across the nuclide chart for different temperatures. In Ref. [35], we have presented calculations for even-even  $8 \leq Z \leq 104$  nuclei for temperatures  $T = 0-2$  MeV. Calculations are performed assuming axially-deformed reflection-symmetric nuclei with time-reversal symmetry. The optimal configuration is obtained by constrained FT-RHB calculation by minimizing the subtracted free energy  $\bar{F}$  with respect to the quadrupole deformation  $\beta_2$ . Calculations start by selecting a mesh of 11 equidistant  $\beta_2$  points between  $\beta_2 = -0.7$  and  $\beta_2 = 0.6$ . Constrained calculations are then performed for the first 20 iterations after which the constraint is lifted, and calculations converge to their local minimum in the PES. No proton-neutron mixing is assumed, meaning that only the isovector  $pp$  interaction is considered. The fermion (and boson) wave functions are expanded in  $N_{osc} = 20$  h.o. shells. Within one iteration the FT-RHB equations are solved twice, once for the Nucl+Vap system and then for Vap system, coupled by the chemical potential subsidiary condition in Eq. (6.24) and Coulomb field in Eq. (6.25). The nuclear landscape of even-even nuclei is determined starting from the two-proton, and terminating at the two-neutron drip line. The drip lines at finite temperature are defined as

$$S_{2n} = \bar{F}(Z, N) - \bar{F}(Z, N - 2), \quad S_{2p} = \bar{F}(Z, N) - \bar{F}(Z - 2, N), \quad (6.28)$$

where  $S_{2n(2p)}$  is the two-neutron(proton) separation energy, and  $\bar{F}(Z, N)$  is the subtracted free energy of a nucleus. Within the BLV subtraction procedure, the ensemble average of an observable  $\langle \mathcal{O}[\bar{\rho}] \rangle_T$  at temperature  $T$ , is a function of the subtracted density  $\bar{\rho}$ . For the relativistic EDFs, where we can distinguish between the scalar ( $\rho_s$ ) and vector ( $\rho_v$ ) densities, the baryonic density is equal to the vector density. Therefore, all observables of interest are expressed from the subtracted vector density  $\bar{\rho}_v$ . First, we are interested in studying the temperature dependence of deformation. The proton(neutron) quadrupole moment is defined as [158]

$$Q_{20}^{p(n)} = \int d^3\mathbf{r} \bar{\rho}_v^{p(n)}(\mathbf{r})(2z^2 - r^2), \quad (6.29)$$

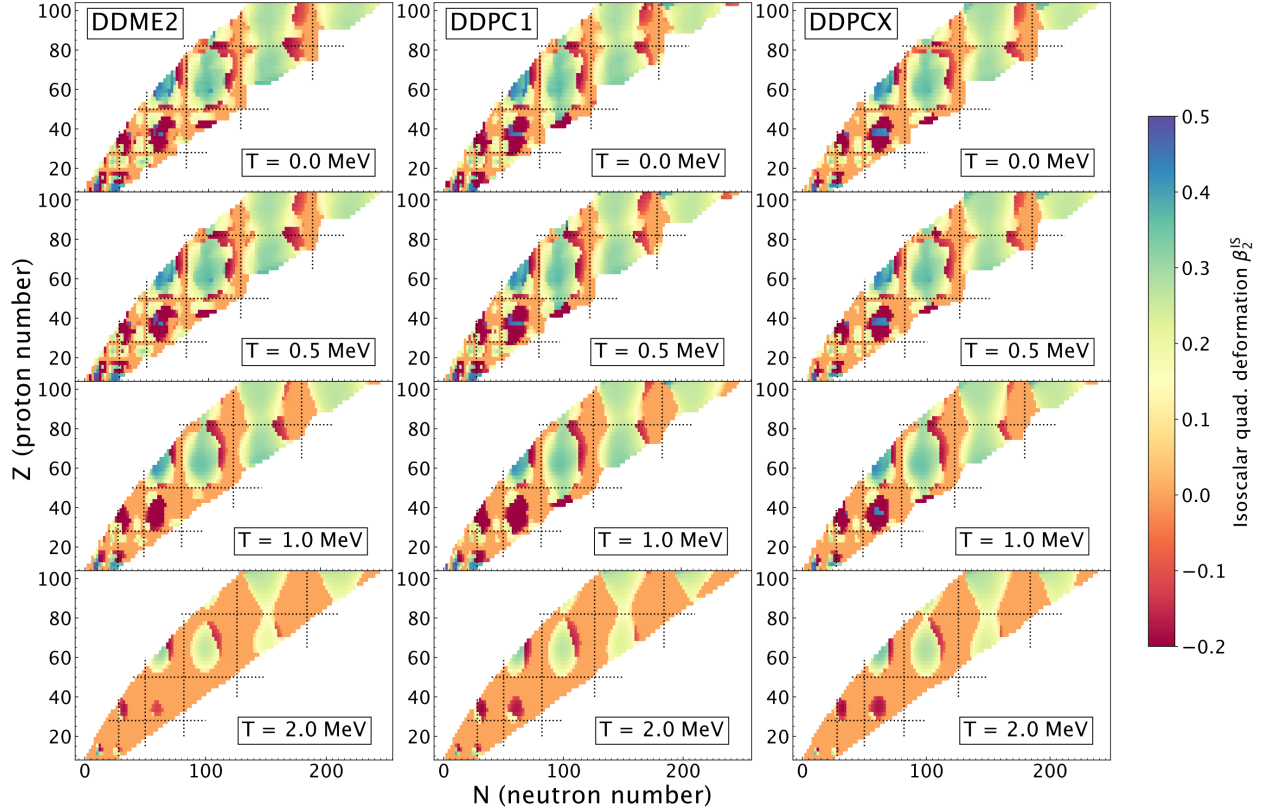


Figure 6.7: The temperature dependence of the isoscalar quadrupole deformation  $\beta_2^{IS}$  across the nuclide chart at  $T = 0, 0.5, 1.0$  and  $2.0$  MeV, calculated with DD-ME2, DD-PC1 and DD-PCX relativistic EDFs.

where  $\bar{\rho}_v^{p(n)}$  is the proton(neutron) subtracted vector density. Instead of expressing the deformation as  $Q_{20}$  we define the dimensionless variable  $\beta_2^{p(n)}$  as [138]

$$\beta_2^{p(n)} = \frac{1}{2} \sqrt{\frac{5}{4\pi}} \frac{3}{4\pi} Z(N) R_0^2 Q_{20}^{p(n)}, \quad (6.30)$$

where  $R_0 = 1.2A^{1/3}$  fm. Using the above expression we can define either the isoscalar quadrupole deformation as  $\beta_2^{IS} = \beta_2^p + \beta_2^n$ <sup>1</sup> and the isovector quadrupole deformation as  $\beta_2^{IV} = \beta_2^n - \beta_2^p$  [158]. In Fig. 6.7 we show the isoscalar quadrupole deformation  $\beta_2^{IS}$  across the nuclide chart for three relativistic EDFs: DD-ME2, DD-PC1, and DD-PCX.

At zero temperature, we observe that most nuclei are deformed in their ground state. Only those

<sup>1</sup>When we write  $\beta_2$  without explicitly mentioning its isospin character, we always assume isoscalar  $\beta_2^{IS}$ .

nuclei with a magic number of nucleons and those in their vicinity are spherical. Between the lines denoting the shell closure numbers, the  $\beta_2^{IS}$  gradually increases until it reaches mid-shell, after which the  $\beta_2^{IS}$  decreases until the magic numbers are reached again. Most nuclei in the nuclide chart display prolate shapes defined as  $\beta_2^{IS} > 0$ . Other, smaller number of nuclei, have oblate shape with  $\beta_2^{IS} < 0$ . We observe that the trends for  $\beta_2^{IS}$  are similar across considered EDFs. At  $T = 0.5$  MeV the deformation properties remain mostly unchanged. Such temperature is not high enough to significantly alter the q.p. structure of most nuclei, apart from those near the neutron drip line. At  $T = 1$  MeV, changes in  $\beta_2^{IS}$  start to be more pronounced, and a significant number of nuclei show spherical shape. Those nuclei which present the shape change are those near the shell closure number. Such shape changes propagate even to mid-shell nuclei where the  $\beta_2^{IS}$  tends to decrease. Islands of prolate shapes start to form, surrounded by spherical shapes and nuclei exhibiting oblate deformation. Finally, at  $T = 2$  MeV, most nuclei are spherical, except those located in mid-shells with initially large deformations. Except for the lightest nuclei considered, we see that all three functionals predict similar temperature evolution of  $\beta_2^{IS}$ .

We conclude that, in general, nuclei transition to spherical configurations once the temperature increases. To further investigate the mechanisms between these shape changes (called the shape phase transitions), in Fig. 6.8(a), we display the temperature evolution of PES in  $^{150}\text{Nd}$  together with the corresponding Nilsson diagram in Fig. 6.8(b), all calculated with the DD-ME2 interaction. The subtracted free energy in Fig. 6.8(a) is calculated relative to the minimum configuration and denoted as  $\Delta\bar{F}$ . In most cases, the PES shows two distinct minima, one from the oblate side and the other from the prolate side. However, for  $^{150}\text{Nd}$ , the PES at zero temperature shows a complicated structure with multiple minima. The optimal  $\beta_2^*$  which minimizes the  $\bar{F}$  is found at  $\beta_2 = 0.29$ . Another minimum at the prolate side is close and located at  $\beta_2 = 0.39$ . The prolate side displays two minima, of which the lowest in energy is the one at  $\beta_2 = -0.22$ . Increasing the temperature to  $T = 0.5$  MeV, no significant changes occur, except that two minima on the prolate side merge into one at  $\beta_2^* = 0.31$ . At  $T = 1$  MeV, both minima get closer to the spherical configuration, while at  $T = 2$  MeV, the PES converges to a spherical minimum, slightly flat around  $\beta_2^* = 0.0$ . In Fig. 6.8(b), we show the temperature evolution of the lowest occupied single-particle Nilsson states for optimal  $\beta_2^*$  up to  $\varepsilon = -30$  MeV. The single-particle energies are obtained by the canonical transformation of the q.p. basis [24]<sup>2</sup>. The Nilsson basis is written in the form  $\Omega^\pi[n_z n_r \Lambda]$ , where the angular

<sup>2</sup>We note that canonical transformation is only an approximation of the q.p. basis at finite temperature. This is because one can not talk about independent q.p. states once the temperature is introduced and the Bloch-Messiah theorem is invalid [58].

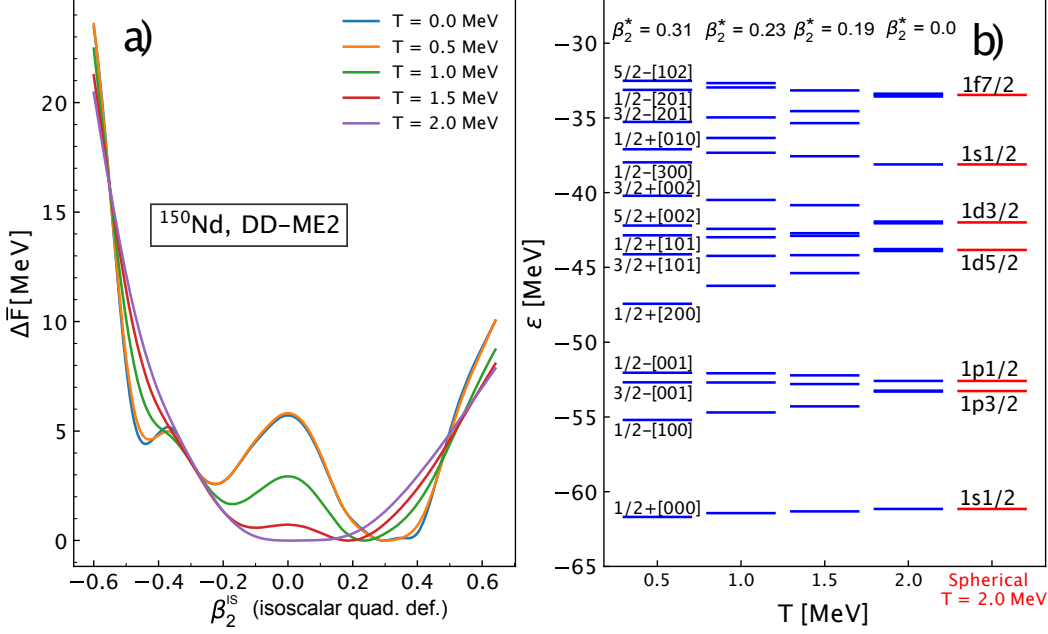


Figure 6.8: (a) The temperature evolution of the potential energy surface (PES) in  $^{150}\text{Nd}$  in the temperature range  $T = 0\text{--}2$  MeV, calculated with the DD-ME2 interaction. The  $\Delta\bar{F}$  represents the relative subtracted free energy with respect to the minimum configuration. (b) The lowest occupied Nilsson states in  $^{150}\text{Nd}$  for the optimal configuration  $\beta_2^*$  for different temperatures, together with the spherical states at  $T = 2$  MeV.

momentum projection  $\Omega$  and parity  $\pi$  were introduced earlier. The  $n_z$  and  $n_r$  represent the quantum numbers in the  $z$  and radial directions, respectively, while  $\Lambda$  is the orbital angular momentum projection. These numbers are not independent, the parity is defined as  $(-)^{\pi} = (-)^{n_z+2n_r+\Lambda}$ , and the angular momentum projection is  $\Omega = m_s + \Lambda$ , where  $m_s$  is the spin projection. The principal quantum number is  $N = n_z + 2n_r + \Lambda$ . At  $T = 0.5$  MeV, we see that the single-particle spectrum is dense. One state in the spherical basis written in the form  $(n, l, j)$  splits into multiple Nilsson states. For instance, the lowest state  $1/2^+[000]$  corresponds to the spherical state  $1s_{1/2}$ . Since  $l = 0$ ,  $\Omega = \pm 1/2$ , because  $\Lambda = 0$ . We consider only  $\Omega > 0$  components due to the time-reversal symmetry. Since  $l = 0$  we have  $\pi = +1$  and only one state  $1/2^+[000]$ . For the principal quantum number  $N = 1$ , we have two spherical orbitals  $1p_{3/2}$  and  $1p_{1/2}$ . Possible projections assuming  $\Omega > 0$  are: (i)  $\Lambda = 0, 1$ , (ii)  $\Omega = 1/2, 3/2$ , and (iii) since  $N = 1$ ,  $(n_z, n_r, \Lambda) \in \{(1, 0, 0), (0, 0, 1)\}$ ,

Table 6.1: Comparison between the spherical and Nilsson basis numbers for a given principal number  $N$ . Degeneracy of each shell in spherical basis is  $2j + 1$ , while the degeneracy in Nilsson basis is 2. Number of nucleons contained in each shell is equal.

Principal number	spherical basis $(n, l, j)$	Nilsson basis $\Omega^\pi [n_z n_r \Lambda]$
$N = 0$	$1s_{1/2}$	$1/2^+ [000]$
$N = 1$	$1p_{3/2}, 1p_{1/2}$	$1/2^- [100], 1/2^- [001], 3/2^- [001]$
$N = 2$	$1d_{5/2}, 2s_{1/2}, 1d_{3/2}$	$1/2^+ [200], 1/2^+ [010], 1/2^+ [101]$ $3/2^+ [101], 3/2^+ [002], 5/2^+ [002]$
$N = 3$	$1f_{7/2}, 2p_{3/2}, 1f_{5/2}$ $2p_{1/2}$	$1/2^- [110], 1/2^- [300], 1/2^- [011]$ $1/2^- [201], 3/2^- [011], 3/2^- [201]$ $3/2^- [102], 5/2^- [102], 5/2^- [003]$ $7/2^- [003]$

giving us three possible states in the Nilsson basis  $1/2^- [100]$ ,  $3/2^- [001]$  and  $1/2^- [001]$ . Following the same procedure, other states can be constructed, each having degeneracy 2. For convenience, we have tabulated the Nilsson levels up to  $N = 3$  in table 6.1. From Fig. 6.8(b), we observe that deformation breaks the degeneracy between different Nilsson states. As the temperature increases, the separation between the Nilsson levels decreases, and they seem to be more attracted to each other. Finally, at  $T = 2$  MeV, the degeneracy is restored, and the states in the Nilsson basis converge to those in the spherical basis. Therefore, a shape phase transition is related to degeneracy restoration between the Nilsson levels of the axially-deformed oscillator. Such a description gives a microscopic justification of observations in Fig. 6.8(a) and Fig. 6.7.

An insightful way to visualize the deformation is by showing the total subtracted vector density  $\rho_v$  at different temperatures. To this aim, we select  $^{180}\text{Gd}$  that has an oblate shape in its ground state, and  $^{210}\text{Gd}$  with a prolate shape. The density plots for the optimal deformation  $\beta_2^*$  are shown in Fig. 6.9 at  $T = 0.5, 1$  and  $2$  MeV. In addition, we also show the PES constrained with respect to  $\beta_2^{IS}$  with the optimal deformation  $\beta_2^*$  indicated. We know that at  $T = 0.5$  MeV temperature does not influence PES significantly, while the PES of  $^{210}\text{Gd}$  is relatively simple, displaying one distinct minimum from the oblate, and the other from the prolate side,  $^{180}\text{Gd}$  shows more complicated behavior, with prolate configuration minimizing the subtracted free energy  $\bar{F}$ . As the temperature increases, the PES smooths out in both cases, with shapes being reduced to slightly more spherical. At  $T = 2$  MeV,  $^{180}\text{Gd}$  attains a spherical shape with a relatively flat minimum configuration. On the other hand,  $^{210}\text{Gd}$  still has an oblate shape with  $\beta_2^* \approx 0.15$ . However, the energy difference between the prolate, spherical, and oblate configurations is quite small because the PES flattens out as the

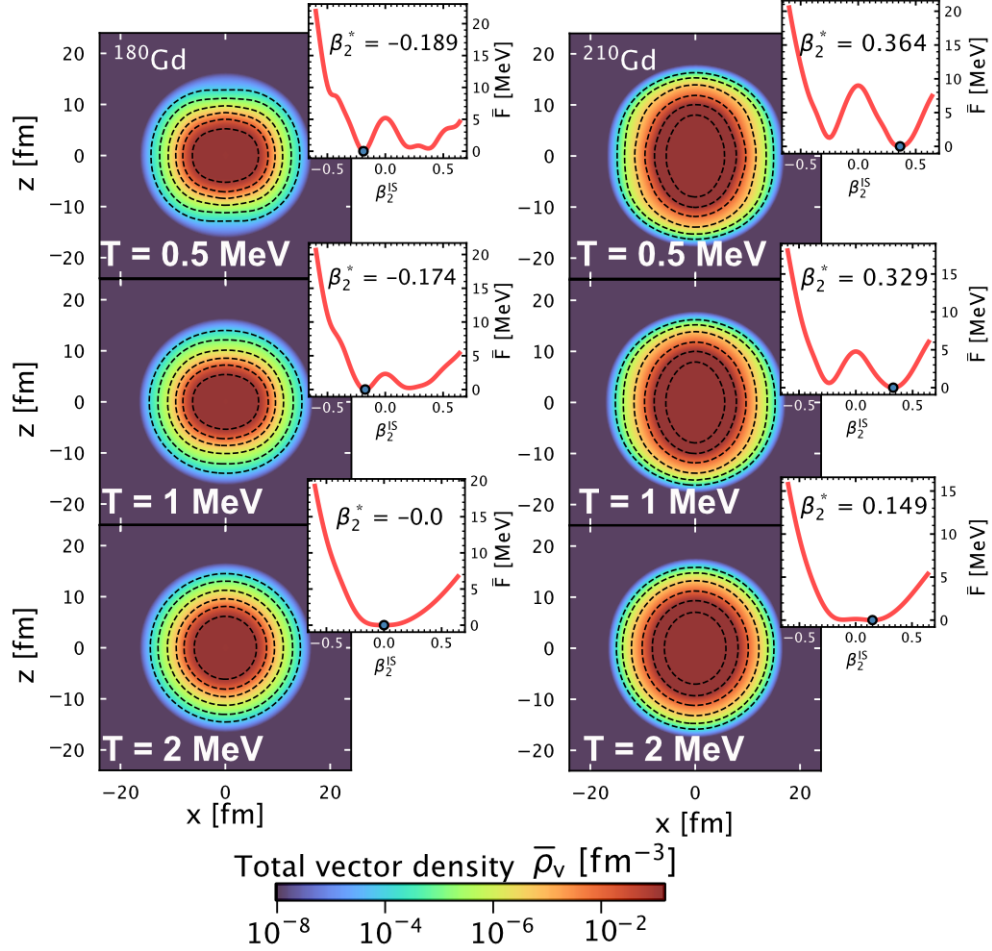


Figure 6.9: The total subtracted vector density  $\bar{\rho}_v$  for  $^{180}\text{Gd}$  and  $^{210}\text{Gd}$  at  $T = 0.5, 1$  and  $2$  MeV for optimal  $\beta_2^*$ . Insets show the potential energy surfaces constrained with respect to the isoscalar quadrupole deformation  $\beta_2^{IS}$  for each density plot.

temperature increases.

The quantity which demonstrates finite temperature and deformation effects on nuclei is entropy. It is not an observable attainable from experiments, and its study is of theoretical significance. The entropy measures the occupation of single-(quasi)particle orbitals and strongly correlates with the underlying microscopic structure. Within the FT-RHB it is calculated as [25]

$$S = -2 \sum_i g_i [f_i \ln f_i + (1 - f_i) \ln(1 - f_i)], \quad (6.31)$$

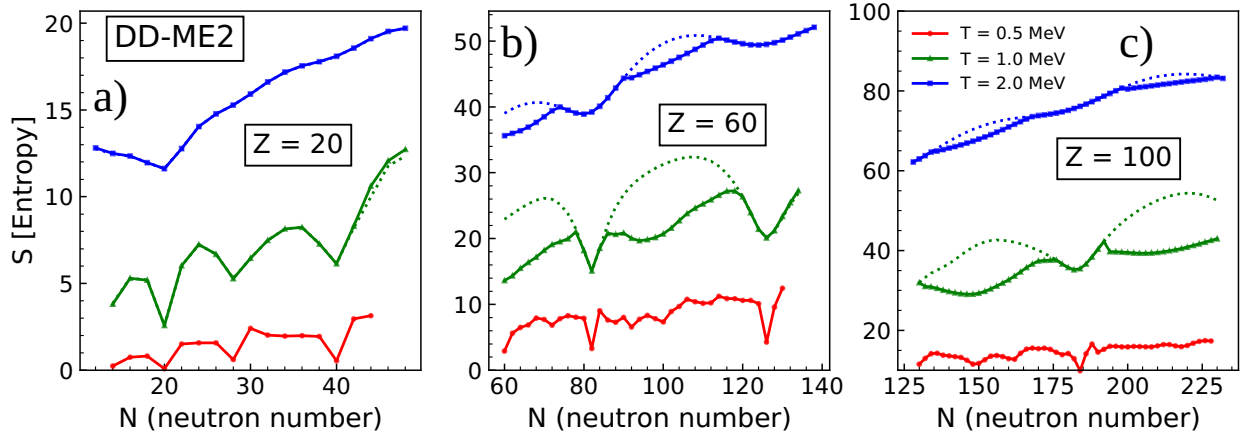


Figure 6.10: The isotopic dependence of entropy for  $Z = 20, 60$  and  $100$  for temperatures  $T = 0.5, 1$  and  $2$  MeV. The solid line denotes calculations with the axially-deformed FT-RHB, while the dotted line represents spherical FT-RHB (only shown for  $T = 1$  and  $2$  MeV).

where  $f_i = (1 + e^{\beta E_i})^{-1}$  are the Fermi-Dirac factors, from which we observe that it is maximized for mid-shell nuclei and minimized for the closed-shell fully occupied nuclei. For axially-deformed nuclei  $g_i = 2$ . In Fig. 6.10(a)-(c), we demonstrate the isotopic dependence of entropy for even-even nuclei in the selected chains at  $T = 0.5, 1$  and  $2$  MeV. The full line represents calculations with axially-deformed FT-RHB, while the dotted line stands for spherical FT-RHB calculations. At  $T = 0.5$ , we observe that for all isotopic chains, the entropy has an irregular temperature dependence with noticeable dips corresponding to  $N = 20, 28,$  and  $40$  in calcium,  $N = 82,$  and  $126$  in neodymium and  $N = 186$  in fermium. Of course, these numbers correspond to shell closure. At  $T = 1$  MeV, the entropy increases for all isotopic chains, mainly due to finite-temperature scattering above the Fermi level. The dips corresponding to shell closure are clearly visible. For the calcium chain, the difference between the spherical and deformed calculations is almost negligible owing to the fact that at  $T = 1$  MeV, most calcium isotopes are spherical. On the other hand, we observe a large discrepancy between the mid-shell nuclei results for neodymium. The results obtained with the spherical calculations follow a simple structure where the entropy is maximal for mid-shell nuclei and overestimate the deformed calculations. Since the deformation effects induce the degeneracy splitting between different Nilsson states, there are more states among which the occupation scatters. This scattering leads to the reduction of entropy compared to the spherical calculation. A similar trend is also noticed for the fermium chain. By increasing the temperature to  $T = 2$  MeV, the differences between the spherical and deformed calculations are significantly reduced. The entropy

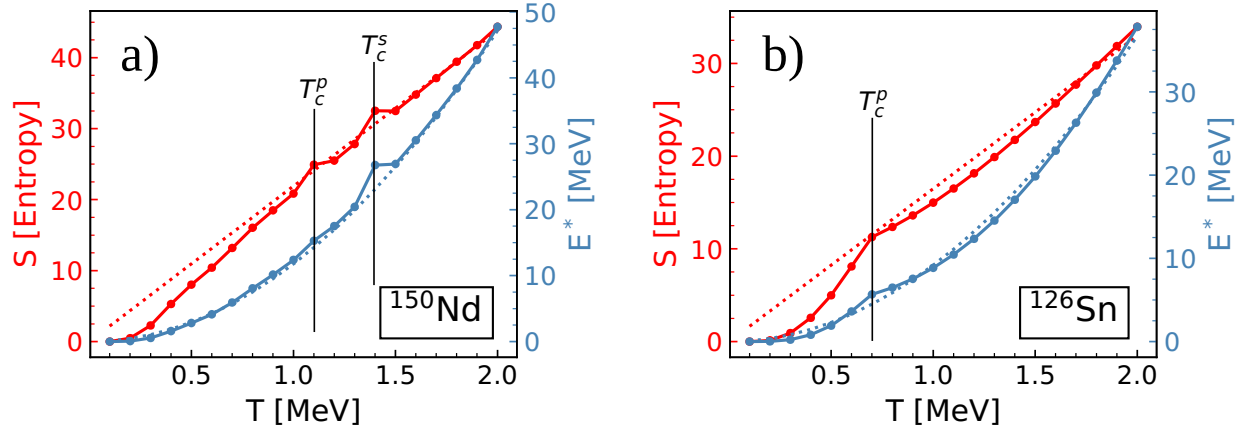


Figure 6.11: The temperature evolution of entropy  $S$  (red) and excitation energy  $E^*$  (blue) for  $^{150}\text{Nd}$  (a) and  $^{126}\text{Sn}$  (b). The dotted lines show the fitting result of  $T \geq 1.5$  MeV points on the Fermi gas model. Calculations are performed with the axially-deformed FT-RHB with the DD-ME2 interaction.

increases, and the dips stemming from the shell closure reduce. This reduction relates to the fact that the energy supplied by the environment is high enough to bridge the shell gaps, and shell effects diminish. For instance, the shell gap at  $N = 40$  in calcium nearly vanishes, while the fermium isotopes show almost no dips in the isotopic entropy dependence. In conclusion, we demonstrated that entropy probes the underlying microscopic structure of the nuclei.

Unlike entropy, the excitation energy  $E^*$  is an observable directly attainable from experiments [177]. It is defined as the total energy difference of the nucleus at temperature  $T$  and zero temperature,  $E^* = E(T) - E(T = 0)$ . The previous discussion on entropy is closely related to the discussion on excitation energy. In Fig. 6.11(a)-(b), we study the temperature dependence of entropy and excitation energy in  $^{150}\text{Nd}$  (mid-shell) and  $^{126}\text{Sn}$  (shell closure). We observe that both entropy and excitation energy increase with temperature, however, with different functional dependence. Furthermore, they both display visible kinks for certain temperatures. For  $^{150}\text{Nd}$ , two such kinks are visible, first at  $T_c^p \approx 1.1$  MeV and second at  $T_c^s \approx 1.4$  MeV, corresponding to the critical temperature of pairing and shape phase transitions. On the other hand,  $^{126}\text{Sn}$  shows only a pairing phase transition at  $T_c^p \approx 0.7$  MeV. Namely, due to its proton shell closure, it is predicted as spherical at all temperatures and has no phase shape transition. We observe that for temperatures above the phase transitions, entropy and excitation energy behave rather regularly. It is interesting to compare their behavior to that of an idealized Fermi gas. The Fermi gas model of a



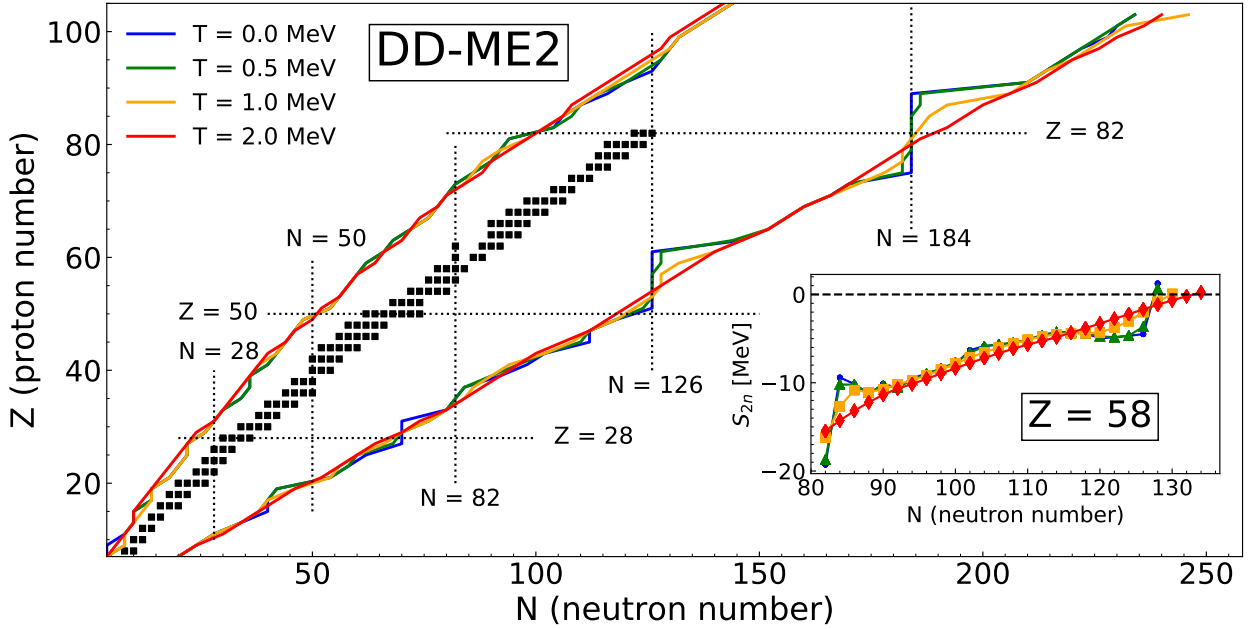


Figure 6.12: Temperature evolution of the two-neutron and two-proton drip lines for even-even  $8 \leq Z \leq 104$  nuclei for temperatures  $T = 0\text{--}2$  MeV. Results are calculated with the relativistic DD-ME2 EDF. Black squares denote the even-even stable nuclei [159]. Proton and neutron shell closure numbers are explicitly denoted. Inserted figure shows two-neutron separation energy  $S_{2n}$  with increasing neutron number  $N$  for cerium isotopic chain ( $Z = 58$ ) at temperatures  $T = 0, 0.5, 1.0$  and  $2.0$  MeV (using same color labels as in the main plot). Black dashed line denotes the drip-line condition  $S_{2n} = 0$ .

nucleus predicts linear dependence of entropy,  $S = 2aT$ , and for excitation energy  $E^* = aT^2$  [177], where the proportionality constant  $a$  depends on the density of states as well as the number of nucleons [183, 184]. In Fig. 6.11(a)-(b), we show the corresponding fit to Fermi gas model dependence for  $T \geq 1.5$  MeV. The fitted values of the level density parameter  $a$ , both for entropy and excitation energy, agree within 10%. Such a result indicates that a simple Fermi gas model reasonably describes nuclei at high temperatures. It confirms the fact that shell effects diminish as the temperature increases.

Finally, we turn our discussion to the temperature dependence of the nuclear drip lines. How much is the nuclear landscape influenced by the finite-temperature effects? In Figure 6.12 we display the two-neutron(proton) drip lines defined by Eq. (6.28) for temperatures  $T = 0, 0.5, 1.0$  and  $2.0$  MeV. Calculations are performed with the DD-ME2 relativistic EDF. One immediately observes that the temperature has an effect on predicted drip lines. Two-neutron drip line is more

influenced by the finite-temperature effects compared to the two-proton drip line, as one would expect. Nuclei in the vicinity of the neutron drip line populate higher-energy levels and are more easily coupled with the states in the particle continuum. On the other hand, such coupling is reduced for proton states due to the increasing height of the Coulomb barrier with increasing proton number. Already at  $T = 0.5$  MeV temperature has a slight effect on drip lines, mainly near neutron shell closures around  $N = 126$  and  $N = 184$ . Although a temperature of 0.5 MeV is low from the nuclear structure standpoint, it is enough to create a tail in the density profile for weakly-bound nuclei, which causes results to diverge with increasing basis size. This is where a prescription to treat the continuum within the FT-RHB theory becomes necessary. As the temperature increases to  $T = 1$  MeV, changes in drip lines become more pronounced. At this temperature most nuclei transition from the superfluid to the normal state due to the pairing collapse, which removes pairing correlations. Furthermore, nuclear deformation tends to decrease with temperature, leading to a transition from the deformed to the spherical state [cf. Fig. 6.7]. However, at  $T = 1$  MeV we find a significant number of nuclei still exhibiting the deformation effects. Shell effects at  $N = 126$  and  $N = 184$  shell closure are washed out since with additional energy in the environment nucleons can bridge the gaps between the neutron shells. At  $T = 2$  MeV shell effects are completely washed out and drip lines are well described by a straight line. Since the shell effects are absent, the free energy takes the form of  $F \sim aT^2$ , where  $a$  is the level density parameter that can be estimated with the use of Bethe's formula [177]. This leads to qualitative agreement of our results at  $T = 2$  MeV with calculations obtained from simpler models such as the hot liquid-drop model [185]. To investigate the details behind the finite-temperature effects on two-neutron drip line in the inset of Fig. 6.12 we show the two-neutron separation energy  $S_{2n}$  [cf. Eq. (6.28)] for even-even isotopes of cerium ( $Z = 58$ ). Calculations with the DD-ME2 interaction predict  $^{184}\text{Ce}$  to be a drip-line nucleus. Due to shell closure at  $N = 126$  we observe a sharp increase in  $S_{2n}$  at  $T = 0$  (blue line) and  $T = 0.5$  MeV (green line). As the temperature increases and nucleons bridge the shell gap, a sharp decrease in  $S_{2n}$  is mediated, and  $S_{2n}$  becomes almost linear, leading to the extension of the drip line. Consequently, at  $T = 1$  MeV  $^{186}\text{Ce}$  is a drip-line nucleus and at  $T = 2$  MeV it is  $^{190}\text{Ce}$ . Such a result leads us to the conclusion that the neutron drip line tends to extend towards increasing neutron number at higher temperatures. The same result was obtained in Refs. [185, 186], albeit with a much simplified model.

To estimate the systematic uncertainties in predicting the two-nucleon drip lines at finite temperature it is instructive to compare results obtained using various EDF parametrizations. In Figure 6.13

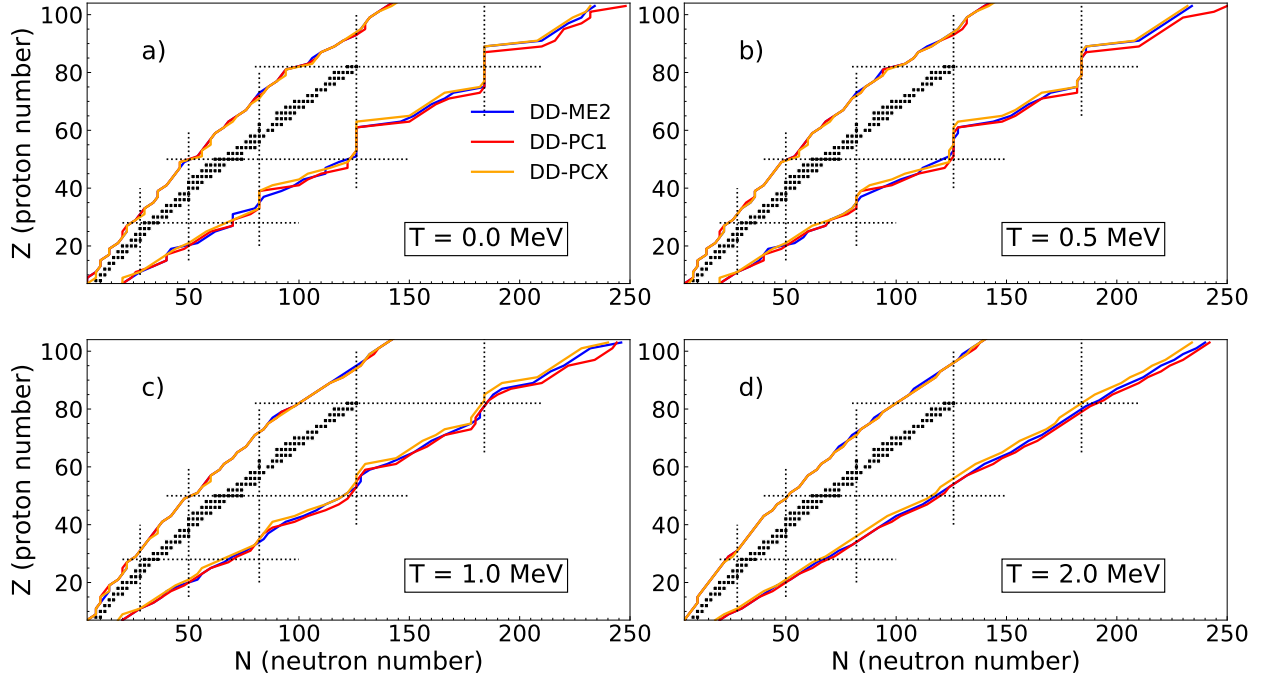


Figure 6.13: (a)-(d) Two-neutron and two-proton drip lines calculated at  $T = 0, 0.5, 1.0$  and  $2.0$  MeV using three different parameterizations of the relativistic EDF: DD-ME2 (blue), DD-PC1 (red) and DD-PCX (orange).

Table 6.2: Number of even-even nuclei between the two-proton and two-neutron drip line in the range  $8 \leq Z \leq 104$ , for DD-ME2, DD-PC1 and DD-PCX functionals at temperatures  $T = 0, 0.5, 1.0$  and  $2.0$  MeV.

$T$ [MeV]	DD-ME2	DD-PC1	DD-PCX
0.0	1623	1671	1565
0.5	1618	1673	1562
1.0	1655	1695	1572
2.0	1681	1716	1588

(a)-(d) we show the two-nucleon drip lines calculated with three relativistic EDFs: DD-ME2 (blue), DD-PC1 (red) and DD-PCX (orange) at  $T = 0, 0.5, 1.0$  and  $2.0$  MeV. Results for the two-proton drip line agree reasonably well between different functionals, therefore, we focus on the differences in the two-neutron drip line. In Fig. 6.13(a), at zero-temperature, moderate differences are visible between the employed functionals. In general, the DD-PCX tends to predict the two-neutron drip line at a lower number of neutrons  $N$ . The two-neutron drip lines calculated with the DD-ME2 and

DD-PC1 functionals tend to be similar up to  $Z \sim 82$ . For  $Z > 82$  two-neutron drip line predicted by the DD-PCX and DD-ME2 is consistent, while the DD-PC1 predicts more neutron-rich nuclei within the drip line. As the pairing interaction decreases in strength in Fig. 6.13(b) at  $T = 0.5$  MeV, differences in the two-neutron drip line tend to be more related to the particle-hole channel of the mean-field Hamiltonian. Furthermore, the two-neutron drip line becomes smoother around the neutron shell closure. At  $T = 1$  MeV in Fig. 6.13(c), pairing correlations have mostly vanished and shell structure around  $N = 126$  and  $N = 184$  is almost washed out. A distinction between, on one hand, the DD-PCX, and on the other hand, DD-PC1 and DD-ME2 is now more pronounced. Two-neutron drip line predicted by the DD-PCX interaction is, for almost all  $Z$ , less neutron-rich compared to the DD-PC1 and DD-ME2 two-neutron drip lines. In Fig. 6.13(d) at  $T = 2.0$  MeV, neutron drip line with all three functionals assumes almost a linear form. However, the slopes of these lines are different, due to the different structure of the mean-field among functionals. The DD-PCX two-neutron drip line is again less neutron-rich compared to the DD-ME2 and DD-PC1 drip lines, which predict a more consistent drip line. To further elaborate on the differences between functionals, in Tab. 6.2 we show number of even-even nuclei within the drip lines for temperatures shown in Fig. 6.13. If  $N_{nucl}$  denotes the number of even-even nuclei between the drip lines, then it can be inferred that  $N_{nucl}(\text{DD-PC1}) > N_{nucl}(\text{DD-ME2}) > N_{nucl}(\text{DD-PCX})$ , for all studied temperatures. This means that at  $T = 2$  MeV, the DD-ME2 functional predicts roughly 100 even-even nuclei more compared to the DD-PCX, which will decay by the equilibrated nucleon evaporation (nuclei between the drip lines). Overall, the number of even-even nuclei between the drip lines at  $T = 2$  MeV, compared to zero-temperature, increases by 58 for DD-ME2, 45 for DD-PC1, and 23 for DD-PCX functional. It is important to stress that finite-temperature effects on the two-neutron drip line are larger than the corresponding systematic uncertainties. In Ref. [35], in addition to the systematic, we have also studied the statistical uncertainties and demonstrated that their influence of the drip line is at most equal to that of systematic uncertainties.

# Chapter 7

## The axially-deformed pnQRPA

In Chapter 3, we demonstrated the basics of the pnQRPA equations assuming spherical symmetry. It is advantageous to use the fact that equations decouple based on the angular momentum and parity  $J^\pi$  blocks once the proper angular momentum coupling is performed. The angular momentum coupling leads to a reasonable dimension of the model space requiring only moderate computational resources. We have applied spherical pnQRPA to study spin-isospin excitations in tin isotopes in Ref. [30]. Since these nuclei have proton shell closed at  $Z = 50$  and are located near the  $N = 82$  neutron magic number, they are spherical or near spherical in their ground state. However, most nuclei discovered so far are axially deformed [159], requiring an extension of the model. The calculations in the axial geometry are significantly more complicated than the spherical calculations. First of all, the dimension of the model space is much larger in comparison to the spherical geometry, since no angular momentum coupling to  $J^\pi$  blocks can be performed. However, in axial deformation, the angular momentum projection  $K$  is still a good quantum number, and if we also consider reflection-symmetric shapes, the pnQRPA equations can be decoupled to  $K^\pi$  blocks. Instead of diagonalizing the pnQRPA matrix for all 2 q.p. excitations, we employ the linear response formalism. In combination with the point-coupling functionals, which have a separable form of the residual interaction, together with the separable pairing interaction, one can achieve a better scalability of the linear response equations. Therefore, the linear response equations can be solved in the reduced space determined by the number of separable terms as demonstrated in Sec. 3.1.

Due to high computational costs, most calculations performed up to date for deformed nuclei assume schematic models, usually with simple separable interactions. Such models have been

applied to study the rotational excitations [75], spin-isospin excitations, and subsequent calculations of  $\beta$ -decay half-lives [144, 187, 188], including the double  $\beta$ -decay in both  $2\nu$  [189, 190] and neutrinoless modes [191]. Although based on relatively simple interactions, such calculations lead to important discoveries concerning the impact of deformation on observables of interest. As computing power and numerical techniques were improved, more sophisticated implementations of the pnQRPA based on the EDF theory could be developed. On the one hand, we have approaches based on the matrix pnQRPA equations, which require diagonalizing large matrices [80, 81, 192–194]. On the other hand, implementations based on the finite-amplitude method (FAM), where one avoids the diagonalization, and solves the equations of motion for each excitation energy, were presented in Refs. [195, 196]. The FAM method has been also applied to spin-isospin excitations but only with non-relativistic EDFs in Refs. [77–79]. Concerning the relativistic EDFs, approaches based on the FAM were developed in Refs. [197, 198] and used to obtain the electric response of axially-deformed nuclei [199]. To date, there are no calculations with relativistic EDFs applied to spin-isospin excitations in deformed nuclei. Therefore, our motivation in this chapter is to develop a pnQRPA solver in axial geometry based on the relativistic EDFs.

This chapter is organized as follows. First, we introduce the axially-deformed pnQRPA formalism and present the calculation techniques both for external field and residual interaction matrix elements in Sec. 7.1. A proper transformation from the single-particle space to the q.p. space is performed without angular momentum coupling. We present a numerical method to obtain the reduced response used to calculate the strength function in Sec. 7.1.4. Secondly, we perform numerical tests of our axially-deformed pnQRPA by comparing it to the spherical pnQRPA from Sec. 3.1, both at zero and finite temperature. After properly testing the model calculations and determining the optimal basis size for the nuclei of interest, we present the calculation of the Gamow-Teller and Fermi transitions of particular even-even  $pf$ -shell nuclei in Sec. 7.3. Calculations are then benchmarked against existing experimental data. In Sec. 7.4, we also perform model calculations of  $GT^+$  strength in  $^{56}\text{Fe}$  by including finite-temperature effects up to  $T = 2$  MeV. Finally, in Sec. 7.5, we study the influence of deformation on the  $\beta$ -decay half-lives, assuming allowed approximation, and compare the results with the available experimental data.

## 7.1 Theoretical formalism

The basics of the pnRQRPA with spherical symmetry are introduced in Chapter 3. Here, we provide the extensions to the axially-deformed nuclei. The pnRQRPA equations keep the same structure, however, the underlying expressions have to be changed. The work presented here is established on the axially-deformed RHB solver in the h.o. basis from Ref. [138]. The theory presented in Chapter 3 is based on wave functions in the coordinate space, therefore, at some point, we have to transform from the h.o. basis to the coordinate space basis. Working in the proton-neutron basis, the set of indices  $\{\pi, \nu\}$  correspond to the q.p. basis, while the set  $\{p, n\}$  is in the single-particle basis. Indices  $\pi(p)$  label the proton states, while the  $\nu(n)$  label the neutron states. The single-particle basis is the basis of the axially-deformed harmonic oscillator. We abbreviate  $k \equiv \{n_z, n_r, \Lambda, m_s\}$ , corresponding to the quantum numbers of the axially-deformed oscillator [cf. Sec. 6.1]. To distinguish between proton and neutron states, we label the single-particle basis as  $k \equiv \{n_z^k, n_r^k, \Lambda^k, m_k\}$ , where  $k \in \{n, p\}$ . The single-particle wave function is therefore given by

$$\Phi_k(r, z, \phi, m_p) = \underbrace{\phi_{n_z^k}(z)\phi_{n_r^k}^{\Lambda^k}(r)}_{R_k(r, z)} \frac{1}{\sqrt{2\pi}} e^{i\phi(\Omega_k - m_k)} \chi_{1/2m_k}, \quad (7.1)$$

where we have introduced  $R_k(r, z) \equiv \phi_{n_z^k}(z)\phi_{n_r^k}^{\Lambda^k}(r)$ . The  $z$ -projection of the angular momentum operator is  $\Omega_k$ , the orbital angular momentum projection is  $\Lambda_k$  and  $m_k$  is the spin projection, with  $\Lambda_k = \Omega_k - m_k$ . By assuming the time-reversal symmetry, the time-reversed single-particle oscillator wave function is

$$\Phi_{\bar{k}} = R_k(r, z) \frac{1}{\sqrt{2\pi}} e^{-i(\Omega_k - m_k)\phi} (-)^{1/2 - m_k} \chi_{1/2 - m_k}, \quad (7.2)$$

where  $\Phi_{\bar{k}} = \hat{T}\Phi_k$ ,  $\hat{T}$  being the time-reversal operator defined in Sec. 6.1. Since we are working in the relativistic formalism, we also have to introduce in the wave function the lower components of the single-particle wave functions

$$\Psi_k \equiv \begin{pmatrix} \Phi_k(r, z) \\ i\Phi_{\bar{k}}(r, z) \end{pmatrix} = \begin{pmatrix} R_k(r, z) \frac{1}{\sqrt{2\pi}} e^{i\phi(\Omega_k - m_k)} \\ iR_{\bar{k}}(r, z) \frac{1}{\sqrt{2\pi}} e^{i\phi(\Omega_k - m_k)} \end{pmatrix} \chi_{1/2m_k}, \quad (7.3)$$

where  $\tilde{k}$  labels the h.o. quantum numbers of the lower components. The corresponding time-reversed wave function is

$$\Psi_{\tilde{k}} = \begin{pmatrix} \Phi_{\tilde{k}}(r, z) \\ -i\Phi_{\tilde{k}}(r, z) \end{pmatrix} = \begin{pmatrix} R_k(r, z) \frac{1}{\sqrt{2\pi}} e^{-i\phi(\Omega_k - m_k)} \\ -iR_{\tilde{k}}(r, z) \frac{1}{\sqrt{2\pi}} e^{i\phi(\Omega_k - m_k)} \end{pmatrix} (-)^{1/2 - m_k} \chi_{1/2 - m_k}. \quad (7.4)$$

In the axial geometry, the pnQRPA equations cannot be organized according to  $J^\pi$  blocks, defined by the total angular momentum  $J$  and parity  $\pi$ . However, since the  $K \equiv J_z$  component of the angular momentum still commutes with the nuclear Hamiltonian, one can show that the pnQRPA equations are block diagonal in different  $K$  blocks. Furthermore, if we assume reflection-invariance so that the nuclear Hamiltonian commutes with the parity operator  $\hat{\Pi}$ , the pnQRPA equations separate into  $K^\pi$  blocks [200]. Therefore, the q.p. pairs within the axially-deformed pnQRPA are selected based on

$$K = \Omega_p - \Omega_n, \quad \pi = \pi_p \times \pi_n, \quad (7.5)$$

where both the states  $k$  ( $\Omega_k > 0$ ) and the time-reversed states  $\tilde{k}$  ( $\Omega_k < 0$ ) have to be explicitly considered. Of course, the dimension of the pnQRPA equation stemming from condition (7.5) is much larger than the spherical pnQRPA equation. Furthermore, explicit consideration of the time-reversed states is required, which complicates the expressions for matrix elements.

We consider either the Fermi ( $J^\pi = 0^+$ ) or the Gamow-Teller ( $J^\pi = 1^+$ ) external field operators. For the Fermi transitions the  $K = 0$  mode is only possible, while for the Gamow-Teller we have  $K = 0, \pm 1$ . The modes  $K = 1$  and  $K = -1$  are degenerate and therefore it is enough to calculate only the  $K = 1$  mode.

In the following, we separately discuss how to calculate the matrix elements of the external field operator, *particle-hole* residual interaction, and the *particle-particle* residual interaction. Lastly, we transform from the single-particle to the q.p. basis and make a connection with the linear response formalism of Sec. 3.1.

### 7.1.1 External field matrix elements

The external field matrix element is defined as

$$\langle p | F_{JK} | n \rangle = \sum_{m_p, m_n} \int r dr dz d\phi [\Psi_p^\dagger F_{JK} \Psi_n], \quad (7.6)$$



where due to the time-reversal symmetry we have to consider 4 combinations of pairs:  $pn$ ,  $p\bar{n}$ ,  $\bar{p}n$  and  $\bar{p}\bar{n}$ . In the following, let's assume the Gamow-Teller form of the external field operator  $F_{1K} \equiv \sigma_{1K}$  so that the  $pn$  matrix element is

$$\langle p|F_{1K}|n\rangle = \Psi_p^\dagger \sigma_{1K} \Psi_n = \begin{pmatrix} \Phi_p^\dagger & -i\Phi_{\bar{p}}^\dagger \end{pmatrix} \begin{pmatrix} \sigma_{1K} & 0 \\ 0 & \sigma_{1K} \end{pmatrix} \begin{pmatrix} \Phi_n \\ i\Phi_{\bar{n}} \end{pmatrix} = \Phi_p^\dagger \sigma_{1K} \Phi_n + \Phi_{\bar{p}}^\dagger \sigma_{1K} \Phi_{\bar{n}}. \quad (7.7)$$

The single-particle matrix elements can be evaluated as

$$\Phi_p^\dagger \sigma_{1K} \Phi_n = \underbrace{\sqrt{3}C_{1/2m_n 1K}^{1/2m_p}}_{\text{spin part}} \underbrace{\delta_{\Omega_p - \Omega_n, K}}_{\phi \text{ integral}} \underbrace{\int r dr dz R_p(r, z) R_n(r, z)}_{\text{radial part}}, \quad (7.8)$$

which is decomposed into the spin part, angular part, and radial integral. Notice that the  $\phi$ -integral part is nothing but the pair selection condition in Eq. (7.5). The analogous expression applies for  $\Phi_{\bar{p}}^\dagger \sigma_{1K} \Phi_{\bar{n}}$ . The radial integral reduces to the orthonormality condition and the matrix element is

$$\langle p|F_{1K}|n\rangle = \sqrt{3}C_{1/2m_n 1K}^{1/2m_p} \delta_{\Omega_p - \Omega_n, K} (\delta_{n_z^p, n_z^n} \delta_{n_r^p, n_r^n} + \delta_{\bar{n}_z^p, \bar{n}_z^n} \delta_{\bar{n}_r^p, \bar{n}_r^n}). \quad (7.9)$$

Using the time-reversal property from Eq. (7.4) we can evaluate external field matrix elements for  $pn$ ,  $p\bar{n}$  and  $\bar{p}\bar{n}$  transition

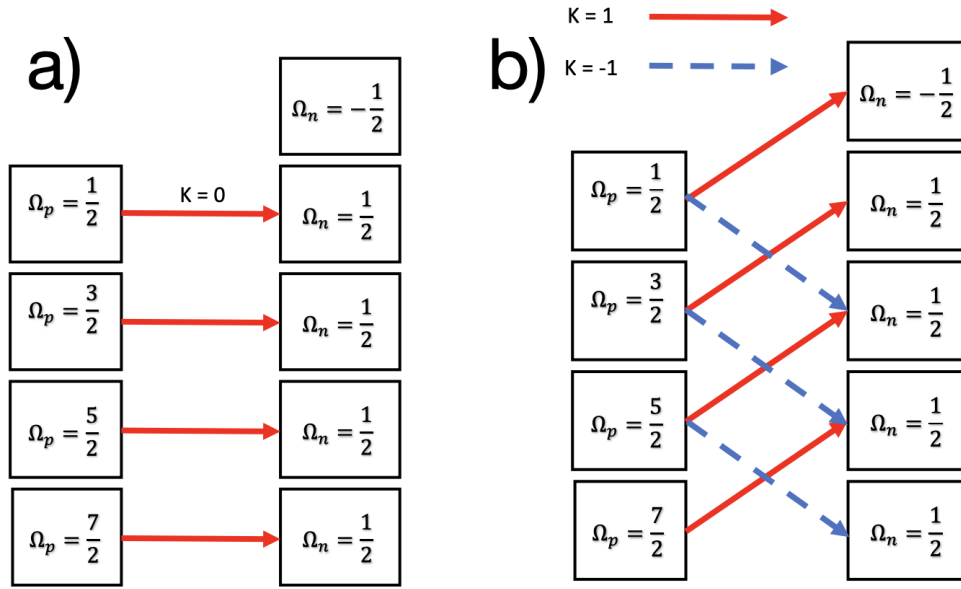
$$\begin{aligned} \langle p|F_{1K}|\bar{n}\rangle &= \sqrt{3}C_{1/2-m_n 1K}^{1/2m_p} \delta_{\Omega_p + \Omega_n, K} (-)^{1/2-m_n} (\delta_{n_z^p, n_z^n} \delta_{n_r^p, n_r^n} - \delta_{\bar{n}_z^p, \bar{n}_z^n} \delta_{\bar{n}_r^p, \bar{n}_r^n}), \\ \langle \bar{p}|F_{1K}|n\rangle &= \sqrt{3}C_{1/2m_n 1K}^{1/2-m_p} \delta_{\Omega_p + \Omega_n, -K} (-)^{1/2-m_p} (\delta_{n_z^p, n_z^n} \delta_{n_r^p, n_r^n} - \delta_{\bar{n}_z^p, \bar{n}_z^n} \delta_{\bar{n}_r^p, \bar{n}_r^n}), \\ \langle \bar{p}|F_{1K}|\bar{n}\rangle &= \sqrt{3}C_{1/2-m_n 1K}^{1/2-m_p} \delta_{\Omega_p - \Omega_n, -K} (-)^{1/2-m_n} (-)^{1/2-m_p} (\delta_{n_z^p, n_z^n} \delta_{n_r^p, n_r^n} + \delta_{\bar{n}_z^p, \bar{n}_z^n} \delta_{\bar{n}_r^p, \bar{n}_r^n}). \end{aligned} \quad (7.10)$$

We can now group matrix elements based on the fact that for GT transitions  $K = 0, 1$ . The results are shown in table 7.1. Some elements will vanish since the time-reversed states are explicitly treated. This means that  $\Omega_{p,n} > 0$  and  $\Omega_p + \Omega_n > 0$  so that some selection rules cannot be fulfilled. Indeed, we conclude that possible pairs for  $K = 0$  are of the form  $pn$  and  $\bar{p}\bar{n}$ , while those of the  $K = 1$  mode are  $pn$ ,  $p\bar{n}$  and  $\bar{p}\bar{n}$ .

The implications of the selection rule are shown in Fig. 7.1(a)-(b). Starting in Fig. 7.1(a) for the  $K = 0$  mode, on the left side we have the proton  $\Omega_p$  blocks, while on the right side we have neutron  $\Omega_n$  blocks. There is a one-to-one correspondence between each proton and neutron block, satisfying the selection rule  $\Omega_p = \Omega_n$ . Only equal states with respect to time reversal are coupled.

Table 7.1: The matrix elements of the external field Gamow-Teller operator in the basis of the axially-deformed harmonic oscillator for  $K = 0$  and  $K = 1$ .

		$J^\pi = 1^+, K = 0$
$pn$		$(\delta_{m_p,1/2}\delta_{m_n,1/2} - \delta_{m_p,-1/2}\delta_{m_n,-1/2})\delta_{\Omega_p,\Omega_n}(\delta_{n_z^p,n_z^n}\delta_{n_r^p,n_r^n} + \delta_{\tilde{n}_z^p,\tilde{n}_z^n}\delta_{\tilde{n}_r^p,\tilde{n}_r^n})$
$p\bar{n}$		0
$\bar{p}n$		0
$\bar{p}\bar{n}$		$(-\delta_{m_p,1/2}\delta_{m_n,1/2} + \delta_{m_p,-1/2}\delta_{m_n,-1/2})\delta_{\Omega_p,\Omega_n}(\delta_{n_z^p,n_z^n}\delta_{n_r^p,n_r^n} + \delta_{\tilde{n}_z^p,\tilde{n}_z^n}\delta_{\tilde{n}_r^p,\tilde{n}_r^n})$
		$J^\pi = 1^+, K = 1$
$pn$		$-\sqrt{2}\delta_{\Omega_p-\Omega_n,1}\delta_{m_p,1/2}\delta_{m_n,-1/2}(\delta_{n_z^p,n_z^n}\delta_{n_r^p,n_r^n} + \delta_{\tilde{n}_z^p,\tilde{n}_z^n}\delta_{\tilde{n}_r^p,\tilde{n}_r^n})$
$p\bar{n}$		$-\sqrt{2}\delta_{\Omega_p+\Omega_n,1}\delta_{m_p,1/2}\delta_{m_n,1/2}(\delta_{n_z^p,n_z^n}\delta_{n_r^p,n_r^n} - \delta_{\tilde{n}_z^p,\tilde{n}_z^n}\delta_{\tilde{n}_r^p,\tilde{n}_r^n})$
$\bar{p}n$		0
$\bar{p}\bar{n}$		$\sqrt{2}\delta_{-\Omega_p+\Omega_n,1}\delta_{m_p,-1/2}\delta_{m_n,1/2}(\delta_{n_z^p,n_z^n}\delta_{n_r^p,n_r^n} + \delta_{\tilde{n}_z^p,\tilde{n}_z^n}\delta_{\tilde{n}_r^p,\tilde{n}_r^n})$


 Figure 7.1: Schematic pair selection for the Gamow-Teller transitions ( $J^\pi = 1^+$ ) for  $K = 0$  (a) and  $K = \pm 1$  (b). The angular momentum projections blocks  $\Omega$  are separated for proton ( $\Omega_p$ ) and neutron ( $\Omega_n$ ) states.

On the other hand, for the  $K = 1$  mode in Fig. 7.1(b) we have the selection rule  $\Omega_p - \Omega_n = 1$ . This means that there will be a transition where  $\Omega_p = 1/2$  and  $\Omega_n = -1/2$ , satisfying the selection rule and of the form  $p\bar{n}$ .

Finally, the matrix elements in the single-particle space have to be transformed to the q.p. space. This is analogous to the discussion in Sec. 3.1.3 for spherical pnRQRPA, with the difference that no coupling to  $J$  is performed. In the q.p. basis the GT external field operator assumes the form

$$\begin{aligned}
 \hat{F}_{1K} &= \sum_{pn} \langle p | F_{1K} | n \rangle c_p^\dagger c_n \\
 &= \sum_{\pi\nu} \sum_{pn} (U^\dagger F_{1K} U)_{\pi\nu} \alpha_\pi^\dagger \alpha_\nu + (U^\dagger F_{1K} V^*)_{\pi\nu} \alpha_\pi^\dagger \alpha_\nu^\dagger + (V^T F_{1K} U)_{\pi\nu} \alpha_\pi \alpha_\nu + (V^T F_{1K} V^*)_{\pi\nu} \alpha_\pi \alpha_\nu^\dagger \\
 &= \sum_{\pi\nu} \sum_{pn} \begin{pmatrix} (U^\dagger F_{1K} U)_{\pi\nu} & (U^\dagger F_{1K} V^*)_{\pi\nu} \\ (V^T F_{1K} U)_{\pi\nu} & (V^T F_{1K} V^*)_{\pi\nu} \end{pmatrix} = \sum_{\pi\nu k k'} F_{kk'}^{(pn)} a_{k\pi} a_{k'\nu},
 \end{aligned} \tag{7.11}$$

where the notation introduced in Sec. 3.1 is used.

## 7.1.2 Particle-hole matrix elements

The underlying relativistic EDF employed in this section is the point-coupling DD-PC1 or DD-PCX. As we showed in Sec. 3.1 by using the point-coupling functionals, we can write the residual interaction as a sum of a product of separable terms. The linear response formalism based on separable interaction has a significantly reduced dimension compared to the same problem in the configuration space. Due to the isospin selection rules, two terms of the Lagrangian density can contribute to the charge-exchange linear response equations. The first is the isovector-vector (TV) term with the matrix element

$$V_{pnn'p'}^{TV} = - \int d^3\mathbf{r}_1 d^3\mathbf{r}_2 \alpha_{TV}[\rho_v] \left[ \bar{\Psi}_p(\mathbf{r}_1) \gamma_\mu^{(1)} \vec{\tau}^{(1)} \Psi_n(\mathbf{r}_1) \right] \left[ \bar{\Psi}_{n'}(\mathbf{r}_2) \gamma^{\mu(2)} \vec{\tau}^{(2)} \Psi_{p'}(\mathbf{r}_2) \right] \delta(\mathbf{r}_1 - \mathbf{r}_2), \tag{7.12}$$

where  $\alpha_{TV}$  is a function of the vector density  $\rho_v$ , and the isovector-pseudovector (TPV) term

$$V_{pnn'p'}^{TPV} = g_0 \int d^3\mathbf{r}_1 d^3\mathbf{r}_2 \left[ \bar{\Psi}_p(\mathbf{r}_1) \gamma_5^{(1)} \gamma_\mu^{(1)} \vec{\tau}^{(1)} \Psi_n(\mathbf{r}_1) \right] \left[ \bar{\Psi}_{n'}(\mathbf{r}_2) \gamma_5^{(2)} \gamma^{\mu(2)} \vec{\tau}^{(2)} \Psi_{p'}(\mathbf{r}_2) \right] \delta(\mathbf{r}_1 - \mathbf{r}_2), \tag{7.13}$$

where  $\bar{\Psi} = \Psi^\dagger \gamma_0$ . In the case of spherical symmetry, these were already introduced in Chapter 3. The TV residual interaction term can be separated into time-like and space-like components,

respectively,

$$\begin{aligned}
 V_{pnn'p'}^{TV(t)} &= -2 \int r dr dz d\phi \alpha_{TV}[\rho_v] [\Psi_p^\dagger(\mathbf{r}) \Psi_n(\mathbf{r})] [\Psi_{n'}^\dagger(\mathbf{r}) \Psi_{p'}(\mathbf{r})], \\
 V_{pnn'p'}^{TV(s)} &= -2 \int r dr dz d\phi \alpha_{TV}[\rho_v] \sum_{\mu} (-)^{\mu} \left[ \Psi_p^\dagger(\mathbf{r}) \begin{pmatrix} 0 & \sigma_{\mu} \\ \sigma_{\mu} & 0 \end{pmatrix} \Psi_n(\mathbf{r}) \right] \\
 &\quad \times \left[ \Psi_{n'}^\dagger(\mathbf{r}) \begin{pmatrix} 0 & \sigma_{-\mu} \\ \sigma_{-\mu} & 0 \end{pmatrix} \Psi_{p'}(\mathbf{r}) \right],
 \end{aligned} \tag{7.14}$$

where factor 2 originates from the isospin matrix element. We see that interaction can be written in the separable form, where the separable channels are defined as

$$Q_{pn}^{TV(t)}(r, z) = \Psi_p^\dagger(r, z) \Psi_n(r, z), \quad Q_{pn}^{TV(s),\mu} = \Psi_p^\dagger(r, z) \begin{pmatrix} 0 & \sigma_{\mu} \\ \sigma_{\mu} & 0 \end{pmatrix} \Psi_n(r, z). \tag{7.15}$$

The integration over  $\phi$  angle is performed implicitly since it will only give the selection rule for the angular momentum projections. The total number of the separable channels for the TV interaction term is  $4 \times N_z^{GH} \times N_r^{GL}$ , where  $N_z^{GH}$  and  $N_r^{GL}$  is the number of Gauss-Hermite and Gauss-Laguerre integration mesh-points in the  $z$ - and  $r$ -directions, respectively. Instead of writing the matrix elements in the basis of the axially-deformed h.o., we transform the oscillator wave functions to the coordinate-space wave functions as in Eq. (6.1). The transformation according to Eqs. (6.10) and (6.11) can be written as

$$\begin{aligned}
 f_i^{\pm}(\mathbf{r}) &= \sum_{n_z n_r \Lambda, m_s = \pm 1/2} f_{[n_z, n_r, \Lambda, \pm 1/2]}^{(i)} \Phi_{[n_z, n_r, \Lambda]}(\mathbf{r}, m_s = \pm 1/2), \\
 g_i^{\pm}(\mathbf{r}) &= \sum_{\tilde{n}_z \tilde{n}_r \tilde{\Lambda}, \tilde{m}_s = \pm 1/2} g_{[\tilde{n}_z, \tilde{n}_r, \tilde{\Lambda}, \pm 1/2]}^{(i)} \Phi_{[\tilde{n}_z, \tilde{n}_r, \tilde{\Lambda}]}(\mathbf{r}, m_s = \pm 1/2),
 \end{aligned} \tag{7.16}$$

for upper and lower components, respectively. In table 7.2 we show the separable channels of the TV interaction for  $pn$  and  $\bar{p}\bar{n}$  types of the transitions in the coordinate-space basis.

Table 7.2: Separable matrix elements of the isovector-vector (TV) interaction in the coordinate-space representation [cf. Eq. (7.18)]. We show the matrix elements for  $pn$  and  $\bar{p}\bar{n}$  types of transitions.

	$pn$	$\bar{p}\bar{n}$
$Q_{pn}^{TV(t)}(r, z)$	$f_p^+ f_n^+ + f_p^- f_n^- + g_p^+ g_n^+ + g_p^- g_n^-$	$f_p^+ f_n^+ + f_p^- f_n^- + g_p^+ g_n^+ + g_p^- g_n^-$
$Q_{pn}^{TV(s),+1}(r, z)$	$i\sqrt{2}[g_p^+ f_n^- - f_p^+ g_n^-]$	$(+)i\sqrt{2}[g_p^- f_n^+ - f_p^- g_n^+]$
$Q_{pn}^{TV(s),0}(r, z)$	$-i[g_p^+ f_n^+ - g_p^- f_n^- - f_p^+ g_n^+ + f_p^- g_n^-]$	$-i[g_p^+ f_n^+ - g_p^- f_n^- - f_p^+ g_n^+ + f_p^- g_n^-]$
$Q_{pn}^{TV(s),-1}(r, z)$	$-i\sqrt{2}[g_p^- f_n^+ - f_p^- g_n^+]$	$(-)i\sqrt{2}[g_p^+ f_n^- - f_p^+ g_n^-]$

Table 7.3: Same as in table 7.2 but for the TPV interaction.

	$pn$	$\bar{p}\bar{n}$
$Q_{pn}^{TPV(t)}(r, z)$	$i[f_p^+ g_n^+ + f_p^- g_n^- - g_p^+ f_n^+ - g_p^- f_n^-]$	$(-i)[f_p^+ g_n^+ + f_p^- g_n^- - g_p^+ f_n^+ - g_p^- f_n^-]$
$Q_{pn}^{TPV(s),+1}(r, z)$	$-\sqrt{2}[f_p^+ f_n^- + g_p^+ g_n^-]$	$\sqrt{2}[f_p^- f_n^+ + g_p^- g_n^+]$
$Q_{pn}^{TPV(s),0}(r, z)$	$f_p^+ f_n^+ + g_p^+ g_n^+ - f_p^- f_n^- - g_p^- g_n^-$	$(-)[f_p^+ f_n^+ + g_p^+ g_n^+ - f_p^- f_n^- - g_p^- g_n^-]$
$Q_{pn}^{TPV(s),-1}(r, z)$	$\sqrt{2}[f_p^- f_n^+ + g_p^- g_n^+]$	$-\sqrt{2}[f_p^+ f_n^- + g_p^+ g_n^-]$

Analogously, the isovector-pseudovector (TPV) residual interaction can be written as

$$\begin{aligned}
 V_{pnn'p'}^{TPV(t)} &= 2g_0 \int r dr dz d\phi \left[ \Psi_p^\dagger(\mathbf{r}) \begin{pmatrix} 0 & 1 \\ 1 & 0 \end{pmatrix} \Psi_n(\mathbf{r}) \right] \left[ \Psi_{n'}^\dagger(\mathbf{r}) \begin{pmatrix} 0 & 1 \\ 1 & 0 \end{pmatrix} \Psi_{p'}(\mathbf{r}) \right], \\
 V_{pnn'p'}^{TPV(s)} &= 2g_0 \int r dr dz d\phi \sum_{\mu} (-)^{\mu} \left[ \Psi_p^\dagger(\mathbf{r}) \begin{pmatrix} \sigma_{\mu} & 0 \\ 0 & \sigma_{\mu} \end{pmatrix} \Psi_n(\mathbf{r}) \right] \left[ \Psi_{n'}^\dagger(\mathbf{r}) \begin{pmatrix} \sigma_{-\mu} & 0 \\ 0 & \sigma_{-\mu} \end{pmatrix} \Psi_{p'}(\mathbf{r}) \right],
 \end{aligned} \tag{7.17}$$

for time-like and space-like components, respectively. The separable channels are defined as

$$Q_{pn}^{TPV(t)}(r, z) = \Psi_p^\dagger(r, z) \begin{pmatrix} 0 & 1 \\ 1 & 0 \end{pmatrix} \Psi_n(r, z), \quad Q_{pn}^{TV(s),\mu} = \Psi_p^\dagger(r, z) \begin{pmatrix} \sigma_{\mu} & 0 \\ 0 & \sigma_{\mu} \end{pmatrix} \Psi_n(r, z). \tag{7.18}$$

Therefore, the total dimension of the TPV interaction terms separable channels is also  $4 \times N_z^{GL} \times N_r^{GL}$ . The corresponding matrix elements in the coordinate-space basis are shown in table 7.3.

The separable matrix elements are transformed to the q.p. basis analogously to the external field

matrix elements in Eq. (7.34)

$$\hat{Q}_{cc'} = \sum_{\pi\nu} \sum_{pn} \begin{pmatrix} (U^\dagger Q_{cc'} U)_{\pi\nu} & (U^\dagger Q_{cc'} V^*)_{\pi\nu} \\ (V^T Q_{cc'} U)_{\pi\nu} & (V^T Q_{cc'} V^*)_{\pi\nu} \end{pmatrix} = \sum_{\pi\nu kk'} Q_{cc',kk'}^{(pn)} a_{k\pi} a_{k'\nu}, \quad (7.19)$$

where  $(c, c')$  label the separable interaction channels.

### 7.1.3 Particle-particle matrix elements

For the particle-particle ( $pp$ ) interaction we assume the separable pairing given already in Eq. (3.65). It is convenient to calculate the matrix element in the axially-deformed h.o. basis

$$\begin{aligned} \langle 12|V|1'2'\rangle &= \langle n_{z_1} n_{r_1} \Lambda_1 m_{s_1} m_{t_1}; n_{z_2} n_{r_2} \Lambda_2 m_{s_2} m_{t_2} | V' (1 - P^r P^\sigma P^T) \\ &\quad \times | n_{z'_1} n_{r'_1} \Lambda_1' m_{s'_1} m_{t'_1}; n_{z'_2} n_{r'_2} \Lambda_2' m_{s'_2} m_{t'_2} \rangle, \end{aligned} \quad (7.20)$$

where each state is denoted with the h.o. quantum numbers  $|1\rangle \equiv |n_{z_1} n_{r_1} \Lambda_1 m_{s_1} m_{t_1}\rangle$ , where  $m_{t_1}$  denotes the isospin projection. The projector operators exchange the position, spin, and isospin of two nucleons such as

$$P^r |\mathbf{r}_1 \mathbf{r}_2\rangle = |\mathbf{r}_2 \mathbf{r}_1\rangle, \quad P^\sigma |SM_S\rangle = (-)^{S-1} |SM_S\rangle, \quad |TM_T\rangle = (-)^{T-1} |TM_T\rangle, \quad (7.21)$$

where  $S$  and  $T$  denote the coupled spin and isospin of two states. It is convenient to couple the wave function to  $S$  and  $T$  as

$$\begin{aligned} |12\rangle &= \phi_{n_{z_1}}(z_1, b_z) \phi_{n_{r_1}}^{\Lambda_1}(r_1, b_\perp) \phi_{n_{z_2}}(z_2, b_z) \phi_{n_{r_2}}^{\Lambda_2}(r_2, b_\perp) \frac{1}{2\pi} e^{i\phi_1 \Lambda_1} e^{i\phi_2 \Lambda_2} \\ &\quad \times \sum_{SM_S} C_{1/2m_{s_1} 1/2m_{s_2}}^{SM_S} |SM_S\rangle \sum_{TM_T} C_{1/2m_{t_1} 1/2m_{t_2}}^{TM_T} |TM_T\rangle. \end{aligned} \quad (7.22)$$

The separable pairing interaction has the form [201]

$$V'(\mathbf{r}_1, \mathbf{r}_2, \mathbf{r}'_1, \mathbf{r}'_2) = -G\delta(\mathbf{R} - \mathbf{R}')P(r, z)P(r', z'), \quad (7.23)$$

where  $\mathbf{R} = \frac{1}{2}(\mathbf{r}_1 + \mathbf{r}_2)$  is the center-of-mass and  $\mathbf{r} = \mathbf{r}_1 - \mathbf{r}_2$  is the relative coordinate. Analogously, for the  $z$ -component we have  $Z = \frac{1}{2}(z_1 + z_2)$  and  $z = z_1 - z_2$ . The form factor has the form of a

Gaussian

$$P(r, z) = \frac{1}{(4\pi a^2)^{3/2}} e^{-\frac{z^2+r^2}{4a^2}}, \quad (7.24)$$

where  $G$  and  $a$  are interaction parameters [201]. Therefore, in the first step, we have to transform the h.o. wave functions from the laboratory to the center-of-mass frame. First, the product of  $z$ -component wave functions can be written as [197]

$$\phi_{n_{z_1}}(z_1)\phi_{n_{z_2}}(z_2) = \sum_{N_z n_z} M_{N_z n_z}^{n_{z_1} n_{z_2}} \phi_{N_z}(Z, \tilde{b}_Z) \phi_{n_z}(z, \tilde{b}_z) (-)^{n_z}, \quad (7.25)$$

where  $\tilde{b}_Z = \sqrt{2}b_z$  and  $\tilde{b}_z = b_z/\sqrt{2}$ , and  $M_{N_z n_z}^{n_{z_1} n_{z_2}}$  is the 1-dimensional Talmi-Moshinsky coefficient [202]. Next, we apply the same transformation to the radial wave functions [197]

$$\phi_{n_{r_1}}^{\Lambda_1}(\mathbf{r}_1)\phi_{n_{r_2}}^{\Lambda_2}(\mathbf{r}_2) = \sum_{N_r \Lambda} \sum_{n_r \lambda} M_{N_r \Lambda n_r \lambda}^{n_{r_1} \Lambda_1 n_{r_2} \Lambda_2} \phi_{N_r}^{\Lambda}(\mathbf{R}, \tilde{b}_R) \phi_{n_r}^{\lambda}(\mathbf{r}, \tilde{b}_r) (-)^{\lambda}, \quad (7.26)$$

where  $\tilde{b}_R = \sqrt{2}b_r$  and  $\tilde{b}_r = b_r/\sqrt{2}$ , where  $M_{N_r \Lambda n_r \lambda}^{n_{r_1} \Lambda_1 n_{r_2} \Lambda_2}$  is the 2-dimensional Talmi-Moshinsky coefficient [202]. The Talmi-Moshinsky coefficients imply the following selection rule that connects quantum numbers in the intrinsic and laboratory frame [197]

$$n_{z_1} + n_{z_2} = N_z + n_z, \quad n_r + N_r = n_{r_1} + n_{r_2} + \frac{|\Lambda_1| + |\Lambda_2| + |\Lambda_1 + \Lambda_2|}{2}, \quad \Lambda_1 + \Lambda_2 = \Lambda + \lambda. \quad (7.27)$$

The total matrix element in the coupled basis is

$$\begin{aligned} \langle 1\bar{2}|V|1'\bar{2}'\rangle &= -G\delta_{\lambda 0}\delta_{\lambda' 0}\delta_{\Lambda\Lambda'} \frac{1}{b_z b_r^2} \sum_{N_z N_r} W_{1\bar{2}}^{N_z} W_{1\bar{2}}^{N_r} W_{1'\bar{2}'}^{N_z} W_{1'\bar{2}'}^{N_r} \\ &\times \sum_{SM_S} \sum_{TM_T} \frac{1}{2} [(-)^{n_z+n'_z} - (-)^{n_z} (-)^{S+T}] (-)^{1/2-m_{s_2}} (-)^{1/2-m'_{s_2}} \\ &\times C_{1/2m_{s_1} 1/2-m_{s_2}}^{SM_S} C_{1/2m'_{s_1} 1/2-m'_{s_2}}^{SM_S} C_{1/2m'_{t_1} 1/2m'_{t_2}}^{TM_T} C_{1/2m_{t_1} 1/2m_{t_2}}^{TM_T}, \end{aligned} \quad (7.28)$$

where we have defined the separable terms analogously to Ref. [138]:

$$W_{1\bar{2}}^{N_z} = \frac{1}{\sqrt{b_z}} M_{n_{z_1} n_{z_2}}^{N_z n_z} \delta_{n_z, \text{even}} \frac{(-)^{n_z/2}}{(2\pi)^{1/4}} \frac{\sqrt{n_z!}}{2^{n_z/2} (n_z/2)!} \left( \frac{b_z^2}{a^2 + b_z^2} \right)^{1/2} \left( \frac{b_z^2 - a^2}{b_z^2 + a^2} \right)^{n_z/2}, \quad (7.29)$$

$$W_{1\bar{2}}^{N_r} = \frac{1}{b_r} M_{n_{r_1} \Lambda_1 n_{r_2} \Lambda_2}^{N_r \Lambda n_r 0} \frac{1}{(2\pi)^{1/2}} \frac{b_r^2}{b_r^2 + a^2} \left( \frac{b_r^2 - a^2}{b_r^2 + a^2} \right)^{n_r}, \quad (7.30)$$

from which we see that  $n_z$  can only assume even values. This means that the spin+isospin part has the form

$$\begin{aligned} & \sum_{SM_S} \sum_{TM_T} \frac{1}{2} [1 - (-)^{S+T}] (-)^{1/2-m_{s_2}} (-)^{1/2-m'_{s_2}} C_{1/2m_{s_1}1/2-m_{s_2}}^{SM_S} C_{1/2m'_{s_1}1/2-m'_{s_2}}^{SM_S} \\ & \times C_{1/2m'_{t_1}1/2m'_{t_2}}^{TM_T} C_{1/2m_{t_1}1/2m_{t_2}}^{TM_T}, \end{aligned} \quad (7.31)$$

from which it follows that  $S + T = \text{odd}$ . Two cases can be distinguished corresponding to either **isovector** ( $T = 1, S = 0$ ) or **isoscalar** ( $T = 0, S = 1$ ) pairing interaction. Considering first the isovector pairing, the separable matrix element is characterized by  $N_r, N_z$  quantum numbers and has the form

$$W_{N_r, N_z}^{T=1, S=0} = \frac{1}{\sqrt{2}} W_{12}^{N_z} W_{12}^{N_r} (-)^{1/2-m_{s_2}} C_{1/2m_{s_1}1/2-m_{s_2}}^{00}, \quad (7.32)$$

where  $1/\sqrt{2}$  stems from the isospin part,  $C_{1/2-1/21/2+1/2}^{10} = 1/\sqrt{2}$ . On the other hand, the isoscalar matrix element is determined by  $M_S$  in addition to  $N_r, N_z$

$$W_{N_r, N_z, M_S}^{T=0, S=1} = -\frac{1}{\sqrt{2}} W_{12}^{N_z} W_{12}^{N_r} (-)^{1/2-m_{s_2}} C_{1/2m_{s_1}1/2-m_{s_2}}^{1M_S}. \quad (7.33)$$

The total  $pp$  residual interaction matrix element can be written in the following form

$$\begin{aligned} V_{pn p' n'}^{pp} &= \langle p \bar{n} | V | p' \bar{n}' \rangle c_p^\dagger c_{\bar{n}}^\dagger c_{\bar{n}'} c_{p'} = \sum_{N_z N_r M_S} (W_{pn}^{N_z N_r M_S})^* W_{p' n'}^{N_z N_r M_S} c_p^\dagger c_{\bar{n}}^\dagger c_{\bar{n}'} c_{p'} \\ &= \sum_{N_z N_r M_S} (W_{pn}^{N_z N_r M_S})^* c_p^\dagger c_{\bar{n}}^\dagger W_{p' n'}^{N_z N_r M_S} c_{\bar{n}'} c_{p'} = \sum_{N_z N_r M_S} \left( \hat{D}_{pn}^{N_z N_r M_S} \right)^\dagger \hat{D}_{p' n'}^{N_z N_r M_S}, \end{aligned}$$

where we have defined a separable term as  $\left( \hat{D}_{pn}^{N_z N_r M_S} \right)^\dagger = (W_{pn}^{N_z N_r M_S})^* c_p^\dagger c_{\bar{n}}^\dagger$ . The total number of separable matrix elements for the isovector interaction is  $N_r \times N_z$ , while for the isoscalar interaction, it is  $3 \times N_z \times N_r$  (factor 3 comes from projections of spin  $S = 1$ ). Next, we have to transform the  $pp$  separable matrix elements from the single-particle to the q.p. basis. One here has to be careful to correctly account for transformation properties of time-reversed state so that we get [58]

$$\hat{W}_{cc'} = \sum_{\pi\nu} \sum_{pn} \begin{pmatrix} -(U^T W_{cc'} V^*)_{\pi\nu} & (U^\dagger W_{cc'} U)_{\pi\nu} \\ -(V^T W_{cc'} V^*)_{\pi\nu} & (V^T W_{cc'} U^*)_{\pi\nu} \end{pmatrix} = \sum_{\pi\nu k k'} W_{cc', kk'}^{(pn)} a_{k\pi} a_{k'\nu}, \quad (7.34)$$



where  $(c, c')$  label the separable  $pp$  residual interaction channels.

### 7.1.4 Calculating the reduced response function $R_{cc'}$

To give a sense of the dimension of matrices involved, we present details of the axially-deformed linear response equations. First, the most numerically involved part is the construction of the unperturbed reduced response defined in Eq. (3.41). The equation can be recast into the matrix form as

$$\underbrace{R^0(\omega)}_{N_{channel} \times N_{channel}} = \sum_{j=1,4} \underbrace{Q_j^T}_{N_{channel} \times N_{pair}} \underbrace{N(\omega)_j}_{N_{pair} \times N_{pair}} \times \underbrace{Q_j}_{N_{pair} \times N_{channel}}, \quad (7.35)$$

where  $N_{channel} = N_{ph} + N_{pp}$  is the total number of channels that can be written as a sum of  $ph$  and  $pp$  channels,  $N_{ph}$  and  $N_{pp}$ , respectively, while  $N_{pair}$  is the total number of q.p. pairs. The matrix  $Q_j$  consists of separable channels of the residual interaction Hamiltonian and has the form

$$Q_j = \begin{pmatrix} Q_{i_1}^{1,j} & \cdots & Q_{i_1}^{N_{ph},j} & W_{i_1}^{1,j} & \cdots & W_{i_1}^{N_{pp},j} \\ \vdots & \ddots & \vdots & \vdots & \ddots & \vdots \\ Q_{i_{N_{pair}}}^{1,j} & \cdots & Q_{i_{N_{pair}}}^{N_{ph},j} & W_{i_{N_{pair}}}^{1,j} & \cdots & W_{i_{N_{pair}}}^{N_{pp},j} \end{pmatrix}, \quad (7.36)$$

where  $j = 1, 4$  stands for the q.p. component. For instance, the separable  $ph$  matrix elements for the pair  $i_1$  will have the following form

$$\begin{aligned} Q_{i_1}^{1,j=1} &= (U^\dagger Q(r_1, z_1) U)_{i_1}, & Q_{i_1}^{1,j=2} &= (U^\dagger Q(r_1, z_1) V^*)_{i_1}, \\ Q_{i_1}^{1,j=3} &= (V^T Q(r_1, z_1) U)_{i_1}, & Q_{i_1}^{1,j=4} &= (V^T Q(r_1, z_1) V^*)_{i_1}, \end{aligned} \quad (7.37)$$

where channel 1 is represented as  $(r_1, z_1)$  in the coordinate space. The total number of  $ph$  channels is  $N_{ph} = 2 \times 8 \times N_z^{GL} \times N_r^{GL}$ . Therefore, the  $Q_j$  matrix for  $j = 1$  is

$$Q_{j=1}^{1 \dots N_{ph}} = \begin{pmatrix} \underbrace{Q_{j=1}^{TPV}}_{4 \times N_z^{GH} \times N_r^{GL}} & \underbrace{Q_{j=1}^{TV}}_{4 \times N_z^{GH} \times N_r^{GL}} & Q_{j=4}^{TPV} & Q_{j=4}^{TV} \end{pmatrix}, \quad (7.38)$$

where  $Q^{TPV}$  corresponds to the TPV and  $Q^{TV}$  is the TV separable interaction matrix, respectively. Note that for  $j = 1$  we also have a mixing of the  $j = 4$  q.p. components. This is a peculiarity of the charge-exchange formalism stemming from the second component of the interaction matrix in Eq. (3.27). Therefore, the total number of  $ph$  channels is given by  $N_{ph} = 8 \times N_z^{GH} \times N_r^{GL}$ . The

$pp$  part of the  $Q$  matrix has a similar structure

$$Q_{j=1}^{N_{ph}+1\dots N_{ph}+N_{pp}} = \begin{pmatrix} \underbrace{W_{j=1}}_{(3-2T) \times N_r \times N_z} & W_{j=4} \end{pmatrix}, \quad (7.39)$$

where  $N_z$  and  $N_r$  are number of shells in  $z$ - and  $r$ -directions [cf. Sec. 7.1.3], while the number of  $pp$  channels is given by  $N_{pp} = (3 - 2T) \times N_r \times N_z$ , meaning that for isovector pairing  $N_{pp} = N_r \times N_z$  and for isoscalar pairing  $N_{pp} = 3 \times N_r \times N_z$ . This means that the total number of channels is

$$N_{channel} = 8 \times N_z^{GH} \times N_r^{GL} + 2 \times (3 - 2T) \times N_r \times N_z. \quad (7.40)$$

The  $N(\omega)$  matrix is diagonal and has the form

$$N(\omega)_{j=1} = \text{diag} \left( \frac{f_{\nu_1} - f_{\pi_1}}{\omega - E_{\pi_1} + E_{\nu_1} + i\eta}, \dots, \frac{f_{\nu_{N_{pair}}} - f_{\pi_{N_{pair}}}}{\omega - E_{\pi_{N_{pair}}} + E_{\nu_{N_{pair}}} + i\eta} \right), \quad (7.41)$$

$$N(\omega)_{j=2} = \text{diag} \left( \frac{1 - f_{\nu_1} - f_{\pi_1}}{\omega - E_{\pi_1} - E_{\nu_1} + i\eta}, \dots, \frac{1 - f_{\nu_{N_{pair}}} - f_{\pi_{N_{pair}}}}{\omega - E_{\pi_{N_{pair}}} - E_{\nu_{N_{pair}}} + i\eta} \right), \quad (7.42)$$

$$N(\omega)_{j=3} = \text{diag} \left( \frac{f_{\nu_1} + f_{\pi_1} - 1}{\omega + E_{\pi_1} + E_{\nu_1} + i\eta}, \dots, \frac{f_{\nu_{N_{pair}}} + f_{\pi_{N_{pair}}} - 1}{\omega + E_{\pi_{N_{pair}}} + E_{\nu_{N_{pair}}} + i\eta} \right), \quad (7.43)$$

$$N(\omega)_{j=4} = \text{diag} \left( \frac{-f_{\nu_1} + f_{\pi_1}}{\omega + E_{\pi_1} - E_{\nu_1} + i\eta}, \dots, \frac{-f_{\nu_{N_{pair}}} + f_{\pi_{N_{pair}}}}{\omega + E_{\pi_{N_{pair}}} - E_{\nu_{N_{pair}}} + i\eta} \right), \quad (7.44)$$

where  $i_1 \equiv (\pi_1, \nu_1)$  and  $i_{N_{pair}} \equiv (\pi_{N_{pair}}, \nu_{N_{pair}})$ . Next, we have to calculate the  $R_{FF}^0$  response, defined as

$$\underbrace{R_{FF}^0(\omega)}_{N_F \times N_F} = \sum_{j=1,4} \underbrace{F_j^T}_{N_F \times N_{pair}} \times \underbrace{N(\omega)}_{N_{pair} \times N_{pair}} \times \underbrace{F_j}_{N_{pair} \times N_F}, \quad (7.45)$$

where  $N_F$  is the dimension of the external field matrix element. Its structure has a similar form as the  $ph$  matrix element in Eq. (7.38)

$$F_{j=1}^{1\dots N_F} = \begin{pmatrix} \underbrace{F_{j=1}}_{N_z^{GH} \times N_r^{GL}} \end{pmatrix}, \quad (7.46)$$

from where we see that the dimension of the external field matrix is  $N_F = N_z^{GH} \times N_r^{GL}$ . Finally, we define the  $R_{cF}^0$  reduced response matrix as

$$\underbrace{R^0(\omega)_{cF}}_{N_{channel} \times N_F} = \sum_{j=1,4} \underbrace{Q_j^T}_{N_{channel} \times N_{pair}} \underbrace{N(\omega)_j}_{N_{pair} \times N_{pair}} \times \underbrace{F_j}_{N_{pair} \times N_F}, \quad (7.47)$$

of the dimension  $N_{channel} \times N_F$ , mixing both the residual interaction and the external field matrix element. The  $v_{cc'}$  interaction matrix in Eq. (3.27) is diagonal (since we consider no derivative terms in the residual interaction) and is given by

$$v_{cc'} = \text{diag} \left( \underbrace{+\frac{g_0}{2\pi}}_{N_z^{GH} \times N_r^{GL}}, \underbrace{-\frac{g_0}{2\pi}}_{3 \times N_z^{GH} \times N_r^{GL}}, \underbrace{+\frac{\alpha_{TV}}{2\pi}}_{N_z^{GH} \times N_r^{GL}}, \underbrace{-\frac{\alpha_{TV}}{2\pi}}_{3 \times N_z^{GH} \times N_r^{GL}}, \underbrace{G}_{(3-2T) \times N_z \times N_r}, \dots \right), \quad (7.48)$$

where one has to be careful about the signs of the time-like and space-like components of TV and TPV interaction. The ... denote the repeating of the same terms due to the second term in Eq. (3.27). After all the necessary matrices are calculated, we first invert the matrix  $\delta_{cc'} - \sum_{c''} R_{cc''}^0 v_{c''c'}$  and then calculate the  $R_{cF}$  response

$$R_{cF}(\omega) = \sum_{c'} [\delta_{cc'} - \sum_{c''} R_{cc''}^0(\omega) v_{c''c'}]^{-1} R_{c''F}^0(\omega). \quad (7.49)$$

Finally, the response function is obtained as

$$R_{FF}(\omega) = \sum_{cc'} R_{cF}^0(\omega) v_{cc'} R_{cF}(\omega), \quad (7.50)$$

its imaginary part giving the strength function [see Eq. (3.33)].

Therefore, from the computational perspective, for a given energy  $\omega$ , one has to multiply matrices of the size  $N_{channel} \times N_{pair}$  in Eq. (7.35),  $N_F \times N_{pair}$  in Eq. (7.45) and their cross-term in Eq. (7.47), all for  $j = 1, 4$ . After that, the square matrix  $R_{cc'}^0$  of the size  $N_{channel}$  has to be inverted and multiplied with  $R_{cF}^0$  in Eq. (7.49), other operations being less computationally expensive. To illustrate, if we use  $N_{osc} = 16$  h.o. shells, then  $N_z^{GH} = N_r^{GL} \sim 16$  for the radial mesh and  $N_z = N_r \sim 16$  for the pairing interaction. Therefore,  $N_{ph} \sim 4096$  and  $N_{pp} \sim 1500$  for the more expensive isoscalar pairing (500 for isovector). The total number of channels is  $N_{channel} \sim 5600$ . The number of pairs for the  $K = 0$  mode of the GT transitions is  $N_{pair} \sim 50000$ , meaning that the

largest matrix size for the multiplication is on the order of  $5600 \times 50000$  and for matrix inversion  $5600 \times 5600$ , easily manageable on a moderate computer cluster.

## 7.2 Numerical tests

For the first numerical test, we choose  $^{28}\text{O}$  which is a doubly-magic nucleus. However, to introduce non-vanishing pairing correlations, we artificially increase the pairing strength of the DD-PC1 interaction from  $G_{p,n} = -728 \text{ MeV fm}^{-3}$  to  $G_{p,n} = -1500 \text{ MeV fm}^{-3}$ . Such large pairing interaction breaks the shell closure in  $^{28}\text{O}$ . For initial numerical tests, we employ a small basis space of  $N_{osc} = 8$  h.o. shells without any additional cut-off on the 2 q.p. basis. We employ a smearing parameter  $\eta = 0.25 \text{ MeV}$  to better distinguish differences between individual peaks. As a rule of thumb, we found that using  $N_z^{GL} = N_r^{GL} \sim N_{osc}$  provides reasonable convergence of the radial integrals. Results calculated with the axially-deformed pnRQRPA are compared with the spherical pnRQRPA from Sec. 3.1. To make the comparison possible, the axially-deformed RHB calculations are constrained to a spherical shape. In Fig. 7.2(a) we show the comparison between the Fermi strength function in the  $\beta^-$  direction ( $\text{IAS}^-$ ). In this case, we have a total of  $N_{pair} \sim 5000$  2 q.p. pairs contributing to the linear response equations (only  $K = 0$  projection). The agreement of the strength function between the deformed and spherical pnRQRPA is excellent. In Fig. 7.3(b) we show the comparison for the  $\text{GT}^-$  strength function for both  $K = 0$  and  $K = 1$  modes. Note that  $K = \pm 1$  modes are degenerate and that the total strength is  $S_{tot} = 3 \times S(K = 0) = 3 \times S(K = 1)$ , where  $S(K = 0, 1)$  is the strength function for the  $K = 0, 1$  mode. The degeneracy between the  $K = 0$  and  $K = 1$  in the spherical limit is well reproduced, in addition to the overall comparison with the spherical pnRQRPA. The total number of pairs for  $K = 0$  mode is  $N_{pair} \sim 5000$  and  $N_{pair} \sim 8500$  for the  $K = 1$  mode.

Next, we generalize our tests to also include the finite-temperature effects. The FT-pnRQRPA response function in  $^{28}\text{O}$  with  $N_{osc} = 8$  is shown in Fig. 7.3(a) at  $T = 1 \text{ MeV}$  and 7.3(b) at  $T = 3 \text{ MeV}$ . Due to the degeneracy mentioned previously, only the  $K = 0$  results are shown and the total strength of the deformed FT-pnRQRPA is multiplied with the degeneracy factor,  $3 \times S(K = 0)$ . We observe that the agreement between two different FT-pnRQRPA codes is excellent. Since the pairing interaction has been artificially increased, the pairing is present even at  $T = 3 \text{ MeV}$ , where the smearing due to the Fermi-Dirac distribution of the q.p. states is significant. Therefore, this test presents the most general verification of our axially-deformed FT-pnRQRPA implementation,

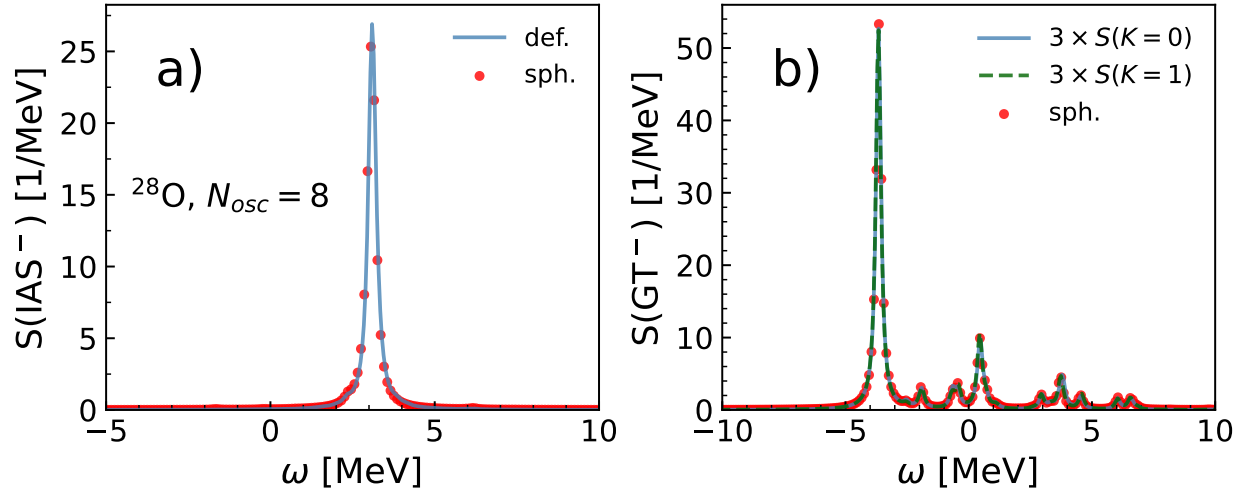


Figure 7.2: Comparison between the spherical and axially-deformed pnQRPA results for  $^{28}\text{O}$  for the IAS $^-$  (a) and GT $^-$  (b) strength function, with  $N_{osc} = 8$  oscillator shells. The strength function calculated with the spherical pnQRPA is represented with red circles, while the solid line shows different components of the axially-deformed response:  $K = 0$  mode is represented with solid blue and  $K = 1$  mode with dashed green. The response function of the deformed FT-pnQRPA is multiplied by 3 to account for degeneracy.

which includes both pairing and temperature effects. We note that the spherical FT-pnQRPA was already benchmarked against the corresponding matrix FT-pnQRPA in Ref. [30]. Such tests confirm the consistency between different theoretical approaches and codes.

Finally, it is instructive to find the optimal basis size for realistic calculations of spin-isospin response. To this aim, we select  $^{70}\text{Fe}$ , which is a rather neutron-rich isotope of iron, and calculate its GT $^-$  response for a varying number of h.o. shells,  $N_{osc}$ . The RHB ground state is constrained to  $\beta_2 = +0.3$  and the calculations are performed at zero temperature. Results are shown in Fig. 7.4 for  $N_{osc} = 8$ –16 with a step of 2, for both  $K = 0$  (a) and  $K = 1$  (b) projections. From the figure, we infer that the reasonable convergence for the GT $^-$  strength is achieved once  $N_{osc} = 12$ . The strength function for  $N_{osc} = 14$  and  $N_{osc} = 16$  is almost indistinguishable. We note that the conclusion from this work is in agreement with Ref. [194], based on non-relativistic EDF calculations, where good convergence for  $A \sim 70$  nuclei is obtained with  $N_{osc} = 13$ .

Therefore, in the following calculations, we use  $N_{osc} = 16$  which guarantees good convergence for  $pf$ -shell nuclei considered in this chapter. However, the number of 2 q.p. pairs at  $N_{osc} = 16$  and without any cut-off becomes very large. In table 7.4 we show the total number of 2 q.p.

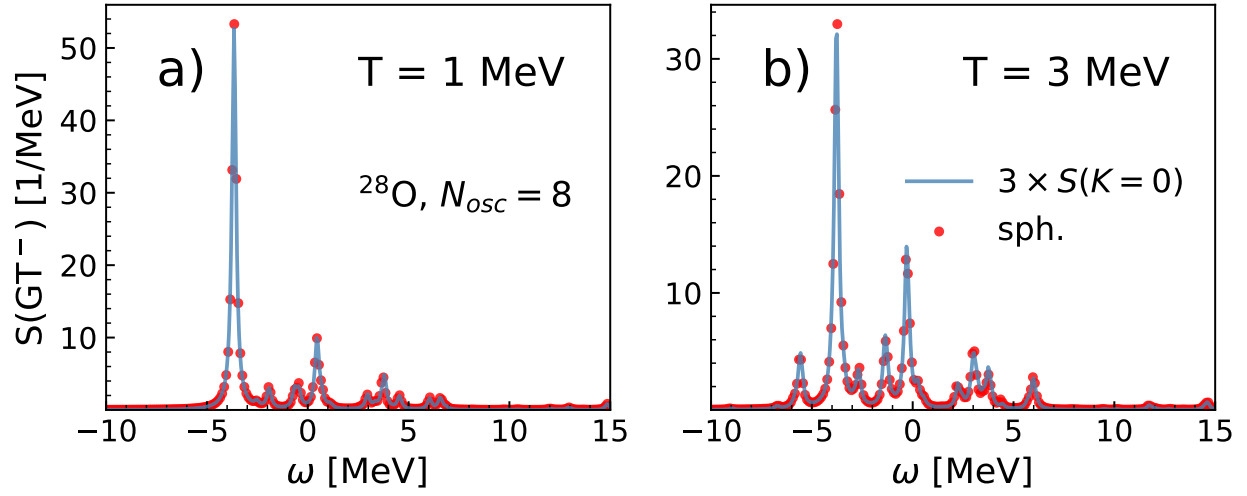


Figure 7.3: Comparison between the spherical and axially-deformed FT-pnRQRPA results at  $T = 1$  MeV (a) and 3 MeV (b). Results are calculated for  $^{28}\text{O}$  with  $N_{osc} = 8$  and a modified pairing strength.

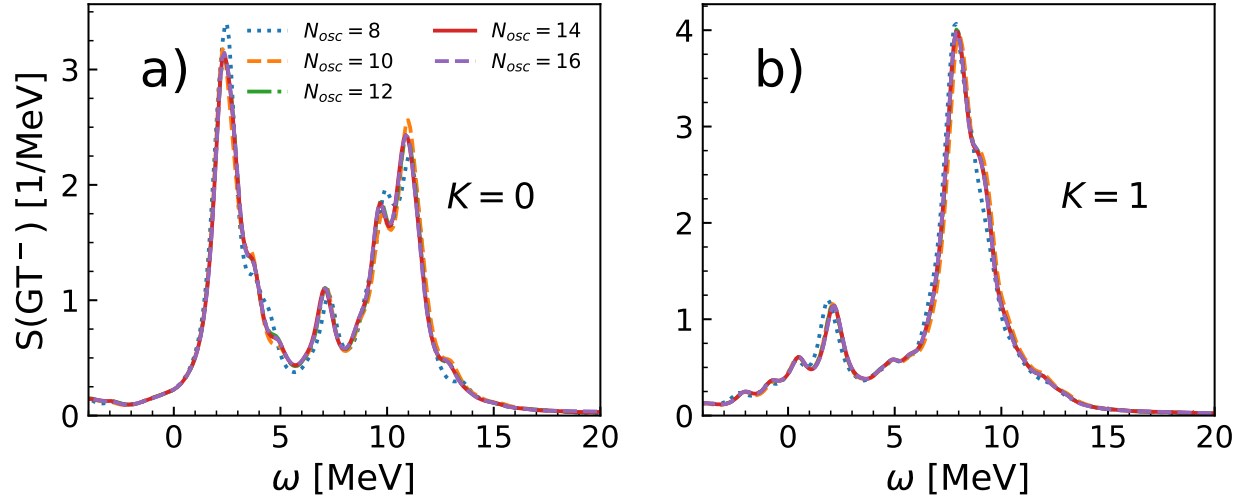


Figure 7.4: Convergence tests of the GT<sup>-</sup> strength for  $^{70}\text{Fe}$  with  $\beta_2 = +0.3$  for a varying number of oscillator shells  $N_{osc}$  and no additional cut-off to the 2 q.p. basis. Results are shown for the  $K = 0$  (a) and  $K = 1$  (b) projections.

pairs  $N_{pair}$  for  $K = 0$  and  $K = 1$  modes for  $^{70}\text{Fe}$  with  $\beta_2 = +0.3$ . Therefore, solving for one projection with  $N_{osc} = 16$  would correspond to diagonalizing a square matrix with a dimension 180000. Here, our linear response formalism based on the reduced response function for separable

Table 7.4: Number of proton-neutron 2 q.p. pairs  $N_{pair}$  for  $K = 0$  and  $K = 1$  projections of the Gamow-Teller response for an increasing number of oscillator shells  $N_{osc}$ .

$N_{osc}$	$N_{pair}(K = 0)$	$N_{pair}(K = 1)$
8	5002	4857
10	12444	12188
12	26894	26481
14	52432	51808
16	94482	93585

interaction is advantageous. We have to perform a sum over  $N_{pair}$  and invert a matrix with a size of  $5400 \times 5400$ . The sum over the 2 q.p. pairs can be easily parallelized. However, we can further limit the basis size by introducing a cut-off on the sum of 2 q.p. configuration energies  $E_{cut}$ , defined as  $E_{2qp} = E_\pi + E_\nu$  so that  $E_{2qp} \leq E_{cut}$ . In Fig. 7.5 we show calculations of the  $K = 0$  projection in  $^{70}\text{Fe}$  with  $\beta_2 = +0.3$  and  $N_{osc} = 16$ , where  $E_{cut} = 50, 100$  and  $150$  MeV. Results by employing  $E_{cut}$  are compared with results calculated in Fig. 7.4 with no cut-off on q.p. configuration energies. We observe that  $E_{cut} = 100$  MeV yields a response function practically indistinguishable from that without any cut-off. The number of 2 q.p. pairs is almost halved compared to that without the cut-off, providing a significant speed-up of the calculation. Even the result with  $E_{cut} = 50$  MeV provides a reasonable convergence because calculation time is almost 10 times faster compared to no cut-off. Therefore, in the following calculations, we employ  $E_{cut} = 100$  MeV.

### 7.3 Spin-isospin excitations in axially-deformed nuclei

In Section 3.4 we have presented results with the pnQRPA assuming spherical symmetry, for the Fermi ( $J^\pi = 0^+$ ) and the GT ( $J^\pi = 1^+$ ) strength function. Here, we generalize the discussion of spin-isospin excitations to deformed nuclei. The optimal quadrupole deformation  $\beta_2^*$  is the one which minimizes the binding energy (or free energy at finite temperature). Therefore, at the RHB level, we have to construct a PES and find optimal  $\beta_2^*$  that determines the ground-state shape of the nucleus. It is interesting to study how the shape and excitation energy of the resonance is influenced by the deformation effects. First, we investigate the Gamow-Teller strength function in selected  $pf$ -shell nuclei, for which experimental data is available. Model calculations are performed with the DD-PC1 and DD-PCX relativistic EDFs. In addition, we also investigate the  $\text{GT}^-$  strength in  $^{58,60,62}\text{Fe}$ , providing a much richer structure of the strength function. We decompose the total

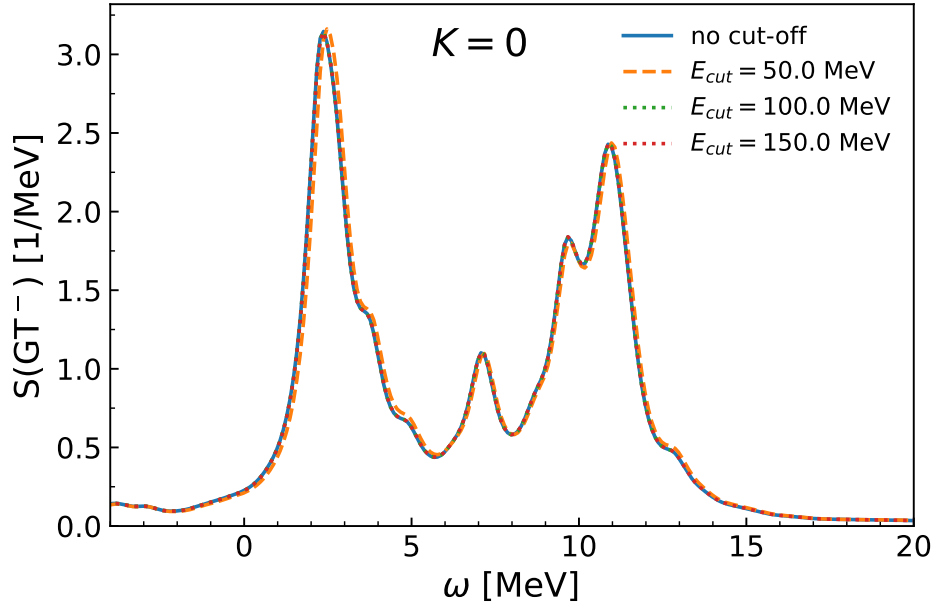


Figure 7.5: Convergence tests of the  $K = 0$   $GT^-$  strength for  $^{70}\text{Fe}$  with  $\beta_2 = +0.3$  for  $N_{osc} = 16$  and varying cut-off on 2 q.p. configuration energy  $E_{cut}$ .

strength function to  $K = 0$  and  $K = 1$  projections and study their behavior for oblate and prolate configurations. On the example of even-even iron isotopes we also investigate the  $IAS^-$  strength function and compare it with the available experimental data. Lastly, we generalize our discussion to finite temperature and study the temperature evolution of the  $GT^+$  strength in  $^{56}\text{Fe}$ . An interesting competition between the pairing, temperature, and deformation effects occurs which determines the total strength function. All calculations are performed with  $N_{osc} = 16$  h.o. shells and 2 q.p. energy cutoff  $E_{cut} = 100$  MeV, unless not explicitly mentioned otherwise. We have verified that such a basis size is enough to obtain good convergence of the strength function for nuclei of interest. We neglect the contribution of anti-particle transitions, being a good approximation for the charge-exchange case [203]. The strength functions are smeared with  $\eta = 1$  MeV.

### 7.3.1 The Gamow-Teller resonance

The external field operator in the GT case has the form  $\hat{F}_{J=1,K} = \sigma_{1K}\tau_{\pm}$ , where  $K = 0, \pm 1$ . Due to the Pauli spin matrix  $\sigma_{1K}$  it has a selection rule for the spin part  $\Delta S = 1$ , giving it a significantly richer structure compared to the simpler Fermi transitions. The calculations are also



more computationally intensive since one has to perform them twice, for  $K = 0$  and  $K = 1$  projections. The total strength is calculated as

$$S(\text{GT}^\pm, \omega) = S(K = 0, \omega) + 2 \times S(K = 1, \omega). \quad (7.51)$$

For the GT external field, only the isoscalar pairing ( $S = 1, T = 0$ ) is present in the  $pp$  residual interaction channel. Based on the study of  $\beta$ -decay rates (presented in Sec. 7.5) and  $\text{GT}^+$  strength function in comparison with the available experimental data in Sec. 7.3, we adopt a value  $V^{is} = 0.8$ . It is interesting to study if the deformation effects play any role in the GT transition strength. To this aim, we select  $^{60}\text{Ni}$ , and study its GT strength in the  $\beta^+$  direction ( $\text{GT}^+$ ). To determine the optimal shape, we perform a constrained RHB calculation in Fig. 7.6 with respect to the quadrupole deformation  $\beta_2$ . We observe that PES has three stationary points: oblate minimum at  $\beta_2^* = -0.19$  corresponding to the optimal configuration, a spherical maximum, and prolate minimum  $\beta_2 = 0.13$ . For these three stationary points in the PES, we have performed the pnRQRPA calculation for the  $\text{GT}^+$  response in Fig. 7.6(b). We observe that spherical and prolate configurations lead to considerably different strength functions. Furthermore, both deformed configurations are significantly different compared to the spherical ones. We observe that the spherical  $\text{GT}^+$  strength function for  $^{60}\text{Ni}$  consists of a single peak (smeared with 1 MeV) at  $\omega = 2.3$  MeV. On the other hand, both prolate and oblate configurations show more fragmentation of the  $\text{GT}^+$  strength function and reduced strength of the main peak. We notice that the prolate configuration has more fragmentation and overall reduced strength compared to the oblate one. This is related to the fact that the oblate shape has a larger value of the quadrupole moment, thus deformation plays a bigger role. Note that for the prolate shape, which has a lower quadrupole moment, the main peak is split only into two peaks. Of course, the fragmentation strength in the deformed pnRQRPA results from the degeneracy breaking of the Nilsson q.p. orbitals.

It is imperative to perform a comparison of the  $\text{GT}^+$  strength function with the available data. Unfortunately, the GT strength function has been measured only for a handful of nuclei in the  $pf$ -shell and a limited excitation energy range [93, 94, 99, 103]. This means that only a part of the total strength function is covered by the experiment, and usually, it is not the part containing the main resonance peak. The experiments are often performed by some type of a charge-exchange reaction such as  $(n, p)$  or  $(^3\text{He}, t)$ , which can excite, among others, GT excitations. In the following, we compare the axially-deformed pnRQRPA  $\text{GT}^+$  strength function with the available experimental data. In Ref. [93], the  $\text{GT}^+$  strength function in  $^{56}\text{Fe}$  is excited by a  $(n, p)$  reaction, while the

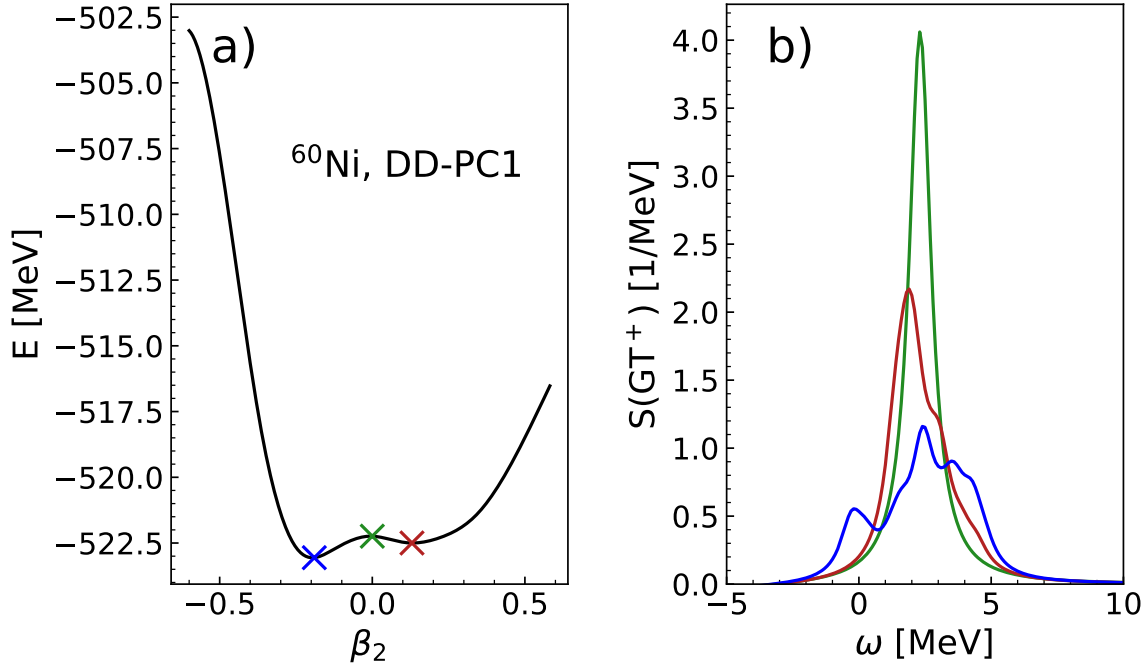


Figure 7.6: (a) The PES for  $^{60}\text{Ni}$  as calculated with the axially-deformed RHB with the DD-PC1 interaction. Three stationary points (marked with an X) correspond to the oblate (blue), spherical (green), and prolate (red) configurations. (b) The  $\text{GT}^+$  strength calculated from the corresponding stationary points in PES as a function of the excitation energy in the parent nucleus  $\omega$ .

strength function is measured up to 10 MeV for  $^{56}\text{Mn}$ . Also with a  $(n, p)$  type of reaction the strength function was measured for even-even nickel isotopes  $^{60,62,64}\text{Ni}$  in Ref. [94]. More recently, the  $\text{GT}^+$  strength was also measured for  $^{46}\text{Ti}$  in Ref. [103] and  $^{64}\text{Zn}$  in Ref. [99], nuclei whose EC rates are of importance for the evolution of late-stage CCSNe. In Fig. 7.7(a)-(f) we compare the measured  $\text{GT}^+$  strength function for the previously mentioned nuclei, to calculations obtained with the axially-deformed pnQRPA, by employing DD-PC1 and DD-PCX relativistic EDFs. In addition to the axially-deformed calculations we also show the results calculated with the spherical pnQRPA using the DD-PC1 interaction. First, we note that all presented nuclei display axially-deformed shapes, either prolate (like  $^{56}\text{Fe}$  and  $^{46}\text{Ti}$ ) or oblate ( $^{60,62,64}\text{Ni}$  and  $^{64}\text{Zn}$ ), results being consistent between both DD-PC1 and DD-PCX interaction. We have summarized the optimal quadrupole deformations  $\beta_2^*$  for considered nuclei using both interactions in table 7.5.

From Fig. 7.7 one can infer a large discrepancy between the spherical and deformed calculations. By inspecting the spherical strength function (green dashed line) calculated with the DD-PC1

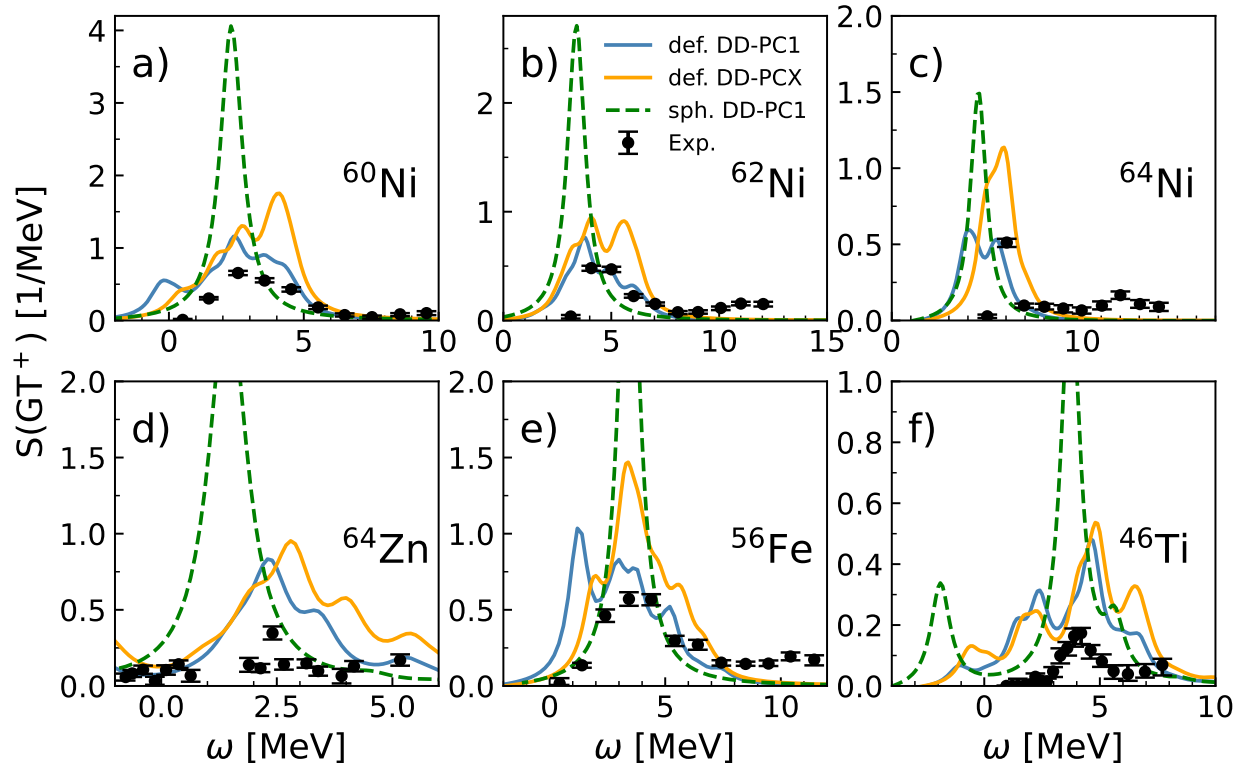


Figure 7.7: The  $GT^+$  strength function for particular  $pf$ -shell nuclei shown with respect to the excitation energy in parent nucleus  $\omega$ . The calculations are performed with the axially-deformed pnRQRPA with DD-PC1 (blue) and DD-PCX (orange) interactions and the spherical pnRQRPA for the DD-PC1 interaction (green dashed). The results are compared with the available experimental data from Refs. [93, 94, 99, 103] (black circles). The isoscalar pairing strength is set to  $V^{is} = 0.8$  in all calculations.

interaction, we notice that it is mostly concentrated in a one resonance peak. Only a slightly more proton-rich system such as  $^{46}\text{Ti}$  displays more structure in the spherical  $GT^+$  response. Of course, a direct comparison between the spherical strength function and experimental strength is not possible. We can only compare the position of the experimental centroid energy to the corresponding resonance energy in spherical  $GT^+$  strength function. We see that the main peak in the spherical strength function matches with the corresponding peak in the experimental strength for all considered nuclei within 1 MeV. This is an expected result considering the simplicity of the spherical pnRQRPA and its lower density of states in the RHB ground state. However, agreement in the excitation energy of the main peak suggests that if additional correlations are included, maybe

a more direct comparison between the strength functions is possible. The first step is taking into account that all considered nuclei are deformed and comparing the experimental distribution with the axially-deformed pnQRPA calculations. Due to the larger density of states calculated with the axially-deformed pnQRPA and degeneracy splitting between the q.p. Nilsson orbitals once the deformation is non-vanishing, the strength function will be significantly more fragmented compared to spherical calculations. We observe that the deformed pnQRPA results (solid blue line) with the DD-PC1 interaction lead to a significant reduction of strength and fragmentation of the main resonance peak, compared to the spherical calculations. Overall, the calculated strength function compares better to experimental data. The comparison is improved for all considered nuclei. For instance, deformation effects lead to very good agreement with experimental data for  $^{60}\text{Ni}$  and  $^{62}\text{Ni}$ , both having oblate ground states. In  $^{64}\text{Ni}$  the deformation effects lead to a splitting of the main resonance peak and a slight shift of the strength function to higher excitation energies, in better agreement with the experimental data. Although the deformed pnQRPA still overestimates the experimental strength in oblate-deformed  $^{64}\text{Zn}$ , we observe a shift to higher excitation energies, resulting in better agreement with the main peak of experimental strength. In both  $^{56}\text{Fe}$  and  $^{46}\text{Ti}$ , which have a prolate shape in the ground state, the inclusion of deformation effects leads to better agreement with the experimental data. Although, there are some peaks predicted by the deformed pnQRPA calculation not present in the experimental data, especially at lower excitation energies. Since the deformation effects are included, we expect that the differences between the experimental data and our calculations is mainly attributable to coupling with higher-order configurations. Namely, the relatively simple pnQRPA theory includes only the contribution of 2 q.p. excitations to the response function. In our calculations  $\eta = 1$  MeV, providing a smearing of the strength function, thus the width is not microscopically determined. Expanding the present formalism by including the coupling of 2 q.p. excitations to the phonons (QPVC) would lead to more fragmentation of the strength function, and possibly a better agreement with the experimental data [132, 133, 135, 150]. However, we note that the deformed QPVC at the level of the residual interaction is at present far from the implementation and its numerical realization, due to significant complications in the model. The first steps in this direction were only recently applied to the calculation of the ground-state properties [204]. Furthermore, Eq. (7.51) is only an approximation valid for large deformations (so-called *needle approximation*). The problem is that the transformation from the intrinsic system of the nucleus to the laboratory system has to be performed, which mixes contributions of different angular momenta  $J$ . Therefore, a proper

Table 7.5: The optimal quadrupole deformation  $\beta_2^*$  for particular  $pf$ -shell nuclei using both the DD-PC1 and DD-PCX interactions.

nucleus	$\beta_2^*(\text{DD-PC1})$	$\beta_2^*(\text{DD-PCX})$
$^{60}\text{Ni}$	-0.19	- 0.16
$^{62}\text{Ni}$	-0.22	-0.18
$^{64}\text{Ni}$	-0.13	-0.09
$^{64}\text{Zn}$	-0.24	-0.13
$^{56}\text{Fe}$	0.24	0.21
$^{46}\text{Ti}$	0.24	0.22

projection method for the response of the deformed nuclei should be implemented as discussed in Refs. [192, 205].

To assess the possible systematic uncertainties within our calculations, we also perform the deformed pnRQRPA calculations by employing the DD-PCX interaction (solid orange line). The DD-PCX relativistic EDF was fitted not only using the ground-state properties of nuclei but also considering the excitations [21]. From Fig. 7.7 we observe that results calculated with the DD-PCX lead to visible differences for some nuclei, compared to the DD-PC1 calculations. For instance, the agreement with experimental data is slightly worsened for  $^{60,62}\text{Ni}$ , as the strength function for the DD-PCX is pushed to slightly higher excitation energies. On the other hand, although the strength is overestimated, the DD-PCX leads to better agreement with the experimental centroid in  $^{64}\text{Ni}$ . For other considered nuclei we also observe a slight shift to higher excitation energies. In  $^{56}\text{Fe}$ , the strength function is more collected around the main resonance peak, which better describes the excitation energy of the main peak in the experimental distribution. For  $^{64}\text{Zn}$  and  $^{46}\text{Ti}$  the strength function retains a similar shape when compared to the DD-PC1, just  $\sim 0.5$  MeV shifted to higher energies. Therefore, based on our calculations with two different functionals we can conclude that considering deformation effects leads to a better overall agreement between the theoretical and experimental  $\text{GT}^+$  strength function.

In the following, we turn our attention to the  $\text{GT}^-$  strength function. Nuclei displaying significant  $\text{GT}^-$  strength are often neutron-rich, thus obtaining the experimental data is much more difficult. In fact, most of the experimental data exist for nuclei with (or around) the shell closure, such as tin isotopes [95]. Due to the proximity of shell closure, those nuclei mainly have a spherical shape, therefore considering the deformation effects is of no importance for the strength function. We have compared the results of our spherical pnRQRPA with the DD-PC1 interaction for particular tin

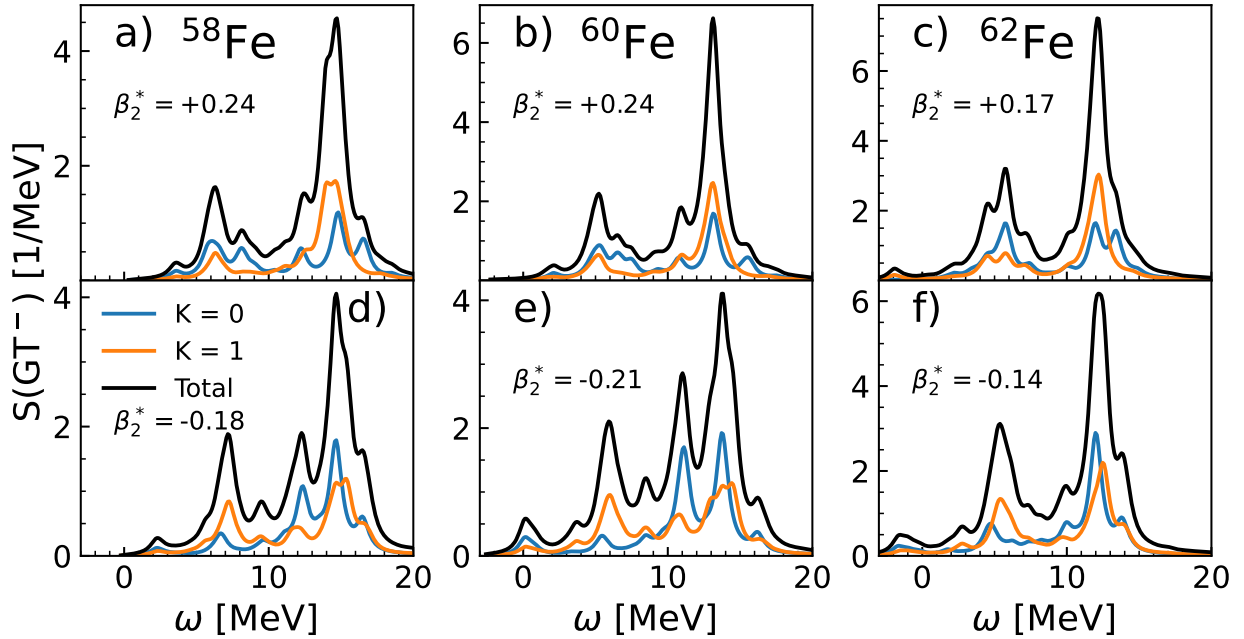


Figure 7.8: The  $GT^-$  strength function in selected even-even isotopes of iron, shown for the prolate (a)-(c), and oblate (d)-(f) configuration. The total strength function (solid black) is decomposed to the  $K = 0$  (solid blue) and  $K = 1$  (solid orange) projections of the total angular momentum  $J = 1$ . Excitation energy  $\omega$  is shown with respect to the ground state of the parent nucleus.

isotopes in Ref. [30]. The low-lying  $GT^-$  strength function is especially important for calculating the  $\beta$ -decay half-lives (see Sec. 7.5). We have investigated the  $GT^-$  strength function for  $^{58}\text{Fe}$ ,  $^{60}\text{Fe}$  and  $^{62}\text{Fe}$ , with the deformed pnQRPA using the DD-PC1 interaction. Considered nuclei present both an oblate and prolate minima, therefore, we are interested in studying how the shape of the nucleus influences its strength function. To this aim, in Fig. 7.8(a)-(f) we show the  $GT^-$  strength function for selected iron isotopes but decomposed to contributions of specific angular momentum projections,  $K = 0$  and  $K = 1$ , for both prolate shapes in Fig. 7.8(a)-(c), and oblate shapes in Fig. 7.8(d)-(f). The total strength is calculated as in Eq. (7.51). We observe that the  $GT^-$  strength function consists of the low-lying peak and a resonance peak (GTR) located at higher excitation energies. A similar structure was also inferred for spherical calculations in Fig. 3.5. However, unlike the spherical calculation presented in Sec. 3.4, the deformed  $GT^-$  response function has a richer structure. The following interesting structure is observed depending on the shape of the nucleus; for prolate shapes ( $\beta_2 > 0$ ), the low-lying strength is dominated by the  $K = 0$  component,

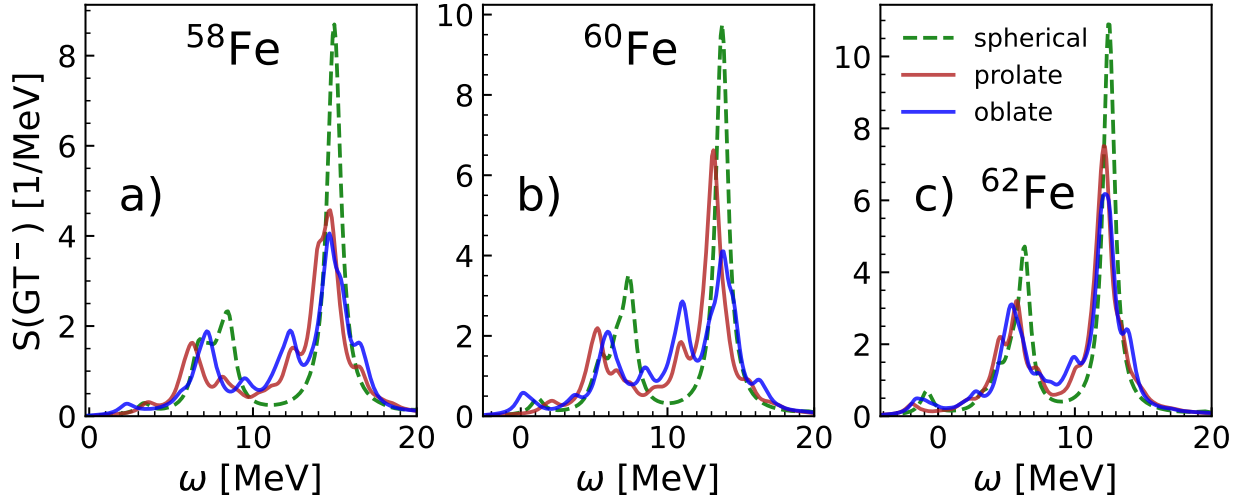


Figure 7.9: The total  $GT^-$  strength function in  $^{58}\text{Fe}$ ,  $^{60}\text{Fe}$  and  $^{62}\text{Fe}$ , shown for the prolate (solid red), oblate (solid blue) and spherical (dashed green) configuration. Excitation energy  $\omega$  is shown with respect to the ground state of the parent nucleus.

while the GTR strength is dominated by the  $K = 1$  component. On the other hand, the opposite is true for the oblate shape ( $\beta_2 < 0$ ), where the low-lying strength is dominated by the  $K = 1$  mode. In the case of spherical nuclei, both  $K = 0$  and  $K = 1$  modes are degenerate, however, in deformed nuclei, the degeneracy is broken and they are split. For the oblate shape, the  $K = 0$  mode is pushed to lower excitation energies and  $K = 1$  to higher, while the opposite is true for the prolate shape. The amount of splitting between the modes is proportional to the magnitude of  $\beta_2$ . Such interesting degeneracy splitting was already observed in Refs. [81, 192, 193] for the like-particle response function and Refs. [77, 80] in the charge-exchange case.

Finally, in Fig. 7.9(a)-(c) we show the total  $GT^-$  strength function for the prolate, oblate, and spherical configurations. We note that the shape of the nucleus in its ground state significantly influences the strength function. Compared to the spherical strength function, which consists mainly of two peaks, the deformed strength function displays much more structure. For nuclei with larger quadrupole deformations,  $^{58}\text{Fe}$  and  $^{60}\text{Fe}$ , we observe a larger difference compared to the spherical strength function. For the corresponding nuclei, oblate configurations show more fragmentation in the GTR region in comparison to the prolate ones, where the GTR is more collective. By inspecting Fig. 7.8(d)-(f) we observe that a large splitting of the GTR strength originates for the  $K = 0$  mode, which is more dominant at higher excitation energies. On the other hand,  $^{62}\text{Fe}$  has a lower value

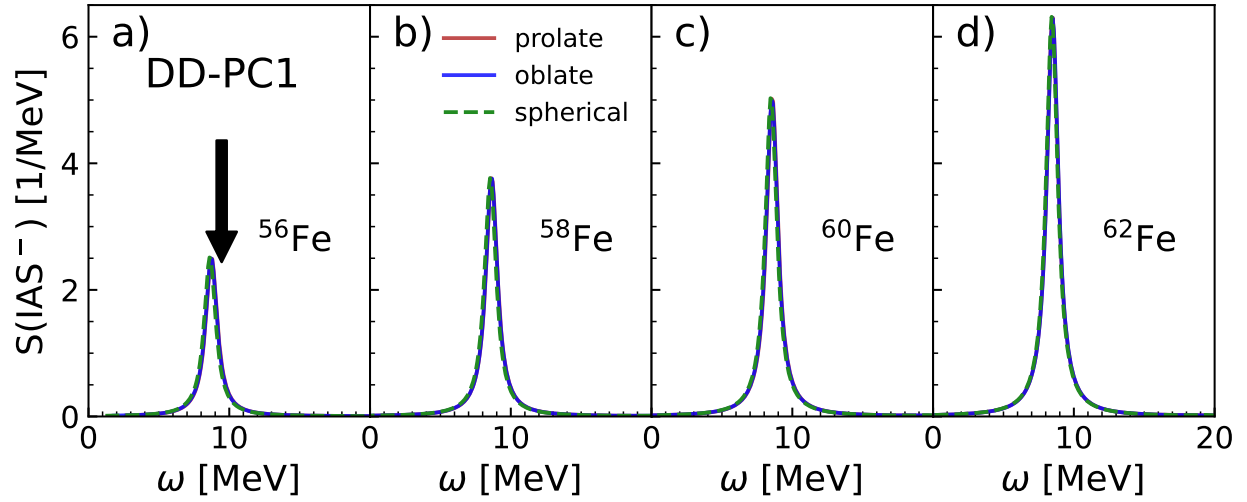


Figure 7.10: The  $IAS^-$  strength function in selected even-even isotopes of iron, shown for the prolate, oblate, and spherical configuration. Excitation energy  $\omega$  is shown with respect to the ground state of the parent nucleus. The experimental centroid energy from Ref. [206] is denoted with a black arrow.

of  $\beta_2$  compared to  $^{58,60}\text{Fe}$ , thus its strength function between the prolate and oblate shapes is more similar. Furthermore, the differences between the spherical and both deformed configurations are reduced. Overall, a significantly richer structure predicted by deformed pnQRPA follows from a higher density of states for axially-deformed nuclei compared to the spherical ones. Therefore, we expect that deformed calculations have more strength contributing to the  $Q_\beta$  window and therefore they could significantly alter  $\beta$ -decay half-lives compared to spherical nuclei.

### 7.3.2 The Isobaric Analog Resonance

In the following, we study the Fermi ( $J^\pi = 0^+$ ) strength function within the axially-deformed pnQRPA. Its relatively simple structure  $\hat{F}_{J=0, K=0} = \tau_\pm$ , allows only transitions with the same quantum numbers in the Nilsson basis. This means that the Fermi strength function has a much simpler structure compared to the GT. Furthermore, only the  $K = 0$  component of the angular momentum projection is allowed. From previous calculations based on spherical pnQRPA in Ref. [30], we know that the Fermi strength function is indeed located in one peak, at excitation energy corresponding to the Coulomb energy difference between the even-even parent and odd-odd daughter nucleus, corrected by the residual interaction. However, this is only the case if both the  $ph$



and  $pp$  residual interaction terms are derived self-consistently from the underlying relativistic EDF. This is exactly the case for our calculations since only the isovector ( $T = 1, S = 0$ ) component of the  $pp$  interaction contributes, the same as in the ground state. Furthermore, we can safely omit the TPV term from the  $ph$  residual interaction since its contribution is negligible, with TV being the dominant component. Calculations are performed using the DD-PC1 interaction with  $N_{osc} = 16$  and no other cut-off for the 2 q.p. basis. In Fig. 7.10(a)-(d) we show the Fermi strength function for  $^{56,58,60,62}\text{Fe}$  for prolate, oblate, and spherical configurations. As noted previously,  $^{56,58,60}\text{Fe}$  are predicted as prolate, while  $^{62}\text{Fe}$  is oblate, although with almost a flat minimum. We observe that deformation has almost no influence on the Fermi strength function, with differences between the prolate and oblate configurations being at most 0.05 MeV in  $^{56}\text{Fe}$ . The experimental centroid energy from Ref. [206] is denoted by a black arrow, obtained from the  $(^3\text{He}, t)$  charge-exchange reaction. The strong IAS state was extracted at  $\omega \approx 8.9$  MeV, being 0.5 MeV higher compared to our calculations. We have also performed calculations with the DD-PCX interaction for  $^{56}\text{Fe}$  and found that the strength is shifted around 0.13 MeV to higher energies, slightly closer to the experimental data. Although we found that the Fermi strength function is almost independent of the deformation, it still provides a reliable test of our numerical implementation.

## 7.4 Finite-temperature effects

It is interesting to investigate what happens with the GT strength with increasing temperature. Unlike the calculations performed in Sec. 3.4, here we generalize the discussion by also considering the deformation. Therefore, calculations presented in this section include: (i) pairing correlations, (ii) finite-temperature effects, and (iii) deformation effects. As an illustrative example, we study the temperature evolution of the  $\text{GT}^+$  strength in  $^{56}\text{Fe}$  in the temperature interval  $T = 0\text{--}2$  MeV. Since  $^{56}\text{Fe}$  is a nucleus found in abundance in the core of massive stars just before the collapse, understanding its GT strength function and subsequent implications for the EC rate are of importance. From the previous discussion in Chapter 6 we know that a nucleus undergoes a pairing collapse at  $T_c^p$  and a shape phase-transition at  $T_c^s$ . Therefore, at high enough temperatures, nuclei are spherical and in a normal state. Results are shown in Fig. 7.11. In Fig. 7.11(a)–(d) we show the temperature evolution of the PES in  $^{56}\text{Fe}$  together with the optimal  $\beta_2^*$ , while in Fig. 7.11(e)–(h) we display the temperature evolution of the  $\text{GT}^+$  response. Calculations are performed with the axially-deformed FT-pnRQRPA for optimal  $\beta_2^*$  and also with the spherical FT-pnRQRPA ( $\beta_2^* = 0$ ).

As already discussed in Sec. 7.3.1,  $^{56}\text{Fe}$  has a prolate shape in the ground state at zero temperature. The strength function is substantially more fragmented compared with the corresponding spherical calculation, which consists of just one peak. The main peak in spherical calculations is determined by the  $(\pi 1f_{7/2}, \nu 1f_{5/2})$  2 q.p. transition. In the axially-deformed calculations, this 2 q.p. excitation corresponds to multiple transitions due to the degeneracy splitting of the Nilsson quantum numbers. Here we will not attempt to list all those transitions, but they can be inferred from table 6.1 for  $N = 3$  principal quantum number. By increasing the temperature to  $T = 0.5$  MeV, in Fig. 7.11(b) we observe that the PES is almost unchanged, as well as the spherical  $\text{GT}^+$  strength function in Fig. 7.11(f). We have only a slight reduction of the total strength, in addition to a shift of  $\approx 0.1$  MeV to lower excitation energies. However, we can observe that the deformed strength function is visibly altered, with low-lying strength at  $\approx 1.3$  MeV being redistributed to higher energies. Since the PES is only slightly changed at  $T = 0.5$  MeV, the observed effect is mainly influenced by a reduction in pairing correlations. Namely, at optimal ground state with  $\beta_2^* = 0.23$  pairing vanishes for both neutron and proton states, while it is still present in the spherical state. This sudden pairing collapse is related to the grand-canonical treatment of the FT-RHB. By taking into account both thermal and quantal fluctuations we would get a non-vanishing pairing even at higher temperatures [207]. However, such considerations would further complicate our calculations, and our aim in this section is to study the general effects of temperature on deformed nuclei. Of course, due to the higher density of states for the deformed nucleus, even small temperatures can alter the underlying Nilsson q.p. states. The effect is more pronounced compared to the spherical nucleus with higher degeneracy of states. At  $T = 1$  MeV in Fig. 7.11(c) we observe that the PES starts to "flatten", meaning that the free energy difference between the oblate and prolate configurations reduces, however,  $\beta_2^* = 0.21$  is still the state which minimizes the total energy. In Fig. 7.11(g) we observe that the spherical  $\text{GT}^+$  strength is still contained in only one peak, shifted by further 0.5 MeV to lower energies. The pairing interaction now vanishes both for proton and neutron states. On the other hand, the deformed strength function shows more pronounced changes. The strength starts being collected to the main resonance peak, which has similar excitation energy as the main peak of the spherical calculation. At  $T = 2$  MeV the optimal configuration is spherical, while the PES is relatively "flat", as shown in Fig. 7.11(d), meaning that we have an agreement between the  $\text{GT}^+$  strength function corresponding to spherical and deformed calculations in Fig. 7.11(h). The  $\text{GT}^+$  strength is shifted by  $\approx 0.8$  MeV compared to the zero temperature spherical GTR, with its strength also slightly reduced. Therefore, by inspecting the temperature evolution of the spherical

GT<sup>+</sup> strength, we would conclude that it is almost unchanged. On the other hand, taking a look at the deformed response, we observe significant changes as the nucleus undergoes both pairing and shape phase transitions and eventually agrees with the spherical strength function at  $T = 2$  MeV. Therefore, the temperature dependence of the GT<sup>+</sup> strength function depends on the interplay between pairing, deformation, and finite-temperature effects. As we have seen, in the case of <sup>56</sup>Fe, temperature primarily reduces the nucleus to a spherical shape, thereby restoring the collectivity of the GTR. The effect of pairing collapse is primarily amplified by the increased density of states in the deformed nucleus, while in the spherical case, it almost does not affect <sup>56</sup>Fe.

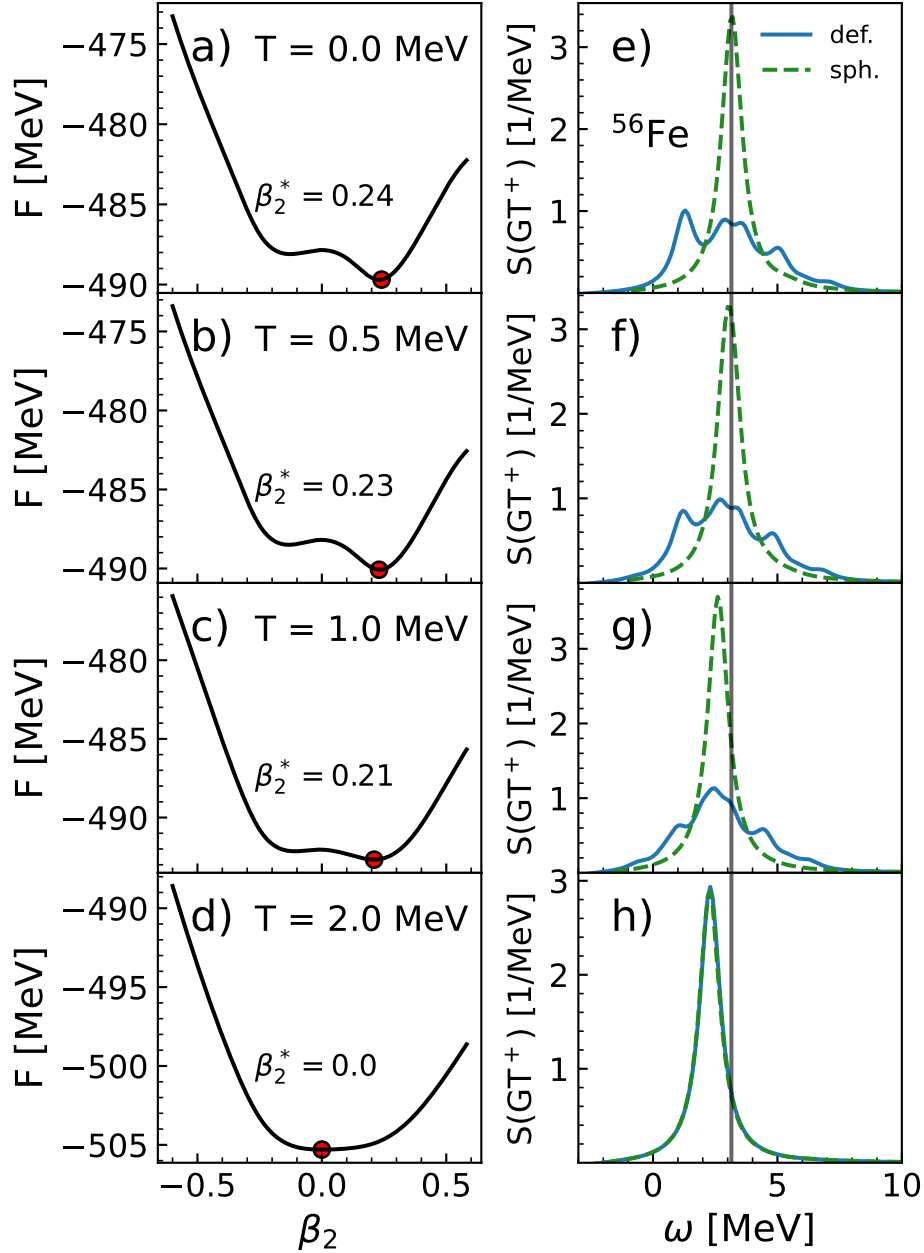


Figure 7.11: (a)–(d) The potential energy surface in  $^{56}\text{Fe}$  for temperatures  $T = 0$ – $2$  MeV. The optimal deformation  $\beta_2^*$  which minimizes the binding energy  $E$  is denoted by a red circle. (e)–(h) Temperature evolution of the  $GT^+$  strength distribution in  $^{56}\text{Fe}$  calculated for optimal  $\beta_2^*$  and temperatures  $T = 0$ – $2$  MeV with the axially-deformed (solid blue) and spherical (dashed green) FT-pnQRPA. Calculations are performed with the DD-PC1 interaction. The gray line in panels (e)–(h) is shown to guide the eye.

## 7.5 Influence of deformation on $\beta$ -decay half-lives

Finally, we want to study the effect of deformation on the  $\beta$ -decay half-lives. As we have seen in Sec. 7.3.1, the deformation effects can significantly affect the  $GT^-$  strength function, which determines the  $\beta$ -decay lifetimes in the allowed approximation. We only consider the zero-temperature results. Since the deformation effects tend to decrease with temperature, results will be most influenced by deformation at zero temperature. Furthermore, the model has to be first benchmarked against the available experimental data before extending it to other calculations. Starting from the general expression in Eq. (5.3) at zero temperature, and reducing it to the allowed approximation, we can write the expression for the  $\beta$ -decay rate as

$$\lambda_{1+}^{\beta} = \frac{\ln 2}{\kappa} \frac{1}{2\pi i} \oint_{\mathcal{C}} d\omega f(\Delta_{nH} - \omega) S_F(\omega), \quad (7.52)$$

where the rate is calculated by multiplying the strength function  $S_F(\omega)$  for the  $GT^-$  external field with the phase-space factor  $f(W_0)$ . The initial-final energy can be expressed in terms of the excitation energy with respect to the parent nucleus  $\omega$  as  $W_0^{(i,f)} (m_e c^2) = \Delta_{nH} - \omega$ . The above integral is calculated in the complex plane around a suitably chosen contour  $\mathcal{C}$  that encloses the  $Q_{\beta}$  window with  $\text{Re}[\omega] \in [-\lambda_{np}, \Delta_{nH}]$ , where the difference between the neutron and proton chemical potential is  $\lambda_{np} = \lambda_n - \lambda_p$ . The phase-space factor at zero temperature and in the allowed approximation is simply given by

$$f(W_0) = \int_1^{W_0} dW p W (W_0 - W)^2 L_0 F_0(Z + 1, W), \quad (7.53)$$

where the Fermi function  $F_0(Z, W_0)$  is defined as [77, 79, 154]

$$F_0(Z, W) = 4(2pR)^{-2(1-\gamma_1)} \frac{|\Gamma(\gamma_1 + iy)|^2}{\Gamma(2\gamma_1 + 1)^2} e^{\pi y}, \quad (7.54)$$

where  $\gamma_1 = \sqrt{1 - (\alpha Z)^2}$ ,  $y = \alpha Z W / p$  and  $R = 1.2A^{1/3}$  fm is the nuclear radius. The Coulomb wave function  $L_0$  is approximated as  $L_0 = \frac{1}{2}(1 + \gamma_1)$ , with other quantities defined in Sec. 5.1. The problem with calculating the rate using Eq. (7.52) is that the Fermi function is not analytical in the complex domain. Therefore, in Ref. [77] it is proposed to replace the exact phase-space integral

$f(W_0)$  with its polynomial expansion  $f_{poly}(W_0)$  in the form

$$f_{poly}(W_0) = \sum_{n=0}^N a_n W_0^n = \sum_{n=0}^N a_n (\Delta_{nH} - \omega)^n, \quad (7.55)$$

where  $N$  is the order of the polynomial. In Fig. 7.12(a) we show an example of the fit to the phase-space integral of  $^{42}\text{S}$  to a  $N = 10$  polynomial. Such a function agrees with the phase-space factor on the real axis, which is only important for calculating the contour integral.

The circular contour  $\mathcal{C}$  in the complex plane is shown in Fig. 7.12(b). The radius of the circle is  $R = (\lambda_{np} + \Delta_{nH})/2 \equiv \omega_{max}$ , and the contour is parameterized with

$$\omega(t) = \frac{\omega_{max}}{2} e^{it} - \frac{\lambda_{np}}{2} + \frac{\Delta_{nH}}{2}, \quad t \in [0, 2\pi). \quad (7.56)$$

The integral in Eq. (7.52) can be rewritten as

$$\lambda_{1+} = \frac{\ln 2}{\kappa} \frac{\omega_{max}}{2} \int_0^{2\pi} dt e^{it} f_{poly}[\omega(t)] S[\omega(t)]. \quad (7.57)$$

We see that its imaginary part should be vanishing, only the real part contributing to the rate. Later, we will use this fact as a numerical check for our calculation. To demonstrate calculation of  $\beta$ -decay half-lives using Eq. (7.52) we perform an example calculation on  $^{42}\text{S}$ . In Fig. 7.12(c) we show the  $\text{GT}^-$  strength in  $^{42}\text{S}$  within the  $Q_\beta$  window for which  $\omega \in [\lambda_{np}, \Delta_{nH}]$ . As demonstrated previously in Sec. 3.1, the  $\text{GT}^-$  strength is proportional to the residues of integration around the singularities of the response function shown in Fig. 7.12(c). According to Eq. (7.52) the strength has to be multiplied by the phase-space factor  $f_{poly}(\Delta_{nH} - \omega)$ , which decreases exponentially towards the upper limit of the  $Q_\beta$  window  $\omega = \Delta_{nH}$ . Therefore, the most contribution to the strength function is going to come from the part of the strength function closer to the lower limit of the  $Q_\beta$  window  $\omega = \lambda_{np}$ . In the following calculation, we employ  $N_{osc} = 14$  while in the pnRQRPA we use  $E_{cut} = 100$  MeV. By performing the constrained RHB calculation we have determined that  $^{42}\text{S}$  is prolate in its ground state with  $\beta_2^* = 0.30$ . The  $\text{GT}^-$  strength function for  $^{42}\text{S}$  in Fig. 7.12(c) is decomposed to  $K = 0$  and  $K = 1$  projections. In addition, the results are also shown as calculated with the spherical pnRQRPA. We observe that the deformed pnRQRPA calculation yields more strength in the  $Q_\beta$  window, especially at lower energies which contribute more to the rate integral. Therefore, just based on studying the  $\text{GT}^-$  strength function we can infer that deformed pnRQRPA

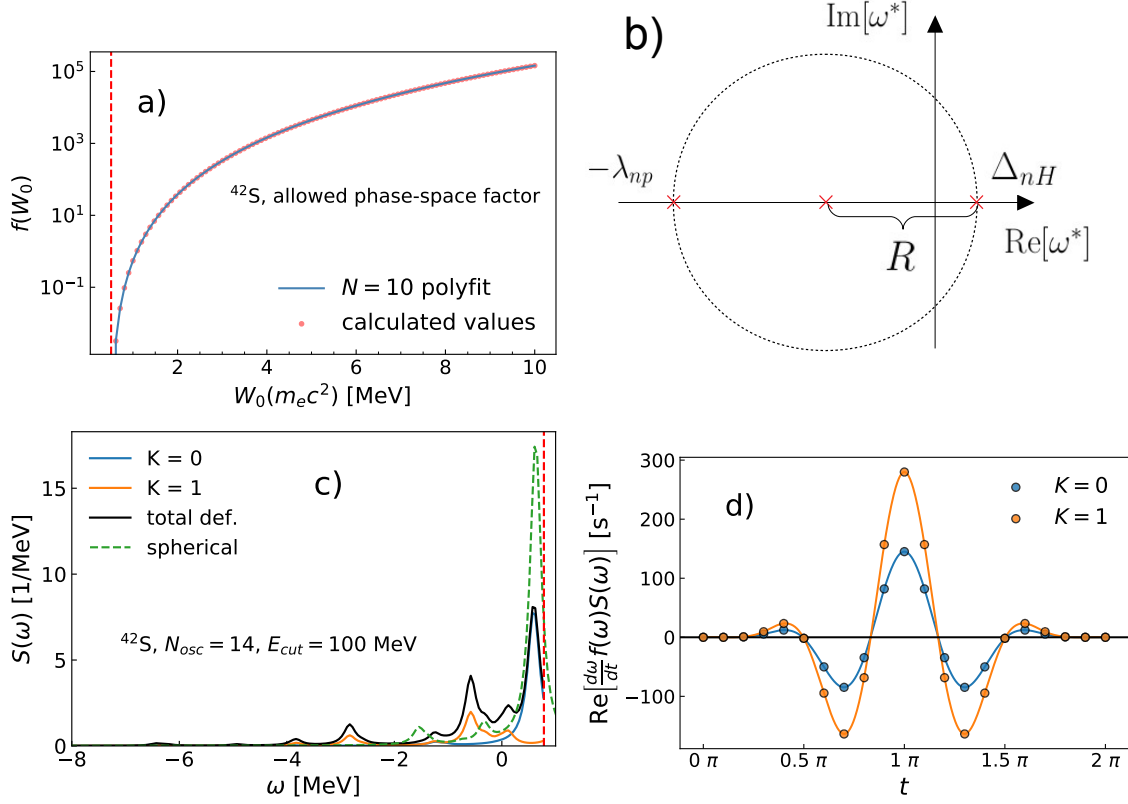


Figure 7.12: (a) The calculated values of the phase-space integral in Eq. (7.53) (red circles) together with a  $N = 10$  polynomial fit (solid blue). (b) The circular contour for the complex integration of the rate integral in Eq. (7.52). (c) The GT<sup>-</sup> strength function in <sup>42</sup>S calculated with the axially-deformed pnRQRPA (solid black) decomposed to contributions of  $K = 0$  (solid blue) and  $K = 1$  (solid orange) projections. Also shown are the spherical pnRQRPA results (dashed green). (d) The real part of the integrand in Eq. (7.57) is calculated for  $K = 0$  (blue circles) and  $K = 1$  (orange circles). The solid lines denote the cubic spline interpolation of the calculated points.

calculations predict shorter half-lives compared to the spherical in <sup>42</sup>S. In Fig. 7.12(d) we show the integrand in Eq. (7.57) both for  $K = 0$  and  $K = 1$  modes. We observe that the integrand is smooth enough to perform a spline interpolation and integration with any simple quadrature rule such as Simpson's. Indeed, such a result was also found in Ref. [77].

At this point, we calculate the  $\beta$ -decay half-life for the whole sulfur isotopic chain ( $Z = 16$ ). The q.p. basis is determined by  $N_{osc} = 16$  and  $E_{cut} = 100$  MeV, this range is more than enough to yield converged low-lying strength function for all considered nuclei. First, we perform the

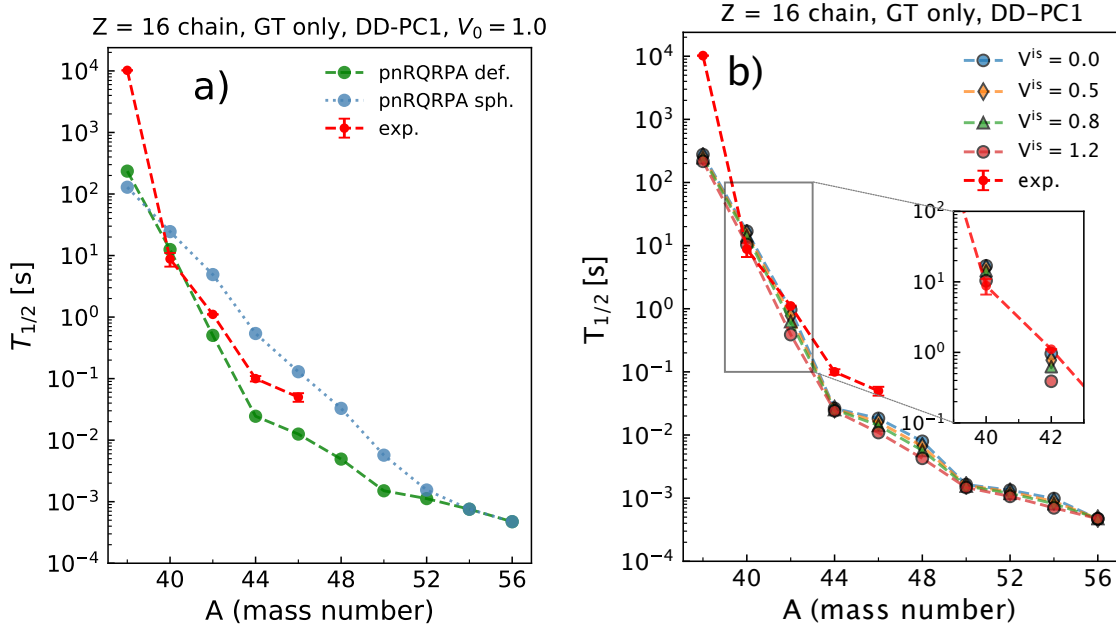


Figure 7.13: (a) The isotopic dependence of the  $\beta$ -decay half-lives  $T_{1/2}$  for sulfur calculated with the axially-deformed (green) and spherical (blue) pnQRPA, compared to the experimental data from Ref. [159]. Calculations are performed with the DD-PC1 interaction with isoscalar pairing strength  $V^{is} = 1.0$ . (b) The axially-deformed pnQRPA half-lives for different values of the isoscalar pairing strength  $V^{is}$  in the range 0–1.2. The indicated area of the main plot is enlarged in the inserted axis for better visualization.

calculations with the isoscalar pairing set to  $V^{is} = 1.0$  (same as isovector) and compare the results with the spherical pnQRPA calculations in Fig. 7.13(a). All the results are obtained by using the DD-PC1 interaction. For the axially-deformed pnQRPA, only the optimal  $\beta_2^*$  is used to calculate the half-life. We observe that, apart from  $^{38}\text{S}$ , the half-lives calculated with the axially-deformed pnQRPA are significantly reduced compared to the spherical calculations. For  $^{44}\text{S}$ , this reduction is more than an order of magnitude. Therefore, we can see that deformation effects lead to important changes in  $\beta$ -decay half-lives. Compared to the available experimental data, results for  $^{38}\text{S}$ ,  $^{40}\text{S}$ ,  $^{42}\text{S}$ , and  $^{44}\text{S}$  agree better once the deformation is included in the model. Note that for  $^{54,56}\text{S}$  both spherical and deformed calculations agree, since  $\beta_2^* \sim 0.0$  for those nuclei. This agreement further validates the implementation of our model, since the half-lives are calculated based on two independent pnQRPA implementations. It is interesting to study what happens when we vary the isoscalar pairing strength  $V^{is}$ . Based on the results presented in sections 3.1 and 5.2, we know



that an increase in the isoscalar pairing strength leads to a reduction of  $\beta$ -decay half-lives. In Ref. [208], employing a large-scale fitting procedure of isoscalar pairing strength on experimental  $\beta$ -decay half-lives with the spherical pnQRPA, we have deduced that for the DD-PC1 functional the isoscalar pairing strength should be  $V^{is} \approx 1.8$  for  $^{38}\text{S}$  and decrease to  $V^{is} \approx 1.0$  for  $^{56}\text{S}$ . Such large isoscalar pairing strength is caused by spherical calculations overestimating the experimental half-lives. On the other hand, we have demonstrated that deformation provides another mechanism for the reduction of half-lives. This means that isoscalar pairing strength for axially-deformed nuclei should be lower. To investigate how the isoscalar pairing alters the half-lives of deformed nuclei, in Fig. 7.13(b) we present the calculations for  $V^{is} = 0.0, 0.5, 0.8$  and  $1.2$ , in the range from vanishing residual  $pp$  interaction to being slightly larger than the corresponding isovector pairing at the RHB level.

We observe that increasing  $V^{is}$  leads to the shortening of half-lives. However, the effect of changing  $V^{is}$  on sulfur isotopes has a more moderate effect compared to the deformation effect in Fig. 7.13(a). The effect of the isoscalar pairing on half-lives is most pronounced for mid-shell nuclei. Note that isotopes with  $N = 28, 34$ , and  $40$  are independent of the variation of  $V^{is}$  due to shell closures. The magic numbers  $N = 28$  and  $40$  are known and well studied, while  $N = 34$  is an emerging shell number recently studied in lighter nuclei [209]. Since our calculations with deformation effects included tend to underestimate the experimental half-lives, except for  $^{30}\text{S}$  and  $^{40}\text{S}$ , a lower value of isoscalar pairing strength is needed, compared to spherical pnQRPA calculation. Based on results shown in Fig. 7.13(b) we employ  $V^{is} = 0.8$  in the following calculations. Note that determining  $V^{is}$  using the results only for one isotopic chain is not enough to generalize our results. Most studies done so far have found an isotopic dependence of the isoscalar pairing strength [34, 131, 161, 208]. A global study, similar to the one performed in Refs. [208, 210], will have to be performed for the axially-deformed pnQRPA before making systematic calculations. As the main purpose of this work is to explain the influence of deformation of  $\beta$ -decay half-lives, we take a single value  $V^{is} = 0.8$ , for all considered nuclei.

To generalize our conclusions, that deformation effects are important in determining the  $\beta$ -decay half-lives, we extend our calculations to even-even nuclei in Ti, Cr, Fe, and Zn isotopic chains. Note that we have omitted Ca and Ni isotopic chains with shell closure numbers,  $Z = 20$  and  $Z = 28$ , respectively, since most of the considered nuclei are spherical. By setting the isoscalar pairing strength to  $V^{is} = 0.8$ , there are no free-parameters in the model. The results are shown in Fig. 7.14(a)-(e). First, in Fig. 7.14(a) we display the isotopic dependence of the optimal quadrupole

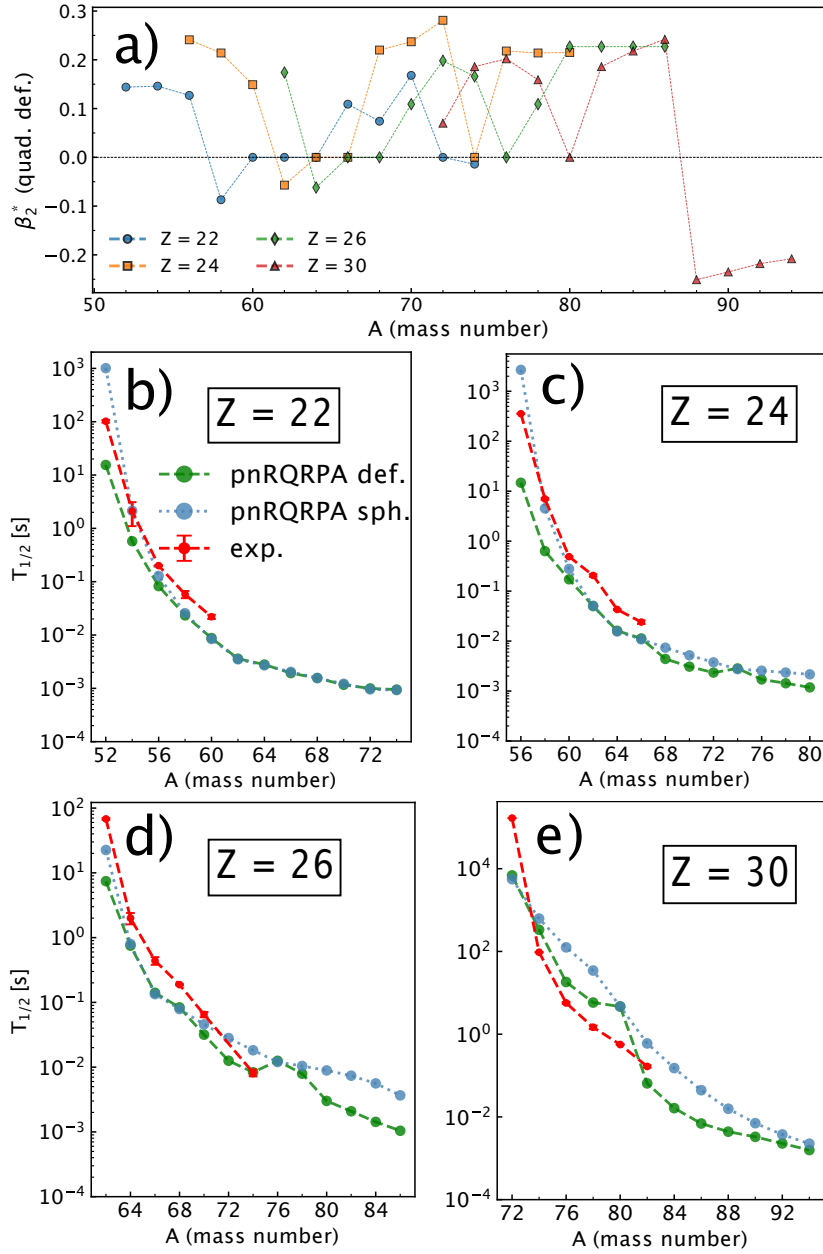


Figure 7.14: (a) Isotopic dependence of the quadrupole deformation  $\beta_2^*$  for even-even nuclei in Ti, Cr, Fe, and Zn isotopic chains. The  $\beta$ -decay half-lives calculated with the axially-deformed (green) and spherical pnQRPA (blue), compared to the experimental data from Ref. [159] for Ti (b), Cr (c), Fe (d) and Zn (e) isotopic chains.

deformation  $\beta_2^*$ . Most considered nuclei display prolate shapes, while fewer are either spherical or prolate-deformed. In Fig. 7.14(b) the half-lives for the titanium isotopic chain are shown. The deformation effects have a large role in reducing the half-lives for  $^{52}\text{Ti}$  and  $^{54}\text{Ti}$ , being both prolate in their ground state. For  $^{58}\text{Ti}$  we have a shape change from prolate to oblate configurations, however, its impact on the half-life is negligible compared to the spherical calculation. Even though we have non-vanishing deformation for some heavier Ti isotopes, its effect on the half-life seems to be negligible. Apart from  $^{52}\text{Ti}$ , it seems that spherical pnQRPA is in better agreement with the experimental data. In Fig. 7.14(c) we show the results for the chromium chain, where it seems that deformation tends to reduce the half-lives more significantly but in a turn, underestimates the experimental data. For the iron chain in Fig. 7.14(d) the deformation effects also reduce the half-lives. The spherical pnQRPA compares slightly better with experiment up to  $^{72}\text{Fe}$ . Notice that deformation effects bring the half-life of  $^{74}\text{Fe}$  within experimental uncertainty. Due to  $N = 50$  shell closure in  $^{76}\text{Fe}$  the nucleus is spherical, with heavier isotopes assuming prolate shape and significantly reducing the half-lives up to  $^{86}\text{Fe}$ . Up to now, we can conclude that spherical calculations performed better in reproducing the experimental data than the deformed pnQRPA. However, in Fig. 7.14(e) for zinc isotopes, we see that there exists a significant difference between experimental half-lives and those obtained in spherical calculations. The reduction of half-lives induced by deformation effects seems to bring the calculations to better agreement with the experiment. We observe a "kink" in isotopic dependence of half-lives for  $^{80}\text{Zn}$  due to shell closure, making the nucleus more stable. As can be seen in Fig. 7.14(a)  $^{80}\text{Zn}$  is indeed spherical, thus both deformed and spherical pnQRPA agree in their results. However, beyond the shell closure,  $^{82}\text{Zn}$  has a prolate shape, bringing the half-lives closer to the experimental data. Therefore, we conclude that the main effect of deformation is to reduce the  $\beta$ -decay half-lives. This is because more states contribute to the  $Q_\beta$  window in the deformed nucleus due to a larger density of states. Furthermore, the value of the isoscalar pairing  $V^{is}$  should be reduced, compared to the isovector pairing in the RHB ground-state, to better reproduce the experimental data. In the calculations above, we see that  $V^{is} = 0.8$  is probably too large for lighter systems, while it does well for zinc.

The deformation effects have a sizeable influence on half-lives. Based on the limited set of nuclei for which we have presented our results, it is certain that the  $V^{is}$  parameterization should be improved. Namely, both the deformation and  $V^{is}$  act to decrease the half-lives. Therefore, employing the  $V^{is}$  determined from spherical calculations leads to underestimating the experimental half-lives with the deformed calculations. Certainly, the deformed pnQRPA is a more general

version of the spherical pnRQRPA since most nuclei are known to be deformed in their ground state. Furthermore, the effect of reducing the half-lives can be more than an order of magnitude. However, more details should be considered within the model to grasp all the mechanisms that contribute to half-lives. First of all, in this work we have only considered the allowed GT transitions, omitting the first forbidden. For most of the  $pf$ -shell nuclei this is an excellent approximation, as demonstrated in Ref. [78], where it is seen that first-forbidden transitions start to contribute for  $Z > 60$ . Second, a more precise treatment of  $V^{is}$  should be implemented, instead of adopting a constant value. Third, the rotational invariance of the nucleus should be restored, which would influence the strength function, and thereby the half-lives. In Ref. [77] it was found that such corrections can be on the order of 10%. Finally, going beyond the scope of this thesis, one should consider the coupling of the 2 q.p. excitations to higher correlations, for instance, within the QPVC model [132, 150, 161].

# Chapter 8

## Conclusion

The main goal of this thesis is to establish a robust theoretical framework for studying nuclear charge-exchange excitations and the weak interaction rates in extreme astrophysical environments such as supernovae and neutron star mergers. Examples of such processes investigated within this thesis include electron capture and  $\beta$ -decays. We have developed a novel theoretical framework to improve the description of the underlying microscopic effects required for the rate calculations. The framework encompasses finite-temperature correlations, particle continuum contributions, de-excitations, and effects such as pairing and deformation. The framework allows performing large-scale calculations of high interest for nuclear astrophysics.

In Chapter 3, we have introduced the linear response FT-pnRQRPA based on the FT-RHB in spherical symmetry. The model is based on the point-coupling functionals DD-PC1 and DD-PCX in the  $ph$  channel, while in the  $pp$  channel, we assume the separable pairing interaction. The same form of the  $pp$  interaction was used both in the isoscalar and isovector channels. After benchmarking the implementation against the matrix FT-pnRQRPA, model calculations of the temperature evolution of spin-isospin excitations were performed for the even-even tin isotopes at temperatures  $T = 0$ –1.5 MeV. First, it is shown that the Fermi strength function is almost temperature independent and collected within a single resonance peak for all considered temperatures. The zero temperature IAS excitation energies compare well with the available experimental data, with results within 1 MeV for DD-PC1 and DD-PCX functionals. The GT strength function, having a more complicated structure, displays significant changes with increasing temperature. The temperature effect is especially pronounced for  $^{120}\text{Sn}$  and  $^{124}\text{Sn}$ , where the GTR energy is fragmented at zero temperature. As the temperature is increased, the degeneracy in the GTR is restored already at  $T = 0.9$  MeV.

The main effect of temperature in tin isotopes is to reduce the influence of pairing correlations, which eventually vanish at critical temperature  $T_c^p$  at  $T \sim 1$  MeV. Furthermore, the repulsive residual interaction softens with increasing temperature, slightly shifting the strength function to lower excitation energies. We have compared our results with the experimental centroid energies in  $^{112}\text{Sn}$ ,  $^{116}\text{Sn}$ , and  $^{132}\text{Sn}$  and found an agreement within 2 MeV. Consideration of the higher-order correlations, going beyond the RPA, is necessary to provide a more detailed comparison with the experimental strength function.

A detailed investigation of electron capture rates within the FT-pnRQRPA is given in Chapter 4. We start by establishing a theoretical formalism based on the FT-HBCS+FT-pnRQRPA [32]. Model calculations are performed on particular  $pf$ -shell nuclei where we found that the inclusion of pairing correlations can modify the EC rates by a significant amount. Pairing and temperature effects should be included for a complete description of the rates. We also generalized our results by extending the theoretical calculations to include transitions with negative energy (de-excitations) [31]. The de-excitations fully determine the EC rates above  $T > 0.5$  MeV for neutron-rich nuclei, found in abundance during the late stages of CCSNe explosions. To improve the performance of our numerical implementation, we used an integration technique based on calculating the neutrino distribution function. The predictive power of the FT-HBCS theory is improved by adjusting the pairing strength across the nuclide chart. The isoscalar pairing strength  $V^{is}$  is constrained by the experimental data on  $\beta$ -decay half-lives. Therefore, no free parameters are present within the model. We have benchmarked our calculations of EC rates on nuclei near the  $N = 50$  shell-closure against the non-relativistic FT-HFB+FT-pnFAM and shell-model (for  $^{86}\text{Kr}$ ) [33]. Agreement between the model calculations is satisfying, especially at higher temperatures. The EC rate sets obtained with our relativistic model and the non-relativistic FT-FHB+FT-pnFAM are used to perform 1D core-collapse simulations. Important observables, such as the density evolution of electron-to-baryon ratio  $Y_e$ , peak neutrino luminosity, and the enclosed mass at core bounce, are consistent between the two rate sets. Such a result leads us to conclude that the main correlations in the EC rates important for the CCSNe simulations are well constrained within the current theoretical models, and theoretical uncertainties are negligible. Our relativistic calculation includes the first-forbidden  $0^-$ ,  $1^-$ , and  $2^-$  multipoles, in addition to the allowed GT. Including the first-forbidden transitions leads to more noticeable differences in observables, mainly by increasing the overall rate.

We have applied the FT-HBCS+FTpnRQRPA framework to calculate  $\beta$ -decay half-lives in Chapter 5. By benchmarking our model with the experimental half-lives at zero temperature,

as well as the shell-model calculations at finite temperature, we have obtained excellent results. Our model includes allowed and first-forbidden transitions, temperature, and stellar density effects. Using an example calculation of temperature evolution of the half-lives in  $pf$ -shell nuclei up to  $T = 1.5$  MeV, we found that nuclei with initially longer half-lives are altered the most. These are nuclei found close to the stability valley and the vicinity of closed shells. On the other hand, neutron-rich nuclei with short half-lives at zero temperature show only moderate temperature effects. To obtain reasonable agreement with the shell-model calculations, we found that including de-excitations is crucial, especially for nuclei with strong  $\beta^+$  strength. As the temperature increases, the contribution of first-forbidden transitions becomes more important. Furthermore, by increasing the stellar density, we confirmed that it leads to a considerable reduction of the rates (an increase of half-lives) for  $\rho Y_e \geq 10^7$  g/cm<sup>3</sup>. A large-scale calculation of half-lives of even-even  $8 \leq Z \leq 82$  nuclei is performed at  $T = 5$  GK and  $T = 10$  GK for densities  $\rho Y_e = 10^7$  g/cm<sup>3</sup> and  $10^{10}$  g/cm<sup>3</sup>. The calculated data set is of high interest to the nuclear astrophysics community.

Up to Chapter 6 all results have assumed spherical symmetry. In Chapter 6, we present results for global bulk properties of even-even  $8 \leq Z \leq 104$  nuclei at finite temperature using the three state-of-the-art relativistic EDFs [35]. Calculations are performed with the FT-RHB theory supplemented with the continuum subtraction procedure using the BLV prescription. First, the importance of the continuum subtraction in weakly-bound nuclei is demonstrated, on an example of 1D coordinate-space solver and then extended to the axially-deformed FT-RHB calculation of <sup>210</sup>Gd. Without the subtraction procedure, potential energy surfaces with quadrupole constraint at finite temperature show considerable dependence on the size of the basis in which the FT-RHB equations are discretized. By subtracting the contribution of the nucleon vapor, results become independent of the basis size. The applicability of calculations in the h.o. basis is verified by benchmarking it against the corresponding coordinate-space solver, having an excellent agreement of subtracted free energy  $\bar{F}$ , entropy  $\bar{S}$  and the neutron chemical potential  $\lambda_n$  at high temperatures. The bulk properties of nuclei with increasing temperature are mainly influenced by: (i) a decrease of the pairing gaps, leading to a transition from a superfluid to a normal state, (ii) a shape-phase transition from axially deformed to spherical configuration, (iii) vanishing of magic nucleon numbers around shell closures. Since the nuclear shell effects tend to diminish with increasing temperature, more bound nuclei exist within the drip lines. This is especially pronounced around  $N = 126$  and  $N = 184$  shell closure.

We also account for nuclear deformation in the excited states by extending the FT-pnRQRPA

developed in Chapter 3 to axially-deformed nuclei in Chapter 7. The implementation is based on the linear response formalism with point-coupling relativistic EDFs and a separable pairing interaction. Considering excitations in axial geometry requires extensions of the model resulting in a significantly larger dimension of the model space. After verifying our implementation and convergence properties, we calculated Fermi and GT strength. The Fermi strength function is not influenced by the deformation effects, while the GT strength function shows considerable fragmentation. We compared the calculated  $GT^+$  strength with available experimental data in  $pf$ -shell nuclei, confirming that the agreement is better once the deformation is included. Unlike the spherical calculations, which show mostly  $GT^+$  strength located in one peak, the deformation effects tend to fragment the strength function and bring it closer to the shape of the experimental distribution. By calculating the  $GT^-$  strength in  $^{58,60,62}\text{Fe}$  for both oblate and prolate configurations, we demonstrate considerable changes in the strength function compared to the spherical calculations. The temperature evolution of the  $GT^+$  strength function shows almost no changes up to  $T = 2$  MeV. However, by including deformation effects, the first changes in the strength function are visible already at  $T = 0.5$  MeV. Therefore, the newly developed FT-pnRQRPA considers nuclear pairing, finite-temperature effects, and deformation, providing numerous enticing applications. As one such application, we have considered the influence of deformation on  $\beta$ -decay half-lives at zero temperature. Calculation of half-lives in the sulfur isotopic chain demonstrates that the axially-deformed pnRQRPA leads to a considerable reduction of half-lives compared to the spherical pnRQRPA by more than an order of magnitude. By performing calculations for Ti, Cr, Fe, and Zn isotopic chains, with isoscalar pairing strength  $V^{is} = 0.8$ , we found a systematic reduction of the half-lives by the deformation effects.

With the newly developed theoretical frameworks, we aim to further extend our study to nuclear astrophysics. The research of EC rates at finite temperature performed in Ref. [33] on diamond region nuclei has to be broadened to calculations throughout the nuclide chart by considering the deformation effects. The same applies to the  $\beta$ -decay rates at zero and finite temperature. At zero temperatures, a systematic calculation of  $\beta$ -decay rates is underway, which will serve as an input for  $r$ -process simulations, with exciting implications for modeling nuclear abundances. With improved theoretical considerations accomplished in this thesis, we can calculate both EC and  $\beta$ -decay rates throughout the nuclide chart of high interest to the entire nuclear astrophysics community. Furthermore, considering hot nuclei, and exploring the limits of the nuclear landscape at high temperatures can unveil the intriguing dynamics of neutron star mergers and supernovae.



# Appendix A

## Linear response theory derivations

In this Appendix we derive some of the important expressions used throughout Chapters 3 and 7.

### A.1 Deriving the time-dependent Hartree-Fock-Bogoliubov equations

First, we have to derive the time-dependent HFB (TDHFB) equation (3.12), starting from the q.p. operators in the Heisenberg picture as defined in Eq. (3.11). The time derivative of the generalized density matrix yields

$$\dot{\mathcal{R}}(t)_{\mu\mu'} = \langle \dot{a}^\dagger(t)_{\mu'} a(t)_\mu \rangle_T + \langle a^\dagger(t)_{\mu'} \dot{a}(t)_\mu \rangle_T, \quad (\text{A.1})$$

which together with the Heisenberg equations of motion for the q.p. operators

$$i\dot{a}(t)_\mu = [a(t)_\mu, H], \quad i\dot{a}^\dagger(t)_\mu = [a^\dagger(t)_\mu, H], \quad (\text{A.2})$$

gives:

$$\dot{\mathcal{R}}_{\mu\mu'} = -i\langle [a_{\mu'}^\dagger, H] a_\mu \rangle_T - i\langle a_{\mu'}^\dagger [a_\mu, H] \rangle_T. \quad (\text{A.3})$$

The commutators appearing in the above expression can be reduced to

$$\begin{aligned}
 [a_{\mu'}^\dagger, H] &= \frac{1}{2} \sum_{\nu\nu'} \mathcal{H}_{\nu\nu'} [a_{\mu'}^\dagger, a_\nu^\dagger a_{\nu'}] = \frac{1}{2} \sum_{\nu\nu'} \mathcal{H}_{\nu\nu'} (\delta_{\mu'\bar{\nu}} a_{\nu'} - a_\nu^\dagger \delta_{\mu'\nu'}), \\
 [a_\mu, H] &= \frac{1}{2} \sum_{\nu\nu'} \mathcal{H}_{\nu\nu'} [a_\mu, a_\nu^\dagger a_{\nu'}] = \frac{1}{2} \sum_{\nu\nu'} \mathcal{H}_{\nu\nu'} (\delta_{\mu'\nu} a_{\nu'} - a_\nu^\dagger \delta_{\mu'\bar{\nu}}),
 \end{aligned} \tag{A.4}$$

where  $\mathcal{H}_{\mu\mu'}$  label the matrix elements of the Hamiltonian  $H$  in the q.p. configuration space. The time derivative of the density matrix becomes

$$\begin{aligned}
 \dot{\mathcal{R}}_{\mu\mu'} &= -i \frac{1}{2} \sum_{\nu\nu'} \mathcal{H}_{\nu\nu'} \left( \langle \delta_{\mu'\bar{\nu}} a_{\nu'} a_\mu - \delta_{\mu'\nu'} a_\nu^\dagger a_\mu \rangle + \langle \delta_{\mu\nu} a_{\mu'}^\dagger a_{\nu'} - \delta_{\nu\bar{\nu}'} a_{\mu'}^\dagger a_\nu^\dagger \rangle \right) \\
 &= -i \frac{1}{2} \sum_{\nu\nu'} \mathcal{H}_{\nu\nu'} (\delta_{\mu'\bar{\nu}} \mathcal{R}_{\mu\bar{\nu}'} - \delta_{\mu'\nu'} \mathcal{R}_{\mu\nu} + \delta_{\mu\nu} \mathcal{R}_{\nu'\mu'} - \delta_{\mu\bar{\nu}'} \mathcal{R}_{\bar{\nu}\mu'}) \\
 &= -\frac{i}{2} \left( \sum_{\nu'} \mathcal{H}_{\bar{\mu}'\nu'} \mathcal{R}_{\mu\bar{\nu}'} - \sum_{\nu} \mathcal{H}_{\nu\mu'} \mathcal{R}_{\mu\nu} + \sum_{\nu'} \mathcal{H}_{\mu\nu'} \mathcal{R}_{\nu'\mu} - \sum_{\nu} \mathcal{H}_{\nu\bar{\mu}} \mathcal{R}_{\bar{\nu}\mu'} \right) \\
 &= -\frac{i}{2} \left( -\sum_{\nu'} \mathcal{R}_{\mu\bar{\nu}'} \mathcal{H}_{\bar{\nu}'\mu'} - \sum_{\nu} \mathcal{R}_{\mu\nu} \mathcal{H}_{\nu\mu'} + \sum_{\nu'} \mathcal{H}_{\mu\nu'} \mathcal{R}_{\nu'\mu'} + \sum_{\nu} \mathcal{H}_{\mu\bar{\nu}} \mathcal{R}_{\bar{\nu}\mu'} \right) \\
 &= -i [\mathcal{H}, \mathcal{R}]_{\mu\mu'}.
 \end{aligned} \tag{A.5}$$

We have used the anti-commutation property of the q.p. operators from Eq. (3.9). Again, we have linearized the Hamiltonian by keeping only the terms that appear in the usual RHB equation, consisting only of the product of two q.p. operators

$$\mathcal{H}_{\mu\mu'} = \begin{pmatrix} H^{11} & H^{20} \\ -H^{20*} & -H^{11*} \end{pmatrix} \xrightarrow{\mathcal{W}^\dagger \mathcal{H} \mathcal{W}} \begin{pmatrix} h & \Delta \\ -\Delta^* & -h^* \end{pmatrix}, \tag{A.6}$$

where  $\mathcal{W}$  denotes the Bogoliubov transformation [58].

## A.2 Linear response equation in the proton-neutron basis

The super-matrix formulation of the generalized density and Hamiltonian is introduced in Eqs. (3.18) and (3.19). Here we start from the TDHFB equation in the proton-neutron super-matrix

space

$$i\delta\dot{\mathbb{R}}(t) = [\mathbb{H}_0, \delta\mathbb{R}(t)] + [\delta\mathbb{H}(t) + \mathbb{F}(t), \mathbb{R}_0], \quad (\text{A.7})$$

and explicitly write the corresponding proton and neutron blocks to get the following form:

$$\begin{aligned} i \begin{pmatrix} 0 & \delta\dot{\mathbb{R}}^{(pn)} \\ \delta\dot{\mathbb{R}}^{(np)} & 0 \end{pmatrix} &= \left[ \begin{pmatrix} \mathbb{H}_0^{(p)} & 0 \\ 0 & \mathbb{H}_0^{(n)} \end{pmatrix}, \begin{pmatrix} 0 & \delta\mathbb{R}^{(pn)} \\ \delta\mathbb{R}^{(np)} & 0 \end{pmatrix} \right] \\ &+ \left[ \begin{pmatrix} \delta\mathbb{H}^{(p)} & \delta\mathbb{H}^{(pn)} \\ \delta\mathbb{H}^{(np)} & \delta\mathbb{H}^{(n)} \end{pmatrix} + \mathbb{F}(t), \begin{pmatrix} 0 & \delta\mathbb{R}^{(pn)} \\ \delta\mathbb{R}^{(np)} & 0 \end{pmatrix} \right], \end{aligned} \quad (\text{A.8})$$

which reduces to

$$\begin{aligned} i \begin{pmatrix} 0 & \delta\dot{\mathbb{R}}^{(pn)} \\ \delta\dot{\mathbb{R}}^{(np)} & 0 \end{pmatrix} &= \begin{pmatrix} 0 & \mathbb{H}_0^{(p)} \delta\mathbb{R}^{(pn)} \\ \mathbb{H}_0^{(n)} \delta\mathbb{R}^{(np)} & 0 \end{pmatrix} - \begin{pmatrix} 0 & \delta\mathbb{R}^{(pn)} \mathbb{H}_0^{(n)} \\ \delta\mathbb{R}^{(np)} \mathbb{H}_0^{(p)} & 0 \end{pmatrix} \\ &+ \begin{pmatrix} (\delta\mathbb{H}^{(p)} + \mathbb{F}^{(p)})\mathbb{R}_0^{(p)} - \mathbb{R}_0^{(p)}(\delta\mathbb{H}^{(p)} + \mathbb{F}^{(p)}) & (\delta\mathbb{H}^{(pn)} + \mathbb{F}^{(pn)})\mathbb{R}_0^{(n)} - \mathbb{R}_0^{(p)}(\delta\mathbb{H}^{(pn)} + \mathbb{F}^{(pn)}) \\ (\delta\mathbb{H}^{(np)} + \mathbb{F}^{(np)})\mathbb{R}_0^{(p)} - \mathbb{R}_0^{(n)}(\delta\mathbb{H}^{(np)} + \mathbb{F}^{(np)}) & (\delta\mathbb{H}^{(n)} + \mathbb{F}^{(n)})\mathbb{R}_0^{(n)} - \mathbb{R}_0^{(n)}(\delta\mathbb{H}^{(n)} + \mathbb{F}^{(n)}) \end{pmatrix}. \end{aligned} \quad (\text{A.9})$$

Now we can take only the upper right block (*i.e.* the  $pn$  component) from the above equation to get the linearized TDHFB equation in the reduced space

$$i\delta\dot{\mathbb{R}}^{(pn)}(t) = \mathbb{H}_0^{(p)} \delta\mathbb{R}^{(pn)} - \delta\mathbb{R}^{(pn)} \mathbb{H}_0^{(n)} + (\delta\mathbb{H}^{(pn)} + \mathbb{F}^{(pn)})\mathbb{R}_0^{(n)} - \mathbb{R}_0^{(p)}(\delta\mathbb{H}^{(pn)} + \mathbb{F}^{(pn)}). \quad (\text{A.10})$$

By writing the time-dependence of above equation as in Eq. (3.21) and introducing the q.p. basis we get

$$- \omega \delta\mathcal{R}_{\pi\nu} = H_{0\pi\pi'} \delta\mathcal{R}_{\pi'\nu} - \delta\mathcal{R}_{\pi\nu'} H_{0\nu'\nu} + (\delta H + F)_{\pi\nu'} \mathcal{R}_{0\nu'\nu} - \mathcal{R}_{0\pi\pi'} (\delta H + F)_{\pi'\nu}, \quad (\text{A.11})$$

thus lowering the dimension of our problem by half. Using the fact that the static part of the generalized matrix and the mean-field Hamiltonian in the q.p. basis are diagonal used as the starting point for the section 3.1

$$\mathcal{R}_{0\mu\mu'} = f_\mu \delta_{\mu\mu'}, \quad H_{0\mu\mu'} = E_\mu \delta_{\mu\mu'}, \quad (\text{A.12})$$

with  $f_{\bar{\mu}} = 1 - f_{\mu}$ ,  $E_{\bar{\mu}} = -E_{\mu}$ , we have derived the linear response equation

$$-\omega \delta \mathcal{R}_{\pi\nu} = (E_{\pi} - E_{\nu}) \delta \mathcal{R}_{\pi\nu} - (f_{\pi} - f_{\nu})(\delta H_{\pi\nu} + F_{\pi\nu}). \quad (\text{A.13})$$

In the above,  $\pi$  denotes the proton q.p. and  $\nu$  neutron q.p. states. We have written the linear response equation in the proton-neutron notation.

### A.3 Derivation of the interaction term $\mathbb{W}$

Here we show the derivation of the expression for the interaction matrix  $\mathbb{W}$  in Eq. (3.27) in the proton-neutron basis. We mostly follow Ref. [107], deriving the equations in more details where necessary, and extending the approach to charge-exchange 2 q.p. excitations. We start by the variation of Bogoliubov transformation between the proton-neutron states

$$\begin{pmatrix} \bar{a}_{\pi}^{\dagger} \\ \bar{a}_{\pi} \end{pmatrix} = \left[ 1 + \begin{pmatrix} h^* & g^* \\ -g & -h \end{pmatrix} \right]_{\pi\nu} \begin{pmatrix} a_{\nu}^{\dagger} \\ a_{\nu} \end{pmatrix} \implies \begin{aligned} \bar{a}_{\pi}^{\dagger} &= a_{\pi}^{\dagger} + i \sum_{\nu'} (h_{\pi\nu'}^*(t) a_{\nu'}^{\dagger} + g_{\pi\nu'}^*(t) a_{\nu'}), \\ \bar{a}_{\pi} &= a_{\pi} - i \sum_{\nu'} (h_{\pi\nu'}(t) a_{\nu'} + g_{\pi\nu'}(t) a_{\nu'}^{\dagger}), \end{aligned} \quad (\text{A.14})$$

where  $h(t) = h(t)^{\dagger}$  and  $g(t) = -g(t)^T$  since the transformation needs to be unitary. The causal equation of motion for the density operator can be written as

$$\mathcal{R}(t) = U(t, t_0) \mathcal{R}(t_0) U^{\dagger}(t, t_0), \quad (\text{A.15})$$

where the time evolution operator is defined by the Schrödinger equation

$$i(d/dt)\mathcal{R}(t) = [H, \mathcal{R}(t)]. \quad (\text{A.16})$$

The thermal equilibrium is obtained by setting  $(d/dt)\mathcal{R}(t) = 0$  thus

$$[H, \mathcal{R}(t_0)] = 0, \quad (\text{A.17})$$

obtaining the FT-RHB equation. In the presence of the time-dependent external field  $F(t)$  we get

$$i(d/dt)\mathcal{R}(t) = [H + F(t), \mathcal{R}(t)]. \quad (\text{A.18})$$

If the external field couples weakly to the system we can write  $\mathcal{R}(t) = \mathcal{R}_0 + \mathcal{R}_1(t)$  and inserting in the above equation

$$i(d/dt)\mathcal{R}_1(t) + [\mathcal{R}_1(t), H] = -[\mathcal{R}_0, F(t)]. \quad (\text{A.19})$$

A general unitary transformation can be expressed through the Hermitian operator  $W(t, t_0)$  as

$$U(t) = e^{iW(t)}, \quad (\text{A.20})$$

and if the external perturbation is weak we can expand the exponential in a Taylor series

$$U(t) = 1 + iW(t) + \frac{i^2}{2}W(t)^2 + \dots, \quad U^\dagger(t) = 1 - iW(t) + \frac{i^2}{2}W(t)^2 + \dots \quad (\text{A.21})$$

Thus the density operator  $\mathcal{R}(t) = \mathcal{R}_0(t) + \mathcal{R}_1(t) + \dots$  can be expressed as

$$\mathcal{R}_0(t) = \mathcal{R}(t_0), \quad \mathcal{R}_1(t) = i[W(t), \mathcal{R}(t_0)], \dots \quad (\text{A.22})$$

Time evolution of quasiparticle creation and annihilation operators is now given by

$$\bar{a}_\pi^\dagger = U(t)a_\pi^\dagger U^\dagger(t) = a_\pi^\dagger + i[W(t), a_\pi^\dagger] + \dots \quad (\text{A.23})$$

$$\bar{a}_\pi = U(t)a_\pi U^\dagger(t) = a_\pi + i[W(t), a_\pi] + \dots \quad (\text{A.24})$$

Also, we can vary the quasiparticle transformation as in Eq. (A.14):

$$\begin{aligned} \bar{a}_\pi^\dagger &= a_\pi^\dagger + i \sum_{\nu'} (h_{\pi\nu'}^*(t)a_{\nu'}^\dagger + g_{\pi\nu'}^*(t)a_{\nu'}) \\ \bar{a}_\pi &= a_\pi - i \sum_{\nu'} (h_{\pi\nu'}(t)a_{\nu'} + g_{\pi\nu'}(t)a_{\nu'}^\dagger) \end{aligned} \quad (\text{A.25})$$

Comparing these two equations, the following form of the  $W(t)$  operator can be deduced

$$W(t) = \sum_{\pi\nu} \begin{pmatrix} h & -g^* \\ g & -h^* \end{pmatrix} a_\pi^\dagger a_\nu \equiv \sum_{\pi\nu} \delta\mathcal{R}_{\pi\nu}(t) a_\pi^\dagger a_\nu, \quad (\text{A.26})$$

where we are using the notation of Eq. (3.8) in the doubled q.p. space. The external field operator has a periodic time dependence

$$F(t) = \sum_{\pi\nu} F_{\pi\nu} a_{\pi}^{\dagger} a_{\nu} e^{-i\omega t} + \text{h.c.} , \quad (\text{A.27})$$

inducing the periodic oscillations of induced density

$$\delta\mathcal{R}(t) = \sum_{\pi\nu} \delta\mathcal{R}_{\pi\nu} a_{\pi}^{\dagger} a_{\nu} e^{-i\omega t} + \text{h.c.} . \quad (\text{A.28})$$

We now insert this into the time-dependent equation (A.19), multiply from the right side by  $a_{\nu}^{\dagger} a_{\pi}$  and take the trace to project the response function

$$i\text{Tr}(\dot{\mathcal{R}}_1 a_{\nu}^{\dagger} a_{\pi}) + \text{Tr}([\mathcal{R}_1(t), H] a_{\nu}^{\dagger} a_{\pi}) = -\text{Tr}([\mathcal{R}_0, F(t)] a_{\nu}^{\dagger} a_{\pi}). \quad (\text{A.29})$$

Since there is no mixing in time, we can just collect the terms with  $e^{-i\omega t}$  to get

$$\begin{aligned} i\text{Tr}(\dot{\mathcal{R}}_1 a_{\nu}^{\dagger} a_{\pi}) &= i\text{Tr} \left\{ i \left[ (-i\omega) \sum_{\pi'\nu'} \delta\mathcal{R}_{\pi'\nu'} a_{\pi'}^{\dagger} a_{\nu'} e^{-i\omega t}, \mathcal{R}_0 \right] a_{\nu}^{\dagger} a_{\pi} \right\} \\ &= i\omega \sum_{\pi'\nu'} \delta\mathcal{R}_{\pi'\nu'} \text{Tr} \left\{ \left[ a_{\pi'}^{\dagger} a_{\nu'}, \mathcal{R}_0 \right] a_{\nu}^{\dagger} a_{\pi} \right\} e^{-i\omega t} \\ &= i\omega \sum_{\pi'\nu'} \delta\mathcal{R}_{\pi'\nu'} \text{Tr} \left\{ a_{\pi'}^{\dagger} a_{\nu'} \mathcal{R}_0 a_{\nu}^{\dagger} a_{\pi} - \mathcal{R}_0 a_{\pi'}^{\dagger} a_{\nu'} a_{\nu}^{\dagger} a_{\pi} \right\} e^{-i\omega t} \\ &= i\omega \sum_{\pi'\nu'} \delta\mathcal{R}_{\pi'\nu'} \text{Tr} \left\{ \mathcal{R}_0 a_{\nu}^{\dagger} a_{\pi} a_{\pi'}^{\dagger} a_{\nu'} - \mathcal{R}_0 a_{\pi'}^{\dagger} a_{\nu'} a_{\nu}^{\dagger} a_{\pi} \right\} e^{-i\omega t} \\ &= i\omega \sum_{\pi'\nu'} \delta\mathcal{R}_{\pi'\nu'} \left\{ \langle a_{\nu}^{\dagger} a_{\pi} a_{\pi'}^{\dagger} a_{\nu'} \rangle - \langle a_{\pi'}^{\dagger} a_{\nu'} a_{\nu}^{\dagger} a_{\pi} \rangle \right\} e^{-i\omega t} \\ &= i\omega \sum_{\pi'\nu'} \delta\mathcal{R}_{\pi'\nu'} \left\{ \langle [a_{\nu}^{\dagger} a_{\pi}, a_{\pi'}^{\dagger} a_{\nu'}] \rangle \right\} e^{-i\omega t}, \end{aligned} \quad (\text{A.30})$$

where we have used the cyclic property of the trace and  $\text{Tr}(\mathcal{R}_0 \dots) = \langle \dots \rangle$ . For the second term we have

$$\begin{aligned}
 \text{Tr} \{ [\mathcal{R}_1(t), H] a_\nu^\dagger a_\pi \} &= \text{Tr} \{ [i[W(t), \mathcal{R}_0], H] a_\nu^\dagger a_\pi \} \\
 &= i \text{Tr} \{ W(t) \mathcal{R}_0 H a_\nu^\dagger a_\pi - \mathcal{R}_0 W(t) H a_\nu^\dagger a_\pi - H W(t) \mathcal{R}_0 a_\nu^\dagger a_\pi + H \mathcal{R}_0 W(t) a_\nu^\dagger a_\pi \} \\
 &= i \langle H a_\nu^\dagger a_\pi W(t) \rangle - \langle W(t) H a_\nu^\dagger a_\pi \rangle - \langle a_\nu^\dagger a_\pi H W(t) \rangle + \langle W(t) a_\nu^\dagger a_\pi H \rangle \\
 &= i \langle [H, a_\nu^\dagger a_\pi], W(t) \rangle.
 \end{aligned} \tag{A.31}$$

The third term is

$$\text{Tr} \{ [\mathcal{R}_0, F(t)] a_\nu^\dagger a_\pi \} = \langle [F(t), a_\nu^\dagger a_\pi] \rangle. \tag{A.32}$$

Thus the linear response equation is obtained as

$$\begin{aligned}
 i\omega \sum_{\pi'\nu'} \delta \mathcal{R}_{\pi'\nu'} \left\{ \langle [a_\nu^\dagger a_\pi, a_{\pi'}^\dagger a_{\nu'}] \rangle \right\} + \delta \mathcal{R}_{\pi'\nu'} i \langle [H, a_\nu^\dagger a_\pi], a_{\pi'}^\dagger a_{\nu'} \rangle = \\
 - \sum_{\pi'\nu'} F_{\pi'\nu'} \langle [a_{\pi'}^\dagger a_{\nu'}, a_\nu^\dagger a_\pi] \rangle.
 \end{aligned} \tag{A.33}$$

The Hamiltonian operator has the separable form in the single-particle basis

$$\hat{H} = \sum_p \varepsilon_p c_p^\dagger c_p + \sum_n \varepsilon_n c_n^\dagger c_n + \chi \sum_{pnp'n'} D_{pn}^* D_{p'n'} c_p^\dagger c_{p'} c_n^\dagger c_{n'}, \tag{A.34}$$

where the first two terms correspond to the diagonal single-particle part (*mean-field*), and the third term represents the separable residual interaction, where  $v_{pnp'n'} = \chi D_{pn}^* D_{p'n'}$ . By transforming in the quasiparticle basis we get

$$\hat{H} = \underbrace{\sum_{\pi} E_{\pi} \alpha_{\pi}^{\dagger} \alpha_{\pi} + \sum_{\nu} E_{\nu} \alpha_{\nu}^{\dagger} \alpha_{\nu}}_{\hat{H}^0} + \chi \sum_{\pi\nu\pi'\nu'} D_{\pi\nu}^* D_{\pi'\nu'} \alpha_{\nu}^{\dagger} \alpha_{\pi} \alpha_{\pi'}^{\dagger} \alpha_{\nu'}, \tag{A.35}$$

where  $\hat{H}_0$  is the mean-field Hamiltonian (Notice  $\alpha$  instead of  $a$  in  $E_\pi, E_\nu$  parts). We can now evaluate the commutators using the generalized Wick theorem

$$\begin{aligned} \langle [a_\nu^\dagger a_\pi, a_{\pi'}^\dagger a_{\nu'}] \rangle &= \delta_{\pi\pi'} \delta_{\nu\nu'} (f_\nu - f_\pi), \\ \langle [H^0, a_\nu^\dagger a_\pi, a_{\pi'}^\dagger a_{\nu'}] \rangle &= (E_\nu - E_\pi)(f_\nu - f_\pi) \delta_{\nu\nu'} \delta_{\pi\pi'}, \\ \langle [H, a_\nu^\dagger a_\pi, a_{\pi'}^\dagger a_{\nu'}] \rangle &= (f_\pi - f_\nu)(f_{\nu'} - f_{\pi'}) (\mathcal{D}_{\pi'\nu'}^* \mathcal{D}_{\pi\nu} + \mathcal{D}_{\bar{\pi}'\bar{\nu}'}^* \mathcal{D}_{\bar{\pi}\bar{\nu}} + \text{Fock terms}), \end{aligned} \quad (\text{A.36})$$

where we keep the direct terms. By inserting in the linear response equation we get (neglecting Fock terms)

$$\begin{aligned} i\omega \delta \mathcal{R}_{\pi'\nu'} \delta_{\pi\pi'} \delta_{\nu\nu'} (f_\nu - f_\pi) + \delta \mathcal{R}_{\pi'\nu'} i(E_\nu - E_\pi)(f_\nu - f_\pi) \delta_{\nu\nu'} \delta_{\pi\pi'} \\ + \sum_{\pi'\nu'} \delta \mathcal{R}_{\pi'\nu'} i(f_\pi - f_\nu)(f_{\nu'} - f_{\pi'}) (\mathcal{D}_{\pi'\nu'}^* \mathcal{D}_{\pi\nu} + \mathcal{D}_{\bar{\pi}'\bar{\nu}'}^* \mathcal{D}_{\bar{\pi}\bar{\nu}}) = +F_{\pi'\nu'} \delta_{\pi\pi'} \delta_{\nu\nu'} (f_\nu - f_\pi). \end{aligned} \quad (\text{A.37})$$

To get the linear response equation we need to redefine

$$\delta \tilde{\mathcal{R}}_{\pi\nu} = i \delta \mathcal{R}_{\pi\nu} (f_\nu - f_\pi), \quad (\text{A.38})$$

so that the linear response equation is rewritten as

$$\begin{aligned} (\omega - E_\pi + E_\nu) \delta \tilde{\mathcal{R}}_{\pi\nu} &= +F_{\pi\nu} (f_\nu - f_\pi) \delta_{\pi\pi'} \delta_{\nu\nu'} + \sum_{\pi'\nu'} \delta \tilde{\mathcal{R}}_{\pi'\nu'} (f_\nu - f_\pi) (\mathcal{D}_{\pi'\nu'}^* \mathcal{D}_{\pi\nu} + \mathcal{D}_{\bar{\pi}'\bar{\nu}'}^* \mathcal{D}_{\bar{\pi}\bar{\nu}}) \\ &= (f_\nu - f_\pi) (F_{\pi\nu} + \delta H_{\pi\nu}), \end{aligned} \quad (\text{A.39})$$

where the factor  $i$  was included in the definition (A.38). The above equation is in agreement with Eq. (3.20) and with the following definition of the induced Hamiltonian

$$\delta H_{\pi\nu} = \sum_{\pi'\nu'} \tilde{\mathcal{R}}_{\pi'\nu'} (\mathcal{D}_{\pi'\nu'}^* \mathcal{D}_{\pi\nu} + \mathcal{D}_{\bar{\pi}'\bar{\nu}'}^* \mathcal{D}_{\bar{\pi}\bar{\nu}}) \equiv \sum_{\pi'\nu'} \mathbb{W}_{\pi\nu\pi'\nu'} \tilde{\mathcal{R}}_{\pi'\nu'}. \quad (\text{A.40})$$

This proves form of the interaction term in Eq. (3.27).



## Appendix B

# Interpretation of the FT-pnRQRPA strength function

In this Appendix, we demonstrate the origins of the detailed balance factor, first appearing in Eq. (3.33). The exact response function  $R_{FF}^e$  is obtained from the expression [75]

$$R_{FF}^e = \frac{1}{Z} \sum_{i,f} e^{-\beta\omega_i} \left[ \frac{|\langle f|\hat{F}|i\rangle|^2}{\omega - \omega_{fi}} - \frac{|\langle f|\hat{F}^\dagger|i\rangle|^2}{\omega + \omega_{fi}} \right], \quad (\text{B.1})$$

where  $|i(f)\rangle$  is the initial(final) state with the energy  $\omega_{i(f)}$  and  $\omega_{fi} = \omega_f - \omega_i$ . The external field operator is  $\hat{F}$  (for which we assume  $\hat{F} \neq \hat{F}^\dagger$ ), and  $Z$  is the partition function defined in Sec. 2.3. Taking the imaginary part of the exact response function we get

$$\text{Im}[R_{FF}^e] = \frac{1}{Z} \sum_{i,f} e^{-\beta\omega_i} \left[ |\langle f|\hat{F}|i\rangle|^2 \delta(\omega - \omega_{fi}) - |\langle f|\hat{F}^\dagger|i\rangle|^2 \delta(\omega + \omega_{fi}) \right], \quad (\text{B.2})$$

defined both for positive and negative excitation energies  $\omega$ . The double summation in above expression implies two types of transitions: (i) excitations  $i \rightarrow f$ , in addition to (ii) de-excitations  $f \rightarrow i$ . This is clear in the case when  $\hat{F}$  is the like particle operator, so that both  $i$  and  $f$  are within the same nucleus. However, if we suppose that  $\hat{F}$  is the charge-exchange operator, then the states  $i$  and  $f$  connect different nuclei. It is not clear that the daughter nucleus will have excited states at exactly matching energies as the parent. However, if the density of states is high, which is certainly true for highly excited nuclei, one can imagine the situation shown in Fig. B.1. This means that the

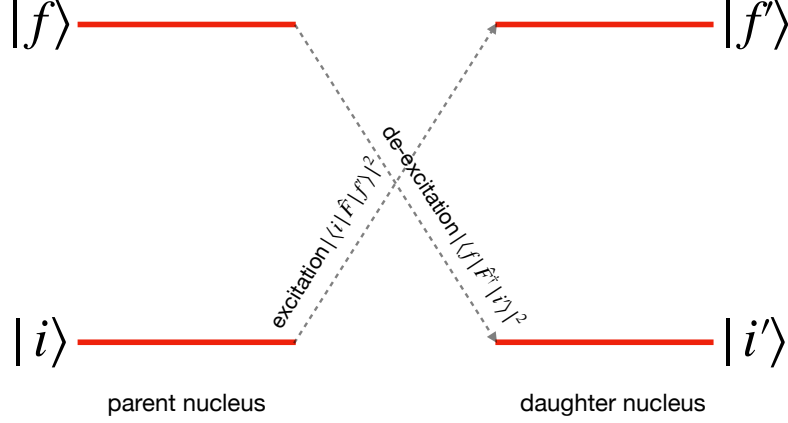


Figure B.1: The schematic energy diagram concerning the transitions between the states in the parent nucleus ( $i, f$ ) and those in the daughter nucleus ( $i', f'$ ). Both the excitation transition  $i \rightarrow f'$  dictated by the charge-exchange external field operator  $\hat{F}$  and de-excitation transition  $f \rightarrow i'$  dictated by  $\hat{F}^\dagger$  are shown.

transition  $i \rightarrow f'$  with energy  $\omega_{if}$  will correspond to transition  $f' \rightarrow i$  with energy  $\omega_{if} = -|\omega_{fi}|$ , where the states  $i', f'$  are found in the daughter nucleus.

To make the analogy complete, we drop the primes in the following. We rewrite Eq. (B.2) as

$$\begin{aligned} \text{Im}[R_{FF}^e] &= \frac{1}{Z} \sum_{i < f} e^{-\beta\omega_i} \left[ |\langle f|\hat{F}|i\rangle|^2 \delta(\omega - \omega_{fi}) - |\langle f|\hat{F}|i\rangle|^2 \delta(\omega + \omega_{fi}) \right] \\ &+ \frac{1}{Z} \sum_{i < f} e^{-\beta\omega_f} \left[ |\langle i|\hat{F}|f\rangle|^2 \delta(\omega - \omega_{if}) - |\langle i|\hat{F}|f\rangle|^2 \delta(\omega + \omega_{if}) \right], \end{aligned} \quad (\text{B.3})$$

by explicitly considering the terms in the double summation. Now, we fix excitation energy to  $\omega = \omega_{fi}$ , so that the imaginary part of the response function becomes

$$\begin{aligned} \text{Im}[R_{FF}^e]|_{\omega=\omega_{fi}} &= \frac{1}{Z} \sum_{i < f} \left\{ e^{-\beta\omega_i} |\langle f|\hat{F}|i\rangle|^2 - e^{-\beta\omega_f} |\langle i|\hat{F}^\dagger|f\rangle|^2 \right\} \delta(\omega - \omega_{fi}) \\ &= \frac{1}{Z} \sum_{i < f} e^{-\beta\omega_i} |\langle f|\hat{F}|i\rangle|^2 [1 - e^{-\beta\omega}] \delta(\omega - \omega_{fi}), \end{aligned} \quad (\text{B.4})$$

where in the second term we have used  $|\langle f|\hat{F}|i\rangle|^2 = |\langle i|\hat{F}^\dagger|f\rangle|^2$ . The *physical* strength function at finite temperature is given by [75]

$$S_F^{phys} = \frac{1}{Z} \sum_{i,f} e^{-\beta\omega_i} |\langle f|\hat{F}|i\rangle|^2 \delta(\omega - \omega_{fi}). \quad (\text{B.5})$$

Therefore, by inspecting expression derived in Eq. (B.4), we notice that the factor  $(1 - e^{-\beta\omega})^{-1}$  has to be divided from the exact response function, so that

$$S_F^{phys} = -\frac{1}{\pi} \text{Im} \left[ \frac{R_{FF}^e}{1 - e^{-\beta\omega}} \right]. \quad (\text{B.6})$$

Since the FT-pnRQRPA provides the approximation of the exact response function, the same conclusions should apply [31].

# Appendix C

## Low-momentum transfer limit of the Walecka model

In this section we present some of the calculation details within the Walecka model of the weak-interaction. Expression that we use to calculate the EC cross sections is derived in Refs. [152, 153]

$$\begin{aligned}
 \frac{d\sigma_{ec}}{d\Omega} &= \frac{G_F^2 g_V^2 \cos^2 \theta_C}{2\pi} \frac{F(Z, E_e)}{2J_i + 1} \\
 &\left\{ \sum_{J \geq 1} \mathcal{W}(E_e, E_\nu) \left\{ (1 - (\hat{\nu} \cdot \hat{\mathbf{q}})(\boldsymbol{\beta} \cdot \hat{\mathbf{q}})) \left[ |\langle J_f || \hat{\mathcal{T}}_J^{mag} || J_i \rangle|^2 + |\langle J_f || \hat{\mathcal{T}}_J^{el} || J_i \rangle|^2 \right] \right. \right. \\
 &\quad \left. \left. - 2\hat{\mathbf{q}} \cdot (\hat{\nu} - \boldsymbol{\beta}) \text{Re} \langle J_f || \hat{\mathcal{T}}_J^{mag} || J_i \rangle \langle J_f || \hat{\mathcal{T}}_J^{el} || J_i \rangle^* \right\} \right. \\
 &\quad \left. + \sum_{J \geq 0} \mathcal{W}(E_e, E_\nu) \left\{ (1 - \hat{\nu} \cdot \boldsymbol{\beta} + 2(\hat{\nu} \cdot \hat{\mathbf{q}})(\boldsymbol{\beta} \cdot \hat{\mathbf{q}})) |\langle J_f || \hat{\mathcal{L}}_J || J_i \rangle|^2 + (q + \hat{\nu} \cdot \boldsymbol{\beta}) |\langle J_f || \hat{\mathcal{M}}_J || J_i \rangle|^2 \right. \right. \\
 &\quad \left. \left. - 2\hat{\mathbf{q}} \cdot (\hat{\nu} + \boldsymbol{\beta}) \text{Re} \langle J_f || \hat{\mathcal{L}}_J || J_i \rangle \langle J_f || \hat{\mathcal{M}}_J || J_i \rangle^* \right\} \right\}, \tag{C.1}
 \end{aligned}$$

where the momentum transfer  $\mathbf{q} = \boldsymbol{\nu} - \mathbf{k}$  is difference between the electron and neutrino momenta,  $\hat{\mathbf{q}}$  and  $\hat{\nu}$  are the corresponding unit vectors, and  $\boldsymbol{\beta} = \mathbf{k}/E_e$ . Neutrino energy is denoted by  $E_\nu$  while the electron energy is  $E_e$ . The Fermi function  $F(Z, E_e)$  corrects cross section for the distortion of the electron wave function by the Coulomb field of the nucleus [154]. The Fermi constant is  $G^2 = G_F^2 g_V^2 \cos^2 \theta_c$ , where  $g_V$  is the vector coupling constant and  $\theta_C$  Cabbibo angle. We also

include the recoil term

$$\mathcal{W}(E_e, E_\nu) = \frac{E_\nu^2}{(1 + E_e/M_T(1 - \hat{\nu} \cdot \boldsymbol{\beta}))}, \quad (\text{C.2})$$

where  $M_T$  is the mass of target nucleus. The nuclear transition matrix elements are taken between the initial state  $|J_i\rangle$  and final state  $|J_f\rangle$ , corresponding to charge  $\hat{M}_J$ , longitudinal  $\hat{L}_J$ , transverse electric  $\hat{\mathcal{T}}_J^{el}$  and magnetic  $\hat{\mathcal{T}}_J^{mag}$  operators defined in Refs. [152, 153]. In this Appendix we investigate the reduction of Eq. (C.1) in the Gamow-Teller ( $J^\pi = 1^+$ ),  $q \rightarrow 0$  limit. Out of the four mentioned spherical tensor operators, only non-vanishing in this limit is  $\hat{\mathcal{T}}_J^{el}$ . It has the form

$$\hat{\mathcal{T}}_J^{el} = \frac{q}{M_N} \left[ F_1^V \Delta'_{JM}(\mathbf{r}) + \frac{1}{2} \mu^V \Sigma_{JM}(\mathbf{r}) \right] + iF_A \Sigma'_{JM}(\mathbf{r}), \quad (\text{C.3})$$

where form-factors  $F_1^V, \mu^V, F_A$  and operators  $\Delta'_{JM}, \Sigma_{JM}, \Sigma'_{JM}$  are defined in Ref. [152, 153]. Obviously, for  $q \rightarrow 0$  the first term that contains the ratio  $q/M_N$ , where  $M_N$  is the nucleon mass can be neglected. Therefore, we are left with  $\hat{\mathcal{T}}_J^{el} \approx iF_A \Sigma'_{JM}(\mathbf{r})$  which is given by [152, 153]

$$\Sigma'_{JM}(\mathbf{r}) = \left[ -\sqrt{\frac{J}{2J+1}} \mathbf{M}_{JJ+1}^M(\mathbf{r}) + \sqrt{\frac{J+1}{2J+1}} \mathbf{M}_{JJ-1}^M(\mathbf{r}) \right] \cdot \boldsymbol{\sigma}, \quad (\text{C.4})$$

where  $\mathbf{M}_{JL}^M = j_J(qr) \mathbf{Y}_{JL1}^M(\Omega_r)$ ,  $j_J(qr)$  is the spherical Bessel function of rank  $J$  and  $\mathbf{Y}_{JL1}^M(\Omega_r)$  is the vector spherical harmonic [211]. In the limit  $q \rightarrow 0$  we can use the expansion of spherical Bessel functions [178]

$$j_J(qr) \rightarrow \frac{(qr)^J}{(2J+1)!!}, \quad (\text{C.5})$$

so that for  $J = 1$  in the low-momentum transfer limit we have

$$\hat{\mathcal{T}}_J^{el} = \frac{iF_A}{\sqrt{6\pi}} \sigma_{1M}. \quad (\text{C.6})$$

Now let's turn back to Eq. (C.1) and include only the term with the reduced matrix element  $|\langle J_f || \hat{\mathcal{T}}_J^{el} || J_i \rangle|^2$

$$\frac{d\sigma_{ec}}{d\Omega} = \frac{G_F^2 g_V^2 \cos^2 \theta_C}{2\pi} \frac{F(Z, E_e)}{2J_i + 1} \mathcal{W}(E_\nu, E_e) (1 - (\hat{\nu} \cdot \hat{\mathbf{q}})(\boldsymbol{\beta} \cdot \hat{\mathbf{q}})) |\langle J_f || \hat{\mathcal{T}}_J^{el} || J_i \rangle|^2, \quad (\text{C.7})$$

$$(\text{C.8})$$

and furthermore, near the threshold  $\beta \rightarrow 0$ , the recoil factor reduces to  $\mathcal{W}(E_\nu, E_e) \approx E_\nu^2$ , so that the total cross section is

$$\begin{aligned}\sigma_{ec} &= 4\pi \frac{G_F^2 g_V^2 \cos^2 \theta_C}{2\pi} \frac{F(Z, E_e)}{2J_i + 1} E_\nu^2 \frac{g_A^2}{6\pi} |\langle J_f || \boldsymbol{\sigma} \vec{\tau}_+ || J_i \rangle|^2 \left( \times \frac{3}{2} \right) \\ &= \frac{(G_F g_V \cos \theta_C)^2}{2\pi} F(Z, E_e) (E_0^{(i,f)} - E_e)^2 B(\text{GT}^+),\end{aligned}$$

where  $E_0^{(i,f)} = E_i + M_{N_i} c^2 - E_f - M_{N_f} c^2$  is difference between initial and final nuclear state energy and  $B(\text{GT}^+) = \frac{g_A^2}{2J_i + 1} |\langle J_f || \boldsymbol{\sigma} \tau_+ || J_i \rangle|^2$  is the Gamow-Teller matrix element. Factor in red comes from the reduced isospin matrix element. Therefore, the low-energy long-wavelength limit  $\beta \rightarrow 0, q \rightarrow 0$  of the Walecka model corresponds to a simple expression in Eq. (4.2), known as the allowed approximation.

# Appendix D

## Shape factor for first-forbidden transitions

We present the expressions for the first-forbidden transitions  $J^\pi = 0^-, 1^-$  and  $2^-$ , by following the derivations presented in Refs. [154, 212, 213]. To correctly assess the  $\beta$ -decay half-lives it is important to use good expressions for the electron radial wave functions. They correspond to the solutions of the radial Dirac equations for the outgoing electron in a Coulomb field of a nucleus [213]. The expressions for the shape-factor are given in terms of lepton functions  $M_K(k_e, k_\nu)$  and  $m_K(k_e, k_\nu)$ , which include combination of nuclear matrix elements and energy dependent phase-space factors. They are spherical tensors of rank  $K$ , while  $k_e$  and  $k_\nu$  are the angular momentum quantum numbers of electron and neutrino, respectively. In this Appendix we consider only the spherical symmetry, meaning that expressions presented are valid in both laboratory and intrinsic system. The extension to axial-geometry can be found in Ref. [77]. The matrix elements are expressed in terms of the vector  ${}^V F_{KLs}^N$  and axial  ${}^A F_{KLs}^N$  form factors, where  $L$  is the multipolarity,  $s$  is the spin, and the radial dependence is  $r^{L+2N}$ . The radial expansion of electron wave functions leads to factors  $I(k_e, m, n, \rho; r)$ , denoting the expansion coefficients in the powers of  $(\alpha Z)$  [154]. The numbers  $m, n$  and  $\rho$  denote the expansion powers, tabulated in Ref. [154]. The

general expression for the shape-factor  $C(W)$  [cf. Eq. (5.3)] is calculated from [212]

$$\begin{aligned}
 C(W) = & \sum_{\substack{k_e, k_\nu \\ k_e + k_\nu = L+1}} \lambda_{k_e} \left\{ M_L^2(k_e, k_\nu) + m_L^2(k_e, k_\nu) - \frac{2\mu_{k_e}\gamma_{k_e}}{k_e W} M_L(k_e, k_\nu) m_L(k_e, k_\nu) \right\} \\
 & + \sum_{\substack{k_e, k_\nu \\ k_e + k_\nu = L+2}} \lambda_{k_e} \left\{ M_L^2(k_e, k_\nu) - \frac{2\mu_{k_e}\gamma_{k_e}}{k_e W} M_L(k_e, k_\nu) m_L(k_e, k_\nu) + M_{L+1}^2(k_e, k_\nu) \right. \\
 & \left. - \frac{2\mu_{k_e}\gamma_{k_e}}{k_e W} M_{L+1}(k_e, k_\nu) m_{L+1}(k_e, k_\nu) \right\} \\
 & + \delta_{\Delta J, 0} \left\{ M_0^2(1, 1) + m_0^2(1, 1) - \frac{2\mu_1\gamma_1}{W} M_0(1, 1) m_0(1, 1) \right\}, \tag{D.1}
 \end{aligned}$$

where  $\gamma_{k_e} = \sqrt{k_e^2 - (\alpha Z)^2}$ ,  $\mu_{k_e} = \frac{k_e W}{\gamma_{k_e}}$ . The definition of  $\lambda_{k_e}$  is expressed through the Coulomb amplitudes  $\alpha_{k_e}$ , and can be found in Refs. [154, 212, 213]. In this work, we set  $\lambda_2 = 1$  and  $\mu_1 = 1$  as in Ref. [131].

The shape factor  $C(W)$  of the  $0^-$  transition can be calculated from Eq. (D.1) as

$$C(W) = M_0^2(1, 1) + m_0^2(1, 1) - 2\frac{\mu_1\gamma_1}{W} M_0(1, 1) m_0(1, 1), \tag{D.2}$$

where  $M_0(1, 1)$  is expressed through the form factors as

$$M_0(1, 1) = {}^A F_{000}^0 - \frac{1}{3}\alpha Z^A F_{011}^0(1, 1, 1, 1) - \frac{1}{3}W_0 R^A F_{011}^0, \tag{D.3}$$

$W_0$  is the end-point energy determined from  $W_0 = (M_i - M_f)/(m_e c^2)$ , where  $M_{i(f)}$  are the initial(final) nuclear masses, and  $R$  is the nuclear radius. The form factor  $F_{011}^0(1, 1, 1, 1)$  contains the radial function  $I(1, 1, 1, 1; r)$ . As in Ref. [131], we assume the uniform spherical distribution. The expressions for the form factors can be found in Ref. [212]

$$\begin{aligned}
 {}^A F_{000}^0 &= g_A \mathcal{M}_{000}^0 = g_A \int \gamma_5 T_{000}, \\
 -{}^A F_{011}^0(1, 1, 1, 1) &= g_A \mathcal{M}_{011}^0(1, 1, 1, 1) = g_A \int \left(\frac{r}{R}\right) I(1, 1, 1, 1; r) \gamma_5 T_{011}, \\
 -{}^A F_{011}^0 &= g_A \mathcal{M}_{011}^0 = g_A \int \left(\frac{r}{R}\right) \gamma_5 T_{011}, \tag{D.4}
 \end{aligned}$$



where  $g_A$  is the axial coupling constant, and  $\mathcal{M}_{KLs}^N$  the corresponding matrix element. The integration in the above expressions is abbreviated as in Refs. [154, 212, 213]. For instance

$$\int \left(\frac{r}{R}\right) \gamma_5 T_{011} \equiv \langle J_f^{\pi_f} || (r/R) \gamma_5 T_{011} \tau_{\mp} || J_i^{\pi_i} \rangle, \quad (\text{D.5})$$

where  $J_{i(f)}$  is the initial(final) angular momentum and  $\pi_{i(f)}$  initial(final) parity. For simplicity, in the following we label  $|i(f)\rangle \equiv |J_{i(f)}^{\pi_{i(f)}}\rangle$ . For  $\beta^{\mp}$ -decay, the isospin operator is  $\tau_{\mp}$ . In the following, we assume that the proton-neutron basis is arranged in the  $\beta^{\mp}$  direction, so that the isospin matrix element gives unity. The final expression for  $M_0(1, 1)$  is therefore

$$M_0(1, 1) = g_A \int \gamma_5 T_{000} + \frac{1}{3} \alpha Z g_A \int \left(\frac{r}{R}\right) I(1, 1, 1, 1; r) \gamma_5 T_{011} + \frac{1}{3} W_0 R g_A \int \left(\frac{r}{R}\right) \gamma_5 T_{011}, \quad (\text{D.6})$$

and for  $m_0(1, 1)$

$$m_0(1, 1) = -\frac{1}{3} m_e R^A F_{011}^0 = -\frac{1}{3} m_e R g_A \int \left(\frac{r}{R}\right) \gamma_5 T_{011}. \quad (\text{D.7})$$

The angular matrix elements are defined in Ref. [154] as

$$T_{LL0}^M = i^L Y_{LM}, \quad T_{KL1}^M = \sum_{\mu} C_{1\mu LM-\mu}^{KM} i^L \gamma_5 \sigma^{\mu} Y_{LM-\mu}, \quad (\text{D.8})$$

where the second part is just coupling of  $[\alpha Y_L]_{KM}$ . Note that in Ref. [154] they employ the Biedenharn-Rose (BR) phase convention for the spherical harmonics, unlike the Condon-Shortley (CS) employed in this thesis. The two phase conventions in the spherical basis are defined as [58]

$$\begin{aligned} \text{CS: } |nljm\rangle &= \sum_{m_l, m_s} C_{lm_l 1/2m_s}^{jm} R_{nl}(r) Y_{lm_l}(\theta, \phi) \chi_{1/2m_s}, \\ \text{BR: } |nljm\rangle &= \sum_{m_l, m_s} C_{lm_l 1/2m_s}^{jm} R_{nl}(r) \tilde{Y}_{lm_l}(\theta, \phi) \chi_{1/2m_s}, \end{aligned} \quad (\text{D.9})$$

where  $\tilde{Y}_{lm_l} = i^l Y_{lm_l}$ . Also, we note that the coupling order in Eq. (D.8) is opposite from the one we employ to evaluate the pnRQRPA matrix elements, where  $L$  is first coupled to  $S$ . By applying

the Wigner-Eckart theorem to Eq. (D.6) and reverting to notation of Eq. (D.5) we get

$$M_0(1, 1) = \sqrt{4\pi}g_A \frac{\langle f || [\gamma_5 \tilde{Y}]_0 || i \rangle}{\sqrt{2J_i + 1}} + \sqrt{4\pi} \frac{1}{3} \alpha Z g_A \frac{\langle f || \left(\frac{r}{R}\right) I(1, 1, 1, 1; r) [\boldsymbol{\sigma} \otimes \tilde{Y}_1]_0 || i \rangle}{\sqrt{2J_i + 1}} \\ + \sqrt{4\pi} \frac{1}{3} W_0 R g_A \frac{\langle f || \left(\frac{r}{R}\right) [\boldsymbol{\sigma} \otimes \tilde{Y}_1]_0 || i \rangle}{\sqrt{2J_i + 1}}, \quad (\text{D.10})$$

and correspondingly

$$m_0(1, 1) = -\sqrt{4\pi} \frac{1}{3} m_e R g_A \frac{\langle f || \left(\frac{r}{R}\right) [\boldsymbol{\sigma} \otimes \tilde{Y}_1]_0 || i \rangle}{\sqrt{2J_i + 1}}. \quad (\text{D.11})$$

Now, the matrix element for the  $0^-$  multipole can be rewritten in the notation of Ref. [131]. To this aim, we introduce the following changes;  $\xi = \alpha Z / 2R$  and redefinition of the spherical harmonics

$$C_{LM} = \sqrt{\frac{4\pi}{2L + 1}} Y_{LM}. \quad (\text{D.12})$$

The above expressions can be rewritten as

$$M_0(1, 1) = g_A \frac{\langle f || \gamma_5 || i \rangle}{\sqrt{2J_i + 1}} + \frac{2}{\sqrt{3}} \xi g_A \frac{\langle f || r I(1, 1, 1, 1; r) [\boldsymbol{\sigma} \otimes \mathbf{C}_1]_0 || i \rangle}{\sqrt{2J_i + 1}} \\ + \frac{1}{3} W_0 \sqrt{3} g_A \frac{\langle f || r [\boldsymbol{\sigma} \otimes \mathbf{C}_1]_0 || i \rangle}{\sqrt{2J_i + 1}}, \quad (\text{D.13})$$

and

$$m_0(1, 1) = -\frac{1}{3} \sqrt{3} g_A \frac{\langle f || r [\boldsymbol{\sigma} \otimes \mathbf{C}_1]_0 || i \rangle}{\sqrt{2J_i + 1}}. \quad (\text{D.14})$$

Let us now define the following abbreviations guided by Ref. [131]

$$\xi' v = -g_A \frac{\langle f || \gamma_5 || i \rangle}{\sqrt{2J_i + 1}}, \quad w' = -\frac{2}{\sqrt{3}} g_A \frac{\langle f || r I(1, 1, 1, 1; r) [\boldsymbol{\sigma} \otimes \mathbf{C}_1]_0 || i \rangle}{\sqrt{2J_i + 1}}, \\ w = -\sqrt{3} g_A \frac{\langle f || r [\boldsymbol{\sigma} \otimes \mathbf{C}_1]_0 || i \rangle}{\sqrt{2J_i + 1}}, \quad (\text{D.15})$$

so that the above terms reduce to

$$M_0(1, 1) = -\xi'v - \xi w' - \frac{1}{3}W_0w, \quad (\text{D.16})$$

and

$$m_0(1, 1) = -\frac{1}{3}w. \quad (\text{D.17})$$

By defining  $V = \xi'v + \xi w'$  and  $\zeta_0 = V + 1/3wW_0$ , we finally get

$$C(W) = \zeta_0^2 + \frac{1}{9}w^2 - \frac{2\mu_1\gamma_1}{W}(-\zeta_0) \left(-\frac{1}{3}w\right) = \zeta_0^2 + \frac{1}{9}w^2 - \frac{2\mu_1\gamma_1}{3W}\zeta_0w. \quad (\text{D.18})$$

This result is in the agreement with expressions listed in Ref. [131], apart from keeping  $g_A$  in the matrix element. The shape-factor can be expressed as in Eq. (5.5), through the coefficients  $k$ ,  $ka$ ,  $kb$ , and  $kc$  as

$$\begin{aligned} k &= \zeta_0^2 + \frac{1}{9}w^2, \\ kb &= -\frac{2\mu_1\gamma_1}{3}\zeta_0w, \end{aligned} \quad (\text{D.19})$$

others being zero.

The shape-factor for the  $J^\pi = 1^-$  multipole is given by Eq. (D.1) as

$$C(W) = M_1^2(1, 1) + m_1^2(1, 1) - \frac{2\mu_1\gamma_1}{W}M_1(1, 1)m_1(1, 1) + M_1^2(1, 2) + \lambda_2 M_1^2(2, 1). \quad (\text{D.20})$$

The functions  $M_K$  and  $m_k$  can be found in Ref. [154]. First, we start by expressing the  $M_1(1, 1)$  through the vector and axial form factors as

$$\begin{aligned} M_1(1, 1) &= -{}^V F_{101}^0 - \frac{1}{3}\alpha Z \sqrt{\frac{1}{3}} {}^V F_{110}^0(1, 1, 1, 1) - \frac{1}{3}W_0 R \sqrt{\frac{1}{3}} {}^V F_{110}^0 \\ &\quad - \frac{1}{3}\alpha Z \sqrt{\frac{2}{3}} {}^A F_{111}^0(1, 1, 1, 1) - \frac{1}{3}(W - q)R \sqrt{\frac{2}{3}} {}^A F_{111}^0. \end{aligned} \quad (\text{D.21})$$

In the above,  $q$  is the neutrino momentum related to neutrino energy  $W_\nu$ . The form factors are

defined through the spherical tensor operators from Eq. (D.8)

$$\begin{aligned}
 M_1(1, 1) &= g_V^2 \int T_{101} - \frac{1}{3} \alpha Z \sqrt{\frac{1}{3}} g_V^2 \int \left(\frac{r}{R}\right) T_{110} I(1, 1, 1, 1; r) - \frac{1}{3} W_0 R \sqrt{\frac{1}{3}} g_V^2 \int \left(\frac{r}{R}\right) T_{110} \\
 &\quad - \frac{1}{3} \alpha Z \sqrt{\frac{2}{3}} g_A \int \left(\frac{r}{R}\right) I(1, 1, 1, 1; r) \gamma_5 T_{111} - \frac{1}{3} (W - q) R \sqrt{\frac{2}{3}} g_A \int \left(\frac{r}{R}\right) \gamma_5 T_{111}.
 \end{aligned} \tag{D.22}$$

The vector coupling  $g_V = 1.0$ , and is omitted from the following expressions. The other lepton functions appearing in Eq. (D.20) have the form

$$\begin{aligned}
 m_1(1, 1) &= -\frac{1}{3} m_e R \left[ \sqrt{\frac{1}{3}} F_{110}^0 + \sqrt{\frac{2}{3}} F_{111}^0 \right] \\
 &= -\frac{1}{3} m_e R \left[ \sqrt{\frac{1}{3}} \int \left(\frac{r}{R}\right) T_{110} + \sqrt{\frac{2}{3}} g_A \int \left(\frac{r}{R}\right) T_{111} \right],
 \end{aligned} \tag{D.23}$$

$$\begin{aligned}
 M_1(1, 2) &= \frac{1}{3} q R \left[ \sqrt{\frac{2}{3}} F_{110}^0 + \sqrt{\frac{1}{3}} F_{111}^0 \right] \\
 &= \frac{1}{3} q R \left[ \sqrt{\frac{2}{3}} \int \left(\frac{r}{R}\right) T_{110} + \sqrt{\frac{1}{3}} g_A \int \left(\frac{r}{R}\right) T_{111} \right],
 \end{aligned} \tag{D.24}$$

$$\begin{aligned}
 M_1(2, 1) &= \frac{1}{3} p R \left[ \sqrt{\frac{2}{3}} F_{110}^0 - \sqrt{\frac{1}{3}} F_{111}^0 \right] \\
 &= \frac{1}{3} p R \left[ \sqrt{\frac{2}{3}} \int \left(\frac{r}{R}\right) T_{110} - \sqrt{\frac{1}{3}} g_A \int \left(\frac{r}{R}\right) T_{111} \right],
 \end{aligned} \tag{D.25}$$

where  $p = \sqrt{W^2 - 1}$  is the electron momentum. Introducing the redefinition of spherical harmonics

from Eq. (D.12) and applying the Wigner-Eckart theorem we get for  $M_1(1, 1)$

$$\begin{aligned}
 M_1(1, 1) &= \frac{\langle f || \boldsymbol{\alpha} || i \rangle}{\sqrt{2J_i + 1}} - \frac{2}{3} \xi \frac{\langle f || r I(1, 1, 1, 1; r) \mathbf{C}_1 || i \rangle}{\sqrt{2J_i + 1}} - \frac{1}{3} W_0 \frac{\langle f || r \mathbf{C}_1 || i \rangle}{\sqrt{2J_i + 1}} \\
 &\quad - \frac{2\sqrt{2}}{3} \xi g_A \frac{\langle f || r I(1, 1, 1, 1; r) [\boldsymbol{\sigma} \otimes \mathbf{C}_1]_1 || i \rangle}{\sqrt{2J_i + 1}} - \frac{\sqrt{2}}{3} (W - q) g_A \frac{\langle f || r [\boldsymbol{\sigma} \otimes \mathbf{C}_1]_1 || i \rangle}{\sqrt{2J_i + 1}}.
 \end{aligned} \tag{D.26}$$

While the other expressions appearing in Eq. (D.20) are

$$m_1(1, 1) = -\frac{1}{3} \frac{\langle f || r \mathbf{C}_1 || i \rangle}{\sqrt{2J_i + 1}} - \frac{\sqrt{2}}{3} g_A \frac{\langle f || r [\boldsymbol{\sigma} \otimes \mathbf{C}_1]_1 || i \rangle}{\sqrt{2J_i + 1}}, \tag{D.27}$$

$$M_1(1, 2) = \frac{\sqrt{2}}{3} q \frac{\langle f || r \mathbf{C}_1 || i \rangle}{\sqrt{2J_i + 1}} + \frac{1}{3} q g_A \frac{\langle f || r [\boldsymbol{\sigma} \otimes \mathbf{C}_1]_1 || i \rangle}{\sqrt{2J_i + 1}}, \tag{D.28}$$

$$M_1(2, 1) = \frac{\sqrt{2}}{3} p \frac{\langle f || r \mathbf{C}_1 || i \rangle}{\sqrt{2J_i + 1}} - \frac{1}{3} p g_A \frac{\langle f || r [\boldsymbol{\sigma} \otimes \mathbf{C}_1]_1 || i \rangle}{\sqrt{2J_i + 1}}. \tag{D.29}$$

Now, we introduce the notation from Ref. [131], and define the following abbreviations

$$\begin{aligned}
 \xi' y &= -\frac{\langle f || \boldsymbol{\alpha} || i \rangle}{\sqrt{2J_i + 1}}, & x' &= -\frac{2}{3} \frac{\langle f || r I(1, 1, 1, 1; r) \mathbf{C}_1 || i \rangle}{\sqrt{2J_i + 1}}, \\
 x &= -\frac{\langle f || r \mathbf{C}_1 || i \rangle}{\sqrt{2J_i + 1}}, & u' &= -\frac{2\sqrt{2}}{3} g_A \frac{\langle f || r I(1, 1, 1, 1; r) [\boldsymbol{\sigma} \otimes \mathbf{C}_1]_1 || i \rangle}{\sqrt{2J_i + 1}}, \\
 u &= -\sqrt{2} g_A \frac{\langle f || r [\boldsymbol{\sigma} \otimes \mathbf{C}_1]_1 || i \rangle}{\sqrt{2J_i + 1}}.
 \end{aligned} \tag{D.30}$$

Note that the matrix element  $\xi' y$  (in addition to  $\xi' v$ ) occurs only as the relativistic correction, and couples upper to lower components of wave functions. Using the abbreviations from Ref. [131];  $Y = \xi' y - \xi(u' + x')$  and  $\zeta_1 = Y + \frac{1}{3}(u - x)W_0$ , above terms can be rewritten as

$$\begin{aligned}
 M_1(1, 1) &= -\xi' y + \xi x' + \frac{1}{3} W_0 x + \xi u' + \frac{1}{3} (W - q) u \\
 &= -\xi' y + \xi(x' + u') + \frac{1}{3} W_0(x - u) + \frac{2}{3} W u = -\zeta_1 + \frac{2}{3} W u,
 \end{aligned} \tag{D.31}$$

$$\begin{aligned}
 m_1(1, 1) &= \frac{1}{3}x + \frac{1}{3}u = \frac{1}{3}(x + u), \\
 M_1(1, 2) &= -\frac{\sqrt{2}}{3}qx - \frac{1}{3}\frac{1}{\sqrt{2}}qu = -\frac{q}{3\sqrt{2}}(2x + u), \\
 M_1(2, 1) &= -\frac{\sqrt{2}}{3}px + \frac{1}{3\sqrt{2}}pu = \frac{1}{3\sqrt{2}}p(2x - u).
 \end{aligned}
 \tag{D.32}$$

The shape-factor  $C(W)$  is now

$$\begin{aligned}
 C(W) &= \left[-\zeta_1 + \frac{2}{3}Wu\right]^2 + \frac{1}{9}(x + u)^2 - \frac{2\mu_1\gamma_1}{W} \left[-\zeta_1 + \frac{2}{3}Wu\right] \frac{1}{3}(x + u) \\
 &\quad + \frac{q^2}{18}(2x + u)^2 + \frac{p^2}{18}(2x - u)^2 \\
 &= \zeta_1^2 + \frac{4}{9}W^2u^2 - \frac{4}{3}Wu\zeta_1 + \frac{1}{9}(x + u)^2 - \frac{2\mu_1\gamma_1}{3W} \left[-\zeta_1 + \frac{2}{3}Wu\right] (x + u) \\
 &\quad + \frac{(W_0 - W)^2}{18}(2x + u)^2 + \frac{W^2 - 1}{18}(2x - u)^2 \\
 &= \zeta_1^2 + \frac{1}{9}(x + u)^2 - \frac{4}{9}\mu_1\gamma_1u(x + u) + \frac{W_0^2}{18}(2x + u) - \frac{\lambda_2}{18}(2x - u)^2 \\
 &\quad + W^2 \left[ \frac{4}{9}u^2 + \frac{1}{18}(2x + u)^2 + \frac{\lambda_2}{18}(2x - u)^2 \right] + \frac{1}{W} \frac{2\mu_1\gamma_1}{3}\zeta_1(x + u) \\
 &\quad + W \left[ -\frac{4}{3}u\zeta_1 - \frac{1}{9}W_0(2x + u)^2 \right].
 \end{aligned}
 \tag{D.33}$$

We can further simplify the last term in the above expression for the shape-factor

$$\begin{aligned}
 -\frac{4}{3}u\zeta_1 - \frac{1}{9}W_0(2x + u)^2 &= -\frac{4}{3}u \left( Y + \frac{1}{3}(u - x)W_0 \right) - \frac{1}{9}W_0(2x + u)^2 \\
 &= -\frac{4}{3}uY - \frac{4}{9}uW_0(u - x) - \frac{1}{9}W_0(4x^2 + 4xu + u^2) \\
 &= -\frac{4}{3}uY - \frac{1}{9}W_0 [5u^2 + 4x^2].
 \end{aligned}
 \tag{D.34}$$

By writing the shape factor as  $C(W) = k + kaW + kb/W + kcW^2$  [cf. Eq. (5.5)] we can group

the terms as

$$\begin{aligned}
 k &= \zeta_1^2 + \frac{1}{9}(x+u)^2 - \frac{4}{9}\mu_1\gamma_1u(x+u) + \frac{W_0^2}{18}(2x+u) - \frac{\lambda_2}{18}(2x-u)^2, \\
 ka &= -\frac{4}{3}uY - \frac{1}{9}W_0 [5u^2 + 4x^2], \\
 kb &= \frac{2\mu_1\gamma_1}{3}\zeta_1(x+u), \\
 kc &= \left[ \frac{4}{9}u^2 + \frac{1}{18}(2x+u)^2 + \frac{\lambda_2}{18}(2x-u)^2 \right].
 \end{aligned} \tag{D.35}$$

The shape-factor for the  $J^\pi = 2^-$  multipole is given by Eq. (D.1) as

$$C(W) = M_2^2(1, 2) + \lambda_2 M_2^2(2, 1). \tag{D.36}$$

The lepton function  $M_2(1, 2)$  can be expressed through the tensor operators defined in Eq. (D.8) as in Ref. [154]

$$M_2(1, 2) = -\frac{1}{3}qR^A F_{211}^0 = \frac{1}{3}qRg_A \int \left( \frac{r}{R} \right) \gamma_5 T_{211} = \frac{\sqrt{3}}{3}qg_A \frac{\langle f || r [\boldsymbol{\sigma} \otimes \mathbf{C}_1]_2 || i \rangle}{\sqrt{2J_i + 1}}, \tag{D.37}$$

where we have applied the Wigner-Eckart theorem to obtain the reduced matrix element in the last equality. Similarly, the expression for  $M_2(2, 1)$  is [154]

$$M_2(2, 1) = -\frac{1}{3}pR^A F_{211}^0 = \frac{1}{3}pRg_A \int \left( \frac{r}{R} \right) \gamma_5 T_{211} = \frac{\sqrt{3}}{3}pg_A \frac{\langle f || r [\boldsymbol{\sigma} \otimes \mathbf{C}_1]_2 || i \rangle}{\sqrt{2J_i + 1}}. \tag{D.38}$$

Now, we abbreviate the matrix element appearing in above expressions [131]

$$z = 2g_A \frac{\langle f || r [\boldsymbol{\sigma} \otimes \mathbf{C}_1]_2 || i \rangle}{\sqrt{2J_i + 1}}, \tag{D.39}$$

so that the lepton functions are considerably simplified

$$M_2(1, 2) = \frac{\sqrt{3}}{6}qz, \quad M_2(2, 1) = \frac{\sqrt{3}}{6}pz. \tag{D.40}$$

The shape-factor is finally given by

$$\begin{aligned} C(W) &= \frac{3z^2}{36}(q^2 + \lambda_2 p^2) = \frac{3z^2}{36}[(W_0 - W)^2 + \lambda_2 W^2 - \lambda_2^2] \\ &= \frac{1}{12}z^2[-2W + (W_0^2 - \lambda_2^2) + W^2(1 + \lambda_2^2)]. \end{aligned} \quad (\text{D.41})$$

By writing the shape-factor as  $C(W) = k + kaW + kb/W + kcW^2$  we can group the terms as

$$\begin{aligned} k &= \frac{1}{12}z^2(W_0^2 - \lambda_2^2), \\ ka &= -\frac{1}{6}z^2W_0, \\ kc &= \frac{1}{12}z^2(1 + \lambda_2^2). \end{aligned} \quad (\text{D.42})$$

Now, we can combine all the results for first-forbidden multipoles obtained for the shape-factor, and group the terms as in Eq. (5.5)

$$\begin{aligned} k &= \left[ \zeta_0^2 + \frac{1}{9}w^2 \right]_{(0)} + \left[ \frac{1}{12}z^2(W_0^2 - \lambda_2^2) \right]_{(2)} \\ &+ \left[ \zeta_1^2 + \frac{1}{9}(x+u)^2 - \frac{4}{9}\mu_1\gamma_1u(x+u) + \frac{W_0^2}{18}(2x+u) - \frac{\lambda_2}{18}(2x-u)^2 \right]_{(1)}, \\ ka &= \left[ -\frac{4}{3}uY - \frac{1}{9}W_0[5u^2 + 4x^2] \right]_{(1)} + \left[ -\frac{1}{6}z^2W_0 \right]_{(2)} \\ kb &= \left[ \frac{2\mu_1\gamma_1}{3}\zeta_1(x+u) \right]_{(1)} + \left[ -\frac{2\mu_1\gamma_1}{3}\zeta_0w \right]_{(0)}, \\ kc &= \left[ \frac{4}{9}u^2 + \frac{1}{18}(2x+u)^2 + \frac{\lambda_2}{18}(2x-u)^2 \right]_{(1)} + \left[ \frac{1}{12}z^2(1 + \lambda_2^2) \right]_{(2)}. \end{aligned} \quad (\text{D.43})$$

Numbers after the square brackets indicate the rank of the operators. Results presented in this Appendix agree with those from Ref. [131].

Finally, it is interesting to write down the shape-factor in the allowed approximation using the formalism of Ref. [154]. It is decomposed into two terms

$$C(W) = ({}^V F_{000}^0)^2 + ({}^A F_{101}^0)^2 = \left( \int T_{000} \right)^2 + \left( g_A \int \gamma_5 T_{101} \right)^2, \quad (\text{D.44})$$



where by expressing the form factors from Ref. [154] we get

$$C(W) = \underbrace{1}_{\text{Fermi}} + g_A^2 \underbrace{\left( \frac{\langle f || [\boldsymbol{\sigma} \otimes \mathbf{C}_0]_1 || i \rangle}{\sqrt{2J_i + 1}} \right)^2}_{\text{Gamow-Teller}}, \quad (\text{D.45})$$

the first one corresponds to the Fermi, and the second to Gamow-Teller reduced matrix elements.

# Bibliography

- [1] H.-T. Janka, K. Langanke, A. Marek, G. Martínez-Pinedo, and B. Müller, *Physics Reports* 442(1), 38–74 (2007), The Hans Bethe Centennial Volume 1906-2006.
- [2] H. A. Bethe, *Rev. Mod. Phys.* 62, 801–866 (1990).
- [3] K. Langanke and G. Martínez-Pinedo, *Rev. Mod. Phys.* 75, 819–862 (2003).
- [4] G. Martínez-Pinedo, K. Langanke, and D. J. Dean, *The Astrophysical Journal Supplement Series* 126(2), 493 (2000).
- [5] M. Mumpower, R. Surman, G. McLaughlin, and A. Aprahamian, *Progress in Particle and Nuclear Physics* 86, 86–126 (2016).
- [6] F.-K. Thielemann, et al., *Progress in Particle and Nuclear Physics* 66(2), 346–353 (2011), Particle and Nuclear Astrophysics.
- [7] M. Arnould, S. Goriely, and K. Takahashi, *Physics Reports* 450(4), 97–213 (2007).
- [8] B. R. Barrett, P. Navrátil, and J. P. Vary, *Progress in Particle and Nuclear Physics* 69, 131–181 (2013).
- [9] G. Hagen, T. Papenbrock, M. Hjorth-Jensen, and D. J. Dean, *Reports on Progress in Physics* 77(9), 096302 (2014).
- [10] H. Hergert, *Frontiers in Physics* 8 (2020).
- [11] E. Caurier, G. Martínez-Pinedo, F. Nowacki, A. Poves, and A. P. Zuker, *Rev. Mod. Phys.* 77, 427–488 (2005).
- [12] M. Bender, P.-H. Heenen, and P.-G. Reinhard, *Rev. Mod. Phys.* 75, 121–180 (2003).

- [13] P. Hohenberg and W. Kohn, *Phys. Rev.* 136, B864–B871 (1964).
- [14] S. Shen, H. Liang, W. H. Long, J. Meng, and P. Ring, *Progress in Particle and Nuclear Physics* 109, 103713 (2019).
- [15] T. Nikšić, D. Vretenar, and P. Ring, *Progress in Particle and Nuclear Physics* 66(3), 519–548 (2011).
- [16] J. Meng, *Relativistic Density Functional For Nuclear Structure*, International Review Of Nuclear Physics, World Scientific Publishing Company (2016).
- [17] J. Walecka, *Annals of Physics* 83(2), 491–529 (1974).
- [18] P. Ring, *Progress in Particle and Nuclear Physics* 37, 193–263 (1996).
- [19] G. A. Lalazissis, T. Nikšić, D. Vretenar, and P. Ring, *Phys. Rev. C* 71, 024312 (2005).
- [20] T. Nikšić, D. Vretenar, and P. Ring, *Phys. Rev. C* 78, 034318 (2008).
- [21] E. Yüksel, T. Marketin, and N. Paar, *Phys. Rev. C* 99, 034318 (2019).
- [22] S. Typel, *Phys. Rev. C* 71, 064301 (2005).
- [23] D. Vretenar, A. Afanasjev, G. Lalazissis, and P. Ring, *Physics Reports* 409(3), 101–259 (2005).
- [24] J. Dobaczewski, W. Nazarewicz, T. R. Werner, J. F. Berger, C. R. Chinn, and J. Dechargé, *Phys. Rev. C* 53, 2809–2840 (1996).
- [25] A. L. Goodman, *Nuclear Physics A* 352(1), 30–44 (1981).
- [26] N. Paar, D. Vretenar, E. Khan, and G. Colò, *Reports on Progress in Physics* 70(5), R02 (2007).
- [27] N. Paar, P. Ring, T. Nikšić, and D. Vretenar, *Phys. Rev. C* 67, 034312 (2003).
- [28] N. Paar, T. Nikšić, D. Vretenar, and P. Ring, *Phys. Rev. C* 69, 054303 (2004).
- [29] R. R. Doering, A. Galonsky, D. M. Patterson, and G. F. Bertsch, *Phys. Rev. Lett.* 35, 1691–1693 (1975).

- 
- [30] A. Ravlić, Y. F. Niu, T. Nikšić, N. Paar, and P. Ring, *Phys. Rev. C* 104, 064302 (2021).
- [31] E. M. Ney, A. Ravlić, J. Engel, and N. Paar, *arXiv preprint arXiv:2209.10009* (2022).
- [32] A. Ravlić, E. Yüksel, Y. F. Niu, G. Colò, E. Khan, and N. Paar, *Phys. Rev. C* 102, 065804 (2020).
- [33] S. Giraud, R. G. T. Zegers, B. A. Brown, J.-M. Gabler, J. Lesniak, J. Rebenstock, E. M. Ney, J. Engel, A. Ravlić, and N. Paar, *Phys. Rev. C* 105, 055801 (2022).
- [34] A. Ravlić, E. Yüksel, Y. F. Niu, and N. Paar, *Phys. Rev. C* 104, 054318 (2021).
- [35] A. Ravlić, E. Yüksel, T. Nikšić, and N. Paar, *Expanding the limits of nuclear stability: Drip lines for hot nuclei* (2022), Unpublished, in review at Nature Communications.
- [36] P. Bonche, S. Levit, and D. Vautherin, *Nuclear Physics A* 436(2), 265–293 (1985).
- [37] P. Bonche, S. Levit, and D. Vautherin, *Nuclear Physics A* 427(2), 278–296 (1984).
- [38] C. Von Weizsäcker, *Z. Phys* 96, 431–445 (1935).
- [39] H. A. Bethe and R. F. Bacher, *Rev. Mod. Phys.* 8, 82–229 (1936).
- [40] M. Bender, K. Rutz, P.-G. Reinhard, and J. A. Maruhn, *The European Physical Journal A* 8(1), 59–75 (2000).
- [41] G. F. Bertsch, *Nuclear Pairing: Basic Phenomena Revisited*, 26–39.
- [42] W. Rarita and J. Schwinger, *Phys. Rev.* 59, 436–452 (1941).
- [43] E. Gerjuoy and J. Schwinger, *Phys. Rev.* 61, 138–146 (1942).
- [44] M. G. Mayer and J. H. D. Jensen, *Elementary theory of nuclear shell structure*, Wiley (1960).
- [45] J. Bardeen, L. N. Cooper, and J. R. Schrieffer, *Phys. Rev.* 108, 1175–1204 (1957).
- [46] A. Bohr, B. R. Mottelson, and D. Pines, *Phys. Rev.* 110, 936–938 (1958).
- [47] D. R. Inglis, *Phys. Rev.* 103, 1786–1795 (1956).
- [48] S. Beliaev, *Nuclear Physics* 24(2), 322–325 (1961).

- 
- [49] R. Broglia, *Annals of Physics* 80(1), 60–85 (1973).
- [50] V. Somà, *Frontiers in Physics* 8 (2020).
- [51] A. Lovato, N. Rocco, and R. Schiavilla, *Phys. Rev. C* 100, 035502 (2019).
- [52] H. Hergert, S. Bogner, T. Morris, A. Schwenk, and K. Tsukiyama, *Physics Reports* 621, 165–222 (2016), Memorial Volume in Honor of Gerald E. Brown.
- [53] N. Schunck, J. D. McDonnell, D. Higdon, J. Sarich, and S. M. Wild, *The European Physical Journal A* 51(12), 169 (2015).
- [54] J.-P. Ebran, E. Khan, T. Nikšić, and D. Vretenar, *Phys. Rev. C* 90, 054329 (2014).
- [55] M. Bender, T. Duguet, and D. Lacroix, *Phys. Rev. C* 79, 044319 (2009).
- [56] M. V. Stoitsov, J. Dobaczewski, R. Kirchner, W. Nazarewicz, and J. Terasaki, *Phys. Rev. C* 76, 014308 (2007).
- [57] X. Roca-Maza and N. Paar, *Progress in Particle and Nuclear Physics* 101, 96–176 (2018).
- [58] P. Ring and P. Schuck, *The Nuclear Many-Body Problem*, Physics and astronomy online library, Springer (2004).
- [59] J. Stone and P.-G. Reinhard, *Progress in Particle and Nuclear Physics* 58(2), 587–657 (2007).
- [60] L. M. Robledo, T. R. Rodríguez, and R. R. Rodríguez-Guzmán, *Journal of Physics G: Nuclear and Particle Physics* 46(1), 013001 (2018).
- [61] J.-P. Ebran, A. Mutschler, E. Khan, and D. Vretenar, *Phys. Rev. C* 94, 024304 (2016).
- [62] J. Boguta and H. Stoecker, *Physics Letters B* 120(4), 289–293 (1983).
- [63] S. Typel, T. v. Chossy, and H. H. Wolter, *Phys. Rev. C* 67, 034002 (2003).
- [64] R. Brockmann and W. Weise, *Physics Letters B* 69(2), 167–169 (1977).
- [65] Y. Sugahara and H. Toki, *Progress of Theoretical Physics* 92(4), 803–813 (1994).
- [66] J. N. Ginocchio, *Physics Reports* 414(4), 165–261 (2005).

- 
- [67] B. D. Serot, *Reports on Progress in Physics* 55(11), 1855 (1992).
- [68] L. Savushkin and H. Toki, *The Atomic Nucleus as a Relativistic System*, Physics and astronomy online library, Springer (2004).
- [69] P. G. Reinhard, *Reports on Progress in Physics* 52(4), 439 (1989).
- [70] T. Nikšić, D. Vretenar, P. Finelli, and P. Ring, *Phys. Rev. C* 66, 024306 (2002).
- [71] P. W. Zhao, Z. P. Li, J. M. Yao, and J. Meng, *Phys. Rev. C* 82, 054319 (2010).
- [72] T. Bürvenich, D. G. Madland, J. A. Maruhn, and P.-G. Reinhard, *Phys. Rev. C* 65, 044308 (2002).
- [73] B. V. Carlson and D. Hirata, *Phys. Rev. C* 62, 054310 (2000).
- [74] J. Meng and P. Ring, *Phys. Rev. Lett.* 77, 3963–3966 (1996).
- [75] P. Ring, L. Robledo, J. Egido, and M. Faber, *Nuclear Physics A* 419(2), 261–294 (1984).
- [76] D. J. Rowe, *Phys. Rev.* 162, 866–871 (1967).
- [77] M. T. Mustonen, T. Shafer, Z. Zenginerler, and J. Engel, *Phys. Rev. C* 90, 024308 (2014).
- [78] M. T. Mustonen and J. Engel, *Phys. Rev. C* 93, 014304 (2016).
- [79] E. M. Ney, J. Engel, T. Li, and N. Schunck, *Phys. Rev. C* 102, 034326 (2020).
- [80] K. Yoshida, *Progress of Theoretical and Experimental Physics* 2013(11) (2013), 113D02.
- [81] K. Yoshida and N. V. Giai, *Phys. Rev. C* 78, 064316 (2008).
- [82] D. Vretenar, G. Lalazissis, R. Behnsch, W. Pöschl, and P. Ring, *Nuclear Physics A* 621(4), 853–878 (1997).
- [83] X. Roca-Maza, X. Viñas, M. Centelles, B. K. Agrawal, G. Colò, N. Paar, J. Piekarewicz, and D. Vretenar, *Phys. Rev. C* 92, 064304 (2015).
- [84] F. Osterfeld, *Rev. Mod. Phys.* 64, 491–557 (1992).
- [85] K. Ikeda, S. Fujii, and F. I. Fujita, *Phys. Letters* Vol: 2 (1962).

- 
- [86] Y. Fujita, B. Rubio, and W. Gelletly, *Progress in Particle and Nuclear Physics* 66(3), 549–606 (2011).
- [87] B. Brown and B. Wildenthal, *Atomic Data and Nuclear Data Tables* 33(3), 347–404 (1985).
- [88] K. Blaum, *Physics Reports* 425(1), 1–78 (2006).
- [89] C. B. Hinke, et al., *Nature* 486(7403), 341–345 (2012).
- [90] D. Lubos, et al., *Phys. Rev. Lett.* 122, 222502 (2019).
- [91] Y. Fujita, et al., *Phys. Rev. C* 67, 064312 (2003).
- [92] T. Taddeucci, C. Goulding, T. Carey, R. Byrd, C. Goodman, C. Gaarde, J. Larsen, D. Horen, J. Rapaport, and E. Sugarbaker, *Nuclear Physics A* 469(1), 125–172 (1987).
- [93] S. El-Kateb, et al., *Phys. Rev. C* 49, 3128–3136 (1994).
- [94] A. L. Williams, et al., *Phys. Rev. C* 51, 1144–1153 (1995).
- [95] K. Pham, et al., *Phys. Rev. C* 51, 526–540 (1995).
- [96] M. Sasano, et al., *Phys. Rev. Lett.* 107, 202501 (2011).
- [97] J. Yasuda, et al., *Phys. Rev. Lett.* 121, 132501 (2018).
- [98] G. Martínez-Pinedo, Y. H. Lam, K. Langanke, R. G. T. Zegers, and C. Sullivan, *Phys. Rev. C* 89, 045806 (2014).
- [99] G. W. Hitt, et al., *Phys. Rev. C* 80, 014313 (2009).
- [100] B. Gao, et al., *Phys. Rev. C* 101, 014308 (2020).
- [101] S. Noji, et al., *Phys. Rev. C* 92, 024312 (2015).
- [102] R. Titus, et al., *Phys. Rev. C* 100, 045805 (2019).
- [103] S. Noji, et al., *Phys. Rev. Lett.* 112, 252501 (2014).
- [104] A. L. Cole, T. S. Anderson, R. G. T. Zegers, S. M. Austin, B. A. Brown, L. Valdez, S. Gupta, G. W. Hitt, and O. Fawwaz, *Phys. Rev. C* 86, 015809 (2012).

- [105] K. Langanke, G. Martínez-Pinedo, and R. G. T. Zegers, *Reports on Progress in Physics* 84(6), 066301 (2021).
- [106] S. Giraud, et al., *arXiv preprint arXiv:2210.15866* (2022).
- [107] H. Sommermann, *Annals of Physics* 151(1), 163–203 (1983).
- [108] A. A. Dzhioev, A. I. Vdovin, and C. Stoyanov, *Phys. Rev. C* 100, 025801 (2019).
- [109] G. M. Fuller, W. A. Fowler, and M. J. Newman, *The Astrophysical Journal Supplement Series* 42, 447–473 (1980).
- [110] G. M. Fuller, W. A. Fowler, and M. J. Newman, *The Astrophysical Journal Supplement Series* 48, 279–319 (1982).
- [111] G. M. Fuller, W. A. Fowler, and M. J. Newman, *The Astrophysical Journal Supplement Series* 252, 715–740 (1982).
- [112] G. M. Fuller, W. A. Fowler, and M. J. Newman, *The Astrophysical Journal Supplement Series* 293, 1–16 (1985).
- [113] T. Oda, M. Hino, K. Muto, M. Takahara, and K. Sato, *Atomic Data and Nuclear Data Tables* 56(2), 231–403 (1994).
- [114] K. Langanke and G. Martínez-Pinedo, *Atomic Data and Nuclear Data Tables* 79(1), 1–46 (2001).
- [115] D. J. Dean, K. Langanke, L. Chatterjee, P. B. Radha, and M. R. Strayer, *Phys. Rev. C* 58, 536–544 (1998).
- [116] A. Juodagalvis, K. Langanke, W. Hix, G. Martínez-Pinedo, and J. Sampaio, *Nuclear Physics A* 848(3), 454–478 (2010).
- [117] A. F. Fantina, E. Khan, G. Colò, N. Paar, and D. Vretenar, *Phys. Rev. C* 86, 035805 (2012).
- [118] N. Paar, G. Colò, E. Khan, and D. Vretenar, *Phys. Rev. C* 80, 055801 (2009).
- [119] Y. F. Niu, N. Paar, D. Vretenar, and J. Meng, *Phys. Rev. C* 83, 045807 (2011).
- [120] E. J. Konopinski, *Rev. Mod. Phys.* 15, 209–245 (1943).



- 
- [121] D. H. Wilkinson, *Journal of Physics G: Nuclear and Particle Physics* 29(1), 189 (2002).
- [122] I. S. Towner and J. C. Hardy, *Reports on Progress in Physics* 73(4), 046301 (2010).
- [123] E. Nácher, et al., *Phys. Rev. Lett.* 92, 232501 (2004).
- [124] D. S. Ahn, et al., *Phys. Rev. Lett.* 129, 212502 (2022).
- [125] M. B. Aufderheide, S. D. Bloom, G. J. Mathews, and D. A. Resler, *Phys. Rev. C* 53, 3139–3142 (1996).
- [126] K. Mori, M. A. Famiano, T. Kajino, T. Suzuki, J. Hidaka, M. Honma, K. Iwamoto, K. Nomoto, and T. Otsuka, *The Astrophysical Journal* 833(2), 179 (2016).
- [127] P. Möller, B. Pfeiffer, and K.-L. Kratz, *Phys. Rev. C* 67, 055802 (2003).
- [128] T. Shafer, J. Engel, C. Fröhlich, G. C. McLaughlin, M. Mumpower, and R. Surman, *Phys. Rev. C* 94, 055802 (2016).
- [129] J. Engel, M. Bender, J. Dobaczewski, W. Nazarewicz, and R. Surman, *Phys. Rev. C* 60, 014302 (1999).
- [130] T. Marketin, D. Vretenar, and P. Ring, *Phys. Rev. C* 75, 024304 (2007).
- [131] T. Marketin, L. Huther, and G. Martínez-Pinedo, *Phys. Rev. C* 93, 025805 (2016).
- [132] Y. F. Niu, Z. M. Niu, G. Colò, and E. Vigezzi, *Phys. Rev. Lett.* 114, 142501 (2015).
- [133] Y. Niu, Z. Niu, G. Colò, and E. Vigezzi, *Physics Letters B* 780, 325–331 (2018).
- [134] F. Minato and K. Hagino, *Phys. Rev. C* 80, 065808 (2009).
- [135] E. Litvinova, C. Robin, and H. Wibowo, *Physics Letters B* 800, 135134 (2020).
- [136] J. Walecka, V. Hughes, and C. Wu, *Academis, New York USA* (1975).
- [137] W. Kohn and L. J. Sham, *Phys. Rev.* 140, A1133–A1138 (1965).
- [138] T. Nikšić, N. Paar, D. Vretenar, and P. Ring, *Computer Physics Communications* 185(6), 1808–1821 (2014).

- 
- [139] H. Kucharek and P. Ring, *Zeitschrift für Physik A Hadrons and Nuclei* 339(1), 23–35 (1991).
- [140] J. Berger, M. Girod, and D. Gogny, *Nuclear Physics A* 428, 23–36 (1984).
- [141] Y. Tian, Z.-y. Ma, and P. Ring, *Phys. Rev. C* 79, 064301 (2009).
- [142] Y. Takahashi and H. Umezawa, *International Journal of Modern Physics B* 10(13n14), 1755–1805 (1996).
- [143] H. Umezawa, H. Matsumoto, and M. Tachiki, *Thermo field dynamics and condensed states*, North-Holland, Netherlands (1982).
- [144] P. Sarriguren, E. Moya de Guerra, A. Escuderos, and A. Carrizo, *Nuclear Physics A* 635(1), 55–85 (1998).
- [145] D. Vale, Y. F. Niu, and N. Paar, *Phys. Rev. C* 103, 064307 (2021).
- [146] Y. Gambhir, P. Ring, and A. Thimet, *Annals of Physics* 198(1), 132–179 (1990).
- [147] J. Suhonen, *From Nucleons to Nucleus: Concepts of Microscopic Nuclear Theory*, Theoretical and Mathematical Physics, Springer Berlin Heidelberg (2007).
- [148] E. Yüksel, G. Colò, E. Khan, Y. F. Niu, and K. Bozkurt, *Phys. Rev. C* 96, 024303 (2017).
- [149] E. Yüksel, N. Paar, G. Colò, E. Khan, and Y. F. Niu, *Phys. Rev. C* 101, 044305 (2020).
- [150] C. Robin and E. Litvinova, *The European Physical Journal A* 52(7), 205 (2016).
- [151] D. Gambacurta, M. Grasso, and J. Engel, *Phys. Rev. Lett.* 125, 212501 (2020).
- [152] J. S. O’Connell, T. W. Donnelly, and J. D. Walecka, *Phys. Rev. C* 6, 719–733 (1972).
- [153] J. Walecka, *Theoretical Nuclear and Subnuclear Physics*, Theoretical Nuclear and Subnuclear Physics, Imperial College Press (2004).
- [154] H. Behrens and W. Bühring, *Nuclear Physics A* 162(1), 111–144 (1971).
- [155] Y. Niu, N. Paar, D. Vretenar, and J. Meng, *Physics Letters B* 681(4), 315–319 (2009).
- [156] K. Langanke, E. Kolbe, and D. J. Dean, *Phys. Rev. C* 63, 032801 (2001).

- 
- [157] J. P. Delaroche, M. Girod, J. Libert, H. Goutte, S. Hilaire, S. Péru, N. Pillet, and G. F. Bertsch, *Phys. Rev. C* 81, 014303 (2010).
- [158] S. E. Agbemava, A. V. Afanasjev, D. Ray, and P. Ring, *Phys. Rev. C* 89, 054320 (2014).
- [159] *National Nuclear Data Center (NNDC)*, <https://www.nndc.bnl.gov/>.
- [160] K. Yako, et al., *Phys. Rev. Lett.* 103, 012503 (2009).
- [161] Z. Niu, Y. Niu, H. Liang, W. Long, T. Nikšić, D. Vretenar, and J. Meng, *Physics Letters B* 723(1), 172–176 (2013).
- [162] Z. yu Ma, A. Wandelt, N. Van Giai, D. Vretenar, P. Ring, and L. gang Cao, *Nuclear Physics A* 703(1), 222–239 (2002).
- [163] Z. yu Ma, N. Van Giai, A. Wandelt, D. Vretenar, and P. Ring, *Nuclear Physics A* 686(1), 173–186 (2001).
- [164] C. Sullivan, E. O’Connor, R. G. T. Zegers, T. Grubb, and S. M. Austin, *The Astrophysical Journal* 816(1), 44 (2015).
- [165] K. Langanke and G. Martínez-Pinedo, *Nuclear Physics A* 673(1), 481–508 (2000).
- [166] E. Caurier, K. Langanke, G. Martínez-Pinedo, and F. Nowacki, *Nuclear Physics A* 653(4), 439–452 (1999).
- [167] *GSL scientific library*, <https://www.gnu.org/software/gsl/doc/html/integration.html>.
- [168] G. M. Fuller, W. A. Fowler, and M. J. Newman, *The Astrophysical Journal* 252, 715–740 (1982).
- [169] A. R. Raduta, F. Gulminelli, and M. Oertel, *Phys. Rev. C* 95, 025805 (2017).
- [170] E. O’Connor and C. D. Ott, *Classical and Quantum Gravity* 27(11), 114103 (2010).
- [171] S. E. Woosley and T. A. Weaver, *The Astrophysical Journal Supplement* 101, 181 (1995).
- [172] A. W. Steiner, M. Hempel, and T. Fischer, *The Astrophysical Journal* 774(1), 17 (2013).

- [173] H. Schatz, et al., *Nature* 505(7481), 62–65 (2014).
- [174] R. A. Herrera, C. W. Johnson, and G. M. Fuller, *Phys. Rev. C* 105, 015801 (2022).
- [175] G. Baym, T. Hatsuda, T. Kojo, P. D. Powell, Y. Song, and T. Takatsuka, *Reports on Progress in Physics* 81(5), 056902 (2018).
- [176] S. Aberg, H. Flocard, and W. Nazarewicz, *Annual Review of Nuclear and Particle Science* 40(1), 439–528 (1990).
- [177] E. Suraud, *Nuclear Physics A* 462(1), 109–149 (1987).
- [178] M. Abramowitz and I. Stegun, *Handbook of Mathematical Functions: With Formulas, Graphs, and Mathematical Tables*, Applied mathematics series, Dover Publications (1965).
- [179] J. Meng, *Nuclear Physics A* 635(1), 3–42 (1998).
- [180] A. Arzhanov, T. R. Rodríguez, and G. Martínez-Pinedo, *Phys. Rev. C* 94, 054319 (2016).
- [181] M. V. Stoitsov, J. Dobaczewski, W. Nazarewicz, S. Pittel, and D. J. Dean, *Phys. Rev. C* 68, 054312 (2003).
- [182] W. Pöschl, *Computer Physics Communications* 112(1), 42–66 (1998).
- [183] H. A. Bethe, *Phys. Rev.* 50, 332–341 (1936).
- [184] A. Bohr and B. Mottelson, *Nuclear Structure (In 2 Volumes)*, World Scientific Publishing Company (1998).
- [185] J. Besprosvany and S. Levit, *Physics Letters B* 217(1), 1–4 (1989).
- [186] T. Sil, J. N. De, S. K. Samaddar, X. Viñas, M. Centelles, B. K. Agrawal, and S. K. Patra, *Phys. Rev. C* 66, 045803 (2002).
- [187] P. Sarriguren, *Phys. Rev. C* 91, 044304 (2015).
- [188] P. Sarriguren, E. Moya de Guerra, and A. Escuderos, *Nuclear Physics A* 691(3), 631–648 (2001).

- [189] R. Álvarez-Rodríguez, P. Sarriguren, E. M. de Guerra, L. Paceaescu, A. Faessler, and F. Šimkovic, *Phys. Rev. C* 70, 064309 (2004).
- [190] F. Šimkovic, L. Paceaescu, and A. Faessler, *Nuclear Physics A* 733(3), 321–350 (2004).
- [191] D.-L. Fang, A. Faessler, V. Rodin, and F. Šimkovic, *Phys. Rev. C* 82, 051301 (2010).
- [192] D. P. Arteaga and P. Ring, *Phys. Rev. C* 77, 034317 (2008).
- [193] K. Yoshida and T. Nakatsukasa, *Phys. Rev. C* 83, 021304 (2011).
- [194] M. Martini, S. Péru, S. Hilaire, S. Goriely, and F. Lechaftois, *Phys. Rev. C* 94, 014304 (2016).
- [195] T. Nakatsukasa, T. Inakura, and K. Yabana, *Phys. Rev. C* 76, 024318 (2007).
- [196] P. Avogadro and T. Nakatsukasa, *Phys. Rev. C* 84, 014314 (2011).
- [197] A. Bjelčić and T. Nikšić, *Computer Physics Communications* 253, 107184 (2020).
- [198] T. Nikšić, N. Kralj, T. Tutiš, D. Vretenar, and P. Ring, *Phys. Rev. C* 88, 044327 (2013).
- [199] F. Mercier, A. Bjelčić, T. Nikšić, J.-P. Ebran, E. Khan, and D. Vretenar, *Phys. Rev. C* 103, 024303 (2021).
- [200] S. Péru and H. Goutte, *Phys. Rev. C* 77, 044313 (2008).
- [201] Y. Tian, Z.-y. Ma, and P. Ring, *Phys. Rev. C* 80, 024313 (2009).
- [202] M. Moshinsky, *Nuclear Physics* 13(1), 104–116 (1959).
- [203] L. Guo, W. L. Lv, Y. F. Niu, D. L. Fang, B. S. Gao, K. A. Li, and X. D. Tang, *Phys. Rev. C* 107, 014318 (2023).
- [204] Y. Zhang, A. Bjelčić, T. Nikšić, E. Litvinova, P. Ring, and P. Schuck, *Phys. Rev. C* 105, 044326 (2022).
- [205] H. D. Zeh, *Zeitschrift für Physik* 202(1), 38–48 (1967).
- [206] H. Fujita, et al., *Phys. Rev. C* 88, 054329 (2013).

- [207] V. Martin, J. L. Egido, and L. M. Robledo, *Phys. Rev. C* 68, 034327 (2003).
- [208] N. Popara, A. Ravlić, and N. Paar, *Phys. Rev. C* 105, 064315 (2022).
- [209] E. Leistenschneider, et al., *Phys. Rev. Lett.* 126, 042501 (2021).
- [210] F. Minato, Z. Niu, and H. Liang, *Phys. Rev. C* 106, 024306 (2022).
- [211] D. Varshalovich, A. Moskalev, V. Khersonskii, and W. S. (Singapur), *Quantum Theory of Angular Momentum: Irreducible Tensors, Spherical Harmonics, Vector Coupling Coefficients, 3nj Symbols*, World Scientific Pub. (1988).
- [212] H. Schopper, H. Behrens, and J. Jänecke, In *Landolt-Börnstein: Numerical Data and Functional Relationships in Science and Technology-New Series*, Springer (1969).
- [213] W. Bühring, *Nuclear Physics* 40, 472–488 (1963).

# Curriculum Vitae

**Name:** Ante Ravlić, mag. phys.

**E-mail:** aravlic@phy.hr

**Affiliation:** University of Zagreb, Faculty of Science, Department of Physics, Bijenička cesta 32, 10000 Zagreb, Croatia

## Education

**2014-2019:** University of Zagreb, Faculty of Science, Research oriented study of Physics Master's thesis: "*Stellar electron capture rates on nuclei based on relativistic energy density functionals*", supervisor: prof. dr. Nils Paar (Summa cum laude)

**2019 - Present:** University of Zagreb, Faculty of Science, PhD study in theoretical nuclear physics, PhD thesis: "*Stellar weak interaction processes at finite temperature based on the relativistic energy density functional theory*", supervisor: prof. dr. Nils Paar

## Work experience

**2019 - Present:** Research assistant at University of Zagreb, Faculty of Science

## Awards and fellowships

1) **University of Zagreb Rector's Award (2018):** for research work on project "*Nuclear Superconductivity*" supervised by dr. Suzana Szilner (Ruđer Bošković Institute, Zagreb) and prof. dr. Matko Milin (University of Zagreb, Faculty of Science, Zagreb)

2) **Faculty of Science Dean's Award (2019)**

## Participation in conferences

- 1) YIPQS long-term workshop "Mean-field and Cluster Dynamics in Nuclear Systems 2022 (MCD 2022)", Kyoto, Japan, 9th May – 17th June 2022, online talk on "*Constraining the stellar weak-interaction rates within the relativistic energy density functional theory*"
- 2) STFC Summer School, Sheffield, United Kingdom, 27th March – 3rd April 2022, talk on "*Stellar weak-interaction rates and nuclear energy density functional theory*" (**Best talk award**)
- 3) The 16th International Symposium of Nuclei in the Cosmos (NIC-XVI), Online, 21–25th September 2021, poster presentation "*Description of weak-interaction rates within the relativistic energy density functional theory*" (**Best poster award**)
- 4) Euroschool on exotic ion beams 2021, Online, 13 – 17th September 2021, poster presentation "*Finite-temperature linear response theory based on the point-coupling relativistic energy density functionals*"
- 5) Nuclear burning in massive stars, International conference in Nuclear Astrophysics, Online, 26-30th July 2021, talk on "*Application of relativistic energy density functional theory in description of stellar weak-interaction rates*"
- 6) NUclear physics School for Young Scientists (NUSYS-2019), Lanzhou, China, 12–17th August 2019, poster presentation "*Electron capture on nuclei at finite temperature based on relativistic energy density functional*"
- 7) Nuclear and astrophysics aspects for the rapid neutron capture process in the era of multi-messenger observations, Trento, Italy, 1–5th July 2019, talk on "*Electron capture on nuclei at finite temperature based on relativistic energy density functional*"
- 8) Winter school of Nuclear Astrophysics, Rußbach am Paß Gschütt, Austria, 10–16th March 2019, talk on "*Electron capture in presupernovae stars*"
- 9) International Conference of Physics Students (ICPS), Helsinki, Finland, 8–14th August 2018
- 10) Summer School in Particle and Astroparticle Physics (GraSPA), Annecy-le-Vieux, France, 20–26th July 2017



## Invited seminar talks

- 1) "*Description of stellar weak-interaction rates within the relativistic energy density functional formalism*", GSI Theorie Seminar, GSI/FAIR, Darmstadt, Germany, 25.10.2022.

## Research visits and internships

- 1) GSI/FAIR, Darmstadt, Hessen, Germany, 10th October – 18th December 2022 - project "*Beta-decay rates for r-process nuclei*". Host: Prof. Gabriel Martínez-Pinedo
- 2) FRIB/Michigan State University, East Lansing, Michigan, United States, 1st June – 31st July 2022 - project "*Large-scale calculation of electron-capture rates for core-collapse supernovae simulations*". Host: Prof. Remco Zegers, Co-Host: Prof. Witold Nazarewicz.
- 3) Yildiz Technical University, Istanbul, Turkey, 1st February–2nd March 2020 - collaboration on project "*Finite-temperature beta-decay*". Host: dr. Esra Yüksel.
- 4) University of Lanzhou, Lanzhou, China, 4–11th August 2019 - collaboration on project "*Electron capture in core-collapse supernovae*". Host: Prof. Yifei Niu
- 5) Johannes Gutenberg University, Mainz, Germany, October–December 2018 - Dark matter direct detection, XENON1T experiment. Supervisor: Prof. Uwe Oberlack

# List of Publications

1. **A. Ravlić**, E. Yüksel, Y.F. Niu, G. Colò, E. Khan and N. Paar, "*Stellar electron-capture rates based on finite-temperature relativistic quasiparticle random-phase approximation*", Phys. Rev. C 102, 065804 (2020) <https://journals.aps.org/prc/abstract/10.1103/PhysRevC.102.065804>
2. **A. Ravlić**, E. Yüksel, Y.F. Niu, and N. Paar, "*Evolution of  $\beta$ -decay half-lives in stellar environments*", Phys. Rev. C 104, 054318 (2021) <https://journals.aps.org/prc/abstract/10.1103/PhysRevC.104.054318>
3. **A. Ravlić**, Y.F. Niu, T. Nikšić, N. Paar and P. Ring, "*Finite-temperature linear response theory based on relativistic Hartree Bogoliubov model with point-coupling interaction*", Phys. Rev. C 104, 064302 (2021) <https://journals.aps.org/prc/abstract/10.1103/PhysRevC.104.064302>
4. S. Giraud, R. G. T. Zegers, B. A. Brown, J. M. Gabler, J. Lesniak, J. Rebenstock, E. M. Ney, J. Engel, **A. Ravlić**, and N. Paar, "*Finite-temperature electron-capture rates for neutron-rich nuclei near  $N = 50$  and effects on core-collapse supernova simulations*", Phys. Rev. C 105, 055801 (2022) <https://journals.aps.org/prc/abstract/10.1103/PhysRevC.105.055801>
5. T. Oishi, **A. Ravlić**, and N. Paar, "*Symmetry breaking of Gamow-Teller and magnetic-dipole transitions and its restoration in calcium isotopes*", Phys. Rev. C 105, 064309 (2022) <https://journals.aps.org/prc/abstract/10.1103/PhysRevC.105.064309>
6. N. Popara, **A. Ravlić**, and N. Paar, "*Two-neutrino double- $\beta$  decay matrix elements based on a relativistic nuclear energy density functional*", Phys. Rev. C 105, 064315 (2022) <https://journals.aps.org/prc/abstract/10.1103/PhysRevC.105.064315>

## Submitted for publication

7. **A. Ravlić**, E. Yüksel, T. Nikšić, and N. Paar, "*Expanding the limits of nuclear stability: Drip lines for hot nuclei*" (2022), in review at Nature Communications <https://www.researchsquare.com/article/rs-2325169/v1>
8. E. M. Ney, **A. Ravlić**, J. Engel, and N. Paar, "*Elucidating the finite temperature quasiparticle random phase approximation*" (2022), in review at Phys. Rev. C <https://arxiv.org/abs/2209.10009>

## Conference proceedings

1. **A. Ravlić**, E. Yüksel, Y. Niu, N. Paar, G. Colò, and E. Khan, "*Description of weak-interaction rates within the relativistic energy density functional theory*", EPJ Web of Conferences 260, 11032 (2022) [https://www.epj-conferences.org/articles/epjconf/abs/2022/04/epjconf\\_nic16th2022\\_11032/epjconf\\_nic16th2022\\_11032.html](https://www.epj-conferences.org/articles/epjconf/abs/2022/04/epjconf_nic16th2022_11032/epjconf_nic16th2022_11032.html)